DOCTOR OF PHILOSOPHY

Finite element simulation of the micromagnetic behaviour of nanoelements

Ridley, Philip Harold William

Award date:
2000

Awarding institution:
Bangor University

Finite Element Simulation of the Micromagnetic Behaviour of Nanoelements

Philip Harold William Ridley

Thesis submitted to the University of Wales in Candidature for the degree of Doctor of Philosophy

March 2000

School of Informatics

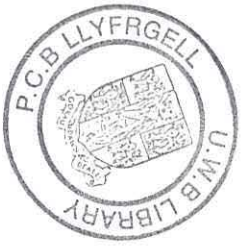

To my mother and father

Summary

Over recent years the investigation into the magnetic behaviour of nanostructured permalloy has become more advanced due to improvements in numerical micromagnetic methods on the theoretical side and high accuracy electron-beam lithography methods experimentally. The interest in such structures of magnetic material is increasing mainly due to the possible potential use in future high-density magnetic storage media applications.

When the material is discretised into a nanoelement structure at the sub micron level theoretical micromagnetic techniques may be employed in order to investigate the magnetization behaviour. This thesis describes a theoretical study of the hysteresis and domain behaviour in thin film permalloy nanoelements.

To carry out our investigations we have developed a dynamical micromagnetic model based on the use of the finite element method. The results presented in this thesis begin with a test of the performance of our model. We then proceed with an investigation into the effect of size, elongation and geometry on the transition states for single nanoelements. The investigation is then extended to look at the magnetization behaviour of arrays of interacting nanoelements in relation to their separation and material properties.

The reversal mechanism of the arrays is very sensitive to the degree of disorder. In the case of an aligned uniaxial anisotropy a highly symmetric cooperative switching mechanism is observed. A large anisotropy has the effect of stabilizing states during the reversal process leading to distinctive switching. A random anisotropy breaks this high symmetry sufficiently to reduce the cooperative switching leading to a relatively random reversal of individual elements. The theoretical predictions are compared with experimental observations.

Contents

List of Tables

List of Figures

Acknowledgements

I would like to begin by expressing thanks to my supervisors, Prof. R. W. Chantrell and Dr. G. W. Roberts for taking me on as a PhD student.

A special thank you goes to the School of Informatics for the provision of a departmental studentship to enable me to pursue this work. I would also like to gratefully acknowledge the financial support of the Defence Evaluation and Research Agency at Farnborough.

The duration of my research has undoubtedly been made more enjoyable by being part of the Computational Magnetism Group. At this point I would like to say a special thanks to Dr. Geoff Coverdale, Jonathan Hannay, Huw Vaughan-Jones, Jackie Jones, Dr. Roman Smirnov-Rueda, Dr. Nick Walmsley and Dr. Mike Wongsam for their help in one form or another over the last few years.

I also express my gratitude to Roy and Gareth for their continued guidance and encouragement throughout the course of this work. Thanks again to Roy for giving me the opportunity to attend several scientific conferences on magnetism. Thanks as well to Gareth for the essential help on the practical implementation of the model.

Acknowledgement also goes to Dr. T. Schrefl of the Institute of Applied and Technical Physics, Vienna University of Technology for useful discussion and Dr. K. J. Kirk of the Department of Physics and Astronomy at the University of Glasgow for useful help and discussion on the larger systems.

My thanks must also go out to members past and present of the experimental magnetics group of Prof. K. O' Grady. Finally, thanks to Informatics for providing a cheerful environment and thanks again to Geoff, Jonathan, Huw, Jackie and Nick for all the memorable events over the last few years.

Chapter 1

Magnetic Materials

1.1 Introduction

The history of magnetism and magnetic materials began when the attractive power of spontaneously magnetized magnetite (Fe_3O_4) was discovered, although the date of this is not known. Early interest in magnetism was due to its application as a navigation aid, the compass. Around 1269AD Peregrinus made a formal explanation of the fact that there existed regions on a magnetic material, termed **magnetic poles**, which would attract a piece of iron more strongly than the rest of the material. Using this scientific knowledge the pivotal compass could be developed.

The interest in magnetism was lost by scientists for many centuries until Gilbert (1540-1603) explained the reason for the existence of magnetic poles and that the Earth could be considered as a huge magnet itself. This encouraged scientists to look into the phenomenon of magnetism. With the aid of mathematics by the eighteenth century the phenomenon of magnetism could be expressed in terms of equations. In 1785 Coulomb (1736-1806) was able to formulate the inverse square law for the magnetic field and also around this time Poisson (1781-1840) published work which forms the basis to the formulation of modern day theoretical magnetics.

This work which Poisson published formulated an expression for the magnetic

force of a magnet in terms of a volume and a surface integral as a function of the magnetization intensity. This theory was then built on by Green and Gauss who produced much work on magnetostatic and electrostatic theory. On the experimental side, the work of Physicists Oersted, Biot and Savart and Ampêre proved that there was a mutual magnetic reaction between an applied electric current and a magnet.

The first recognised study of the magnetic properties of a material was due to the Physicist Faraday in 1831 who discovered electromagnetic induction. Later in the nineteenth century, Maxwell (1831-1879) translated this theory into mathematics. This work laid the mathematical foundation of the modern day theoretical study of magnetic materials.

1.2 Magnetic quantities

The vast majority of materials which exist in the World have magnetic properties which for engineering purposes are the same as those of a vacuum. The exceptions to this are iron(Fe), cobalt(Co) and nickel(Ni) and a number of rare earth magnetic materials. These have the feature that they exhibit magnetization in zero applied magnetic field, i.e. they are spontaneously magnetized. Before explaining more about the origins of magnetism we will now consider how magnetization is measured and what this reveals about the magnetic behaviour of a material.

1.2.1 Magnetic fields

When a piece of iron is subject to an external magnetic field H it will become magnetized. The extent of the magnetization M in the iron will be dependent upon the strength of the field. We therefore need a way of determining this field strength for different materials.

The strength of the external magnetic field H is measured in oersteds (Oe) in the cgs system and the magnetization M is measured in emu/cm^3. Absolute mea-

surement of a magnetic field can be obtained by Nuclear Magnetic Resonance (NMR) by using the spin magnetic moments of nuclei. In practice a Hall probe magnetometer can be used to measure the intensity of H and output can easily be monitored on a PC, however this method must first be calibrated using NMR results.

1.2.2 Magnetic susceptibility

The magnetic susceptibility χ is the single most important characteristic of a material. It is defined by

$$\chi = \frac{M}{H} \tag{1.1}$$

It may be measured directly from a magnetization curve or directly by force and A.C. methods [1]. Materials with small and negative χ include **diamagnets**, for small and positive χ we have **paramagnets** and **antiferromagnets** which all retain no magnetization when the field is removed. Whereas those which posses large and positive χ are **ferromagnets** and **ferrimagnets**.

1.2.3 Magnetic moments

The magnetic properties of a material arise at the atomic level. The atomic magnetic moment has contributions from the electron motion around the atom and also from the electron spin magnetic moment. The magnetic moment is defined by the vector sum of all orbiting electronic moments. This gives a convenient way of classifying types of magnetization from the atomic level. There are only two possibilities that may arise from the summation of moments, either they all cancel out so that the atom as a whole has no magnetic moment termed diamagnetism or we are left with a net magnetic moment which occurs in paramagnetism, ferromagnetism, antiferromagnetism and ferrimagnetism.

1.3 Ferromagnetism

We have mentioned the existence of spontaneously magnetized iron but how can we explain this ability to exhibit magnetization in zero applied field. This may be achieved by the following.

1.3.1 Mean field theory of ferromagnetism

In 1895 Curie made a systematic study of the susceptibility of many materials over a range of temperatures. It was found that the susceptibility was independent of temperature for diamagnets, but it varied inversely with the absolute temperature for paramagnets. This was later shown to be a special case of the Curie-Weiss law. The formal theory of ferromagnetism was proposed by P. J. Wiess in 1907. This theory assumes the existence of a magnetic field within the material whose magnitude is proportional to the bulk magnetization M, i.e.

$$B_m = \lambda M \tag{1.2}$$

where B_m is the mean field and λ is a constant dependent upon the temperature of the material. This leads to a relationship between the temperature and the susceptibility as

$$\chi = \frac{C}{T - T_c} \tag{1.3}$$

where C is the Curie constant, T the absolute temperature and

$$T_c = C\lambda M \tag{1.4}$$

which is another material dependent constant known as the paramagnetic Curie temperature. For $T > T_c$ the material acts as a paramagnet. Equation (1.3) is often referred to as the Curie-Weiss law.

1.3.2 Atomic magnetism and exchange forces

The Curie-Weiss law shows that ferromagnetism may be explained by invoking a large internal field proportional to the magnetization. This model is successful in

predicting the variation of magnetization with temperature but neglects the origin of the internal field. This internal field is actually very large and cannot arise from magnetic sources alone.

The origin of this internal field was first explained by Heisenberg who showed that the molecular field arose from exchange forces which are quantum mechanical in origin. When two atoms are bought closer together, the electrostatic forces between them may be either attractive or repulsive. These may be found by Coulomb's law. The exchange force is a direct consequence of the Pauli exclusion principle. This states that two electrons can have the same energy only if they have opposite spins. As a consequence we would expect that as atoms are forced closer together the most stable configuration will be with the spins on neighbouring atoms anti-parallel, i.e. non-ferromagnetic order should result. However, the exchange force arises in a very subtle way. Because of the indistinguishability of electrons we must take into account the possibility that two electrons on neighbouring atoms simply exchange places. It is this which leads to exchange energy between two neighbouring atoms. The exchange energy is responsible for the ferromagnetic coupling. It can be shown that two atoms i and j with spins $\boldsymbol{S}_i$ and $\boldsymbol{S}_j$ are exchange coupled with an energy, E_{ex} given by

$$\begin{aligned} E_{ex} &= -2J_{ex}\boldsymbol{S}_i \cdot \boldsymbol{S}_j \\ &= -2J_{ex}S_iS_j\cos\theta \end{aligned} \tag{1.5}$$

where J_{ex} is known as the exchange integral and θ is the angle between the spins.

However this is an atomic level quantity, for our micromagnetic considerations this phenomena may be formulated as follows.

Assuming a slowly spatially varying magnetization the exchange energy may be written as

$$E_{ex} = J_{ex}S^2\sum_{n.n}\phi_{i,j}^2 \tag{1.6}$$

with the summation being carried out over nearest neighbours. The $\phi_{i,j}$ represents the angle between two neighbouring spins. For small angles $|\phi_{i,j}| \approx |\boldsymbol{m}_i - \boldsymbol{m}_j|$. A first order expansion in a Taylor series is

$$|\boldsymbol{m}_i - \boldsymbol{m}_j| = |(\boldsymbol{s} \cdot \nabla)\boldsymbol{m}| \tag{1.7}$$

where $\boldsymbol{s}$ is a position vector joining lattice points i and j.
Substituting equation (1.7) into equation (1.6) gives

$$E_{ex} = J_{ex} S^2 \sum_i \sum_{n.n} |(\boldsymbol{s} \cdot \nabla)\boldsymbol{m}|^2 \tag{1.8}$$

where the second summation is over nearest neighbours. Changing the first summation to an integral over the whole body we obtain the micromagnetic formalism for cubic crystals as

$$E_{ex} = \int_V C\,|\nabla \boldsymbol{m}|^2\, dV \tag{1.9}$$

where C is a material dependent constant and $\boldsymbol{m}$ is a unit vector parallel to the local spin of the magnetic moment. Exchange is fundamental to ferromagnetic behaviour.

1.3.3 Magnetic domains

We know that ferromagnetic materials exhibit spontaneous magnetization but they can also exist in a demagnetized state. To reconcile these facts we must consider the existence of **magnetic domains**.

Domains are regions of a material in which the magnetization is saturated, i.e. the magnetization M has a value equal to the spontaneous magnetization. However in the demagnetized state the domains are oriented at random so that the total magnetization is zero.

It was pointed out in ref. [2] that the existence of magnetic domains was a consequence of exchange, anisotropy and magnetostatic energies that are present in a ferromagnetic material. The existence of domain structures arise from the need

to balance the magnetostatic and the exchange energy. The tendency of a material is to lower the magnetostatic energy which is $\propto M^2$. The reduction in the magnetization, M is achieved by the material splitting up into domains. Within each domain the magnetization remains parallel in order to minimize the exchange energy but the overall orientation of the direction of the domains is such that M itself is lowered.

Some possible domain configurations for a hypothetical thin film ferromagnetic material will now be demonstrated.

Since the thickness of the material is very small, we can neglect the domain structure in this direction so the patterns can be represented in two dimensions as shown in Figure 1.1.

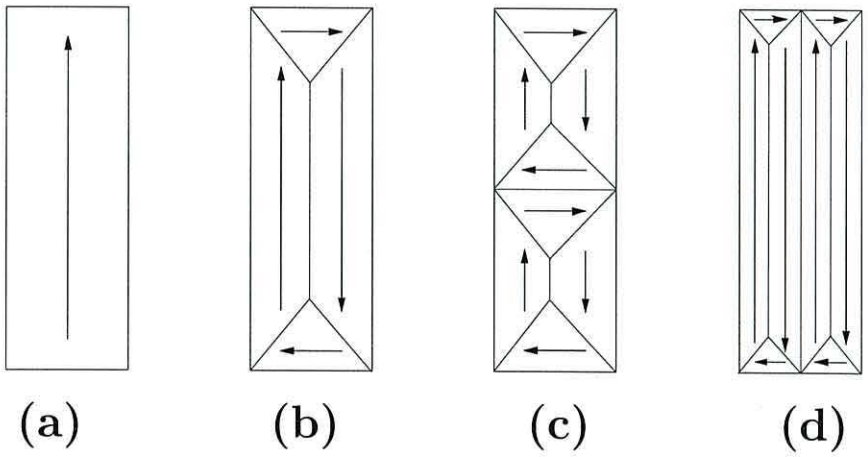

Figure 1.1: Some possible domain configurations in a ferromagnet

In Figure 1.1(a) the net magnetization would be the saturation value M_s, whereas (b), (c) and (d) would exhibit zero net magnetization. The production of the domain wall itself requires energy, as a consequence the energy reduction by splitting up into a small number of domains may not be sufficient to compensate for the increased energy associated with the domain walls involved as shown in Figure 1.1(a).

Experimental techniques used to produce images of domain structures include

- **Bitter pattern** method which involves introducing a colloidal solution into a ferrofluid placed on the surface of a magnetic material.
- **Faraday** and **Kerr** magneto-optical methods whereby a linearly polarised beam of light is aimed at the specimen.
- **Transmission electron microscopy (TEM)**, **Foucalt imaging** and **Lorenz microscopy** where electrons are deflected by the magnetic field gradient in the specimen producing an image of the domains. These methods allow high resolution images to be produced showing fine detail in the domain structure.

1.4 Anisotropy

The term anisotropy refers to the fact that the properties of a magnetic material are dependent on the directions in which they are measured. Anisotropy makes an important contribution to Hysteresis in magnetic materials and is therefore of considerable practical importance. Anisotropy arises from a number of possible causes.

1.4.1 Crystal or Magnetocrystalline Anisotropy

This is the only contribution intrinsic to the material. It has its origins at the atomic level. Firstly in materials with a large anisotropy there is a strong coupling between the spin and orbital moments within an atom. In addition, the atomic orbitals are generally non-spherical.

Because of their shape the orbits prefer to lie in certain crystallographic directions. The spin-orbit coupling then assures a preferred direction for the magnetization termed the **easy direction**. To rotate the magnetization away from the easy direction costs energy - the anisotropy energy. The anisotropy energy depends on the lattice structure of the material.

1.4.2 Shape Anisotropy

Shape anisotropy is caused by the geometry of the material. A practical example of this is in particulate recording media where particles with aspect ratios of between 4 : 1 to 10 : 1 are used. The Hysteresis behaviour of the particles is then directly related to the shape anisotropy caused by their aspect ratios.

1.4.3 Stress Anisotropy

This arises from the change in atomic structures as a material is deformed. It is related to the phenomenon of 'magnetostriction' which is important for magnetic sensor applications.

1.5 Properties of ferromagnets

So far we have mentioned the basic physical ideas behind ferromagnetic materials but in order to investigate their suitability to magnetic recording applications, we must mention their fundamental magnetic properties.

1.5.1 Magnetic saturation

Consider an initially unmagnetized ferromagnet shown in Figure 1.2(a). When an high external field is applied to a ferromagnet, the magnetic moments will align themselves in parallel with this and the material will become magnetized as seen in Figure 1.2(b). If we measure the magnetization M of the ferromagnet in relation to the applied field we see there is a limiting value of M which will get no larger even if the external field is increased. This value M_s is known as the saturation magnetization of the material. M_s represents a value of M for which all the magnetic moments are aligned in the external field direction.

1.5.2 Hysteresis

Hysteresis is the phenomenon whereby the magnetic state depends on the history of the sample in terms of the sequence of application of an external magnetic field. A

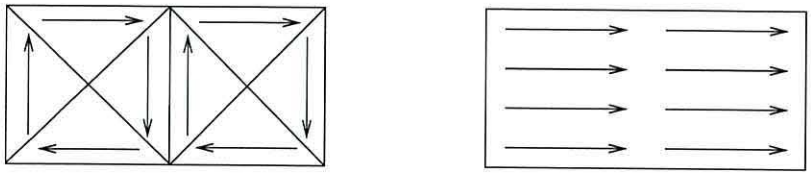

Figure 1.2: Moments in a ferromagnetic material

practical application of the hysteresis behaviour is to give the material a 'memory'. A **hysteresis curve** which is a plot of the magnetization M against the applied field H may be obtained by applying an external field H to the sample which is increased until $M = M_s$ this is represented on Figure 1.3 by the path ab and is known as the **magnetization curve**. The field is then gradually reduced by a fixed field step and we notice that M does not follow the initial path ab but a new one bc. The value of M at c is called the **remanence** of the ferromagnet. The value of the external field needed to make M zero is known as the **coercivity** at d of the ferromagnet and the curve cd is known as the **demagnetizing curve**. Gradually decreasing the applied field further will produce a magnetization M negative to the saturation value at e. The field is then increased with reverse polarity to produce the curve $efgb$. If this processes is repeated the hysteresis loop $bcdefgb$ will be traversed again. The hysteresis loop is influenced by the material anisotropy which produces an energy barrier for the applied field to overcome and thus contributes to the width of the loop.

1.6 Applications of magnetic materials

For technological applications ferromagnetic materials are the most important class of magnetic materials. This is due to their high magnetic susceptibility which enables high magnetic inductions to be obtained with the smallest of applied fields and also their ability to retain magnetization. Further explanation of ferromagnetism can be found in Jiles [3] and Carter [4].

The properties of the variety of magnetic materials which now exist can be controlled by varying the proportions of the constituent components which make up the alloy. They are also strongly influenced by the ways in which the material is prepared, especially any heat treatments used. More detailed discussion may be found in Cullity [5]

From a practical point of view the main division among magnetic materials is between "hard" and "soft" materials. The difference between these two classes of material can be seen in Figure 1.4. Soft materials are characterized by having narrow hysteresis loops, low remanence and small coercivity (they are easy to demagnetize). Hard magnetic materials have broad hysteresis loops, high remenance and a high coercivity. Such materials are difficult to demagnetize and are therefore used for making permanent magnets and magnetic recording.

Permanent magnets are used in a wide variety of applications from consumer and automotive electronics such as loudspeakers and DC motors to biosurgical and industrial uses such as ferromagnetic probes, separators and sensors. The main cause

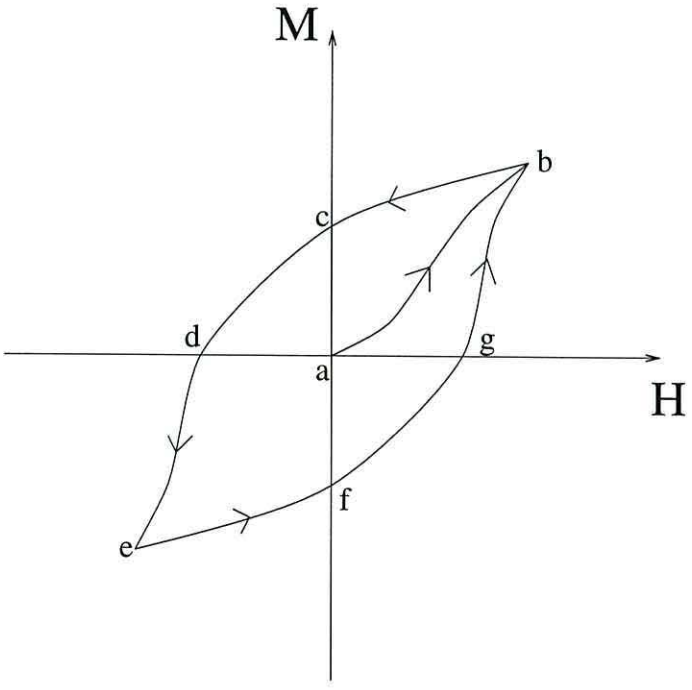

Figure 1.3: Hysteresis loop showing magnetization paths

of hysteresis is the presence of magnetocrystalline anisotropy. In materials with this present the magnetic moments will be in the lowest energy state when they are aligned with the easy direction, the presence of any strong external field will cause them to find new lowest energy states and thus causes a switching action of the moments. Another way of controlling hysteresis is by adding impurities such as non magnetic materials to ferromagnets.

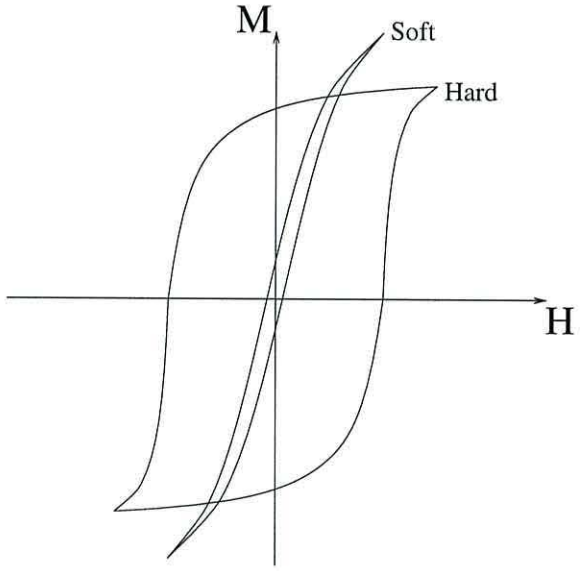

Figure 1.4: Hysteresis loops for Hard and Soft magnetic materials

1.7 Stoner-Wohlfarth Theory

Usually we observe many domain configurations in ferromagnetic specimens. However under certain circumstances, it is possible to observe single domain states. The formation of such states is dependent upon the size of the specimen,the magnetostatic energy and exchange forces. The magnetic hysteresis of non-interacting single domain particles with uniaxial shape anisotropy has been investigated theoretically by Stoner and Wohlfarth [6]. They investigated the behaviour of a single domain ellipsoid of revolution when subjected to increasing magnetic fields at various angles to the easy axis of magnetization of the ellipsoid.

The theory of Stoner and Wohlfarth describes the magnetization process of single domain particles with uniaxial anisotropy as a result of particle shape and size. The theory is based on energy minimization. The magnetization is assumed to be of uniform magnitude and direction, represented by the magnetic moments. The most basic and understood form of magnetization process is rotation. If the spins rotate as a whole in a parallel fashion, this motion is referred to as **coherent rotation** as opposed to **incoherent rotation** where the directions of the spins will vary.

For a given material we can represent the angle of orientation of the magnetization M with the uniaxial anisotropy (easy) direction by θ. The anisotropy energy density is then given by

$$E_a = -K \sin^2 \theta \tag{1.10}$$

where K is the uniaxial anisotropy constant.

The component of magnetization in the direction of the applied field is then given by

$$\begin{aligned} M &= M_s \cos \theta \\ &= \frac{H M_s^2}{2K} \end{aligned} \tag{1.11}$$

Where H_k is the applied field strength needed to saturate the sample, i.e. for $H > H_k$ the magnetization, $M = M_s$.

Two interesting situations can now be investigated. When a field is applied perpendicular to the easy axis direction there will be torques on the magnetization by the applied and anisotropy fields and the magnetization will align itself with the applied field and create no hysteresis as shown in Figure 1.5(a). However, when a field is applied parallel to the easy axis direction the magnetocrystalline anisotropy will keep the magnetization in its original direction. When the field becomes strong enough in the opposite direction this causes the magnetization to line up parallel. The magnetization can therefore be made to follow the direction of the applied field and therefore create hysteresis as in Figure 1.5(b).

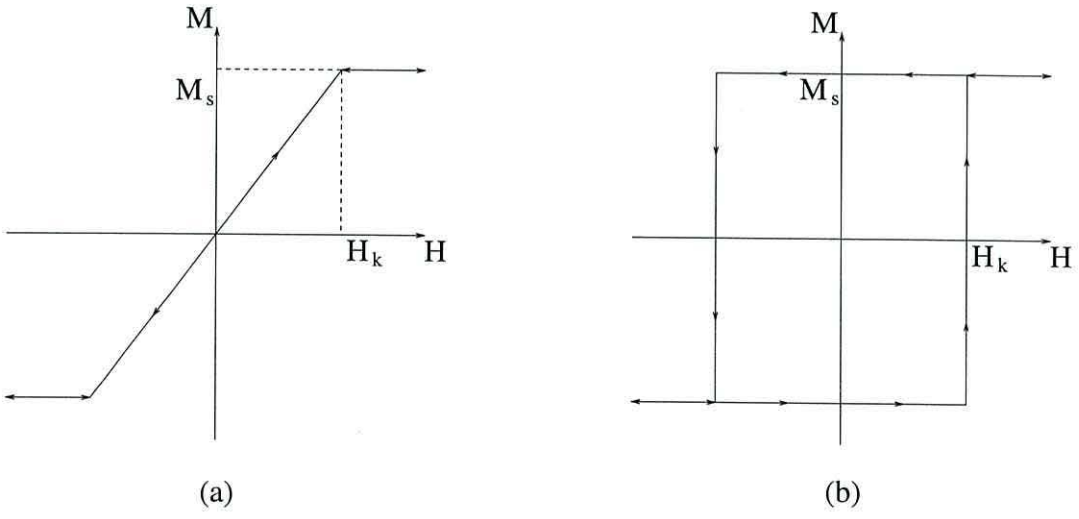

Figure 1.5: Hysteresis loops for single a domain particle with applied field (a) perpendicular and (b) parallel

1.8 Magnetic recording

The modern day methods of electronic information storage rely on magnetic recording processes. Magnetic recording was first demonstrated by the Danish engineer

Poulson who in 1898 created a device called the telegraphone which recorded acoustic signals on a ferromagnetic wire using an electromagnet connected to a microphone. This technology evolved further when in 1927 magnetic tape was invented which could be used in the audio recorders developed in 1948. Since the 1940s there has been much improvement in the technology due to the growth in the availability of new materials for recording (**recording media**). Digital recording for computers was developed by IBM in the mid 1950s and video recording soon followed

Magnetic recording is probably the main reason for the majority of current scientific investigation and research into magnetization processes in recording media. There is much commercial interest from the point of view of information technology due to the demanding storage requirements of computer operating systems on hard disks and their software packages and in entertainment such as audio compact discs and digital video discs. The current state of the art storage density capability is 36GB/sq.in.

Much literature exists on magnetic recording such as Bertram (1994) [7]. The technology behind magnetic recording is far beyond the discussion here but one application of the results provided by our work is to gain an insight into the magnetization processes in a recording medium. Before going any further, it is useful to explain the basics behind the magnetic recording process.

The recording process involves both writing an imprint to the medium and reading from the medium. To make a magnetic imprint onto the media an inductive process is used via electrical impulses from coils wound around an electromagnet which is in the shape of a toriod. The writing head is made from a small pole gap cut into the toroid. When the media is placed below the gap a fringing field causes a change in the magnetization behaviour on the media.

Reading from the media is performed by passing it below a read head. Once the

magnetic imprint on the media is below the read head there will be a fluctuation in the flux density in the magnetic core of the read head. The stray field associated with the imprint on the media (fringing field) will pass through the coil giving rise to an induced voltage which is proportional to the rate of change of the magnetic flux linking the coil. The basic recording process is shown in Figure 1.6, where I is the input current, V is the direction of motion of the media and d is the pole gap.

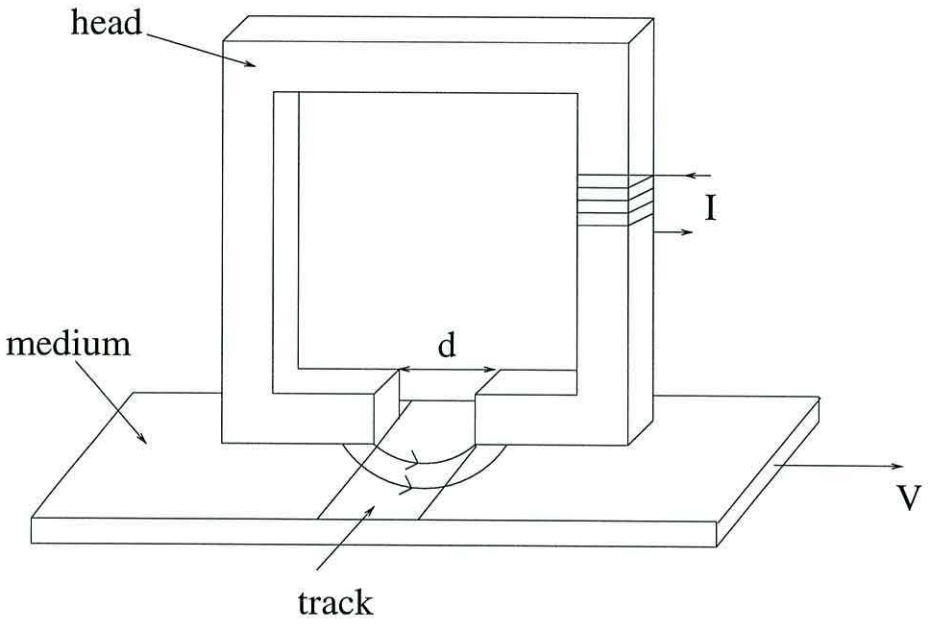

Figure 1.6: The magnetic recording process

The patterns of recorded data are referred to as written **bits**. The recording heads are usually made from soft magnetic materials with $d = 0.3\mu$m. The important criteria for determining a good magnetic material for the head is a high **saturation magnetization** in order to make a large magnetic imprint on the media and a low **remanence** to ensure that no writing takes place when the current is switched off. Typical materials possessing these attributes are AlFe, NiFe (permalloy) and CoZr (cobalt-zirconium). During the writing process, the magnetization may be oriented in different directions relative to the direction of motion of the media, when in the same direction the media is termed **longitudinal** in comparison to

transverse and **perpendicular**, when the media is written to in a transverse and perpendicular direction respectively with respect to the direction of the motion of the media. For a detailed discussion of magnetic recording the tutorial review article by Mallinson [8] is very appropriate.

The requirement of modern day magnetic recording is higher density storage, this is achieved by reducing the track width which is limited by the gap width in the head and by making the bits smaller. The limiting factor in this criteria is a reduction in signal, hence inductive heads are no longer viable and are currently being replaced by Magnetoresistive (MR) sensors.

Magnetoresistance is a change in the electrical resistance of certain materials when exposed to an applied field. This is a very sensitive way to detect the stray field above the transitions between two bits of information. It is not surprising to realise that magnetoresistive heads are now being used in current hard disc technology. A new phenomena Giant Magnetoresistance (GMR) has recently been discovered in certain materials and it is predicted that GMR devices will be predominant by early this century and represent the ultimate sensitive readback device.

1.9 Material requirements

The basic physical attribute which makes a material suitable for magnetic recording is non-equilibrium behaviour. This can be considered as introducing a memory which obviously is essential to any means of information storage. In the case of a magnetic material the non-equilibrium behaviour is represented by a **hysteresis** loop obtained by measuring the magnetization as the applied field is cycled .

A vibrating sample magnetometer (VSM) is the instrument used to test the magnetic material to determine its suitability as a recording medium from the criteria that the material should have

- a high magnetization remanence enabling information to be retained after

the writing process

- a high saturation magnetization which will give a large signal during the reading process

- a high coercivity to prevent erasure of the recorded information. The coercivity should be such that a small external field will not demagnetize the recorded information

The ratio between the remanence and the saturation magnetization of the material defines the **saturation squareness** of the material.

Due to the increasing power of magnetic imaging techniques, the magnetic recording medium has been found to possess structures which are quite complicated. Nowadays mostly **particulate** media is used for magnetic recording, this type of media is made of particles which are usually elongated and are single domain e.g. oxides of iron, oxides of chromium (CrO_2) and barium ferrite (BaFe). Particulate media are used for recording on flexible media.

The usual material for magnetic disk recording is of the thin metallic film type which is made up of small areas of magnetization. The granular nature is necessary to achieve a high coercivity.

A type of recording media which is being investigated for future high density applications is **patterned** media. This type of metallic thin film is composed of a discrete number of areas of magnetic material which are well defined geometric shapes. This is to reduce the signal to noise ratio and increase the recording density.

Investigation into the magnetic properties of this type of media due to the dependence upon the shapes of the geometrical regions of magnetization, their size and separation is the subject of much current research in magnetism including part of this thesis. Imaging techniques such as transmission electron microscopy (TEM) and lithographic techniques are used by experimentalists to produce this type of

media and due to the recent advances in these methods the sizes and shapes of the particles within the media can be controlled by dimensions at the sub micron level.

1.10 Theory of micromagnetics

Previously we have mentioned the behaviour of the net magnetization of a ferromagnetic material in terms of a magnetization vector, $\boldsymbol{M}$ and explained its behaviour in terms of Stoner-Wohlfarth Theory. We now turn our attention to the continuum theory of micromagnetics which was formulated by Brown [9] and was based on an energy minimization approach formally known as Brown's equations. These equations are the final step in the formulation of classical micromagnetics. Firstly, if $\boldsymbol{m}$ is a unit vector parallel to $\boldsymbol{M}$, then the total energy is defined as

$$E_{tot} = \int_V \left(A \left| \nabla \boldsymbol{m} \right|^2 + f_a(\boldsymbol{m}) - M_s(\boldsymbol{H}_{app} \cdot \boldsymbol{m}) - \frac{1}{2} M_s(\boldsymbol{H}_d \cdot \boldsymbol{m}) \right) dV \qquad (1.12)$$

which has contributions from the exchange, anisotropy, external and demagnetizing energies respectively. The approach is to minimize equation (1.12) using standard variational principles. Essentially setting the first variation of the total energy to zero leads to two equations. The first is a surface equation

$$2A \left(\boldsymbol{m} \times \frac{\partial \boldsymbol{m}}{\partial \hat{\boldsymbol{n}}} \right) = \boldsymbol{0} \qquad (1.13)$$

The second is a volume equation

$$\boldsymbol{m} \times \boldsymbol{H}_{tot} = \boldsymbol{0} \qquad (1.14)$$

where the total effective field

$$\boldsymbol{H}_{tot} = \frac{2A}{M_s} \nabla^2 \boldsymbol{m} + \boldsymbol{H}_a + \boldsymbol{H}_{app} + \boldsymbol{H}_d \qquad (1.15)$$

A full discussion of the numerical calculation of the individual field terms in the calculation of $\boldsymbol{H}_{tot}$ will be given in Chapters 3 and 4. Essentially, equation (1.13)

states that the equilibrium solution is found by making the magnetization lie parallel to the local field. Equations (1.13) - (1.14) are referred to as Brown's equations and form the basis of the classical micromagnetic approach via the solution of a stationary problem.

Micromagnetics is a theoretical formalism enabling the prediction of magnetization structures such as domain walls and the investigation of magnetization reversal mechanisms in bulk magnetic materials. As such it forms an important link between atomic scale magnetization behaviour.

The study of micromagnetics is an important and challenging field for the computational physicist, much activity exists in this area. There are two main reasons for this

- The enormous technological advances made to computing facilities have made it possible to use numerical solutions to the micromagnetic problem. This enables the development of advanced theoretical and computational models for comparison with experimental data.

- Secondly, the technological evolution of a number of important magnetic materials has reached a stage at which an increasingly detailed understanding of their fundamental magnetic behaviour has emerged as being of vital importance.

Probably the best example of the practical application of micromagnetics is the area of recording media. Since the beginning of the existence of particulate recording media, advances relied on the simple prescription of decreasing the particle size and increasing the coercivity. However, current information storage density requirements of magnetic recording media needs a new approach. Current research is being undertaken into a number of materials including thin metal films with longitudinal and perpendicular anisotropy and Metal Evaporated (ME) tapes in addition to advanced particulate media. Common to all these disparate materials is the existence of complex magnetization structures and reversal processes

which are highly sensitive to the physical microstructure of the material and to the existence of short (exchange) and long range (magnetostatic) interactions.

1.11 The finite element method in micromagnetics

The evolution of micromagnetics has created some problems which are very difficult to solve in terms of numerical methods. However with the introduction of novel calculations such as hybrid finite element / boundary element methods [10], integro-differential equations [11], finite difference methods [12] and Fast Fourier Transforms (FFTs) [13] into micromagnetics it has become possible to overcome this difficulty.

One problem in modeling micromagnetic behaviour is being able to consider regions of arbitrary geometries. The finite element method (FEM) was first used in micromagnetics to overcome this by Fredkin and Koehler (1987) [14]. Since then many authors have used this method in micromagnetic simulations. Fredkin and Koehler continued their work by improving their method numerically [15] and several authors began using their own variant of finite element method in different micromagnetic modeling situations, Schrefl [16], Kronmüller [17] and Tako [18] are just a few to mention.

The work which is of direct interest to the motivation behind this thesis is that involving the modelling of thin film permalloy platelets at the nanoscale. The experimental work in this area has been carried in [19] and [20] by using electron beam lithographical imaging techniques such as Foucalt and Fresnel methods to look at the domain behaviour and reversal mechanisms of the particles. On the theoretical side Schrefl and coworkers [21] and [22] have looked at the micromagnetic simulations of these experiments by using the FEM and have produced results which emulate the experimental observations with fine detail. Because of its ability to model the material behaviour with a very high precision the FEM is certainly

the way forward to realistically understand the micromagnetic properties of this work even further.

1.12 Summary

In this introductory chapter we have put forward a few general ideas about magnetism and magnetic materials. The magnetic recording process has been described in order to explain the unique feature of magnetic materials (non equilibrium behaviour) which makes them suitable for this application, also the desire to increase storage density in magnetic recording media due to the software requirements of the domestic PC is the driving force behind a lot of research into magnetic recording.

We have mentioned how we quantify different magnetic materials and what features can be examined to determine their suitability for a particular application such as remanence, coercivity and susceptibility. The concept of ferromagnetism has been described together with the properties associated with it. The existence of magnetic domains has been discussed together with the concept of the study of the magnetization behaviour at the micromagnetic level. We have introduced the theory of micromagnetics which enables a theoretical comparison to be made with the high resolution imaging techniques in experimental work. We have also commented on the new numerical methods being introduced into micromagnetics to maintain agreement between experiment and theory.

The rest of this thesis is concerned with the development and implementation of a finite element method in micromagnetics which will later be used to produce some new results on thin film permalloy particles of sizes in the region of microns. These particles are termed nanoelements, which is a purely micromagnetic term and is not necessarily a direct implication of their size.

In Chapter 2 we give a brief introduction to the finite element method includ-

ing its historical beginning, the basic ideas involved and the general mathematical concepts. We also give an example via a finite element solution to a simple problem which is very applicable to our more advanced problem in micromagnetics.

Chapter 3 gives the detailed description of the micromagnetic model which we will employ in our simulations. Here we specify the mathematical physics behind the model and the formulation of the field terms. The magnetization dynamics is detailed which governs the magnetization behaviour of the material. We also give a brief mention of the numerical time integration routine used in the model.

We have devoted Chapter 4 to the complete description of our finite element calculation. Here we look at the problem of obtaining the demagnetizing field via a numerical routine. Existing methods are mentioned together with advantages of using the FEM. We then give a detailed description of the field problem and its solution in terms of a finite element variational approach.

In the first four chapters we have given the description of the motivation behind our model and also its mathematical formulation. Chapter 5 sees the results obtained by using our model to simulate magnetization processes in single non interacting permalloy nanoelements. We start off by looking at efficiency and numerical accuracy of the finite element field calculation and present some results illustrating this. We then test our model with existing published theoretical work and then proceed to obtain new results in terms of domain configurations and hysteresis behaviour.

Chapter 6 is the second part of the results section. This includes the results we have obtained by investigating magnetization domain processes in arrays of interacting nanoelements. Due to the ability of the finite element method to handle regions of arbitrary geometry we are able to investigate the interaction effects of nanoelements arranged in one and two dimensional arrays.

We close the work presented in this thesis in chapter seven by some concluding remarks and an outline of any further work which could be developed in the future to improve the existing model.

At the end of the main discussion we include an appendix giving a brief overview of the finite element mesh generation software used in this work together with some mathematical formulae referenced in the main text and a list of the scientific research papers published arising from this investigation. Finally we give a list of the bibliographical references.

Chapter 2

The finite element method

2.1 Historical background

The fundamental idea of the finite element method (FEM) is to replace a complex system with individual components whose behaviour is more easily understood, then rebuild the original system from such components. This results in the replacement of a global function by a set of piecewise approximations.

This idea is hardly a new one, early Oriental mathematicians used 'finite elements' to evaluate π to reported accuracy of almost forty decimal places. They accomplished this by inscribing and circumscribing regular polygons inside and around a circle. The lengths of the sides of the polygons are readily measured as they are straight, the sum of these lengths will then approximate the circumference, then by dividing this by the diameter of the circle, upper and lower bounds to π are available. By increasing the number of sides of the polygons convergence to an exact solution was found. Indeed, Archimedes used ideas of finite elements to determine areas of plane figures and volumes of solids, but with no idea of limiting procedures he was prevented from discovering the integral calculus long before Newton and Leibniz.

The main application of the FEM today is as a numerical technique for obtaining an approximate solution to differential equations. The fascinating point here is

that modern day physical phenomena described in terms of differential equations will have a finite element solution which utilizes ideas which are much older than those used to set up the equations initially.

The modern use of finite elements began in the field of solid mechanics by solving a continuum model as a discrete system. Probably the first attempts were by Hrenikoff (1941) [23] and McHenry (1943) [24]. These methods belonged to a collection of techniques which were used in the early days of aircraft structural analysis when wings and fuselages were represented by discrete bars and beams.

It soon became apparent that these techniques were inadequate for reliable modelling of modern jet-powered aircraft and new methods were sought. The formal introduction of the FEM is attributed to Turner, Clough, Martin and Topp (1956) [25] who presented the direct stiffness method for assembling triangular elements for the analysis of plane stress problems. The term 'finite element' was first used by Clough (1960) [26] in a paper devoted to plane elasticity problems. This important piece of work is both of great conceptual and computational value to the FEM as it introduces a framework for the direct use of a standard method applicable to discrete systems.

Over the next few years the FEM was being used to solve a wide variety of plane structural problems and it was not long before generalizations to three-dimensional problems were being considered by Argyris (1964) [27]. However it was at this point that researchers faced some difficulty due to convergence problems, but this matter was resolved by Bazeley *et al* (1965) [28]. The common three-dimensional type of problem being considered at this stage was that of plate bending. This could be modelled by the use of plate elements, such as triangles or rectangles, many of which make up a structure known as a shell. However, serious problems occurred in the presence of extreme bending and this led to the creation of shell elements.

The first attempts at shell elements took the form of simple conical shapes known as

axisymmetric elements and were first presented by Grafton and Strome (1963) [29]. A whole sequence of curved shell elements soon followed and are reviewed by Gallagher (1969) [30]. Such elements are still being developed to this day.

As well as being employed in structural modelling, the FEM holds a history of equal importance in other problems which began during the mid 1960s. Such non-structural problems include heat conduction, irrotational flow of ideal fluids and distribution of electrical and magnetic potential. These all come under the heading of field problems. During this time it was becoming apparent that the FEM could be applied to any problem which could be expressed in a variational form, i.e. in the form of a scalar quantity known as a functional, which will be explained later. Theorems such as minimization of total potential energy to achieve equilibrium in mechanical systems and least energy dissipation principles in viscous flow both produce variational forms and therefore the FEM may successfully be implemented in their modelling. Notably a solution to the Poisson equation by the FEM was first described by Zienkiewicz and Cheung (1965) [31].

About the same time a convergence proof of the method was produced from an engineering perspective which utilized the principle of minimum potential energy, although it was not until 1967 when applied mathematician Birkhoff published a convergence proof together with error bounds for the method [32]. At this point engineers and mathematicians were bought together in the understanding that the FEM could be extended to new areas.

By the start of the 1970s the FEM had become a very powerful tool for a wide variety of applications mainly due to its ability to handle regions of complicated geometry with ease. Another breakthrough happened during this time when the FEM was recognised as a form of the already well known weighted residuals approach. This meant that problems where no variational principle existed could be solved e.g. electromagnetic theory as presented by Zienkiewicz (1977) [33].

Since the inception of the FEM, the amount of work using the technique has grown exponentially. This, together with improvements in mathematical algorithms to formulate finite element solutions; have made the FEM attractive to other physical sciences such as biomedical engineering and micromagnetics. The rest of this chapter is devoted to the description of the basic concepts of the FEM with an introduction to how it will be applied to the solution of a micromagnetic field problem.

2.2 Basic concepts of the FEM

If we assume ϕ to be a function defined over some domain, then the finite element analysis of ϕ will involve obtaining its approximation by finding a set of piecewise approximations. In order to do this there are a number of steps to be carried out which are common to any finite element analysis. The first step is known as domain discretisation.

2.2.1 Domain discretisation

Domain discretisation is the process of subdividing the domain occupied by ϕ into a finite number of smaller regions. These regions are called elements each of which have a certain number of associated nodes. The most common elements in two-dimensional discretisation schemes are triangular and rectangular (see Figure 2.1), generalizing to three dimensions, they become tetrahedrons and bricks. Together the collection of elements and nodes make up the finite element mesh (see Figure 2.2). It is clear that the elements will share common nodes within the mesh due to connectivity.

For simplicity if we consider an arbitrary two-dimensional domain with a curved boundary, it is easy to see that the mesh will not exactly cover the entire domain (Figure 2.3). The area that is not covered is known as the source of the mesh error and can be minimized by making the elements smaller (increasing their number), this is known as mesh refinement.

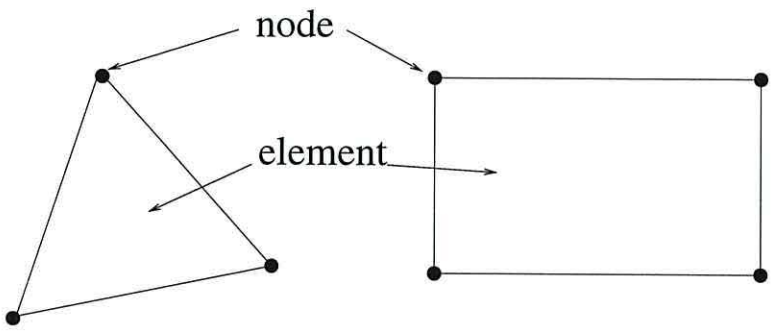

Figure 2.1: Finite elements

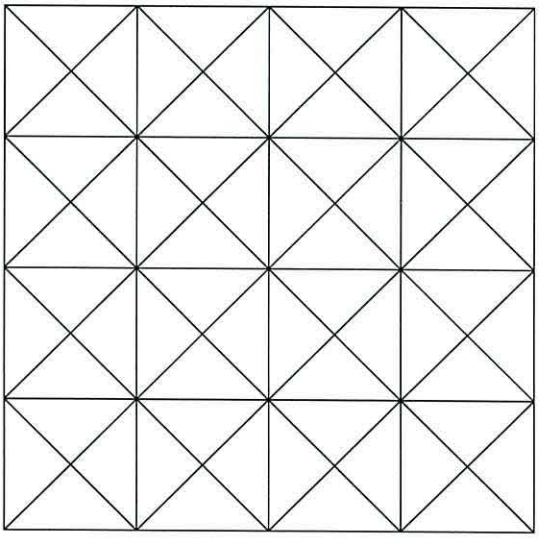

Figure 2.2: Finite element mesh

Mesh refinement may also be used to improve a finite element solution in areas of great spatial variations. The mesh in Figure 2.3 is known as graded due to the regions of extra refinement, whereas in Figure 2.2 we have an ungraded mesh.

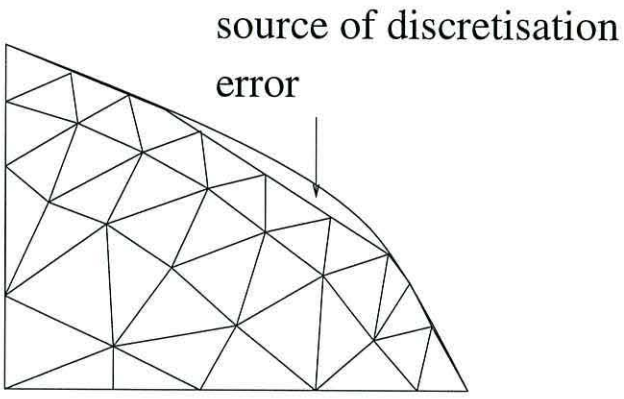

Figure 2.3: Graded finite element mesh

The process of creating a mesh is a difficult one due to two distinct but related tasks, namely nodal definitions and element definitions. The nodes are numbered in such a way as to minimize the computational requirements of the assembling process of the stiffness matrix.

Mesh generation is usually performed by a specialist software package which usually comes with a graphics program for viewing the finished product (see Appendix B for details of the mesh generator used during the course of this work). The mesh generator requires input in the form of a description of the domain with any material properties, it will then output mesh details consisting of node numbers with their co-ordinates and element connectivity and material property data.

The algorithms which are used in the production of meshes have been developed by mathematicians working in computational geometry. A widely used algorithm is the Delaunay triangulation method, which is used to construct meshes for triangular elements and is also a basis for generating tetrahedral elements. A Delaunay

triangulation of a set of points is a triangulation whose vertices (nodes) are the points, having the property that if we take any three points and draw a circle around the triangle produced, then no other point in the set will fall inside this circle. The use of this method ensures that no triangles are produced with small angles, as only triangles with angles away from 0 and π are suitable for FEM analysis. Once we have the data describing a mesh this has to be presented to the main finite element program so that the required analysis may be carried out.

Before beginning to explain the analysis process of the FEM, we must explain a little about interpolation.

2.2.2 Interpolation between nodes

If we consider a continuous quantity ϕ defined over a domain Ω. The mesh will consist of n finite sub-domains Ω^e, i.e. finite elements. After the creation of the mesh, the next step is to make a discrete approximation for ϕ. Usually this will be in the form of a set of polynomials because of their ease of manipulation. The order of the polynomial is related to the number of nodes associated with the element. The polynomial ϕ^e is defined over a particular element e such that the whole set of polynomials form a piecewise continuous function ϕ over Ω^e where $e = 1, 2, ..., n$, i.e.

$$\phi = \sum_{e=1}^{n} \phi^e \tag{2.1}$$

The FEM often requires the calculation of surface or volume integrals over the finite elements. It is customary to perform this integration after a change of variable which maps the region of integration to a geometrically simpler region (the parent element). The reason for this mapping is to simplify the integration process and when this cannot be done exactly, quadrature is also much easier to perform. A brief demonstration of this will now follow.

In one dimension we have a two node lineal element as shown in Figure 2.4. There

Figure 2.4: Two noded lineal element

are two nodes in the element (at $x = x_1$ and $x = x_2$) with one degree of freedom at each node, hence we are looking for a solution of the form

$$\phi^e = c_1 + c_2 x \tag{2.2}$$

The finite element solution will provide us with values of ϕ_1 and ϕ_2 at $x = x_1$ and $x = x_2$ respectively. By making the substitutions

$$N_1(x) = \frac{x_2 - x}{x_2 - x_1} \tag{2.3}$$

$$N_2(x) = \frac{x - x_1}{x_2 - x_1} \tag{2.4}$$

we note that

$$N_1(x_2) = N_2(x_1) = 0 \tag{2.5}$$

$$N_1(x_1) = N_2(x_2) = 1 \tag{2.6}$$

and

$$0 \leq N_1, N_2 \leq 1 \tag{2.7}$$

$$N_1 + N_2 = 1 \tag{2.8}$$

Now by expressing $\phi^e(x)$ by

$$\phi^e(x) = N_1(x)\phi_1 + N_2(x)\phi_2 \tag{2.9}$$

we are able to obtain values for ϕ throughout an element.

Moving on to two dimensions with the continuous function $\phi^e(x, y)$, if we consider a four node rectangular element (Figure 2.5). Here we have four nodes to an

element with one degree of freedom at each node so we are looking for a bilinear solution of the form.

$$\phi^e(x,y) = c_1 + c_2x + c_3y + c_4xy \tag{2.10}$$

To simplify this more complicated mapping it is convenient to choose local coor-

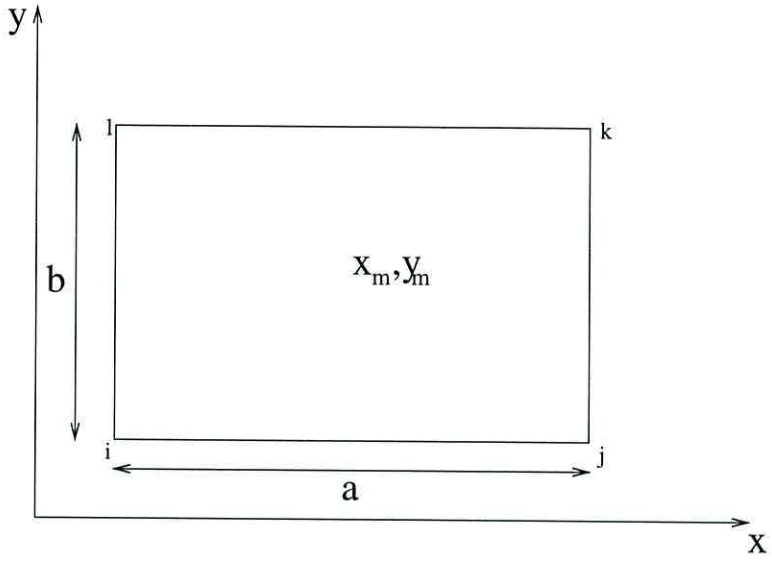

Figure 2.5: Four noded rectangular element

dinates (ζ, η) such that

$$\zeta = \frac{2}{a}(x - x_m) \tag{2.11}$$

$$\eta = \frac{2}{b}(y - y_m) \tag{2.12}$$

where (x_m, y_m) is the centre of the element. By making the substitutions

$$N_i = \frac{1}{4}(1-\zeta)(1-\eta) \tag{2.13}$$

$$N_j = \frac{1}{4}(1+\zeta)(1-\eta) \tag{2.14}$$

$$N_k = \frac{1}{4}(1+\zeta)(1+\eta) \tag{2.15}$$

$$N_l = \frac{1}{4}(1-\zeta)(1+\eta) \tag{2.16}$$

We may interpolate throughout an element by

$$\phi^e(x,y) = N_i(x,y)\phi_i + N_j(x,y)\phi_j + N_k(x,y)\phi_k + N_l(x,y)\phi_l \tag{2.17}$$

Here we notice that an interpolation function associated with a particular node is unity at that node while all others are zero and the sum of the interpolation functions is unity as with the lineal element.

For two-dimensional applications the rectangular element has the main disadvantage that it is only applicable to geometries which are fairly regular. Because of this, it is more convenient to choose the triangular element for use in the two-dimensional application of our research work.

Considering a three node triangular element in two dimensions (Figure 2.6), we have one degree of freedom at each node so

$$\phi^e(x,y) = c_1 + c_2 x + c_3 y \tag{2.18}$$

which may be written

$$\phi^e(x,y) = \begin{pmatrix} 1 & x & y \end{pmatrix} \begin{pmatrix} c_1 \\ c_2 \\ c_3 \end{pmatrix} \tag{2.19}$$

In this case, the mathematics behind the derivation of the interpolation functions will be explained because the idea is also applicable to the other element types. Also these functions are used extensively in the finite element formulation of field terms described in later chapters.

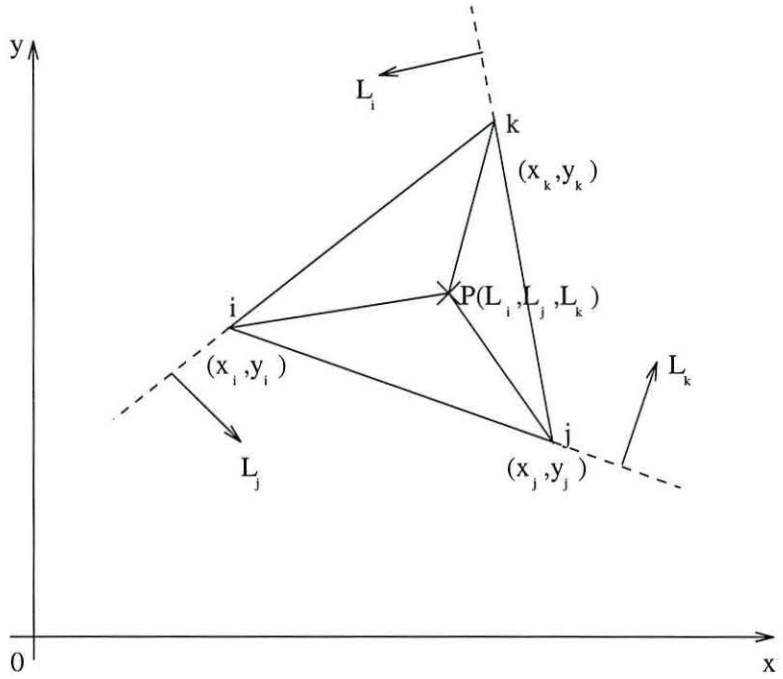

Figure 2.6: Three noded triangular element

If we assume the triangular element with nodes labeled i, j and k which are positioned at global coordinates (x_i, y_i), (x_j, y_j) and (x_k, y_k) respectively with nodal values of ϕ_i, ϕ_j and ϕ_k. Then in matrix form we have the following set of independent simultaneous linear equations.

$$\begin{pmatrix} \phi_i \\ \phi_j \\ \phi_k \end{pmatrix} = \begin{pmatrix} 1 & x_i & y_i \\ 1 & x_j & y_j \\ 1 & x_k & y_k \end{pmatrix} \begin{pmatrix} c_1 \\ c_2 \\ c_3 \end{pmatrix} \tag{2.20}$$

Solving for the above c_1, c_2 and c_3 and substituting into equation (2.19) gives

$$\phi^e(x,y) = \begin{pmatrix} 1 & x & y \end{pmatrix} \begin{pmatrix} 1 & x_i & y_i \\ 1 & x_j & y_j \\ 1 & x_k & y_k \end{pmatrix}^{-1} \begin{pmatrix} \phi_i \\ \phi_j \\ \phi_k \end{pmatrix} \tag{2.21}$$

Using Cramer's rule

$$\phi^e(x,y) = \frac{1}{2A} \begin{pmatrix} 1 & x & y \end{pmatrix} \begin{pmatrix} x_j y_k - x_k y_j & x_k y_i - x_i y_k & x_i y_j - x_j y_i \\ y_j - y_k & y_k - y_i & y_i - y_j \\ x_k - x_j & x_i - x_k & x_j - x_i \end{pmatrix} \begin{pmatrix} \phi_i \\ \phi_j \\ \phi_k \end{pmatrix} \tag{2.22}$$

where A is the area of the element given by

$$A = \frac{1}{2}\begin{vmatrix} 1 & x_i & y_i \\ 1 & x_j & y_j \\ 1 & x_k & y_k \end{vmatrix} \tag{2.23}$$

If we let

$$\begin{aligned} a_i &= x_j y_k - x_k y_j \quad b_i = y_j - y_k \quad c_i = x_k - x_j \\ a_j &= x_k y_i - x_i y_k \quad b_j = y_k - y_i \quad c_j = x_i - x_k \\ a_k &= x_i y_j - x_j y_i \quad b_k = y_i - y_j \quad c_k = x_j - x_i \end{aligned} \tag{2.24}$$

then we can now denote the interpolation functions L_i, L_j and L_k by

$$L_i = \frac{1}{2A}(a_i + b_i x + c_i y) \tag{2.25}$$

$$L_j = \frac{1}{2A}(a_j + b_j x + c_j y) \tag{2.26}$$

$$L_k = \frac{1}{2A}(a_k + b_k x + c_k y) \tag{2.27}$$

These may be used to locate any point $P(L_i, L_j, L_k)$ within the element. By some simple mathematics the relationship between the global coordinates (x, y) and the local triangular coordinates (L_i, L_j, L_k) may be shown to be given by

$$x = L_i x_i + L_j x_j + L_k x_k \tag{2.28}$$

$$y = L_i y_i + L_j y_j + L_k y_k \tag{2.29}$$

The interpolation functions have the property

$$\begin{aligned} L_m(x_n, y_n) &= 1 \quad m = n \\ &= 0 \quad m \neq n \end{aligned}$$

and they are not independent since

$$L_i + L_j + L_k = 1 \tag{2.30}$$

Thus $\phi(x, y)$ may be interpolated linearly throughout an element by

$$\phi(x, y) = L_i \phi_i + L_j \phi_j + L_k \phi_k \tag{2.31}$$

The L_i, L_j and L_k are known as area coordinates.

2.3 Variational methods

The aim of this section is to introduce the main idea behind the analysis process of the FEM by briefly mentioning a few different finite element approaches.

In many physical situations a variational principle will exist governing the phenomena, e.g. minimum potential energy. The solution of this problem will then involve the minimization of some functional. This idea is used in one of many finite element formulations, namely the Rayleigh-Ritz method. If we define a partial differential equation of the form

$$L\phi = f \tag{2.32}$$

defined over some two dimensional domain R and subject to some essential boundary conditions. If the differential operator L is self-adjoint and positive definite, it may be shown that the unique solution to equation (2.32) may be found by minimizing the functional

$$I[\phi] = \int\int_R \phi L\phi dxdy - 2\int\int_R \phi f dxdy \tag{2.33}$$

More complicated boundary conditions may be incorporated into the method by the application of Green's theorem. The Rayleigh-Ritz algorithm requires the choice of a suitable complete set of linearly independent basis functions $\psi_i(x, y)$ for $i = 1, 2, ..., n$ where n is the number of nodes in the discretisation scheme. The exact solution is then approximated by

$$\phi(x, y) = \sum_{i=1}^{n} \phi_i \psi_i \tag{2.34}$$

If we express ϕ as a function of the n unknowns

$$\phi = \phi(\phi_1, \phi_2, ..., \phi_n) \tag{2.35}$$

then the constants ϕ_i are chosen to minimize the functional $I[\phi_1, \phi_2, ..., \phi_n]$, i.e.

$$\frac{\partial I[\phi]}{\partial \phi_j} = 0 \quad j = 1, 2, ..., n \tag{2.36}$$

This leads to n simultaneous linear equations in n unknowns, the solution of which gives the nodal values ϕ_i. It may be proved that the Rayleigh-Ritz finite element solution of ϕ approaches the exact solution as $n \to \infty$, i.e. the solution converges.

A more powerful finite element procedure that is applicable to a wide variety of problems is that of weighted residuals. The Rayleigh-Ritz method is only of use when a suitable functional exists whereas weighted residual methods give an alternative approach when one does not exist or cannot be found.

A commonly used weighted residual method is the Galerkin approach where the test and trial functions are the same weight and works as follows.
If we consider the partial differential equation (2.32). We define the residual by

$$r(\phi) = L\phi - f \tag{2.37}$$

If the exact solution is ϕ_{exact} then

$$r(\phi_{exact}) = 0 \tag{2.38}$$

As in the Rayleigh-Ritz method we define an approximation of the form of equation (2.34). We then set the integral of the residual weighted by test functions equal to zero.

$$\int\int_R r(\phi) w_i dx dy = 0 \quad i = 1, 2, ..., n \tag{2.39}$$

This will produce the n simultaneous linear equations in n unknowns. The advantage of weighted residual methods is that the w_i may be chosen arbitrarily from any set of independent functions, which is of advantage in solving non-linear problems. However, if we choose the w_i to be the same as the interpolation functions ψ_i then we have the Galerkin method.

Another more explicit method is by point collocation. Here we begin with the residual. We then choose n collocation points (nodes) and a polynomial with unknown coefficients which satisfies any essential boundary conditions. We then set

the residual to zero at the collocation points.

The final commonly used weighted residual method to be mentioned here is the method of least squares. Here we proceed as previously described, but this time we apply the method of least squares to the residual, i.e. we seek a solution to

$$\int\int_R r(\phi)^2 \psi_i dxdy = 0 \quad i = 1, 2, ..., n \tag{2.40}$$

2.4 Use of the FEM in the solution of a partial differential equation

Now that we have introduced the FEM and its basic ideas, we will now apply it to the solution of partial differential equations. We will solve a simple Poisson problem, using the Rayleigh-Ritz method. The ideas introduced will then be used to tackle a more difficult problem in Chapter 4.

Consider the two dimensional Poisson equation

$$\nabla^2 \phi = -1 \tag{2.41}$$

defined over the domain R as given by $0 \leq x \leq 1$ and $0 \leq y \leq 1$, subject to the natural boundary conditions

$$\frac{\partial \phi}{\partial x}(0, y) = 0 \qquad \frac{\partial \phi}{\partial y}(x, 0) = 0 \tag{2.42}$$

and the essential boundary conditions

$$\phi(1, y) = 0 \qquad \phi(x, 1) = 0 \tag{2.43}$$

We notice that the solution will be symmetric about $y = x$ as shown in Figure 2.7, so we only need to model either the upper or lower triangular domain. Hence we

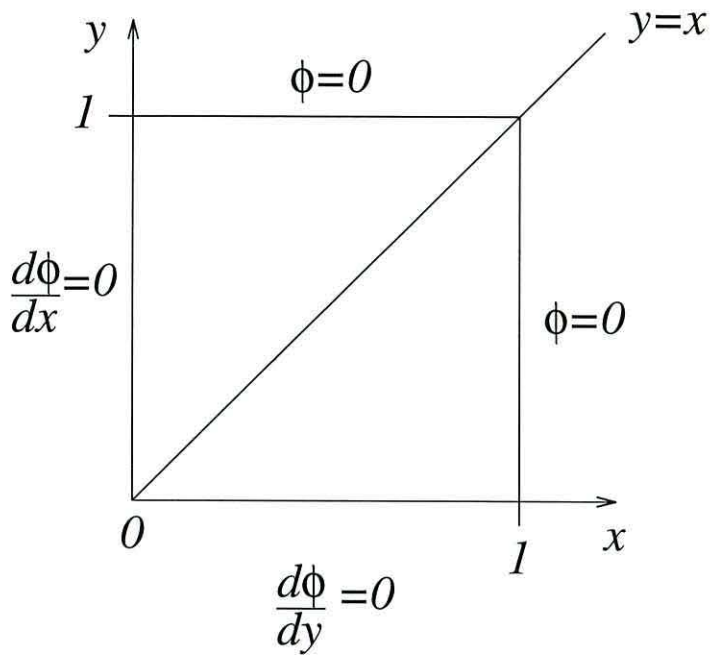

Figure 2.7: The domain of the problem R

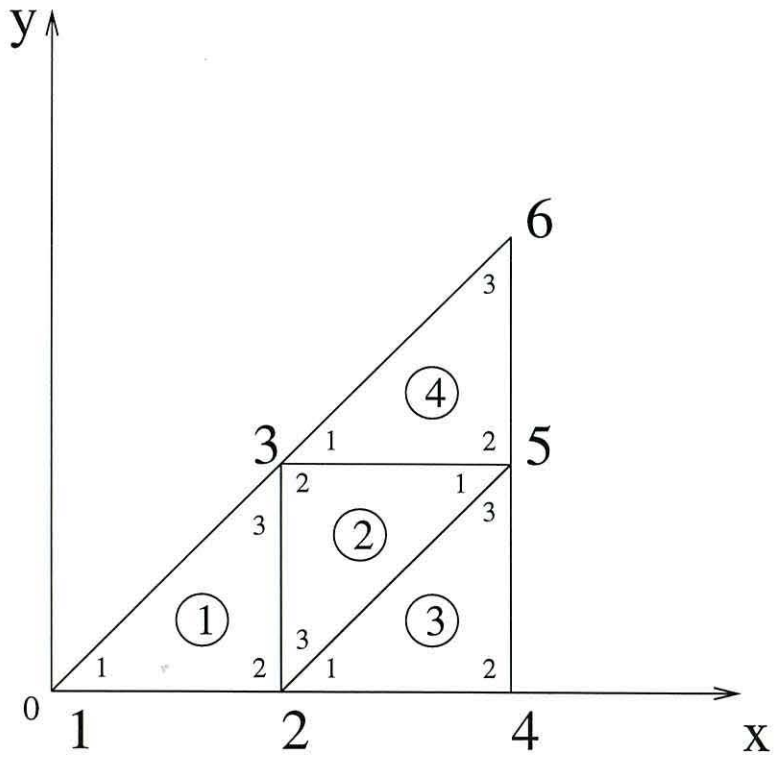

Figure 2.8: The lower triangular domain

shall use linear triangular elements to discretise the lower domain (Figure 2.8).

The nodal coordinate and element connectivity lists are given by -

node	x	y
1	0	0
2	0.5	0
3	0.5	0.5
4	1	0
5	1	0.5
6	1	1

element	node 1	node 2	node 3
1	1	2	3
2	5	3	2
3	2	4	5
4	3	5	6

where the node number in the element connectivity list refers to the local node number.

We are using linear triangular elements so we shall adopt the area coordinate system of interpolation as described in section 2.2 denoted by (L_i, L_j, L_k).
The variational formulation of equation (2.41) using equation (2.33) is given by

$$I[\phi] = \int\int_R \left\{ \left(\frac{\partial \phi}{\partial x}\right)^2 + \left(\frac{\partial \phi}{\partial y}\right)^2 - 2\phi \right\} dxdy \tag{2.44}$$

We have divided R into 4 elements connected by 6 nodes so we will have a discrete solution in the form

$$\phi(x,y) = \sum_{e=1}^{4} \phi^e(x,y) \tag{2.45}$$

where

$$\phi^e(x,y) = \begin{pmatrix} L_1^e & L_2^e & L_3^e \end{pmatrix} \begin{pmatrix} \phi_1^e \\ \phi_2^e \\ \phi_3^e \end{pmatrix} \tag{2.46}$$

and the subscript denotes the local node number.

So

$$I[\phi] = \int\int_R \left\{ \left(\frac{\partial}{\partial x}\sum_{e=1}^{4} \phi^e\right)^2 + \left(\frac{\partial}{\partial y}\sum_{e=1}^{4} \phi^e\right)^2 - 2\sum_{e=1}^{4} \phi^e \right\} dxdy \tag{2.47}$$

Since $\phi^e = 0$ outside element e, the only contribution to $I[\phi]$ from ϕ^e comes from the element itself. Thus

$$\begin{aligned} I[\phi] &= \sum_{e=1}^{4} \left\{ \int\int_R \left(\frac{\partial \phi^e}{\partial x} \right)^2 + \left(\frac{\partial \phi^e}{\partial y} \right)^2 - 2\phi^e \right\} dxdy \\ &= \sum_{e=1}^{4} I^e \end{aligned} \tag{2.48}$$

From equation (2.45) the finite element approximation is of the form

$$I[\phi] = I(\phi_1, \phi_2, \phi_3, \phi_4, \phi_5, \phi_6) \tag{2.49}$$

where the subscripts now refer to the global node numbers. Using the Rayleigh-Ritz procedure to minimize I with respect to the variational parameters $\phi_1, \phi_2, ..., \phi_6$ gives

$$\frac{\partial I}{\partial \phi_i} = 0 \tag{2.50}$$

$$\text{i.e.} \quad \sum_{e=1}^{4} \frac{\partial I^e}{\partial \phi_i} = 0 \qquad i = 1, 2, ..., 6 \tag{2.51}$$

Before developing the element matrices it is useful to express equation (2.51) as a single matrix equation

$$\frac{\partial I^e}{\partial \phi} = \begin{pmatrix} \frac{\partial I^e}{\partial \phi_1} & \frac{\partial I^e}{\partial \phi_2} & \cdots & \frac{\partial I^e}{\partial \phi_6} \end{pmatrix} \tag{2.52}$$

so

$$\sum_{e=1}^{4} \frac{\partial I^e}{\partial \phi} = 0 \tag{2.53}$$

and

$$\frac{\partial I^e}{\partial \phi_i} = \int\int_R \left\{ \frac{\partial}{\partial \phi_i} \left(\frac{\partial \phi^e}{\partial x} \right)^2 + \frac{\partial}{\partial \phi_i} \left(\frac{\partial \phi^e}{\partial y} \right)^2 - 2\frac{\partial \phi^e}{\partial \phi_i} \right\} dxdy \tag{2.54}$$

At this point we note that if node i is not associated with element e, then $\frac{\partial I^e}{\partial \phi_i} = 0$. A contribution will only occur if node i is associated with the element.

$$\phi^e(x, y) = \sum_{i \in e} L_i^e \phi_i^e \qquad \forall i \text{ associated with element } e \tag{2.55}$$

$$\begin{aligned}\frac{\partial}{\partial\phi_i}\left(\frac{\partial\phi^e}{\partial x}\right)^2 &= 2\frac{\partial\phi^e}{\partial x}\frac{\partial}{\partial\phi_i}\left(\frac{\partial\phi^e}{\partial x}\right)\\ &= 2\frac{\partial\phi^e}{\partial x}\frac{\partial}{\partial x}\left(\frac{\partial\phi^e}{\partial\phi_i}\right)\\ &= 2\frac{\partial}{\partial x}\begin{pmatrix} L_1^e & L_2^e & L_3^e\end{pmatrix}\begin{pmatrix}\phi_1^e\\ \phi_2^e\\ \phi_3^e\end{pmatrix}\frac{\partial}{\partial x}\left(\frac{\partial\phi^e}{\partial\phi_i}\right)\end{aligned} \tag{2.56}$$

now

$$\frac{\partial\phi^e}{\partial\phi_i} = L_i^e \tag{2.57}$$

so

$$\frac{\partial}{\partial\phi_i}\left(\frac{\partial\phi^e}{\partial x}\right)^2 = 2\begin{pmatrix}\frac{\partial L_1^e}{\partial x}\frac{\partial L_i^e}{\partial x} & \frac{\partial L_2^e}{\partial x}\frac{\partial L_i^e}{\partial x} & \frac{\partial L_3^e}{\partial x}\frac{\partial L_i^e}{\partial x}\end{pmatrix}\begin{pmatrix}\phi_1^e\\ \phi_2^e\\ \phi_3^e\end{pmatrix} \qquad i=1,2,3 \tag{2.58}$$

similarly

$$\frac{\partial}{\partial\phi_i}\left(\frac{\partial\phi^e}{\partial y}\right)^2 = 2\begin{pmatrix}\frac{\partial L_1^e}{\partial y}\frac{\partial L_i^e}{\partial y} & \frac{\partial L_2^e}{\partial y}\frac{\partial L_i^e}{\partial y} & \frac{\partial L_3^e}{\partial y}\frac{\partial L_i^e}{\partial y}\end{pmatrix}\begin{pmatrix}\phi_1^e\\ \phi_2^e\\ \phi_3^e\end{pmatrix} \qquad i=1,2,3 \tag{2.59}$$

now equation (2.54) becomes

$$\begin{aligned}\frac{\partial I^e}{\partial\phi_i} = 2\int\int_{R^e}\Bigg[&\left(\frac{\partial L_1^e}{\partial x}\frac{\partial L_i^e}{\partial x}+\frac{\partial L_1^e}{\partial y}\frac{\partial L_i^e}{\partial y}\right)\left(\frac{\partial L_2^e}{\partial x}\frac{\partial L_i^e}{\partial x}+\frac{\partial L_2^e}{\partial y}\frac{\partial L_i^e}{\partial y}\right)\\ &\left(\frac{\partial L_3^e}{\partial x}\frac{\partial L_i^e}{\partial x}+\frac{\partial L_3^e}{\partial y}\frac{\partial L_i^e}{\partial y}\right)\Bigg]\begin{bmatrix}\phi_1^e\\ \phi_2^e\\ \phi_3^e\end{bmatrix}dxdy - 2\int\int_{R^e}L_i^e dxdy\end{aligned} \tag{2.60}$$

i.e.

$$\frac{\partial I^e}{\partial\phi_i} = 2\sum_{j\in e}k_{ij}^e\phi_j - 2f_i^e \tag{2.61}$$

where

$$k_{ij}^e = \int\int_{R^e}\left(\frac{\partial L_i^e}{\partial x}\frac{\partial L_j^e}{\partial x}+\frac{\partial L_i^e}{\partial y}\frac{\partial L_j^e}{\partial y}\right)dxdy \tag{2.62}$$

and

$$f_i^e = \int\int_{R^e} L_i^e dxdy \tag{2.63}$$

We require

$$\frac{\partial I^e}{\partial \phi_i} = 0 \tag{2.64}$$

so

$$\sum_{j \in e} k_{ij}^e \phi_j = f_i^e \tag{2.65}$$

Forming these equations over the entire domain R leads to the system of linear equations

$$\boldsymbol{K\phi} = \boldsymbol{f} \tag{2.66}$$

where $\boldsymbol{K}$ is known as the global stiffness matrix and $\boldsymbol{f}$ the force vector (these terms arise from structural mechanics). Using the system of triangular coordinates, we can now assemble the element stiffness matrix as follows :

- The contribution to the i, j position comes from all elements containing nodes i and j e.g. from Figure 2.9, elements 1, 2 and 3 have node i in common and elements 1 and 2 have node j in common. Thus elements 1, 2 and 3 contribute to the i, i position with

  $$k_{i,i} = k_{i,i}^1 + k_{i,i}^2 + k_{i,i}^3$$

  and elements 1 and 2 contribute to the i, j position with

  $$k_{i,j} = k_{i,j}^1 + k_{i,j}^2$$

- The global force vector is assembled in a similar manner.

Referring back to equations (2.25) - (2.27)

$$\frac{\partial L_i}{\partial x} = \frac{b_i}{2A} \qquad \frac{\partial L_i}{\partial y} = \frac{c_i}{2A} \tag{2.67}$$

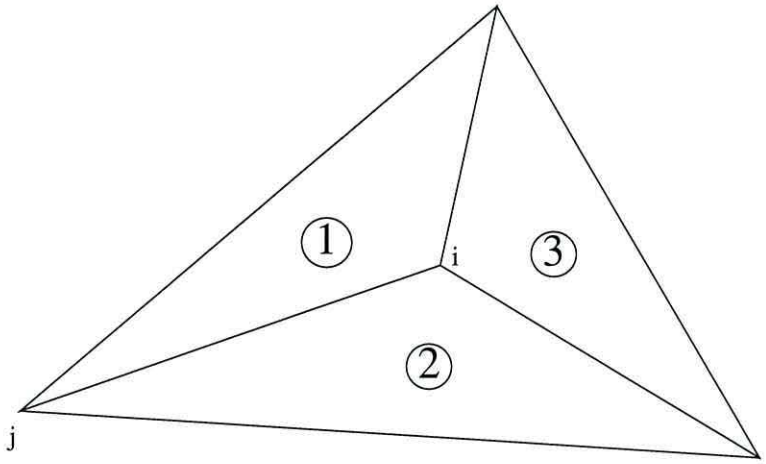

Figure 2.9: Connection between elements 1,2 and 3 through nodes i and j

So we can assemble the stiffness matrix by

$$k_{ij}^e = \frac{1}{4A}\left(b_i^e b_j^e + c_i^e c_j^e\right) \tag{2.68}$$

where the area of an element, $A = \frac{1}{8}$

Similarly from the formula for integration over an element given in Appendix A

$$\begin{aligned} f_i^e &= \int\int_{R^e} L_i^e dxdy \\ &= \frac{A}{3} \end{aligned} \tag{2.69}$$

Thus

$$\begin{aligned} b_1^1 = b_1^3 = b_1^4 = -0.5 \quad & b_1^2 = 0.5 \\ b_2^1 = b_2^3 = b_2^4 = 0.5 \quad & b_2^2 = -0.5 \\ b_3^1 = b_3^3 = b_3^4 = 0 \quad & b_3^2 = 0 \end{aligned}$$

$$\begin{aligned} c_1^1 = c_1^3 = c_1^4 = 0 \quad & c_1^2 = 0 \\ c_2^1 = c_2^3 = c_2^4 = -0.5 \quad & c_2^2 = 0.5 \\ c_3^1 = c_3^3 = c_3^4 = 0.5 \quad & c_3^2 = -0.5 \end{aligned}$$

The stiffness matrix entries are

$k_{11} = k_{11}^1 \qquad k_{12} = k_{12}^1 \qquad k_{13} = k_{13}^1 \qquad k_{14} = k_{15} = k_{16} = 0$

$$k_{22} = k_{22}^1 + k_{33}^2 + k_{11}^3 \quad k_{23} = k_{23}^1 + k_{23}^2 \quad k_{24} = k_{12}^3 \quad k_{25} = k_{13}^2 + k_{13}^3 \quad k_{26} = 0$$

$$k_{33} = k_{33}^1 + k_{22}^2 + k_{11}^4 \quad k_{34} = 0 \quad k_{35} = k_{12}^4 + k_{12}^2 \quad k_{36} = k_{13}^4$$

$$k_{44} = k_{22}^3 \quad k_{45} = k_{23}^3 \quad k_{46} = 0$$

$$k_{55} = k_{22}^4 + k_{11}^2 + k_{33}^3 \quad k_{56} = k_{23}^4$$

$$k_{66} = k_{33}^4$$

and the force vector

$$\begin{aligned} f_1 &= f_1^1 \\ f_2 &= f_2^1 + f_3^2 + f_1^3 \\ f_3 &= f_3^1 + f_2^2 + f_1^4 \\ f_4 &= f_2^3 \\ f_5 &= f_1^2 + f_2^4 + f_3^3 \\ f_6 &= f_3^4 \end{aligned}$$

Thus

$$2\begin{pmatrix} \frac{1}{4} & -\frac{1}{4} & 0 & 0 & 0 & 0 \\ -\frac{1}{4} & 1 & -\frac{1}{2} & -\frac{1}{4} & 0 & 0 \\ 0 & -\frac{1}{2} & 1 & 0 & -\frac{1}{2} & 0 \\ 0 & -\frac{1}{4} & 0 & \frac{1}{2} & -\frac{1}{4} & 0 \\ 0 & 0 & -\frac{1}{2} & -\frac{1}{4} & 1 & -\frac{1}{4} \\ 0 & 0 & 0 & 0 & -\frac{1}{4} & \frac{1}{4} \end{pmatrix} \begin{pmatrix} \phi_1 \\ \phi_2 \\ \phi_3 \\ \phi_4 \\ \phi_5 \\ \phi_6 \end{pmatrix} = \frac{1}{24} \begin{pmatrix} 1 \\ 3 \\ 3 \\ 1 \\ 3 \\ 1 \end{pmatrix} \tag{2.70}$$

applying the essential boundary conditions $\phi_4 = \phi_5 = \phi_6 = 0$ to equation (2.70) then solving gives

$$\begin{pmatrix} \phi_1 \\ \phi_2 \\ \phi_3 \\ \phi_4 \\ \phi_5 \\ \phi_6 \end{pmatrix} = \begin{pmatrix} 0.31250 \\ 0.22917 \\ 0.17708 \\ 0 \\ 0 \\ 0 \end{pmatrix} \tag{2.71}$$

2.5 Summary

In this chapter we have introduced the basic methodology of the FEM. We have shown how it may be applied to the modelling of problems defined over irregular domains - which is a significant advantage any new FEM micromagnetic field calculation has over existing other methods which only consider regular domains. The coupling of the FEM with the idea of a variational principle has been explained and an example of the mathematical solution to a commonly occurring type of partial differential equation has been worked through. The reason for including this example is to illustrate the algorithm used in its solution, as this will be applied to a more complicated problem in Chapter 4. A few concluding remarks will now be given.

When applying a variational finite element method to a particular problem, it is often difficult to decide which is the best method. The distribution of error may vary non-uniformly and some methods may give a very good solution in some areas but not so good elsewhere, see Crandall (1956) [34].

Another consideration to be given to the improvement of a solution is that of mesh refinement. We may choose to increase the number of finite elements (h-type refinement), increase the order of the interpolation polynomials (p-type refinement) or both (hp-type refinement). From a practical point of view the choice of method is dependent upon the local regularity of the solution. This point is discussed by Desai and Abel (1972) [35] who also cite an example due to Clough (1969) [36] in which h-type refinement is found to be better for one problem whereas p-type provides a better approximation for another.

Chapter 3

Micromagnetic model description

3.1 Introduction

The purpose of this chapter is to present the concepts of our theoretical micromagnetic model to simulate the magnetization dynamics of thin permalloy nanoelements.

Theoretical investigation into the behaviour of magnetic materials has progressed steadily since it was first formulated by Brown in the 1950s [9] to the present day where advances in numerical techniques allow more realistic calculations to take place bringing theory closer to reality. However, the majority of numerical simulations in micromagnetics are carried out for very idealized geometries.

Recent advances in modern day magnetic imaging techniques such as transmission electron microscopy (TEM) have shown that there is a need for the micromagnetic modelling of irregular microstructures. To apply this notion, we need to consider a suitable numerical method that can be applied to arbitrary geometries, namely the finite element method (FEM).

In order to model magnetization structures, it is necessary to discretise the material in question into a particular microstructure. Our model uses the idea of patterning the material into rectangular bars with either one, two or no pointed

ends, see Figure 3.1. In micromagnetics these shapes are termed nanoelements and have typical dimensions at the sub micron level. These particles have been studied extensively in experimental imaging work such as that performed in [19] and [20]. Investigation into nanoelement properties has involved looking at their switching

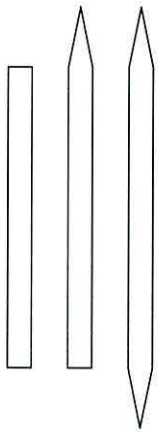

Figure 3.1: Nanoelement geometries

behaviour, domain structures and interaction effects when they are placed in an array formation. The application of the FEM to this work enables us to discretise a particular nanoelement into finite elements and obtain realistic theoretical results. This chapter will concentrate on explaining the field term contributions to our model and the governing equation of motion. The finite element algorithm will be explained in detail in the following chapter.

3.2 Mesh generation

Before any finite element analysis may take place we must define the finite elements and their nodal points which will lie on our theoretical piece of magnetic material. Due to the very small thickness of the permalloy nanoelements it is advantageous to use a two-dimensional finite element model which minimizes the computational requirements. This may be justified by a very small variation in the out of plane component in the Landau-Lifshitz equation of motion used in our model. Thus our model will utilize finite element meshes defined over the x, y plane with the z direction being out of plane.

In order to make our model versatile enough to model arbitrary geometries we chose to use triangular finite elements. The creation of the meshes used in this work has been mainly done by using the mesh generator "Triangle", which is a freely available package [37].

Initially, our model will be used to investigate the material behaviour of single nanoelements and will progress later on to looking at the effects of placing several nanoelements in array formations. Due to this fact and the idea of modelling the problem over a single mathematical domain which will become more clear in the next chapter, it is necessary to model the physical effects outside the nanoelement. This means that we need to mesh two individual regions with one continuous mesh while still maintaining a distinction between the two regions.

To create a mesh, first of all we must define the region in question which will consist of an inner and outer area and then present this data in a format recognisable to "Triangle", see Appendix B. Briefly, this is done by specifying numbered points and their connectivity. At this stage we may also define extra points around areas where mesh refinement is needed. An example of a typical region is shown in Figure 3.2 where the inner region is a rectangular nanoelement with an $8:1$ aspect ratio and the outer region is a suitable distance away where we wish to model the exterior field behaviour.

Once we have defined the region, we must decide upon the constraints on the mesh that we may require, such as the number of elements, aspect ratio of elements and order of elements. By default, "Triangle" uses the Delaunay triangulation method for generating elements. This method is widely used in computational geometry and works by generating nodal points such that if we put a circle around any particular three points (which defines an element), then no other point would fall within or on that circle. This is very suitable for finite element analysis as it ensures that no angles within the triangular elements are close to 0 or π; such cases are undesirable as they are likely to produce inaccurate results in finite element calculations.

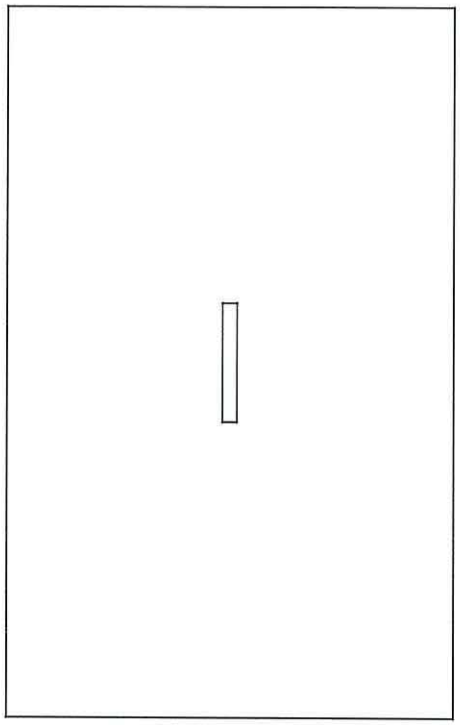

Figure 3.2: Polygonal region defining nanoelement and surrounding area

With the region defined and mesh constraints decided upon we may call "Triangle" with this data in mind and then obtain our mesh, see Figure 3.3. This resulting mesh has a total of 2018 quadratic elements and 4051 nodes. Within the magnetic region (nanoelement) there are 2541 nodes and 1200 elements, the extra refinement here ensures that we will have a high degree of accuracy to take care of the large variation in magnetization changes. When we wish to look at arrays of interacting nanoelements we also require a certain degree of refinement in the surrounding area between nanoelements to take account of increased activity in the interaction effects.

3.3 Field formulation

The fundamental idea of our micromagnetic model is to represent the magnetic moment at a particular point on the platelet by a vector denoted by $\boldsymbol{M}$. For convenience each $\boldsymbol{M}$ is located at a particular node of the finite element mesh.

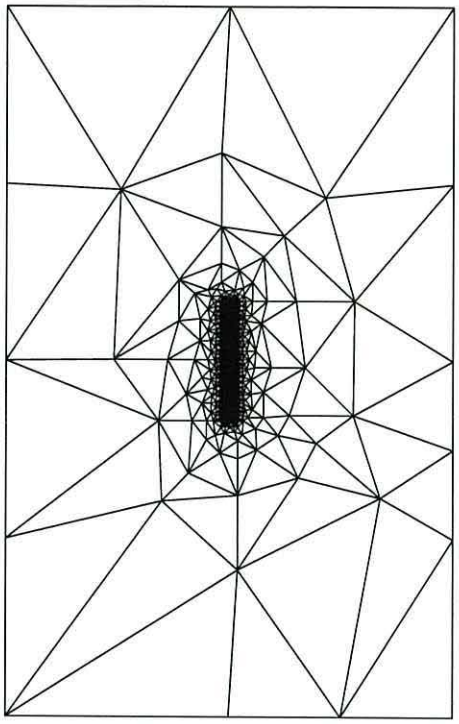

Figure 3.3: Mesh with 4051 nodes and 2018 elements

Throughout our simulations we have chosen to work in reduced units such that $\boldsymbol{M}$ becomes a normalized vector with respect to the saturation magnetization M_s by $\boldsymbol{m} = \dfrac{\boldsymbol{M}}{M_s}$.

We represent the reduced magnetization $\boldsymbol{m}$ in terms of linear finite element interpolation functions as follows. To obtain $\boldsymbol{m}$ throughout an element e, denoted by $\boldsymbol{m}^e$ we interpolate the components of $\boldsymbol{m}^e$ by

$$\begin{aligned} \boldsymbol{m}^e &= \left(m_x^e, m_y^e, m_z^e\right) \\ &= \left(\sum_{i=1}^{3} L_i m_{xi}, \sum_{i=1}^{3} L_i m_{yi}, \sum_{i=1}^{3} L_i m_{zi}\right) \end{aligned} \tag{3.1}$$

where L_i are the linear interpolation functions mentioned in equations (2.25) - (2.27) that are associated with the element e.

If we denote the total system energy by E_t, then $E_t = E_d + E_{ex} + E_a + E_{app}$ with E_d, E_{ex}, E_a and E_{app} representing the demagnetizing, exchange, anisotropy and applied energy terms respectively.

The total effective field, $\boldsymbol{H}_t$ is related to the total system energy by

$$\boldsymbol{H}_t = -\frac{dE_t}{d\boldsymbol{M}} \tag{3.2}$$

3.3.1 Applied field

The energy created by the externally applied field arises as a result of its interaction with the magnetization. In our model this field is introduced in order to produce a hysteresis curve simulation allowing the magnetization to relax under the influence of its presence. The applied field energy is given by

$$E_{app} = \int_V \boldsymbol{H}_{app} \cdot \boldsymbol{M} dV \tag{3.3}$$

This field will be uniform in our simulations but need not be in general. We will only be concerned with applied fields parallel to the x and y axes.

3.3.2 Anisotropy field

The term anisotropy refers to the fact that the properties of a magnetic material are dependent on the directions in which they are measured. In the absence of all external forces, the magnetization $\boldsymbol{M}$ would align itself in one or more specific directions in the crystal lattice. These directions are termed the easy axes of the material and represent the directions of the easy magnetization.

To rotate the magnetization away from the easy direction involves energy - the anisotropy energy, which is dependent upon the lattice structure. For our simulations with Permalloy we shall be concerned with magnetocrystalline anisotropy with a single easy axis, so the material is termed uniaxial with respect to the anisotropy. For a purely uniaxial crystal, the anisotropy energy density, E_a depends on the angle θ between the magnetization vector $\boldsymbol{M}$ and the easy direction. This energy is given by

$$E_a \simeq K_1 \sin^2\theta + K_2 \sin^4\theta \tag{3.4}$$

plus higher order terms of even power in $\sin\theta$. The constants K_1 and K_2 are material dependent. If we neglect K_2 and let the uniaxial anisotropy constant, $K = K_1$, then since E_a is an energy density we have

$$E_a = -\int_V \frac{K}{M_s^2} (\boldsymbol{M} \cdot \hat{\boldsymbol{e}})^2 \, dV \tag{3.5}$$

where V is the volume of the magnetic material and $\hat{\boldsymbol{e}}$ is a unit vector along the direction of the easy axis.

The anisotropy field $\boldsymbol{H}_a$ is then obtained by differentiating with respect to the magnetization $\boldsymbol{M}$ so that

$$\boldsymbol{H}_a = \frac{2K}{M_s^2} (\boldsymbol{M} \cdot \hat{\boldsymbol{e}}) \hat{\boldsymbol{e}} \tag{3.6}$$

Our simulations will have easy directions parallel to either the long or short axis of the nanoelement, i.e. $\hat{\boldsymbol{e}} = (0, 1, 0)$ or $\hat{\boldsymbol{e}} = (1, 0, 0)$. Anisotropy makes an important contribution to hysteresis in magnetic materials and is therefore of considerable practical importance.

3.3.3 Exchange field

The exchange energy was described in Chapter 1 and was formulated in terms of a micromagnetic formalism for cubic crystals as

$$E_{ex} = \int_V \frac{A}{2M_s^2} |\nabla \boldsymbol{M}|^2 \, dV \tag{3.7}$$

The exchange field $\boldsymbol{H}_{ex}$ is then obtained by differentiating with respect to the magnetization $\boldsymbol{M}$ so that

$$\boldsymbol{H}_{ex} = \frac{A}{2M_s^2} \nabla^2 \boldsymbol{M} \tag{3.8}$$

Due to the linear interpolation of $\boldsymbol{M}$ within our finite element spatial discretisation scheme this field cannot be calculated directly from this expression as $\nabla^2 \boldsymbol{M}$ is not defined. So we use the discrete approximation given by

$$\boldsymbol{H}_{ex} = \frac{A}{M_s^2} \sum_{i=1}^{N} \frac{\boldsymbol{M}_j}{|\boldsymbol{r}_i - \boldsymbol{r}_j|^2} \tag{3.9}$$

where $\boldsymbol{r}_i$ and $\boldsymbol{r}_j$ are the position vectors of points i and j respectively, $i \neq j$, N is the number of nodes in the linear interpolation scheme and A is the material dependent exchange constant.

3.3.4 Demagnetizing field

The demagnetizing energy of the magnetic material is given by

$$E_d = -\frac{1}{2}\int_V \boldsymbol{M} \cdot \boldsymbol{H}_d dV \tag{3.10}$$

It has been proved that the governing equations in electromagnetics derived by Maxwell also hold in micromagnetics. Thus it is possible to express the physical law in terms of a single set of equations related to potential theory. For a given magnetization distribution $\boldsymbol{M}$, the associated demagnetizing field $\boldsymbol{H}_d$ can be expressed in terms of the Maxwell equations. Thus

$$\nabla \times \boldsymbol{H}_d = \boldsymbol{J} + \frac{\partial \boldsymbol{D}}{\partial t} \tag{3.11}$$

where $\boldsymbol{J}$ is the electric current density and $\boldsymbol{D}$ the electric flux density. For regions which are current free, it follows that

$$\nabla \times \boldsymbol{H}_d = 0 \tag{3.12}$$

Thus $\boldsymbol{H}_d$ is an irrotational vector field. If we denote the induced field by $\boldsymbol{B}$ where

$$\boldsymbol{B} = \boldsymbol{H}_d + 4\pi \boldsymbol{M} \tag{3.13}$$

and

$$\nabla \cdot \boldsymbol{B} = 0 \tag{3.14}$$

It follows from the previous equation that

$$\nabla \cdot (\boldsymbol{H}_d + 4\pi \boldsymbol{M}) = 0 \tag{3.15}$$

From the laws of vector calculus we may introduce a magnetic scalar potential ϕ, such that

$$\boldsymbol{H}_d = -\nabla \phi \tag{3.16}$$

From equations (3.13) - (3.16)

$$\nabla^2\phi = 4\pi\nabla\cdot\boldsymbol{M} \tag{3.17}$$

So ϕ satisfies the Poisson equation. However, since $\boldsymbol{M} = 0$ outside the magnetic material we have

$$\nabla^2\phi = 0 \tag{3.18}$$

which is the Laplace equation. If we denote the magnetic and non magnetic regions by Ω_{int} and Ω_{ext} respectively and the potential inside and outside the magnetic region by ϕ_{int} and ϕ_{ext} respectively. Then we have

$$\nabla^2\phi_{int} = 4\pi\nabla\cdot\boldsymbol{M} \tag{3.19}$$

$$\nabla^2\phi_{ext} = 0 \tag{3.20}$$

However since there is a dramatic change in material properties between the magnetic and non magnetic regions, equations (3.19) - (3.20) are insufficient on their own in modelling the potential. In order to completely model what is happening we must introduce an interface condition on the boundary of the magnetic material, $\partial\Omega$.

The laws which govern this change in material properties across the boundary are a direct consequence of the nature of the Maxwell equations. At the interface, the tangential component of $\boldsymbol{H}_d$ and the normal component of the induced field, $\boldsymbol{B}$ must be continuous which leads to the following interface condition

$$\frac{\partial\phi_{int}}{\partial n} - \frac{\partial\phi_{ext}}{\partial n} = 4\pi\boldsymbol{M}\cdot\hat{\boldsymbol{n}} \qquad \forall\boldsymbol{x}\in\partial\Omega \tag{3.21}$$

where $\hat{\boldsymbol{n}}$ is the unit normal away from the surface. The continuity condition

$$\phi_{int} = \phi_{ext} \qquad \forall\boldsymbol{x}\in\partial\Omega \tag{3.22}$$

is also required, together with the bounding of the potential at infinity. The demagnetizing field is then calculated by

$$\boldsymbol{H}_d = -\nabla\phi \tag{3.23}$$

In Aharoni [38] the equation for ϕ has been found to satisfy

$$\phi(\boldsymbol{r}) = \int_{V'} \frac{-\nabla' \cdot \boldsymbol{M}(\boldsymbol{r'})}{|\boldsymbol{r} - \boldsymbol{r'}|} dV' + \int_{S'} \frac{\boldsymbol{M}(\boldsymbol{r'}) \cdot \hat{\boldsymbol{n}}}{|\boldsymbol{r} - \boldsymbol{r'}|} dS' \tag{3.24}$$

where the first and second terms define the magnetic volume and surface charge contributions respectively. The demagnetizing field, $\boldsymbol{H}_d$ acts opposite in direction to the magnetization $\boldsymbol{M}$ which creates it. Due to the global nature of the interaction effects of the demagnetizing field its computation is the most time consuming part in any micromagnetic simulation. Analytic solutions of equation (3.24) exist for certain geometries [38], but solutions for irregular domains involve the use of very complicated integration.

Many different numerical methods have been used for finding $\boldsymbol{H}_d$. In the past authors have used such methods as analytic dipolar approximations, finite element/boundary element calculations and integro-differential equations. In the next chapter we will describe a new approach to the formulation of $\boldsymbol{H}_d$ in terms of the finite element method.

3.4 Magnetization dynamics

The field terms which make up $\boldsymbol{H}_t$ are the cause of the change in the magnetization $\boldsymbol{M}$ over time. In order to model this change, we must employ an equation which describes the magnetization dynamics in terms of the evolution of time. The Landau-Lifshitz equation of motion is given by

$$\frac{d\boldsymbol{M}}{dt} = -|\gamma| \boldsymbol{M} \times \boldsymbol{H}_t - \frac{\lambda}{M_s^2} (\boldsymbol{M} \times (\boldsymbol{M} \times \boldsymbol{H}_t)) \tag{3.25}$$

where t is the time, γ is the magneto-mechanical or gyromagnetic ratio, λ is the dissipative constant, $\boldsymbol{M}$ is the magnetization vector and $\boldsymbol{H}_t$ is the total effective field made up contributions from anisotropy, external, exchange and magnetostatic sources neglecting other phenomena such as magnetostriction and thermal effects.

The first term on the right hand side of equation (3.25) describes the precession of the magnetization vector $\boldsymbol{M}$ (magnetic moment) around the effective field $\boldsymbol{H}_t$.

This is related to the angular momentum between $\boldsymbol{M}$, $\boldsymbol{H}_t$ and the electron spin. Thus the equation

$$\frac{d\boldsymbol{M}}{dt} = -|\gamma|\boldsymbol{M} \times \boldsymbol{H}_t \tag{3.26}$$

describes the motion of uniform precession of the magnetization $\boldsymbol{M}$ about the total effective field $\boldsymbol{H}_t$. The motion described in equation (3.26) could never reach equilibrium as $\boldsymbol{M}$ would never align itself with $\boldsymbol{H}_t$. This illustrates the need for the second term on the right hand side of equation (3.26) which was formulated by Landau and Lifshitz [2]. This term exerts a torque on the precessive motion which causes damping on the motion of the magnetization $\boldsymbol{M}$ making it spiral inwards and align itself with $\boldsymbol{H}_t$ achieving equilibrium as shown in Figure 3.4.

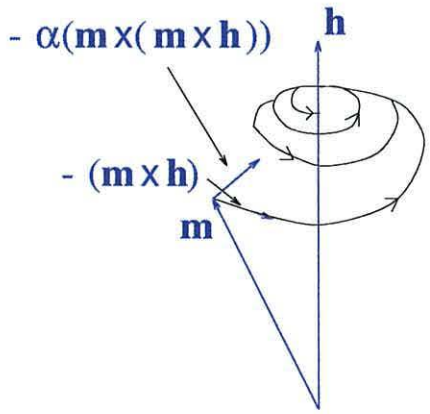

Figure 3.4: The dynamics of the magnetization $\boldsymbol{m}$ in the presence of an effective field $\boldsymbol{h}_t$

Equation (3.25) has been used by several authors successfully in micromagnetic simulations [39], [40], [41]. An alternative way of modelling the magnetization dynamics is by a variation of equation (3.25) proposed by Gilbert and Kelly (1955). This equation formulates the dissipative term to be proportional to the rate of change of the magnetization, i.e.

$$\frac{d\boldsymbol{M}}{dt} = -|\gamma_G|\boldsymbol{M} \times \boldsymbol{H}_t + \frac{\alpha_G}{M_s}\left(\boldsymbol{M} \times \frac{d\boldsymbol{M}}{dt}\right) \tag{3.27}$$

where γ_G is the Gilbert magneto-mechanical ratio and α_G is the Gilbert damping constant.

It is easy to see that when λ and α_G are both small equations (3.25) and (3.27) are approximately equivalent. However when the dissipative term becomes more prominent (when λ and γ_G are much greater than unity), the Gilbert form is preferred purely on physical grounds. A detailed discussion of the differences between the two equations of motion under different physical conditions is given by Mallinson [42]. In our simulations, we will be concerned with a constant premultiplying factor of unity before the damping term, so in effect we have a choice of which equation of motion to use. However, the Landau-Lifshitz equation is easier to solve numerically, hence that is the form which we shall use in our simulations.

If we define $H_k = \dfrac{2K}{M_s}$ to be the anisotropy field strength where K is the uniaxial anisotropy constant, then we can scale the effective field terms with respect to the anisotropy field strength for convenience. Also, to simplify computations in the numerical method of solution of equation (3.25) it is convenient to rewrite it in a non-dimensionalised form, i.e. in reduced units. Hence we scale the total effective field $\boldsymbol{H}_t$ with respect to the anisotropy field strength so that $\boldsymbol{h}_t = \dfrac{\boldsymbol{H}_t}{H_k}$ where $\boldsymbol{h}_t$ is the reduced total effective field, the reduced time $\tau = t|\gamma|H_k$, $\alpha = \dfrac{\lambda}{|\gamma|M_s}$ is the reduced damping constant and the reduced magnetization, $\boldsymbol{m} = \dfrac{\boldsymbol{M}}{M_s}$. The reduced form of equation (3.25) is then

$$\frac{d\boldsymbol{m}}{d\tau} = -\boldsymbol{m} \times \boldsymbol{h}_t - \alpha(\boldsymbol{m} \times (\boldsymbol{m} \times \boldsymbol{h}_t)) \tag{3.28}$$

To obtain the desired rapid convergence to equilibrium, we set α to unity in our simulations since this gives the most rapid relaxation [42].

We may formulate equation (3.28) in terms of the components of $\boldsymbol{m}$ either directly in Cartesian component form or by the use of spherical polar coordinates. The finite element formulation in our model requires us to solve for the reduced magnetization $\boldsymbol{m}$ pointwise at a node in the finite element discretisation scheme.

Thus if there are N nodes in the system and if we use Cartesian components x, y and z, we will have to solve $3N$ equations at each time step. In the case of using spherical polar coordinates, since $|\boldsymbol{m}| = 1$, $r = 1$ so we only need to find changes in θ and ϕ, hence we will have to solve $2N$ equations at each time step. However the use of spherical polar coordinates involves calculation of the intrinsic functions sin and cos, so there is no computational advantage in using this method hence for convenience we chose the Cartesian component form.

The components of reduced magnetization $\boldsymbol{m}$ are given by m_x, m_y and m_z along the directions of the x, y and z axes respectively, similarly we have h_x, h_y and h_z for the components of effective field $\boldsymbol{h}_t$. Hence

$$\boldsymbol{m}(\tau) = (m_x(\tau), m_y(\tau), m_z(\tau)) \tag{3.29}$$

$$\boldsymbol{h}_t(\tau) = (h_x(\tau), h_y(\tau), h_z(\tau)) \tag{3.30}$$

and equation (3.28) in component form is

$$\begin{aligned}
\frac{dm_x(\tau)}{d\tau} &= -(m_y h_z - m_z h_y) - \alpha(m_y(m_x h_y - m_y h_x) - m_z(m_z h_x - m_x h_z)) \\
\frac{dm_y(\tau)}{d\tau} &= -(m_z h_x - m_x h_z) - \alpha(m_z(m_y h_z - m_z h_y) - m_x(m_x h_y - m_y h_x)) \\
\frac{dm_z(\tau)}{d\tau} &= -(m_x h_y - m_y h_x) - \alpha(m_x(m_z h_x - m_x h_z) - m_y(m_y h_z - m_z h_y))
\end{aligned} \tag{3.31}$$

The set of differential equations (3.31) are coupled through the components of the reduced magnetization $\boldsymbol{m}$. To solve them we need to use a numerical method to integrate the components on the right hand side with respect to the reduced time τ, but since the equations are coupled it is not possible to solve any one by itself, hence we must find an appropriate numerical solver to do this. There are many routines available to solve sets of differential equations so we must choose the one best suited to our application in terms of accuracy, stability and computational requirements.

3.4.1 Euler method

To introduce this method let us consider its application to solution of the following ordinary differential equation

$$\frac{dy}{dt} = f(t, y) \tag{3.32}$$

subject to the initial condition $y(t_0) = y_0$.

Euler's method is the simplest way to get a solution. The idea is that since we know $y = y_0$ at $t = t_0$ from equation (3.32) we also know the slope $\frac{dy}{dt}$ at this point. Hence we can use this initial slope to get a tangent line approximation to the value of y at a nearby point, say $t = t_0 + h$. Thus

$$y(t_o + h) = y(t_0) + hf(t_0, y(t_0)) \tag{3.33}$$

$$= y_0 + hf(t_o, y_0) \tag{3.34}$$

Now we know y at a new point, so from equation (3.32) we also know the slope, so a new tangent line can be constructed to get y at another point $(t_0 + 2h)$ so

$$y(t_o + 2h) = y(t_0 + h) + hf(t_0 + h, y(t_0 + h)) \tag{3.35}$$

This procedure can be repeated to obtain an approximation to y at any point. Thus if h is the size of the time step, in general Euler's method may be written as

$$y_{n+1} = y_n + hf(t_n, y_n) \tag{3.36}$$

where $t_{n+1} = t_n + h$ and $y_n = y(t_n)$.

In order to solve systems of ordinary differential equations such as equation (3.28) the Euler method generalizes to vector component form as follows.

If

$$\mathbf{y} = \begin{pmatrix} y_1 \\ y_2 \\ \dots \\ y_m \end{pmatrix} \tag{3.37}$$

The system of differential equations may be written in component form as

$$\frac{d\boldsymbol{y}}{dt} = \boldsymbol{f}(t, \boldsymbol{y}) \tag{3.38}$$

$$= \begin{pmatrix} f_1 \\ f_2 \\ \cdots \\ f_m \end{pmatrix} \tag{3.39}$$

with the initial conditions

$$\boldsymbol{s} = \begin{pmatrix} s_1 \\ s_2 \\ \cdots \\ s_m \end{pmatrix} \tag{3.40}$$

then

$$\boldsymbol{y}_{n+1} = \boldsymbol{y}_n + h\boldsymbol{f}(t_n, \boldsymbol{y}_n) \tag{3.41}$$

where $t_{n+1} = t_n + h$ and $\boldsymbol{y}_n = \boldsymbol{y}(t_n)$

3.4.2 Runge-Kutta method

A more accurate alternative to the Euler method is that of the Runge-Kutta method. With this procedure the numerical scheme is slightly more complicated than with Euler, a derivation of the formulae from the Taylor expansions is given in a book on numerical analysis by Burden [43]. If we turn our attention to the solution of equation (3.32), the fourth order Runge-Kutta solution is obtained as follows

$$y_{n+1} = y_n + \frac{h}{6}(k_1 + 2k_2 + 2k_3 + k_4) \tag{3.42}$$

where

$$\begin{aligned} k_1 &= f(t_n, y_n) \\ k_2 &= f\left(t_n + \frac{h}{2}, y_n + \frac{hk_1}{2}\right) \\ k_3 &= f\left(t_n + \frac{h}{2}, y_n + \frac{hk_2}{2}\right) \\ k_4 &= f(t_n + h, y_n + hk_3) \end{aligned}$$

Here we see that there are 4 function evaluations required at each time step. This method also generalises to a form suitable for use in the solution of a system of ordinary differential equations.

Before describing the generalization, it is convenient to slightly modify the way that we write the set of differential equations $\frac{d\boldsymbol{y}}{dt} = \boldsymbol{f}(t, \boldsymbol{y})$. It is not necessary to treat the variable t separately from the others in $\boldsymbol{y}$. We may bring t in disguise into $\boldsymbol{y}$ by introducing a new variable and a new differential equation

$$\frac{dy_{m+1}}{dt} = 1 \tag{3.43}$$

with the initial condition $y_{m+1}(t_0) = t_0$.
In this way we increase the number of differential equations by one to obtain a simpler system

$$\frac{d\boldsymbol{y}}{dt} = \boldsymbol{f}(\boldsymbol{y}) \tag{3.44}$$

with initial conditions

$$\boldsymbol{y}(t_0) = \boldsymbol{s} \tag{3.45}$$

We may now represent the Runge-Kutta method for a system of ordinary differential equations in vector component form as

$$\boldsymbol{y}_{n+1} = \boldsymbol{y}_n + \frac{h}{6}(\boldsymbol{k}_1 + 2\boldsymbol{k}_2 + 2\boldsymbol{k}_3 + \boldsymbol{k}_4) \tag{3.46}$$

where

$$\begin{aligned}
\boldsymbol{k}_1 &= \boldsymbol{f}(\boldsymbol{y}_n) \\
\boldsymbol{k}_2 &= \boldsymbol{f}\left(\boldsymbol{y}_n + \frac{h\boldsymbol{k}_1}{2}\right) \\
\boldsymbol{k}_3 &= \boldsymbol{f}\left(\boldsymbol{y}_n + \frac{h\boldsymbol{k}_2}{2}\right) \\
\boldsymbol{k}_4 &= \boldsymbol{f}(\boldsymbol{y}_n + h\boldsymbol{k}_3)
\end{aligned}$$

3.4.3 Predictor-Corrector methods

The two procedures explained so far have solved equation (3.32) and its vector generalization by means of single step numerical methods. In other words, if we know $\boldsymbol{y}(t)$ at a particular time, t, then $\boldsymbol{y}(t+h)$ can be found without any knowledge of the solution at points earlier than t. More efficient methods can be devised if several values $\boldsymbol{y}(t)$, $\boldsymbol{y}(t-h)$, $\boldsymbol{y}(t-2h)$, ... are utilized in finding $\boldsymbol{y}(t+h)$, i.e. multi-step methods. Such methods are not self starting since at the beginning no values of $\boldsymbol{y}$ are known, so it is usual to start by obtaining the first few initial slopes by using a single step method such as Euler or Runge-Kutta.

One example of a multi-step formula is the Adams-Bashforth scheme given in vector form by

$$\boldsymbol{y}_{n+1} = \boldsymbol{y}_n + \frac{h}{24}\left[55\boldsymbol{f}(\boldsymbol{y}_n) - 59\boldsymbol{f}(\boldsymbol{y}_{n-1}) + 37\boldsymbol{f}(\boldsymbol{y}_{n-2}) - 9\boldsymbol{f}(\boldsymbol{y}_{n-3})\right] \quad (3.47)$$

Since the solution $\boldsymbol{y}$ has been calculated at the four points t, $t-h$, $t-2h$ and $t-3h$, then equation (3.47) can be used to compute $\boldsymbol{y}(t+h)$. This procedure can be done systematically so only one evaluation of $\boldsymbol{f}$ is needed at each time step. This is a considerable saving over the fourth order Runge-Kutta method. However equation (3.47) is never used by itself but in conjunction with another formula as part of a predictor corrector scheme.

There are many predictor corrector methods discussed in [44] with different orders of accuracy, each consists of two formulae the predictor part and the corrector part. The predictor equation is used to compute the value at the next time step explicitly and the corrector part then uses this predicted value in an implicit formula to obtain the corrected value. The Adams-Bashforth formula is the predictor part of the Adams-Moulton predictor corrector method. The corrector equation is given by the Adams-Moulton formula

$$\boldsymbol{y}_{n+1} = \boldsymbol{y}_n + \frac{h}{24}\left[9\boldsymbol{f}(\boldsymbol{y}^*_{n+1}) + 19\boldsymbol{f}(\boldsymbol{y}_n) - 5\boldsymbol{f}(\boldsymbol{y}_{n-1}) + \boldsymbol{f}(\boldsymbol{y}_{n-2})\right] \quad (3.48)$$

Here $\boldsymbol{y}^*_{n+1}$ is the predicted value of $\boldsymbol{y}_{n+1}$ computed from equation (3.47), the equation (3.48) then gives $\boldsymbol{y}_{n+1}$ more accurately.

3.4.4 Comparison of numerical schemes

The numerical solvers for ordinary differential equations discussed in this chapter are only explained briefly. The mathematical justifications of these methods are described in most books on numerical analysis such as [43], [44] and [45] together with other schemes. It is worthwhile to note that most schemes are derived from the Taylor expansion of $y(t)$ around t

$$y(t+h) = y(t) + h\frac{dy(t)}{dt} + \frac{h^2}{2}\frac{d^2y(t)}{dt^2} + \frac{h^3}{6}\frac{d^3y(t)}{dt^3} + ... + \frac{h^r}{r!}\frac{d^ry(t)}{dt^r} + ... \quad (3.49)$$

This idea is also used to quantify the accuracy of a method. The order of accuracy of a particular method is found by substituting the form of the numerical approximation into the Taylor series expansion and then comparing up to which order term the series is successfully reproduced. This is the order of accuracy of the numerical scheme. For instance the Euler method is only first order accurate whereas the Runge-Kutta method mentioned here is fourth order accurate. However accuracy is not the only concern in micromagnetic simulations and a further important consideration is that of numerical stability.

This arises due to the presence of the dissipative term in the Landau-Lifshitz equation which creates an exponentially decaying solution. We need to solve the differential equations describing the Cartesian components of magnetization at each node in the discretisation scheme. However activity in the change of magnetization at any particular node will be varying throughout the material. Nodes located at areas that change most rapidly will govern the stability of the numerical solver.

Authors that have carried out micromagnetic simulations in the past have used a variety of numerical schemes for solving the time evolution of the system Victora [46] used a Runge-Kutta method, Tako *et al* a predictor corrector scheme [47]. Our initial simulations for single nanoelements [48] were carried out successfully using the Euler method to solve equation (3.28) with a reduced time step of order 10^{-2}. However when we came to do simulations on arrays of interacting particles

we found smaller time steps were necessary due to the decrease in mesh spacing as a consequence of the refined mesh. Predictor corrector schemes have been found to remain stable with slightly larger time steps [44]. With this in mind we implemented the Adams-Moulton method for our simulations on arrays of interacting nanoelements. Under these conditions we needed a reduced time step of the order 10^{-3} - 10^{-6} depending upon the size of the system.

3.5 Summary

In this chapter we have given a detailed description of the micromagnetic model which we will use in our simulations. The nanoelement geometries have been introduced together with the general idea behind the method we shall use to create their discretised form. We have defined the pointwise magnetic moment and how it will be approximated by the use of a finite element interpolation scheme.

We have described the mathematical formulation of the micromagnetic field terms and how they will be obtained. At this stage however we have not given full details of the implementation of our finite element variational method to the calculation of the demagnetizing field, this is left until the following chapter.

The Landau-Lifshitz equation of motion has been introduced as our means to modelling the magnetization dynamics. We have given a brief description of the underlying mathematical physics which governs it and finally we have described the numerical schemes which we shall employ to solve it.

Chapter 4

Demagnetizing field calculation

4.1 Introduction

In order to model the micromagnetic behaviour of a material, one must consider the effective field sources of exchange, anisotropy and magnetostatic. When we look at the mathematical modelling of the exchange and anisotropy terms we see that these depend locally on the magnetization behaviour at a particular position on the material. This is clearly not the case in the magnetostatic field calculation, which depends upon the global behaviour of the magnetization distribution throughout the material.

The demagnetizing field acts opposite in direction to the magnetization which creates it, hence the magnetization is the principal source of the demagnetizing field in any ferromagnetic material. Due to its long range nature the magnetostatic (demagnetizing) field calculation is the most time consuming due its computational requirements. Previous authors have used a variety of numerical methods on this calculation. Dipolar approximations were used by Walmsley [49] who also employed an analytical expression for a uniformly magnetized sphere and oblate spheroid in spherical polar coordinates for the stray field so that this could be used in Lorentz imaging techniques. Other popular methods include a Fast Fourier Transform based scalar potential method as used by Berkov and coworkers [50].

In this chapter, we discuss the problem of the magnetostatic field calculation in terms of computational requirements and efficiency with a detailed mathematical description of the implementation of the numerical method which we are going to use in our simulations - the finite element method.

Although this is not the first time the FEM has been used in micromagnetics as mentioned at the end of Chapter 1, we shall develop a novel approach.

4.2 Method of obtaining the demagnetizing field

In the previous chapter, we have seen that the demagnetizing field, $\boldsymbol{H}_d$ may be calculated via a magnetic scalar potential, ϕ which is expressed by the equations (3.19) - (3.22) then

$$\boldsymbol{H}_d = -\nabla\phi \tag{4.1}$$

The equations for ϕ have been found to satisfy [38]

$$\phi(\boldsymbol{r}) = \int_{V'} \frac{-\nabla' \cdot \boldsymbol{M}(\boldsymbol{r'})}{|\boldsymbol{r} - \boldsymbol{r'}|} dV' + \int_{S'} \frac{\boldsymbol{M}(\boldsymbol{r'}) \cdot \hat{\boldsymbol{n}}}{|\boldsymbol{r} - \boldsymbol{r'}|} dS' \tag{4.2}$$

where the magnetic volume charge is defined by

$$\rho(\boldsymbol{r'}) = -\nabla' \cdot \boldsymbol{M}(\boldsymbol{r'}) \tag{4.3}$$

and the surface charge by

$$\sigma(\boldsymbol{r'}) = \boldsymbol{M}(\boldsymbol{r'}) \cdot \hat{\boldsymbol{n}} \tag{4.4}$$

From equation (4.2) we can write the demagnetizing field $\boldsymbol{H}_d$ as

$$\boldsymbol{H}_d = \int_{V'} \frac{-(\boldsymbol{r} - \boldsymbol{r'})\nabla \cdot \boldsymbol{M}(\boldsymbol{r'})}{|\boldsymbol{r} - \boldsymbol{r'}|^3} dV' + \int_{S'} (\boldsymbol{r} - \boldsymbol{r'}) \frac{\boldsymbol{M}(\boldsymbol{r'}) \cdot \hat{\boldsymbol{n}}}{|\boldsymbol{r} - \boldsymbol{r'}|} dS' \tag{4.5}$$

Although these equations represent elegant closed form solutions for the potential and demagnetizing field, they are not the best form for numerical computation.

Analytic solutions of equation (4.2) exist for certain geometries [38] and will be discussed later on in this chapter but solutions for irregular domains involve very complex methods which can involve 6-fold integration. In terms of the numerical calculation this involves a scaling with N^2 where N is the number of cells into which the body is discretised. This leads to a rapid degradation of computational speed with system size and in practice alternative techniques must be used which will now be discussed.

4.3 Finite element formulation of the scalar potential

In the previous chapter the equation (3.1) described a representation of the reduced magnetization, $\boldsymbol{m}$ in terms of linear finite element interpolation functions. We have also seen how the demagnetizing field, $\boldsymbol{H}_d$ may be expressed in terms of a magnetic scalar potential ϕ. To use this approach we need to be able to calculate ϕ from the set of equations (3.19) - (3.22).

With the finite element method in mind we can now proceed to formulate a solution for a reduced form of ϕ by working in terms of the reduced magnetization $\boldsymbol{m}$ and the reduced demagnetizing field $\boldsymbol{h}_d$ where $\boldsymbol{h}_d = \dfrac{\boldsymbol{H}_d}{H_k}$. Before applying our method let us note that we have two regions in question Ω_{int} where the magnetization distribution is non-zero and Ω_{ext} where this distribution is the zero vector field. The abrupt difference in material properties is taken care of along the interface, $\partial\Omega$ by the condition

$$\frac{\partial \phi_{int}}{\partial \hat{n}} - \frac{\partial \phi_{ext}}{\partial \hat{n}} = 4\pi \boldsymbol{m} \cdot \hat{\boldsymbol{n}} \qquad \forall \boldsymbol{x} \in \partial\Omega \tag{4.6}$$

which may also be written as

$$\nabla \phi_{int} \cdot \hat{\boldsymbol{n}} - \nabla \phi_{ext} \cdot \hat{\boldsymbol{n}} = 4\pi \boldsymbol{m} \cdot \hat{\boldsymbol{n}} \qquad \forall \boldsymbol{x} \in \partial\Omega \tag{4.7}$$

With this in mind we notice that $\nabla \cdot \boldsymbol{m}$ is zero when $\boldsymbol{m} = \boldsymbol{0}$, hence we may solve equation (3.19) over the two mathematical domains Ω_{int} and Ω_{ext}.

We notice that the equations are defined over entire space, however under experimental observation the demagnetizing field is known to become weaker as we go further away from the magnetic region. With this in mind it is sensible to implement a method which gives a solution over a finite part of external space surrounding the magnetic material in question. The entire problem is then solved over a single mathematical domain consisting of a magnetic and non-magnetic region, with an artificial boundary condition imposed on the outer region's boundary $\partial\Re$. However, we must also incorporate the interface condition into the method.

Hence our method will solve equations (3.19) - (3.22) over a single mathematical domain (Figure 4.1) with equation (4.6) being satisfied along the interface and an artificial boundary condition of $\phi = 0$ on $\partial\Re$.

4.3.1 Explicit interface condition

We shall now describe a novel method for finding ϕ by the use of the FEM. The essence of the method is to replace the open boundary by a suitably large closed boundary $\partial\Re$ which is far enough away from the magnetic region Ω_{int} and enclosing Ω_{ext}.

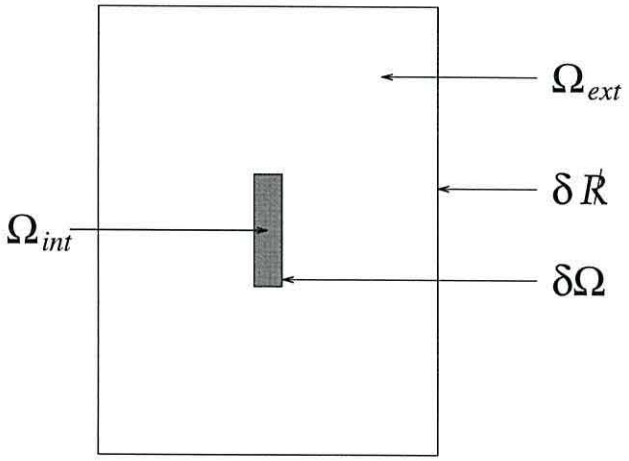

Figure 4.1: Model of region as a single mathematical domain

Effectively we are now solving the Poisson equation globally over a single mathe-

matical domain.

$$\nabla^2\phi = 4\pi\nabla\cdot\boldsymbol{m} \tag{4.8}$$

Let us denote the global potential ϕ by

$$\phi = \phi_{int} + \phi_{ext} \tag{4.9}$$

and the region Ω by

$$\Omega = \Omega_{int} + \Omega_{ext} \tag{4.10}$$

Using equation (2.33), the variational formulation of the Poisson equation is then given by

$$\begin{aligned} I[\phi] = & \int\int_{\Omega}\left(\frac{\partial\phi}{\partial x}\right)^2 + \left(\frac{\partial\phi}{\partial y}\right)^2 d\Omega \\ & -2\int\int_{\Omega}\phi(4\pi\nabla\cdot\boldsymbol{m})d\Omega \end{aligned} \tag{4.11}$$

Since we know that the field becomes weaker the further away we are from Ω_{int}, it is sensible to impose the artificial Dirichlet boundary condition

$$\phi = 0 \qquad \forall\boldsymbol{x}\in\partial\Re \tag{4.12}$$

In order to obtain ϕ we will apply the standard Rayleigh-Ritz stationary functional method. As with any FEM solution, a suitable transformation method is used to map each element to a simple parent element in order to simplify the integration over the whole region. Since we are using triangular elements, it is convenient to use the system of local area coordinates (L_i, L_j, L_k) introduced by equations (2.25) - (2.27). Referring to equations (2.45) - (2.70), we may proceed to assemble the finite element stiffness matrix with element contributions given by

$$k^e_{ij} = \int\int_{R^e}\left(\frac{\partial L^e_i}{dx}\frac{\partial L^e_j}{dx} + \frac{\partial L^e_i}{dy}\frac{\partial L^e_j}{dy}\right)dxdy \tag{4.13}$$

Since we are interpolating $\boldsymbol{m}$ linearly within an element

$$\begin{aligned} 4\pi\nabla\cdot\boldsymbol{m} &= 4\pi\nabla\cdot(m_x,m_y) \\ &= 4\pi\left(\frac{\partial}{\partial x},\frac{\partial}{\partial y}\right)\cdot\left(\sum_{i=1}^{3}L_i^e m_{xi}^e,\sum_{i=1}^{3}L_i^e m_{yi}^e\right) \\ &= 4\pi\left(\sum_{i=1}^{3}\frac{\partial L_i^e}{\partial x}m_{xi}^e+\sum_{i=1}^{3}\frac{\partial L_i^e}{\partial y}m_{yi}^e\right) \\ &= \frac{2\pi}{A}\left(\sum_{i=1}^{3}b_i^e m_{xi}^e+c_i^e m_{yi}^e\right) \end{aligned} \tag{4.14}$$

The element force vector is calculated from

$$\begin{aligned} f_i^e &= -\int_{R^e}L_i^e(4\pi\nabla\cdot\boldsymbol{m})dxdy \\ &= -(4\pi\nabla\cdot\boldsymbol{m})\int_{R^e}L_i^e dxdy \\ &= -\frac{2\pi}{A}\left(\sum_{i=1}^{3}b_i^e m_{xi}^e+c_i^e m_{yi}^e\right)\int_{R^e}L_i^e dxdy \end{aligned} \tag{4.15}$$

Using the following result given in Appendix A

$$\int_A L_1^m L_2^n L_3^p dA = \frac{2Am!n!p!}{(m+n+p+2)!} \tag{4.16}$$

gives

$$f_i^e = -\left(\frac{2\pi}{3}\right)\left(\sum_{i=1}^{3}b_i^e m_{xi}^e+c_i^e m_{yi}^e\right) \tag{4.17}$$

There has been no consideration yet given to the interface. To bring this into the method we proceed as follows :

- There will be the same number of outer boundary elements as there are boundary nodes.
- If a node lies on the interface, replace its formulation in the corresponding row in the stiffness matrix and element force vector with the interface condition given by equation (4.7).
- The interface condition is formulated via an outer boundary element and its corresponding interior boundary element.

The mathematical formulation of this will now be described, but first some consideration must be given to the orientation of normals to the boundary elements around the magnetic region and their formulation via the interpolation functions. For any particular finite element we have one associated normal per side, i.e. $\hat{\boldsymbol{n}}_{12}$, $\hat{\boldsymbol{n}}_{23}$ and $\hat{\boldsymbol{n}}_{13}$ as shown in Figure 4.2.

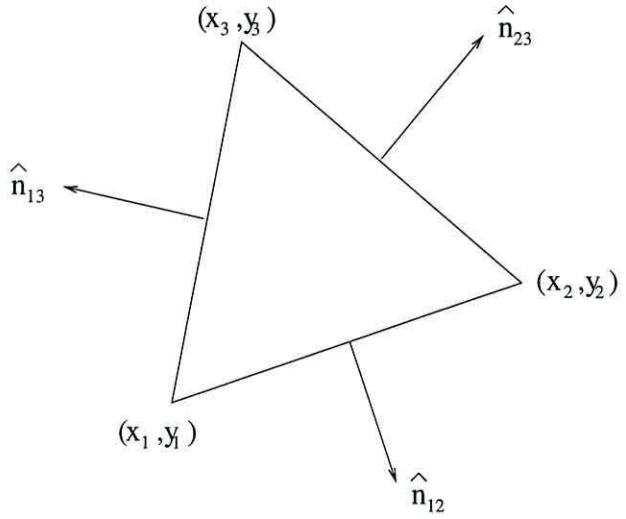

Figure 4.2: Normals exterior to an element

We may then calculate these normals from the local coordinates by

$$\begin{aligned} \hat{\boldsymbol{n}}_{12} &= \frac{(y_2 - y_1, x_1 - x_2)}{\sqrt{(x_1 - x_2)^2 + (y_1 - y_2)^2}} \\ &= \frac{(-b_3, -c_3)}{(b_3^2 + c_3^2)^{\frac{1}{2}}} \end{aligned} \tag{4.18}$$

$$\begin{aligned} \hat{\boldsymbol{n}}_{23} &= \frac{(y_3 - y_2, x_2 - x_3)}{\sqrt{(x_2 - x_3)^2 + (y_2 - y_3)^2}} \\ &= \frac{(-b_1, -c_1)}{(b_1^2 + c_1^2)^{\frac{1}{2}}} \end{aligned} \tag{4.19}$$

$$\begin{aligned} \hat{\boldsymbol{n}}_{13} &= \frac{(y_1 - y_3, x_3 - x_1)}{\sqrt{(x_1 - x_3)^2 + (y_1 - y_3)^2}} \\ &= \frac{(-b_2, -c_2)}{(b_2^2 + c_2^2)^{\frac{1}{2}}} \end{aligned} \tag{4.20}$$

where the expressions for b_i and c_j are given by equation (2.24) in terms of the local coordinates x and y.

For linear elements the interface condition may be formulated as follows with the normal $\hat{\boldsymbol{n}}$ computed from the appropriate formula chosen from equations (4.18) - (4.20) depending upon which side of the element lies on the interface and is taken outward from the magnetic region.

$$\begin{aligned}
\nabla\phi_{int}\cdot\hat{\boldsymbol{n}} - \nabla\phi_{ext}\cdot\hat{\boldsymbol{n}} &= \nabla\sum_{i=1}^{3} L_i\phi_i^{int}\cdot\hat{\boldsymbol{n}} - \nabla\sum_{i=1}^{3} L_i\phi_i^{ext}\cdot\hat{\boldsymbol{n}} \\
&= \sum_{i=1}^{3}\left(\frac{\partial L_i}{\partial x}\phi_i^{int}, \frac{\partial L_i}{\partial y}\phi_i^{int}\right)\cdot\hat{\boldsymbol{n}} \\
&\quad -\sum_{i=1}^{3}\left(\frac{\partial L_i}{\partial x}\phi_i^{ext}, \frac{\partial L_i}{\partial y}\phi_i^{ext}\right)\cdot\hat{\boldsymbol{n}} \\
&= \frac{1}{2A^{int}}\sum_{i=1}^{3}\left(b_i^{int}\phi_i^{int}, c_i^{int}\phi_i^{int}\right)\cdot\hat{\boldsymbol{n}} \\
&\quad -\frac{1}{2A^{ext}}\sum_{i=1}^{3}\left(b_i^{ext}\phi_i^{ext}, c_i^{ext}\phi_i^{ext}\right)\cdot\hat{\boldsymbol{n}} \\
&= \frac{1}{2A^{int}}\sum_{i=1}^{3}\left(b_i^{int}\phi_i^{int}n_x + c_i^{int}\phi_i^{int}n_y\right) \\
&\quad -\frac{1}{2A^{ext}}\sum_{i=1}^{3}\left(b_i^{ext}\phi_i^{ext}n_x + c_i^{ext}\phi_i^{ext}n_y\right) \\
&= \frac{1}{2A^{int}}\sum_{i=1}^{3}\left(b_i^{int}\phi_i^{int}n_x + c_i^{int}\phi_i^{int}n_y\right) \\
&\quad -\frac{1}{2A^{ext}}\sum_{i=1}^{3}\left(b_i^{ext}\phi_i^{ext}n_x + c_i^{ext}\phi_i^{ext}n_y\right) \qquad (4.21)
\end{aligned}$$

and

$$4\pi\boldsymbol{m}\cdot\hat{\boldsymbol{n}} = 4\pi\sum_{i=1}^{3} L_i m_{xi}n_x + L_i m_{yi}n_y \qquad (4.22)$$

Where A^{int} and A^{ext} represent the area of the interior and exterior boundary elements respectively.

At this stage it is worthwhile to note that in order to keep the computational requirements to a minimum our initial studies used linear finite elements. However, linear elements were found unsuitable for our method, even after intensive mesh refinement in areas of great spatial variation. This was found to be due to the enforcing of continuity in ϕ and the interface condition along $\partial\Omega$. This problem was resolved by the use of quadratic finite elements.

4.3.2 Quadratic formulation

The quadratic nodal displacement functions N_i are formed from the linear functions as follows

$$N_i = 2L_i(L_i - 1) \qquad i = 1, 2, 3 \tag{4.23}$$

$$N_4 = 4L_1L_2 \tag{4.24}$$

$$N_5 = 4L_2L_3 \tag{4.25}$$

$$N_6 = 4L_1L_3 \tag{4.26}$$

giving a quadratic interpolation scheme for ϕ enabling higher order interpolation within the domain. Thus

$$\phi^e = (N_1^e N_2^e N_3^e N_4^e N_5^e N_6^e) \begin{pmatrix} \phi_1^e \\ \phi_2^e \\ \phi_3^e \\ \phi_4^e \\ \phi_5^e \\ \phi_6^e \end{pmatrix} \tag{4.27}$$

The stiffness matrix $\boldsymbol{K}$ is formed in a similar manner to the linear case by integrating over elements. A contribution to an entry is obtained from a particular element by

$$k_{ij}^e = \int\int_{R^e} \left(\frac{\partial N_i^e}{dx}\frac{\partial N_j^e}{dx} + \frac{\partial N_i^e}{dy}\frac{\partial N_j^e}{dy} \right) dxdy \tag{4.28}$$

Due to the higher order interpolation functions the integration is more difficult than in the linear case, the result for the upper triangular part is given in [51] by

$$k_{11} = \frac{1}{4A}(b_1^2 + c_1^2) \qquad k_{12} = -\frac{1}{12A}(b_1b_2 + c_1c_2) \qquad k_{13} = -\frac{1}{12A}(b_1b_3 + c_1c_3)$$

$$k_{14} = \frac{1}{3A}(b_1b_2 + c_1c_2) \qquad k_{15} = 0 \qquad k_{16} = \frac{1}{3A}(b_1b_3 + c_1c_3)$$

$$k_{22} = \frac{1}{4A}(b_2^2 + c_2^2) \qquad k_{23} = -\frac{1}{12A}(b_2b_3 + c_2c_3) \qquad k_{24} = \frac{1}{3A}(b_1b_2 + c_1c_2)$$

$$k_{25} = \frac{1}{3A}(b_2b_3 + c_2c_3) \qquad k_{26} = 0$$

$$k_{33} = \frac{1}{4A}(b_3^2 + c_3^2) \qquad k_{34} = 0 \qquad k_{35} = \frac{1}{3A}(b_2b_3 + c_2c_3) \qquad k_{36} = \frac{1}{3A}(b_1b_3 + c_1c_3)$$

$$k_{44} = \frac{2}{3A}(b_2^2 + b_1b_2 + b_1^2 + c_2^2 + c_1c_2 + c_1^2)$$

$$k_{45} = \frac{1}{3A}(b_2b_3 + 2b_1b_3 + b_2^2 + b_1b_2 + c_2c_3 + 2c_1c_3 + c_2^2 + c_1c_2)$$

$$k_{46} = \frac{1}{3A}(2b_2b_3 + b_1b_3 + b_1b_2 + b_1^2 + 2c_2c_3 + c_1c_3 + c_1c_2 + c_1^2)$$

$$k_{55} = \frac{2}{3A}(b_3^2 + b_2b_3 + b_2^2 + c_3^2 + c_2c_3 + c_2^2)$$

$$k_{56} = \frac{1}{3A}(b_3^2 + b_2b_3 + b_1b_3 + 2b_1b_2 + c_3^2 + c_2c_3 + c_1c_3 + 2c_1c_2)$$

$$k_{66} = \frac{2}{3A}(b_3^2 + b_1b_3 + b_1^2 + c_3^2 + c_1c_3 + c_1^2)$$

Where b_i and c_i belong to a particular element and A is the area of the element.

The derivatives of the shape functions are derived as follows. For corner nodes

$$N_i = L_i(2L_i - 1) \qquad i = 1, 2, 3 \tag{4.29}$$

and so

$$\begin{aligned} \frac{\partial N_i}{\partial x} &= \left(\frac{\partial N_i}{\partial L_i}\right)\left(\frac{\partial L_i}{\partial x}\right) \\ &= (4L_i - 1)\frac{b_i}{2A} \\ &= \frac{b_i}{2A^2}(2a_i + 2b_ix + 2c_iy - A) \end{aligned} \tag{4.30}$$

$$\begin{aligned} \frac{\partial N_i}{\partial y} &= \left(\frac{\partial N_i}{\partial L_i}\right)\left(\frac{\partial L_i}{\partial y}\right) \\ &= (4L_i - 1)\frac{c_i}{2A} \\ &= \frac{c_i}{2A^2}(2a_i + 2b_ix + 2c_iy - A) \end{aligned} \tag{4.31}$$

For mid side nodes

$$N_i = 4L_jL_k \qquad i = 4, 5, 6 \tag{4.32}$$

so

$$\begin{aligned}\frac{\partial N_i}{\partial x} &= \frac{\partial(4L_jL_k)}{\partial x} \\ &= 4L_j\frac{\partial L_k}{\partial x} + 4L_k\frac{\partial L_j}{\partial x} \\ &= 4L_j\left(\frac{b_k}{2A}\right) + 4L_k\left(\frac{b_j}{2A}\right) \\ &= \frac{1}{A^2}[a_jb_k + a_kb_j + (b_jc_k + b_kc_j)y + 2b_jb_jx] \end{aligned} \tag{4.33}$$

$$\begin{aligned}\frac{\partial N_i}{\partial y} &= \frac{\partial(4L_jL_k)}{\partial y} \\ &= 4L_j\frac{\partial L_k}{\partial y} + 4L_k\frac{\partial L_j}{\partial y} \\ &= 4L_j\left(\frac{c_k}{2A}\right) + 4L_k\left(\frac{c_j}{2A}\right) \\ &= \frac{1}{A^2}[a_jc_k + a_kc_j + (b_jc_k + b_kc_j)x + 2c_jc_jy] \end{aligned} \tag{4.34}$$

In order to formulate the interface condition, let us first note that

$$\nabla\phi = \left(\frac{\partial\phi}{\partial x}, \frac{\partial\phi}{\partial y}\right) \tag{4.35}$$

where

$$\begin{aligned}\frac{\partial\phi}{\partial x} &= \sum_{i=1}^{3}\frac{\phi_ib_i}{2A^2}(2a_i + 2b_ix + 2c_iy - A) \\ &\quad + \sum_{i=4}^{6}\frac{\phi_i}{A^2}\left[a_jb_k + a_kb_j + (b_jc_k + b_kc_j)y + 2b_jb_kx\right] \end{aligned} \tag{4.36}$$

and

$$\begin{aligned}\frac{\partial\phi}{\partial y} &= \sum_{i=1}^{3}\frac{\phi_ic_i}{2A^2}(2a_i + 2b_ix + 2c_iy - A) \\ &\quad + \sum_{i=4}^{6}\frac{\phi_i}{A^2}\left[a_jc_k + a_kc_j + (b_jc_k + b_kc_j)x + 2c_jc_ky\right] \end{aligned} \tag{4.37}$$

Thus

$$\nabla\phi_{int}\cdot\hat{\boldsymbol{n}}-\nabla\phi_{ext}\cdot\hat{\boldsymbol{n}}=\left[\sum_{i=1}^{3}\frac{\phi_i^{int}b_i^{int}}{(2A^{int})^2}(2a_i^{int}+2b_i^{int}x+2c_i^{int}y-A^{int})\right.$$
$$\left.+\sum_{i=4}^{6}\frac{\phi_i^{int}}{(A^{int})^2}\left(a_j^{int}b_k^{int}+a_k^{int}b_j^{int}+(b_j^{int}c_k^{int}+b_k^{int}c_j^{int})y+2b_j^{int}b_k^{int}x\right)\right]n_x$$
$$+\left[\sum_{i=1}^{3}\frac{\phi_i^{int}c_i^{int}}{(2A^{int})^2}(2a_i^{int}+2b_i^{int}x+2c_i^{int}y-A^{int})\right.$$
$$\left.+\sum_{i=4}^{6}\frac{\phi_i}{(A^{int})^2}\left(a_j^{int}c_k^{int}+a_k^{int}c_j^{int}+(b_j^{int}c_k^{int}+b_k^{int}c_j^{int})x+2c_j^{int}c_k^{int}y\right)\right]n_y$$
$$-\left[\sum_{i=1}^{3}\frac{\phi_i^{ext}b_i^{ext}}{(2A^{ext})^2}(2a_i^{ext}+2b_i^{ext}x+2c_i^{ext}y-A^{ext})\right.$$
$$\left.+\sum_{i=4}^{6}\frac{\phi_i^{ext}}{(A^{ext})^2}\left(a_j^{ext}b_k^{ext}+a_k^{ext}b_j^{ext}+(b_j^{ext}c_k^{ext}+b_k^{ext}c_j^{ext})y+2b_j^{ext}b_k^{ext}x\right)\right]n_x$$
$$-\left[\sum_{i=1}^{3}\frac{\phi_i^{ext}c_i^{ext}}{(2A^{ext})^2}(2a_i^{ext}+2b_i^{ext}x+2c_i^{ext}y-A^{ext})\right.$$
$$\left.+\sum_{i=4}^{6}\frac{\phi_i}{(A^{ext})^2}\left(a_j^{ext}c_k^{ext}+a_k^{ext}c_j^{ext}+(b_j^{ext}c_k^{ext}+b_k^{ext}c_j^{ext})x+2c_j^{ext}c_k^{ext}y\right)\right]n_y \quad (4.38)$$

and

$$4\pi\boldsymbol{m}\cdot\hat{\boldsymbol{n}} \;=\; 4\pi\sum_{i=1}^{3}L_i m_{xi}n_x+L_i m_{yi}n_y \quad (4.39)$$

which is calculated as before since we are still using linear interpolation for $\boldsymbol{m}$. We then incorporate the interface condition by using this formulation directly within the stiffness matrix for nodes which lie on the interface as shown in Figure 4.3.

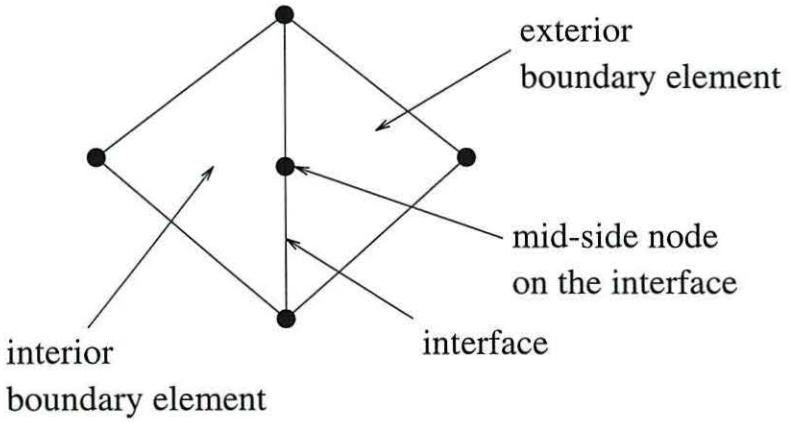

Figure 4.3: Quadratic elements along the interface

Before proceeding any further, the final stage of the construction of the stiffness matrix and element force vector is to enforce the artificial boundary condition given by equation (4.12). This is easily achieved by setting the stiffness matrix so that values of ϕ on $\partial\Re$ are zero. This computation leads up to the formation of a system of n linear equations, where n is the number of nodes in the spatial discretisation scheme.

We now need to solve the set of equations

$$\boldsymbol{K}\boldsymbol{\phi} = \boldsymbol{F} \tag{4.40}$$

where $\boldsymbol{K}$ is a non-singular $n \times n$ sparse matrix, $\boldsymbol{F}$ is a known vector and ϕ is an unknown vector both of length n. The way we choose to solve these equations will influence the efficiency of the demagnetizing field calculation.

If we store $\boldsymbol{K}$ as a $n \times n$ array in memory then we may easily implement a direct method of solution such as Gaussian elimination. We are not able to use a more efficient solver such as the conjugate gradient method with an initial starting solution since $\boldsymbol{K}$ will not be symmetric due to the interface formulation. With this in mind our initial simulations used a factorization of $\boldsymbol{K}$ in terms of lower ($\boldsymbol{L}$) and upper ($\boldsymbol{U}$) triangular matrices, so that $\boldsymbol{K} = \boldsymbol{L}\boldsymbol{U}$ where

$$\boldsymbol{L}\boldsymbol{x} = \boldsymbol{F} \tag{4.41}$$

$$\boldsymbol{U}\boldsymbol{\phi} = \boldsymbol{x} \tag{4.42}$$

This system can easily be solved by performing forward and backward substitutions, thus ϕ may be obtained by matrix multiplication which reduces the computation at each time step, provided no re-meshing is involved. To implement this approach we used the LU factorization routines from the LAPACK library [52].

When n becomes large it is impractical to store the matrix $\boldsymbol{K}$ in this way and to use this method of solution. There are many ways of improving this method one would be to use a technique called the frontal method [53] which involves constructing $\boldsymbol{K}$ at the same time as the elimination process is performed. Only the

part of the matrix being worked on is stored in memory.

Another direct technique would be to reorder the unknowns, so that the structure of the matrix is changed. This reduces the number of non zero entries needed during the elimination. This is discussed in more detail in [54].

Alternative to the direct methods of solution, we could look at iterative methods which are discussed in detail in [55]. In short, these methods take an approximation to $\boldsymbol{\phi}$ and obtain a better solution by iterative refinement until convergence is obtained. A popular iterative approach used in fluid dynamics is GMRES (Generalized Minimal Residual) [56], however the storage requirements are quite high. Another disadvantage to the iterative methods of solution is that we may lose some accuracy.

We require a method of solution which minimizes storage requirements while maximizing speed and accuracy of the solution, hence we have employed an efficient method of storing the entries of $\boldsymbol{K}$ coupled with a solver that takes advantage of this, namely the y12m routines from the netlib library [52]. We implement the storage of the entries in $\boldsymbol{K}$ as follows

4.3.3 Storage of sparse matrices

The stiffness matrix $\boldsymbol{K}$ depends upon the finite element mesh and will always be very sparse. For a typical mesh less than 1% of the entries will be non-zero, hence we need an efficient method of storage for $\boldsymbol{K}$. From a programming point of view it is straightforward to store $\boldsymbol{K}$ as a $n \times n$ array in memory but for large n this soon becomes a disadvantage due to the need for large storage requirements and inefficiency in the solver.

The strategy we have used is to store $\boldsymbol{K}$ by a method which is a variation of the Harwell-Boeing sparse matrix format described in [53]. We specify $\boldsymbol{K}$ by the three arrays $\boldsymbol{K}_{val}$, $\boldsymbol{K}_{row}$ and $\boldsymbol{K}_{col}$. The non-zero entries are stored in $\boldsymbol{K}_{val}$ with

their corresponding row and column numbers in $\boldsymbol{K}_{row}$ and $\boldsymbol{K}_{col}$, respectively. For example if

$$\boldsymbol{K} = \begin{pmatrix} 4 & 0 & 0 & 2 \\ 0 & 2 & 0 & 0 \\ 0 & 0 & 1 & 0 \\ 2 & 0 & 0 & 2 \end{pmatrix} \tag{4.43}$$

Then a representation of this matrix by our storage method could be

$$\begin{aligned} \boldsymbol{K}_{val} &= \begin{pmatrix} 4 & 2 & 2 & 1 & 2 \end{pmatrix} \\ \boldsymbol{K}_{row} &= \begin{pmatrix} 1 & 1 & 2 & 3 & 4 \end{pmatrix} \\ \boldsymbol{K}_{col} &= \begin{pmatrix} 1 & 4 & 2 & 3 & 4 \end{pmatrix} \end{aligned}$$

Note that this is representation is not unique, this will depend upon how the entries are built up from element connectivity. In this case the resulting storage requirements are not much better than in the initial setup, however it is quite easy to see that when $\boldsymbol{K}$ is much larger, our method is more advantageous.

It is not a trivial task to construct these matrices from the finite element formulation. The method we have adopted works as follows

- Loop through all elements $e = 1, 2, ..., n_{tri}$.
- For each individual element e calculate the contribution to $\boldsymbol{K}_{ig,jg}$ where ig, jg are the global node numbers that correspond to the local node numbers il, jl. Hence if we consider the quadratic element in Figure 4.4, then the connectivity between nodes may be represented by the matrix

$$\boldsymbol{C} = \begin{pmatrix} 1 & 1 & 1 & 1 & 0 & 1 \\ 1 & 1 & 1 & 1 & 1 & 0 \\ 1 & 1 & 1 & 1 & 0 & 1 \\ 1 & 1 & 0 & 1 & 1 & 1 \\ 0 & 1 & 1 & 1 & 1 & 1 \\ 1 & 0 & 1 & 1 & 1 & 1 \end{pmatrix} \tag{4.44}$$

Thus for each element e we must calculate the contributions to $\boldsymbol{K}_{ig,jg}$ from local il, jl if there is a connection.

- Hence for each element e we have a maximum of 30 possible non-zero entries. So the number of maximum non-zero entries will be related to the number of elements, i.e. $30 \times n_{tri}$.

- In order to allocate array size we define $\boldsymbol{K}_{val}$, $\boldsymbol{K}_{row}$ and $\boldsymbol{K}_{col}$ to be of size $30 \times n_{tri}$. This is a significant saving over storing $\boldsymbol{K}$ as an $n \times n$ array.

- When we add an local contribution from node il, jl to a global node ig, jg we must loop over existing entries in $\boldsymbol{K}_{row}$ and $\boldsymbol{K}_{col}$ to determine whether this global position has been referenced before, if it has then we must add the contribution from il, jl to $\boldsymbol{K}_{val}$, else we must make a new entry in $\boldsymbol{K}_{val}$ and address its global location in the arrays $\boldsymbol{K}_{row}$ and $\boldsymbol{K}_{col}$.

- Move on to the next element $e + 1$.

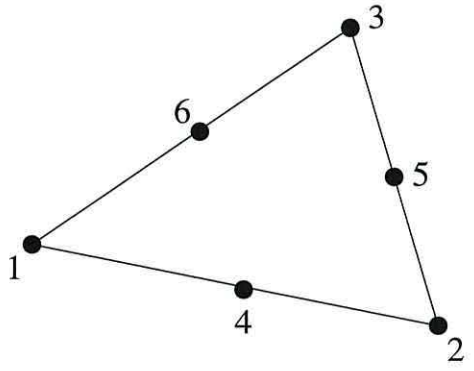

Figure 4.4: A quadratic finite element

Other routines for handling sparse matrices are explained in depth in [57]. After performing the above procedure on all the elements, we will have built up our stiffness matrix $\boldsymbol{K}$ and force vector $\boldsymbol{F}$ so we our now in a position to present the three arrays $\boldsymbol{K}_{val}$, $\boldsymbol{K}_{row}$, $\boldsymbol{K}_{col}$ and $\boldsymbol{F}$ to the netlib sparse matrix solver routine and hence obtain ϕ and thus $\boldsymbol{h}_d$ globally.

4.3.4 Implicit interface condition

This section describes how the scalar potential ϕ may be formulated by a Galerkin method [58]. Here the interface condition is integrated into the method implicitly by the application of Green's theorem. We use the same underlying idea of modelling the solution over a single mathematical domain as in the previous section.

Let the Galerkin residual R be denoted by

$$R = R_{int} + R_{ext} \tag{4.45}$$

By application of the Galerkin method to equations (3.19) - (3.22), i.e. setting the integral of the residual, weighted by the basis functions to zero.

$$R = \int_{\Omega} W_i(\nabla^2\phi - 4\pi\nabla\cdot\boldsymbol{m})d\Omega = 0 \tag{4.46}$$

Green's Theorem states

$$\int_V \nabla\psi_1\cdot\nabla\psi_2 dV + \int_V \psi_2\nabla^2\psi_1 dV = \int_S \psi_2\nabla\psi_1\cdot d\boldsymbol{S} \tag{4.47}$$

Hence

$$R = -\int_{\Omega}\nabla W_i\cdot\nabla\phi d\Omega - \int_{\Omega} W_i(4\pi\nabla\cdot\boldsymbol{m})d\Omega + \int_{\partial\Omega} W_i\nabla\phi\cdot d\boldsymbol{S} \tag{4.48}$$

so

$$\begin{aligned} R_{int} &= -\int_{\Omega_{int}}\nabla W_i\cdot\nabla\phi_{int}d\Omega_{int} - \int_{\Omega_{int}} W_i(4\pi\nabla\cdot\boldsymbol{m})d\Omega_{int} \\ &\quad + \int_{\partial\Omega_{12}} W_i\nabla\phi_{int}\cdot d\boldsymbol{S} \qquad (4.49) \\ R_{ext} &= -\int_{\Omega_{ext}}\nabla W_i\cdot\nabla\phi_{ext}d\Omega_{ext} + \int_{\partial\Omega_{21}} W_i\nabla\phi_{ext}\cdot d\boldsymbol{S} \\ &= -\int_{\Omega_{ext}}\nabla W_i\cdot\nabla\phi_{ext}d\Omega_{ext} - \int_{\partial\Omega_{12}} W_i\nabla\phi_{ext}\cdot d\boldsymbol{S} \qquad (4.50) \end{aligned}$$

where $\partial\Omega_{12}$ and $\partial\Omega_{21}$ denote integrating along the interface clockwise and anti-clockwise respectively. Hence

$$\begin{aligned} R &= -\int_{\Omega}\nabla W_i\cdot\nabla\phi d\Omega - \int_{\Omega_{int}} W_i(4\pi\nabla\cdot\boldsymbol{m})d\Omega_{int} \\ &\quad + \int_{\partial\Omega_{12}} W_i(\nabla\phi_{int} - \nabla\phi_{ext})\cdot d\boldsymbol{S} \qquad (4.51) \end{aligned}$$

Using the interface condition gives

$$\begin{aligned}(\nabla\phi_{int} - \nabla\phi_{ext}) \cdot d\boldsymbol{S} &= (\nabla\phi_{int} - \nabla\phi_{ext}) \cdot \hat{\boldsymbol{n}} dS \\ &= 4\pi \boldsymbol{m} \cdot \hat{\boldsymbol{n}} dS \end{aligned} \tag{4.52}$$

so we now have

$$R = -\int_{\Omega} \nabla W_i \cdot \nabla\phi d\Omega - \int_{\Omega_{int}} W_i (4\pi \nabla \cdot \boldsymbol{m}) d\Omega_{int} + \int_{\partial\Omega_{12}} W_i 4\pi \boldsymbol{m} \cdot \hat{\boldsymbol{n}} dS \tag{4.53}$$

From the previous it is clear that the interface condition has been implicitly formulated. The finite element formulation may now be found by the formation of the stiffness matrix $\boldsymbol{K}$ and element force vector $\boldsymbol{F}$ given by

$$\boldsymbol{K} = \int_{\Omega} \nabla W_i \cdot \nabla\phi d\Omega \tag{4.54}$$

$$\boldsymbol{F} = -\int_{\Omega_{int}} W_i 4\pi \nabla \cdot \boldsymbol{m} d\Omega_{int} + \int_{\partial\Omega_{12}} W_i 4\pi \boldsymbol{m} \cdot \hat{\boldsymbol{n}} dS \tag{4.55}$$

4.3.5 Linear finite element formulation

The difference between this method and the previous explicit approach is that we found that we were able to formulate the problem by using linear interpolation. Again by using the system of local triangular coordinates (L_i, L_j, L_k), we can proceed to construct the stiffness matrix and element force vector. First of all it is convenient to make the basis functions equivalent to our set of linear interpolation functions, hence

$$\boldsymbol{K} = \int_{\Omega} \nabla L_i \cdot \nabla\phi d\Omega \tag{4.56}$$

which may be constructed in the usual way with element contributions being given by

$$k_{ij}^e = \int\int_{R^e} \left(\frac{\partial L_i^e}{\partial x} \frac{\partial L_j^e}{\partial x} + \frac{\partial L_i^e}{\partial y} \frac{\partial L_j^e}{\partial y} \right) dxdy \tag{4.57}$$

Due to the implicit formulation of the method, the element force vector will now consist of terms involving $\nabla \cdot \boldsymbol{m}$ and $\boldsymbol{m} \cdot \hat{\boldsymbol{n}}$

$$\begin{aligned}\boldsymbol{F} &= -\int_{\Omega_{int}} L_i 4\pi \nabla \cdot \boldsymbol{m} d\Omega_{int} + \int_{\partial\Omega_{12}} L_i 4\pi \boldsymbol{m} \cdot \hat{\boldsymbol{n}} dS \\ &= \boldsymbol{f} + \bar{\boldsymbol{f}} \end{aligned} \tag{4.58}$$

Hence

$$\boldsymbol{f} = -\int_{\Omega_{int}} L_i 4\pi \nabla \cdot \boldsymbol{m} d\Omega_{int} \tag{4.59}$$

where element contributions are given by

$$f_i^e = -4\pi \left(\frac{1}{2A}\right) \left(\sum_{j=1}^{3} b_j m_{xj} + c_j m_{yj}\right) \int_A L_i dA \tag{4.60}$$

Using the formula in Appendix A gives

$$f_i^e = -\left(\frac{2\pi}{3}\right) \left(\sum_{j=1}^{3} b_j^e m_{xj}^e + c_j^e m_{yj}^e\right) \tag{4.61}$$

Let us now consider the interface contribution

$$\bar{\boldsymbol{f}} = \int_{\partial\Omega_{12}} L_i 4\pi \boldsymbol{m} \cdot \hat{\boldsymbol{n}} dS \tag{4.62}$$

To explain a contribution to this line integral we must consider boundary elements that are external to the magnetic region since an internal boundary elements at a corner may be common to two sides of the interface. Let us take for example the local side 13 as being on the interface which we denote by $\Gamma 13$. Along this side $L_2 = 0$ so $L_3 = (1 - L_1)$. The normal outward from the magnetic region will now be oriented into the finite element, i.e.

$$\hat{\boldsymbol{n}}_{13} = \frac{(b_2, c_2)}{(b_2^2 + c_2^2)^{\frac{1}{2}}} \tag{4.63}$$

and along the side

$$dS = (b_2^2 + c_2^2)^{\frac{1}{2}} dL_1 \tag{4.64}$$

We can rewrite the x and y components of $\boldsymbol{m}$ which denoted by m_x and m_y respectively by

$$\begin{aligned} m_x &= \sum_{i=1}^{3} L_i m_{xi} \\ &= L_1 m_{x1} + (1 - L_1) m_{x3} \end{aligned} \tag{4.65}$$

and

$$\begin{aligned} m_y &= \sum_{i=1}^{3} L_i m_{yi} \\ &= L_1 m_{y1} + (1 - L_1) m_{y3} \end{aligned} \tag{4.66}$$

hence

$$\begin{aligned} \bar{f}_1^e &= \int_{\partial\Gamma 13} L_1 (4\pi) \boldsymbol{m} \cdot \hat{\boldsymbol{n}}_{13} dS \\ &= -\int_{\partial\Gamma 31} L_1 (4\pi) \boldsymbol{m} \cdot \hat{\boldsymbol{n}}_{31} dS \\ &= -4\pi \int_0^1 L_1 (b_2 (m_{x1} L_1 + m_{x3} (1 - L_1)) + \\ &\quad (c_2 (m_{y1} L_1 + m_{y3} (1 - L_1))) dL_1 \\ &= -4\pi \left(b_2 \left(\left(\frac{m_{x1}}{3} \right) + \left(\frac{m_{x3}}{6} \right) \right) + c_2 \left(\left(\frac{m_{y1}}{3} \right) + \left(\frac{m_{y3}}{6} \right) \right) \right) \\ &= -\frac{2\pi}{3} (b_2 (2m_{x1} + m_{x3}) + c_2 (2m_{y1} + m_{y3})) \end{aligned} \tag{4.67}$$

By cyclic permutation

$$\bar{f}_3^e = -\frac{2\pi}{3} (b_2 (m_{x1} + 2m_{x3}) + c_2 (m_{y1} + 2m_{y3})) \tag{4.68}$$

Similarly local side 21 gives the following

$$\bar{f}_2^e = -\frac{2\pi}{3} (b_3 (2m_{x2} + m_{x1}) + c_3 (2m_{y2} + m_{y1})) \tag{4.69}$$

$$\bar{f}_1^e = -\frac{2\pi}{3} (b_3 (m_{x2} + 2m_{x1}) + c_3 (m_{y2} + 2m_{y1})) \tag{4.70}$$

and local side 32 gives

$$\bar{f}_3^e = -\frac{2\pi}{3} (b_1 (2m_{x3} + m_{x2}) + c_1 (2m_{y3} + m_{y2})) \tag{4.71}$$

$$\bar{f}_2^e = -\frac{2\pi}{3} (b_1 (m_{x3} + 2m_{x2}) + c_1 (m_{y3} + 2m_{y2})) \tag{4.72}$$

where f_i^e denotes the elemental contribution to the force vector from the local node i. The system of linear equations $\boldsymbol{K}\boldsymbol{\phi} = \boldsymbol{F}$ may now be solved in the same way as described earlier.

4.3.6 Quadratic finite element formulation

Even though the implicit interface method will give sensible results with linear elements, in order to achieve the required accuracy it was found necessary to use a

high discretisation of finite element nodes. We now describe the quadratic element implicit interface formulation. Using the same quadratic interpolation scheme as described in the previous section

$$\phi^e = \sum_{i=1}^{6} N_i^e \phi_i^e \tag{4.73}$$

where the quadratic interpolation functions are denoted by N_i^e.

The volume force vector is

$$\boldsymbol{f} = -\int_{\Omega_{int}} N_i 4\pi \nabla \cdot \boldsymbol{m} d\Omega_{int} \tag{4.74}$$

Element contributions to $\boldsymbol{f}$ are now given by

$$f_i^e = -4\pi \left(\frac{1}{2A^e}\right) \left(\sum_{j=1}^{3} b_j m_{xj} + c_j m_{yj}\right) \int_{A^e} N_i dA^e \tag{4.75}$$

Referring again to Appendix A, for corner nodes

$$\begin{aligned} \int_A N_i dA &= \int_A (2L_i^2 - L_i) dA \\ &= 0 \qquad i = 1, 2, 3 \end{aligned} \tag{4.76}$$

For mid-side nodes, e.g.

$$\begin{aligned} \int_A N_4 dA &= \int_A 4L_1 L_2 dA \\ &= \frac{A}{3} \end{aligned} \tag{4.77}$$

the same holds for N_5 and N_6, so

$$f_i^e = 0 \qquad i = 1, 2, 3 \tag{4.78}$$

$$f_i^e = -\left(\frac{2\pi}{3}\right) \left(\sum_{j=1}^{3} b_j m_{xj} + c_j m_{yj}\right) \qquad i = 4, 5, 6 \tag{4.79}$$

To consider the interface contribution from elements to $\bar{\boldsymbol{f}}$, let us take for example the local side 13 as being on the interface. Then $L_2 = 0$ so $L_3 = 1 - L_1$. Let

us consider both the outward normal $\hat{\boldsymbol{n}}_{13}$ and increment dS along the interface as previously defined in the linear case.

$$N_1 = 2L_1^2 - L_1 \tag{4.80}$$

$$\begin{aligned} N_3 &= 2L_3^2 - L_3 \\ &= 2(1-L_1)^2 - (1-L_1) \\ &= 2L_1^2 - 3L_1 + 1 \end{aligned} \tag{4.81}$$

and mid-side point

$$\begin{aligned} N_6 &= 4L_1L_3 \\ &= 4L_1(1-L_1) \\ &= 4L_1 - 4L_1^2 \end{aligned} \tag{4.82}$$

Using the elementary integration given in Appendix A

$$\int_0^1 L_1 dL_1 = \frac{1}{2} \qquad \int_0^1 L_1^2 dL_1 = \frac{1}{3} \qquad \int_0^1 L_1^3 dL_1 = \frac{1}{4} \tag{4.83}$$

the element contributions to $\bar{\boldsymbol{f}}$ are

$$\begin{aligned} \bar{f}_1^e &= \int_{\partial\Gamma 13} N_1(4\pi)\boldsymbol{m}\cdot\hat{\boldsymbol{n}}_{13}dS \\ &= -\int_{\partial\Gamma 31} N_1(4\pi)\boldsymbol{m}\cdot\hat{\boldsymbol{n}}_{31}dS \\ &= -4\pi\int_0^1 (2L_1^2 - L_1)(b_2(L_1m_{x1} + (1-L_1)m_{x3}) \\ &\quad + c_2(L_1m_{y1} + (1-L_1)m_{y3}))dL_1 \\ &= -4\pi\left(b_2\left(\frac{m_{x1}}{6} + (0)m_{x3}\right) + c_2\left(\frac{m_{y1}}{6} + (0)m_{y3}\right)\right) \\ &= -\frac{2\pi}{3}(b_2m_{x1} + c_2m_{y1}) \end{aligned} \tag{4.84}$$

by cyclic permutation

$$\bar{f}_3^e = -\frac{2\pi}{3}(b_2m_{x3} + c_2m_{y3}) \tag{4.85}$$

$$\begin{aligned}
\bar{f}_6^e &= \int_{\partial\Gamma 13} N_6(4\pi)\boldsymbol{m}\cdot\hat{\boldsymbol{n}}_{13}dS \\
&= -\int_{\partial\Gamma 31} N_6(4\pi)\boldsymbol{m}\cdot\hat{\boldsymbol{n}}_{13}dS \\
&= -4\pi\int_0^1 4(L_1-L_1^2)(b_2(L_1m_{x1}+(1-L_1)m_{x3}) \\
&\quad +c_2(L_1m_{y1}+(1-L_1)m_{y3}))dL_1 \\
&= -16\pi\left(b_2\left(\frac{m_{x1}}{12}+\frac{m_{x3}}{12}\right)+c_2\left(\frac{m_{y1}}{12}+\frac{m_{y3}}{12}\right)\right) \\
&= -\frac{4\pi}{3}(b_2(m_{x1}+m_{x3})+c_2(m_{y1}+m_{y3}))
\end{aligned} \tag{4.86}$$

similarly local side 21 gives the following contribution

$$\bar{f}_2^e = -\frac{2\pi}{3}(b_3m_{x2}+c_3m_{y2}) \tag{4.87}$$

$$\bar{f}_1^e = -\frac{2\pi}{3}(b_3m_{x1}+c_3m_{y1}) \tag{4.88}$$

$$\bar{f}_4^e = -\frac{4\pi}{3}(b_3(m_{x1}+m_{x2})+c_3(m_{y1}+m_{y2})) \tag{4.89}$$

and local side 32 gives

$$\bar{f}_3^e = -\frac{2\pi}{3}(b_1m_{x3}+c_1m_{y3}) \tag{4.90}$$

$$\bar{f}_2^e = -\frac{2\pi}{3}(b_1m_{x2}+c_1m_{y2}) \tag{4.91}$$

$$\bar{f}_5^e = -\frac{4\pi}{3}(b_1(m_{x2}+m_{x3})+c_1(m_{y2}+m_{y3})) \tag{4.92}$$

Once all contributions from elements have been added to the stiffness matrix and element force vector, we may proceed to solve the system of linear equations $\boldsymbol{K}\phi=\boldsymbol{F}$ as before.

4.4 Summary

So far in this thesis, we have described the mathematical formulation of our micromagnetic model and the motivation behind its use. We formulated the model in terms of the Landau-Lifshitz equation of motion and have discussed our use of numerical methods in the solution to this equation. The problem of improving the calculation of the demagnetizing field in terms of computational requirement has been mentioned and in this chapter we have formulated a solution to this problem in terms of triangular finite elements.

Our finite element method has evolved with the view of developing improved solutions to the demagnetizing field problem as compared with existing methods in terms of computational efficiency and accuracy. With this in mind we have introduced a sparse matrix storage routine and linear equations solver to keep storage requirements to a minimum.

We are now in a position to look at the efficiency of the solution with respect to mesh refinement and order of interpolation. This will be described at the beginning of the next chapter by using a refinement indicator and comparison with the analytical solution (under the conditions that this is valid). The next two chapters will be devoted to the most interesting results produced during this period of study. Chapter 5 will contain results from applying our model to simulate the behaviour of non interacting nanoelements and in Chapter 6 we take full advantage of the FEM and generalize the simulation to arrays of interacting nanoelements.

Chapter 5

Investigation of non interacting nanoelements

5.1 Introduction

Now that we have formulated finite element solutions of the demagnetizing field $\boldsymbol{h}_d$ via a magnetic scalar potential ϕ, we are in a position to make a brief comparison via the use of a refinement indicator and an analytical solution in terms of interpolation, computational efficiency and accuracy of our solution between the explicit method and implicit interface formulation using quadratic elements. Throughout this chapter we shall concentrate on non interacting nanoelements only. We shall begin our investigations by giving some brief results on the computational speed and efficiency of our finite element calculation.

Testing the solution to the demagnetizing field calculation is only a partial test of our model so the next step is to perform a full micromagnetic simulation and compare our results with well known published work. Only after full testing of the model may we proceed to simulate new results on the magnetization behaviour in single nanoelements of thin film permalloy. The rest of this chapter will then be concerned with looking at a systematic investigation of the single domain (SD) / multi domain (MD) transition states of these nanoelements. Simulations will be carried out on various particle sizes and aspect ratios.

5.2 Testing the efficiency of the calculation

In order to investigate the efficiency of the calculation we shall use the meshes in Table 5.1 to define a rectangular magnetic region of dimensions 0.2μm $\times$ 1.6μm with a uniform magnetization distribution of $\boldsymbol{m} = (0, 1, 0)$. Referring back to Figure 4.1 for the definitions of $\partial\Re$ and $\partial\Omega$, we define the distances xl and yl which are the x and y distances respectively of $\partial\Re$ from $\partial\Omega$ as shown in Figure 5.1.

The calculation of the scalar potential ϕ where ϕ is the solution to equations (3.19) - (3.22) involves an infinite boundary being approximated by a finite boundary $\partial\Re$. In order to determine how far away $\partial\Re$ should be in order to obtain a reasonable solution we performed a series of calculations. These calculations were carried out on the meshes in Table 5.1 by gradually increasing the distances xl and yl from 0.9μm and 2.0μm respectively in steps of 0.5μm. We found that values greater that 3.9μm and 5.0μm for xl and yl respectively gave maximum differences in ϕ of order 10^{-4} for this particular geometry. Hence for the rest of the numerical comparisons in this chapter we shall fix xl and yl to be 3.9μm and 5.0μm respectively.

In order to give a brief insight into the typical C.P.U. times of our calculations we have recorded the time in seconds to calculate the solution of ϕ for the meshes given in Table 5.1. These calculations were performed on a single 500MHz EV5 processor and are given in Table 5.2 where the C.P.U. time indicates the total time to calculate ϕ including the decomposition of the stiffness matrix and the subsequent matrix multiplication. These results suggest that the scaling of the calculation is lower than the order of $n \log n$ which is certainly better than existing FFT methods.

mesh	quadratic nodes ($\Omega_{int} + \Omega_{ext}$)	linear nodes ($\Omega_{int} + \Omega_{ext}$)	elements ($\Omega_{int} + \Omega_{ext}$)
1	$864 + 972$	$237 + 226$	$391 + 520$
2	$3327 + 1822$	$873 + 418$	$1582 + 986$
3	$9171 + 2770$	$2361 + 629$	$4450 + 1514$

Table 5.1: Meshes with increasing refinement

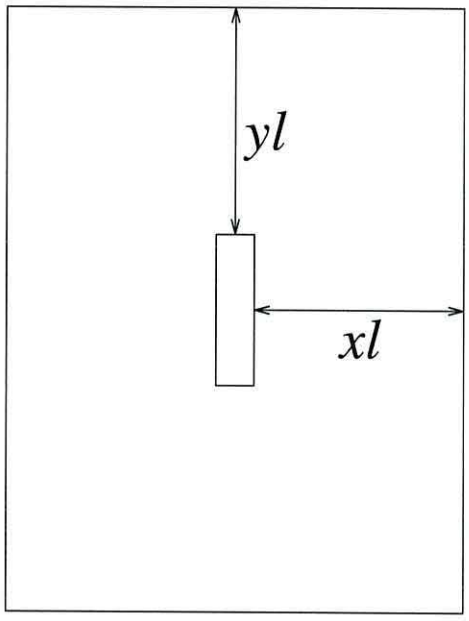

Figure 5.1: Definition of distances xl and yl for $\partial\Re$ away from $\partial\Omega$

mesh	C.P.U. time (s) (quadratic)	C.P.U. time (s) (linear)
1	7.27	1.91
2	31.83	5.10
3	92.42	12.21

Table 5.2: C.P.U. times for calculating the scalar potential

5.2.1 Refinement indicator

As an initial test on the solution we introduce the refinement indicator for $\boldsymbol{h}_d$ [18]

$$\eta_i^d = \frac{[(\nabla \times \boldsymbol{h}_d)^2 + (\nabla \cdot \boldsymbol{h}_d)^2]A_i}{\sum_{j=1}^{N} |\boldsymbol{h}_s|^2} \tag{5.1}$$

where A_i denotes the area of element i and $|\boldsymbol{h}_s|$ is the value of $|\boldsymbol{h}_d|$ computed at the element centre. Previously equation (5.1) has been used to define areas of the simulations where refinement of the mesh was required. However the refinement indicator does not represent a direct calculation of the error in the field calculation. The images in Figure 5.2 show the areas of largest error detected by the refinement indicator for meshes with increasing levels of refinement. The areas highlighted

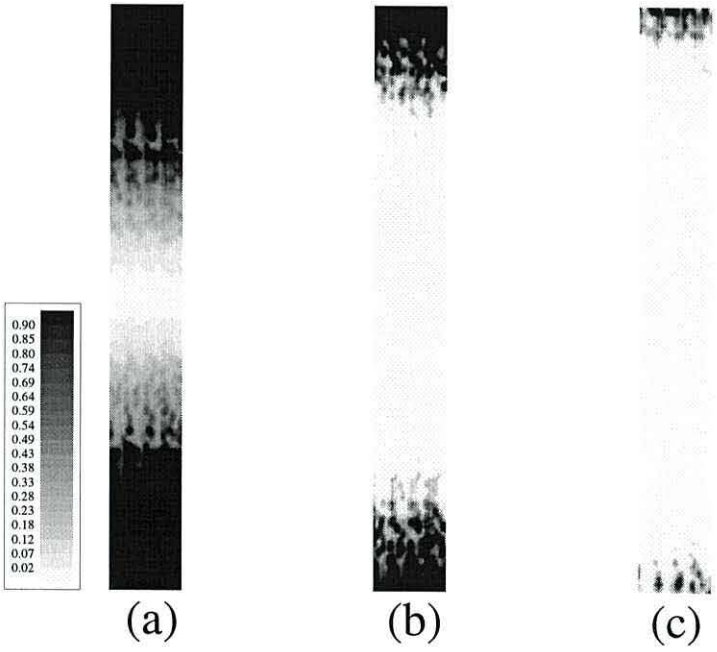

Figure 5.2: Areas for refinement with explicit interface using quadratic elements in (a) mesh 1 (b) mesh 2 and (c) mesh 3

for refinement occur mainly at the element ends where the field has a large spatial variation. We notice that the refinement region becomes less significant as we refine the mesh as shown by 5.2(c).

5.2.2 Analytical solution

In this section we will show the areas of largest error in comparison to the analytical solution. The review [38] gives some methods that have been used for the numerical evaluation of the demagnetizing field. This work includes some analytical formulae for certain regular geometries, one of particular relevance to our application is the solution for a rectangular region. The solution uses a two dimensional distribution of $\boldsymbol{m}$ in the xy plane, when the dimension along z is either zero or infinite. We consider the magnetic region to be defined over the rectangular domain $-a \leq x \leq a$, $-b \leq y \leq b$, it can be proved that equation (4.2) is equivalent inside the magnetic region to

$$\begin{aligned}\phi(x,y) &= 2\int_0^\infty \left[\int_{-b}^{b} \cos\left[(y-\eta)t\right] \left(\int_{-a}^{x} m_x(\xi,\eta)e^{-(x-\xi)t}d\xi \right.\right. \\ &\quad \left. - \int_x^a m_x(\xi,\eta)e^{-(\xi-x)t}d\xi\right) d\eta \\ &\quad + \int_{-a}^{a} \cos\left[(x-\xi)t\right] \left(\int_{-b}^{y} m_y(\xi,\eta)e^{-(y-\eta)t}d\eta \right. \\ &\quad \left.\left. - \int_y^b m_y(\xi,\eta)e^{-(\eta-y)t}d\eta\right) d\xi\right] dt \end{aligned} \tag{5.2}$$

It is convenient to use equation (5.2) as a test of accuracy of our method of solution. To apply this we shall consider an in plane magnetization distribution of $\boldsymbol{m} = (0,1)$ to be defined over the rectangular domain $c \leq x \leq a$, $d \leq y \leq b$, substituting this into the previous equation, we get

$$\begin{aligned}\phi(x,y) &= 2\int_0^\infty \left[\int_c^a \cos[(x-\xi)t] \left(\int_d^y e^{-(y-\eta)t}d\eta - \int_y^b e^{-(\eta+y)t}d\eta\right) d\xi\right] dt \\ &= 2\int_0^\infty \int_c^a \cos[(x-\xi)t] \left[\frac{1}{t}\left[e^{-(y-\eta)t}\right]_d^y - \frac{-1}{t}\left[e^{-(\eta-y)t}\right]_y^b\right] d\xi dt \\ &= 2\int_0^\infty \int_c^a \frac{1}{t}\cos[(x-\xi)t] \left[\left(1-e^{-(y-d)t}\right) + \left(e^{-(b-y)t}-1\right)\right] d\xi dt \\ &= 2\int_0^\infty \frac{1}{t}\left[\int_c^a \cos[(x-\xi)t] \left(e^{-(b-y)t} - e^{-(y-d)t}\right)\right] d\xi dt \\ &= 2\int_0^\infty \left[-\frac{1}{t^2}e^{-(b-y)t}\left[\sin(x-\xi)t\right]_a^c + \frac{1}{t^2}e^{-(y-d)t}\left[\sin(x-\xi)t\right]_a^c\right] dt \\ &= 2\int_0^\infty \left[\frac{1}{t^2}\left(e^{-(y-d)t} - e^{-(b-y)t}\right)\left[\sin(x-\xi)t\right]_a^c\right] dt \\ &= 2\int_0^\infty \left[\frac{1}{t^2}\left(e^{-(y-d)t} - e^{-(b-y)t}\right)\left(\sin(x-a)t - \sin(x-c)t\right)\right] dt \end{aligned} \tag{5.3}$$

To evaluate this integral we refer to the mathematical handbook [59], and use the result that

$$\int_0^\infty \frac{1}{x^2}(e^{-\alpha x} - e^{-\beta x})\sin(ax)dx = \frac{a}{2}\ln\left(\frac{a^2+\beta^2}{a^2+\alpha^2}\right) + \beta\tan^{-1}\left(\frac{a}{\beta}\right) - \alpha\tan^{-1}\left(\frac{a}{\alpha}\right) \tag{5.4}$$

Using this result we obtain

$$\begin{aligned}
\phi(x,y) &= 2\int_0^\infty \frac{1}{t^2}\left(e^{-(y-d)t} - e^{-(b-y)t}\right)(\sin(x-a)t - \sin(x-c)t)\,dt \\
&= 2\left[\left(\frac{x-a}{2}\right)\ln\left(\frac{(x-a)^2+(b-y)^2}{(x-a)^2+(y-d)^2}\right) + (b-y)\tan^{-1}\left(\frac{x-a}{b-y}\right)\right. \\
&\quad \left. - (y-d)\tan^{-1}\left(\frac{x-a}{y-d}\right)\right] \\
&\quad -2\left[\left(\frac{x-c}{2}\right)\ln\left(\frac{(x-c)^2+(b-y)^2}{(x-c)^2+(y-d)^2}\right) + (b-y)\tan^{-1}\left(\frac{x-c}{b-y}\right)\right. \\
&\quad \left. - (y-d)\tan^{-1}\left(\frac{x-c}{y-d}\right)\right]
\end{aligned} \tag{5.5}$$

We can then use a mathematical applications package such as MAPLE to find $-\nabla\phi(x,y)$. From this result we then obtain $\boldsymbol{h}_d$ straight away since $\boldsymbol{h}_d = -\nabla\phi(x,y)$. So if $\boldsymbol{h}_d = (h_d^x, h_d^y)$, then

$$\begin{aligned}
h_d^x &= \ln\left(\frac{(x-a)^2+(b-y)^2}{(x-a)^2+(y-d)^2}\right) \\
&+\frac{(x-a)\left(\dfrac{2x-2a}{(x-a)^2+(y-d)^2} - \dfrac{((x-a)^2+(b-y)^2)(2x-2a)}{((x-a)^2+(y-d)^2)^2}\right)((x-a)^2+(y-d)^2)}{(x-a)^2+(b-y)^2} \\
&+\frac{2}{1+\dfrac{(x-a)^2}{(b-y)^2}} - \frac{2}{1+\dfrac{(x-a)^2}{(y-d)^2}} - \ln\left(\frac{(x-c)^2+(b-y)^2}{(x-c)^2+(y-d)^2}\right) \\
&-\frac{(x-c)\left(\dfrac{2x-2c}{(x-c)^2+(y-d)^2} - \dfrac{((x-c)^2+(b-y)^2)(2x-2c)}{((x-c)^2+(y-d)^2)^2}\right)((x-c)^2+(y-d)^2)}{(x-c)^2+(b-y)^2} \\
&-\frac{2}{1+\dfrac{(x-c)^2}{(b-y)^2}} + \frac{2}{1+\dfrac{(x-c)^2}{(y-d)^2}}
\end{aligned} \tag{5.6}$$

and

$$
\begin{aligned}
h_d^y \;=\; & \frac{(x-a)\left(\dfrac{-2\,b+2\,y}{(x-a)^2+(y-d)^2}-\dfrac{\left((x-a)^2+(b-y)^2\right)(2\,y-2\,d)}{\left((x-a)^2+(y-d)^2\right)^2}\right)\left((x-a)^2+(y-d)^2\right)}{(x-a)^2+(b-y)^2} \\
& -2\tan^{-1}\left(\frac{x-a}{b-y}\right)+2\,\frac{x-a}{(b-y)\left(1+\dfrac{(x-a)^2}{(b-y)^2}\right)}-2\tan^{-1}\left(\frac{x-a}{y-d}\right)+2\,\frac{x-a}{(y-d)\left(1+\dfrac{(x-a)^2}{(y-d)^2}\right)} \\
& -\frac{(x-c)\left(\dfrac{-2\,b+2\,y}{(x-c)^2+(y-d)^2}-\dfrac{\left((x-c)^2+(b-y)^2\right)(2\,y-2\,d)}{\left((x-c)^2+(y-d)^2\right)^2}\right)\left((x-c)^2+(y-d)^2\right)}{(x-c)^2+(b-y)^2} \\
& +2\tan^{-1}\left(\frac{x-c}{b-y}\right)-2\,\frac{x-c}{(b-y)\left(1+\dfrac{(x-c)^2}{(b-y)^2}\right)}+2\tan^{-1}\left(\frac{x-c}{y-d}\right)-2\,\frac{x-c}{(y-d)\left(1+\dfrac{(x-c)^2}{(y-d)^2}\right)}
\end{aligned}
\tag{5.7}
$$

Using this result, we may now make a comparison of our method with the analytical solution. The graphs in Figures 5.3 - 5.5 show the actual calculated error relative to the analytical solution. The errors are calculated from the formula

$$
\text{error} \;=\; \frac{\left|\boldsymbol{h}_d^a-\boldsymbol{h}_d^c\right|^2}{\left|\boldsymbol{h}_d^a\right|^2} \tag{5.8}
$$

where $\boldsymbol{h}_d^a$ and $\boldsymbol{h}_d^c$ represent the analytical solution and the calculated value respectively. In both cases we see that as the number of elements increases the relative error becomes smaller, however we can also see that for the same discretisation we get a smaller error associated with the quadratic case. It is also very clear that the graphs for quadratic elements shown in Figures 5.4 and 5.5 are very similar. The numerical difference in these methods only becomes apparent when we apply the model to arrays of nanoelements. It is true to say that as we increase the number of nodes, the solution becomes better and the maximum relative error decreases. However, we note that the maximum errors mainly occur at nodes belonging to boundary elements. The implication of this is that as we refine a mesh we get nodes located closer to the interface and these will create errors. There may become a stage at which further discretisation is not going to produce any better results.

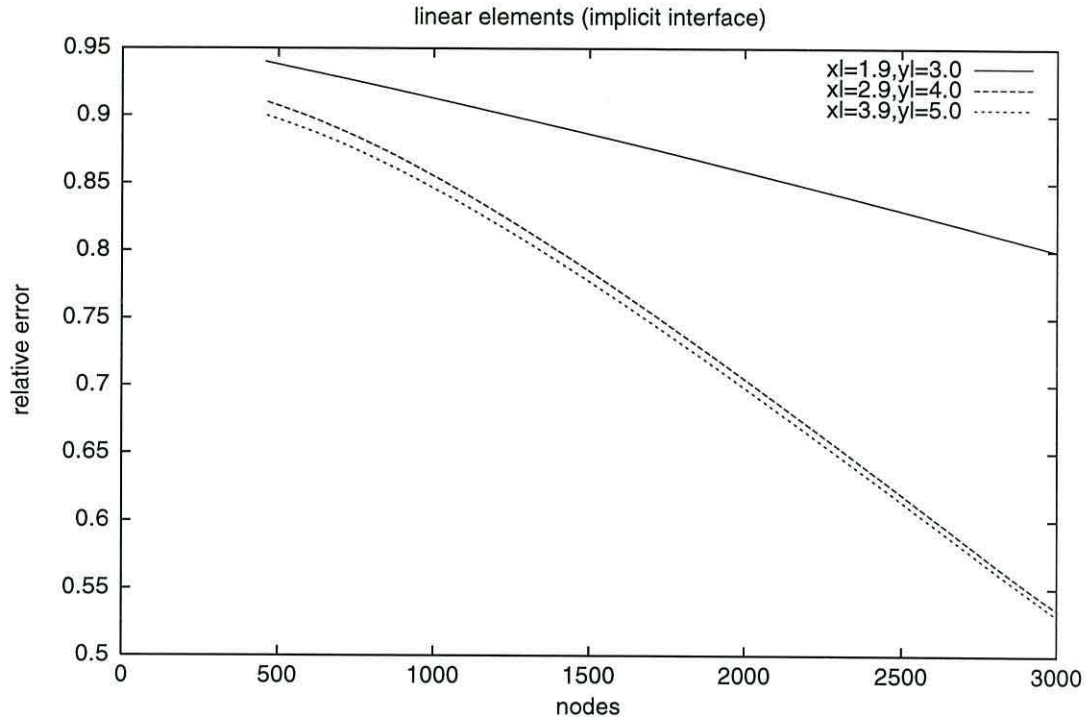

Figure 5.3: Maximum relative error for linear elements

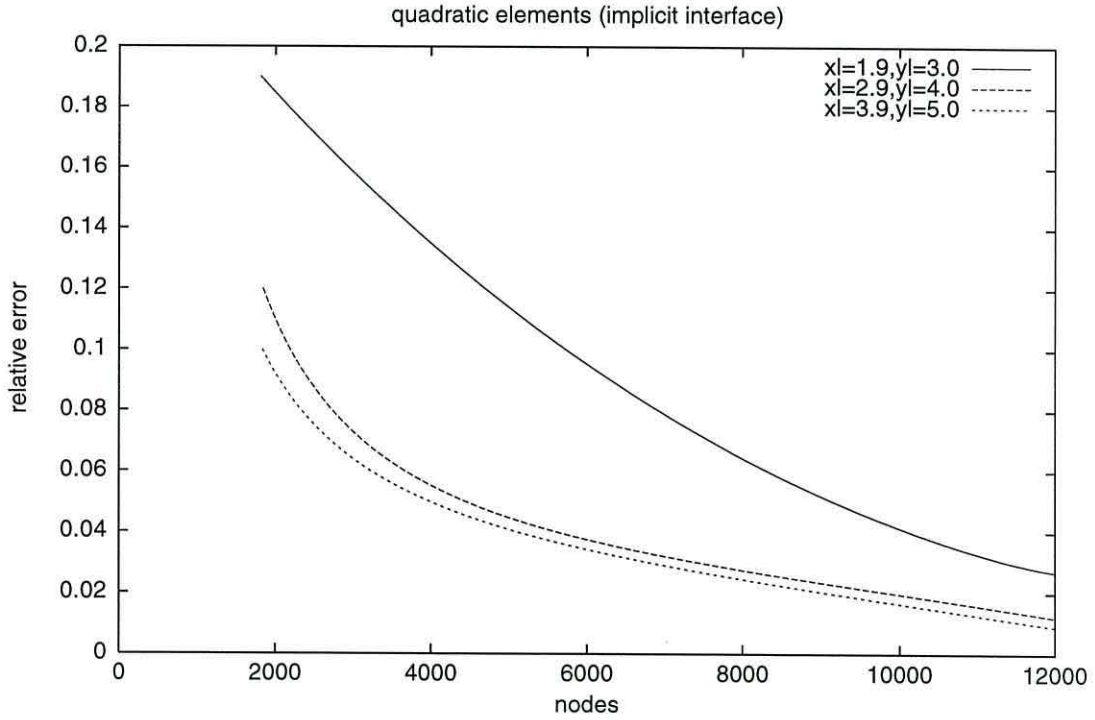

Figure 5.4: Maximum relative error for quadratic elements with implicit interface condition

The improvement of the solution around the interface region would be a substantial piece of further research work but is beyond the scope of this thesis. Also it is quite

possible that the numerical evaluation of the analytical solution becomes more inaccurate closer to the boundary as the integrals involved are singular there. If

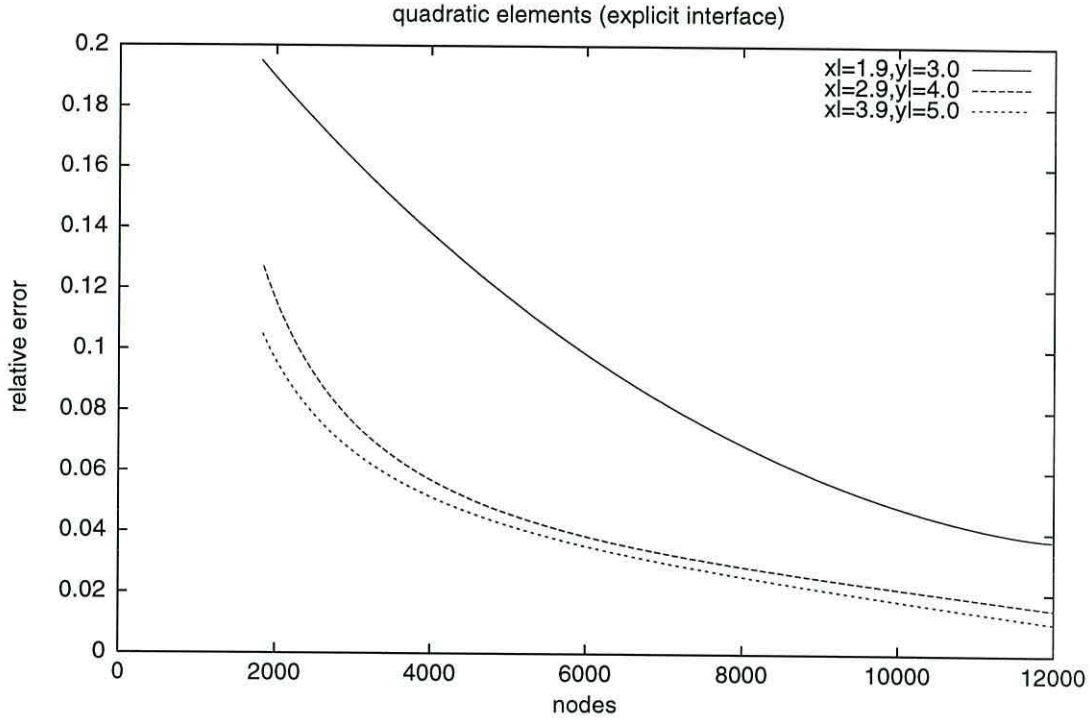

Figure 5.5: Maximum relative error for quadratic elements with explicit interface condition

we turn our attention to the meshes in Table 5.1 we can look more closely at the values of the error at specific points within the magnetic region. We have marked three points as shown in Figure 5.6 where we expect there to be varying difference in the error. Table 5.3 can then be constructed giving values of the error using the implicit method with quadratic elements to maintain highest accuracy. We see from the table that the largest value of the error occurs nearest to the corner of the nanoelement at point 1 where the field is most non-uniform.

mesh	point 1	point 2	point 3
1	9.4×10^{-2}	7.9×10^{-2}	2.7×10^{-2}
2	3.8×10^{-2}	2.6×10^{-2}	2.3×10^{-2}
3	1.5×10^{-2}	1.3×10^{-2}	2.2×10^{-2}

Table 5.3: Pointwise values of the error

The images shown in Figure 5.7 give an indication of where the errors are occurring and again the same situation is reflected as in the case of the refinement indicator. We have the largest errors occurring at the ends of the nanoelement due to the non-uniformity of the field and increasing the mesh refinement minimizes the severity of the errors as shown by the refinement indicator and by comparison with the analytical solution.

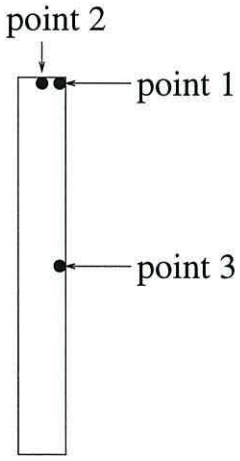

Figure 5.6: Location of points within the magnetic region

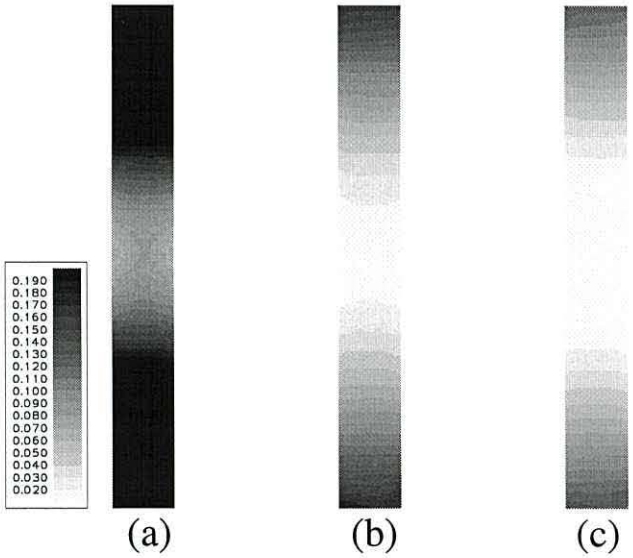

Figure 5.7: Maximum relative error for quadratic elements with implicit interface method using (a) mesh 1 (b) mesh 2 (c) mesh 3

5.3 Initial studies of elongated nanoelements

The purpose of the previous section was to give an indication of the reliability of our finite element method in calculating the demagnetizing field via a scalar potential. Table 5.3 shows that the order of magnitude of the error is about 10^{-2}, so it now seems reasonable to implement the method within the model and perform a micromagnetic simulation using the additional exchange, anisotropy and applied field terms described in Chapter 3 coupled with the Landau-Lifshitz equation of motion to describe the dynamics of the process.

The first simulation we must perform is one that will test all aspects of the model, in addition to this the results we expect to obtain should already have been published so that we may make a direct comparison with what we obtain. With this in mind, we shall begin with a simulation that is comparable to one that was carried out by Schrefl *et al* [22] who investigated the formation of domains in rectangular permalloy nanoelements with anisotropy. These results were obtained from a theoretical model and were also observed experimentally.

The nanoelement that we shall consider is of size 0.2μm $\times$ 1.6μm with a thickness of 20nm and transverse anisotropy. The presence of the transverse anisotropy implies that we should expect some domains in the results. Initially the nanoelements are saturated with a uniform magnetization distribution parallel to the longitudinal axis. For this particular simulation the exchange constant $A = 1.3 \times 10^{-6}$erg/cm, the anisotropy constant $K = 5 \times 10^{5}$erg/cm^3 and the saturation magnetization $M_s = 800$emu/cm^3. These material parameters were obtained from the work of Hefferman *et al* [20].

Our simulation was carried on a finite element mesh with 1024 quadratic elements within the nanoelement to ensure that there are enough to successfully model the change in magnetization throughout a domain wall. Simulations of remanent states were performed as in the case of Schrefl *et al.* The results from our simulation are

given in Figure 5.8, in a format that will be used throughout this thesis with the direction of the magnetic moments being represented by small arrows within the nanoelement and a colour scheme denoting the strength of the magnetization component in the anisotropy direction, in this case transverse, i.e. m_x.

The results in Figure 5.8 show the time evolution of the magnetization of the nanoelement into the zero field equilibrium state. The magnetization (m_y) is measured by summing the total number of longitudinal components and dividing this by the number of finite element nodes.

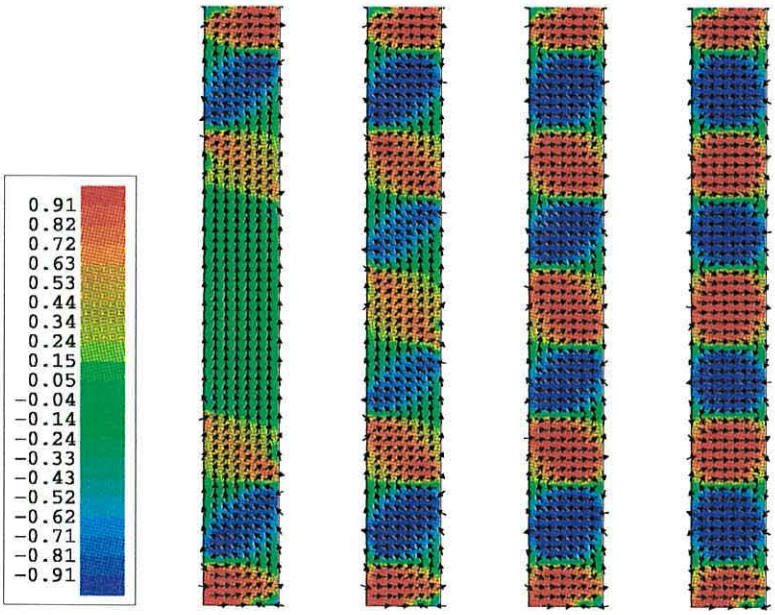

Figure 5.8: Transition in zero field equilibrium for a 0.2μm $\times$ 1.6μm nanoelement after time a) 7ns b) 12ns c) 15ns d) 25ns

In Figure 5.8(a), $m_y = 0.75$, the nucleation of domain structure occurs by vortex formation at opposite ends of the nanoelement giving a large initial change in magnetization. We see that the domain structure then expands throughout the nanoelement as shown in 5.8(b) and 5.8(c) where $m_y = 0.5$ and $m_y = 0.25$ respectively. Finally the equilibrium state in Figure 5.8(d) shows the domain

configuration when $m_y = 0.0$ which is achieved when our convergence criterion of $\left|\frac{d\boldsymbol{m}}{d\tau}\right| < 10^{-6}$ is obtained. The evolution of the domain structure into the zero field equilibrium state is consistent with that of the published work of Schrefl at al.

As an extension to this simulation and a further test we shall introduce an applied field and examine the hysteresis effects. By slow reduction of an applied field, we obtain the hysteresis curve shown in Figure 5.9 and in more detail in Figure 5.10. Here we see a steady initial reduction in magnetization to the point (a) on the curve caused by the reversal beginning from the two opposite ends of the nanoelement. The large change in magnetization which occurs between point (b) and point (c) indicates the formation of domains caused by vortex nucleation at the ends of the nanoelement. The reversal then proceeds from the two element ends with propagating domain structures towards the element centre. Finally at point (d) on the curve the multi-domain formation occupies the entire element which exhibits zero reduced magnetization.

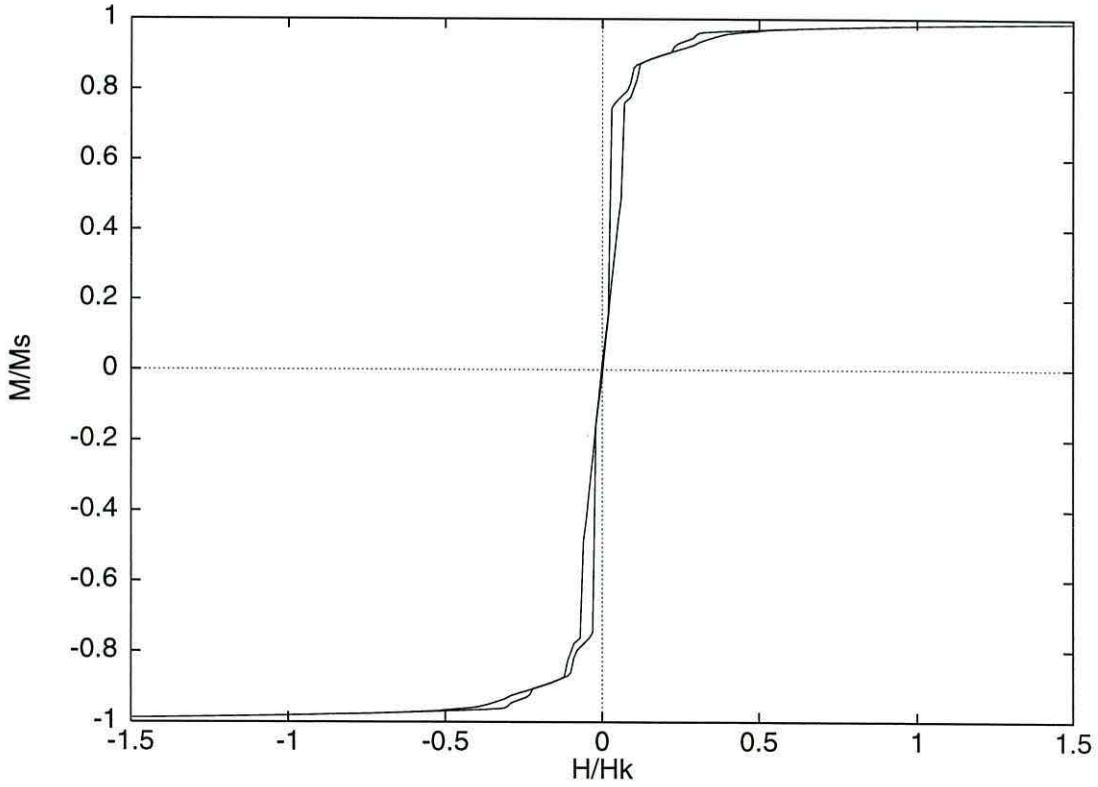

Figure 5.9: Hysteresis loop for a 0.2μm $\times$ 1.6μm nanoelement

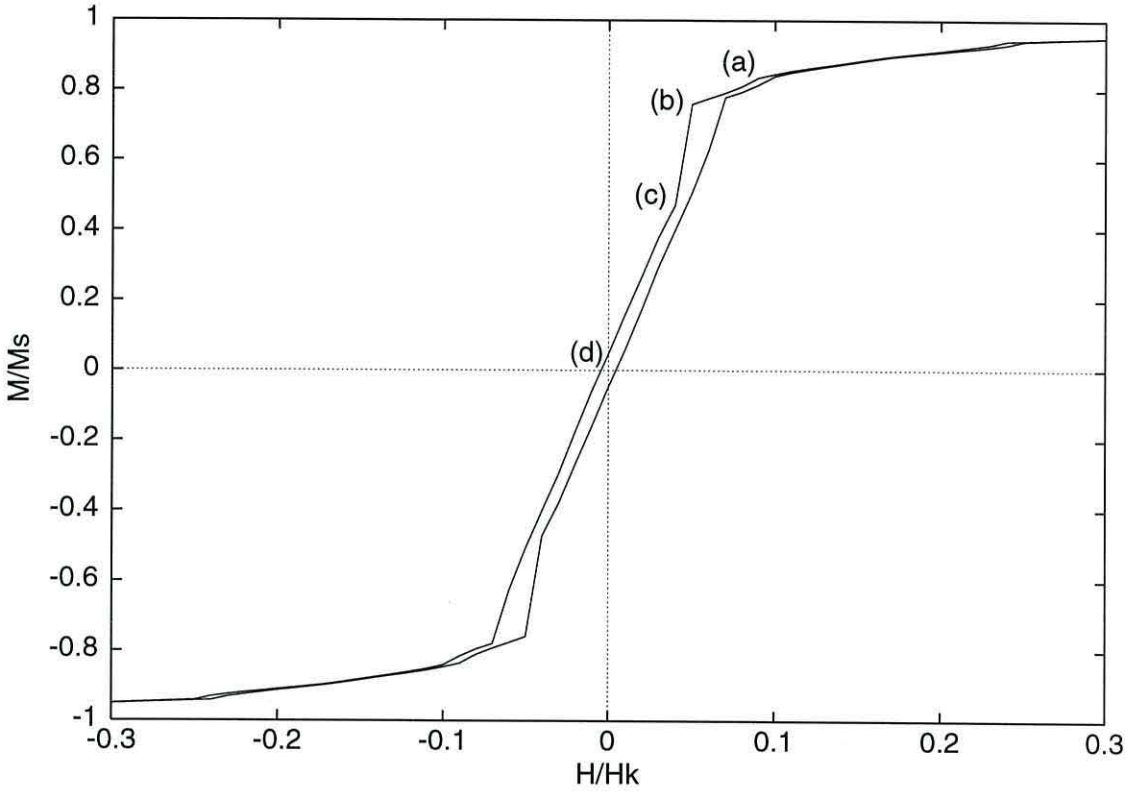

Figure 5.10: The reversal process in detail

5.4 The single domain / multi domain transitions

Now that we have fully tested our model we may proceed to carry out a systematic study of the single domain (SD) to multi domain (MD) transition states on permalloy nanoelements. The motivation behind this is to get some idea on the particle size at which these transitions occur in order to determine their suitability for magnetic recording applications. Previous work has been done experimentally by Smyth *et al* [60] who investigated the effect of particle size and aspect ratio on hysteresis behaviour at the sub micron level.

The transition to SD behaviour occurs for the following reasons. The existence of domains in a magnetic structure with magnetization M is driven by the tendency of a material to try to reduce the magnetostatic energy which is $\propto M^2$. The reduction in M is achieved by the material splitting into domains. Within each domain, the magetization remains parallel in order to minimize the exchange energy but the overall orientation of the direction of the domains is such that the magnetization itself is lowered. However the production of the domain wall itself requires some energy. As a consequence of this, as the size of the system is reduced there comes a point at which the energy reduction by splitting up into a small number of domains is not sufficient to compensate for the increased energy associated with the domain walls involved. At this point there is a transition from MD to SD behaviour via intermediate transition states which are termed as pseudo single domain (PSD).

The PSD states are characterized by their highly non-uniform magnetization structures and the distinction between PSD and SD states is shown in Figures 5.11 and 5.12. Here we see a non-uniform PSD magnetization structure in Figure 5.11 since the bottom right and top left corners differ and a SD magnetization structure in Figure 5.12.

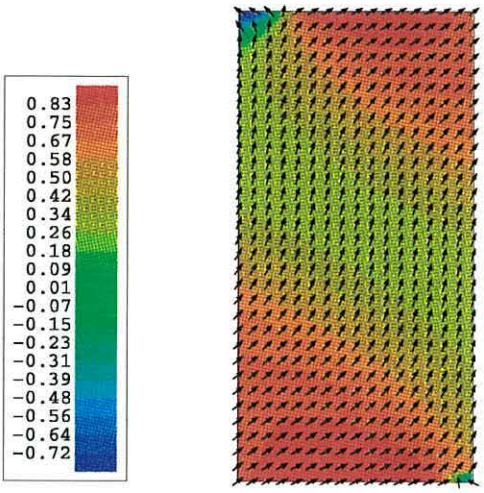

Figure 5.11: Example of a PSD state

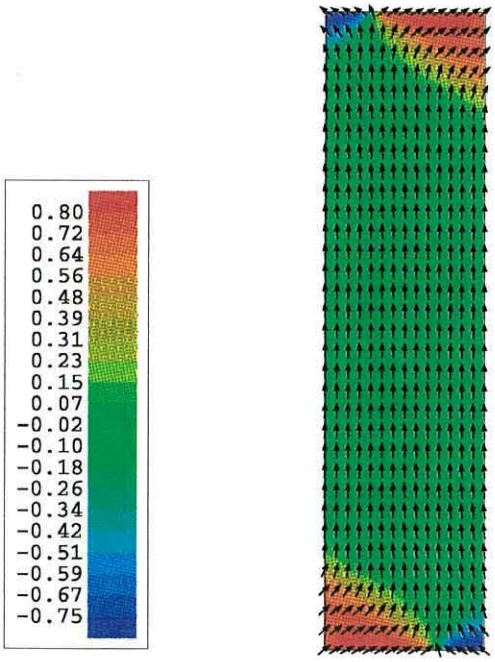

Figure 5.12: Example of a SD state

However in practice the situation is rather more complicated since it is expected that the transition will depend to some extent on the elongation of the nanoelement since this is one of the major factors in determining the overall magnetostatic energy. Consequently, our investigation must include a study of transition effects due to particle aspect ratio as well as size. Hence we shall consider each aspect ratio in turn.

We shall begin our investigation by studying the geometry of a square nanoelement. To produce the remainder of the results in this thesis, we use the generally accepted material parameters for permalloy which were obtained from NIST [61]. They are the exchange constant, $A = 1.3 \times 10^{-6}$erg/cm, the uniaxial anisotropy, $K = 5 \times 10^{3}$erg/cm^3 and the saturation magnetization, $M_s = 800$emu/cm^3. We also fix the thickness of the nanoelements to be 20nm. Unless otherwise stated, we begin our simulation with our particle having a uniform magnetization distribution in a direction from the bottom to the top of the nanoelement and we remove the applied field instantaneously. All of the states were obtained after convergence of the system to equilibrium.

The experimental work by Kirk *et al* [62] shows evidence of domain formation at a size of 2.0μm, which is the size at which we begin in our first series of simulations. Our theoretical result is given by Figure 5.13 where we see a classic 4 domain pattern with a 90^o domain wall as a result of the formation of the central vortex.

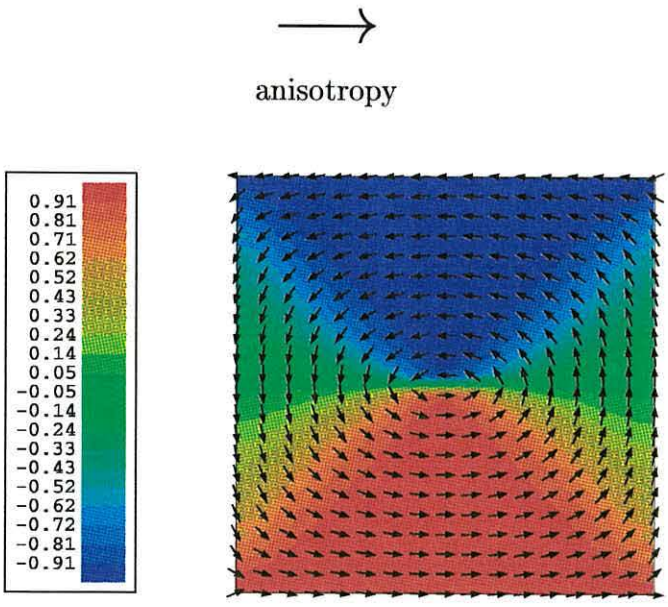

Figure 5.13: 2.0μm $\times$ 2.0μm

Continuing our study by reducing the size of the nanoelement to 1.0μm, we find this is also capable of supporting the increase in energy from the domain wall formation by making the central domain grow and thus forcing vortices outwards as shown by the results in Figure 5.14. Here we also see an increase in surface charge. However this is certainly not the case for a nanoelement of size 0.068μm

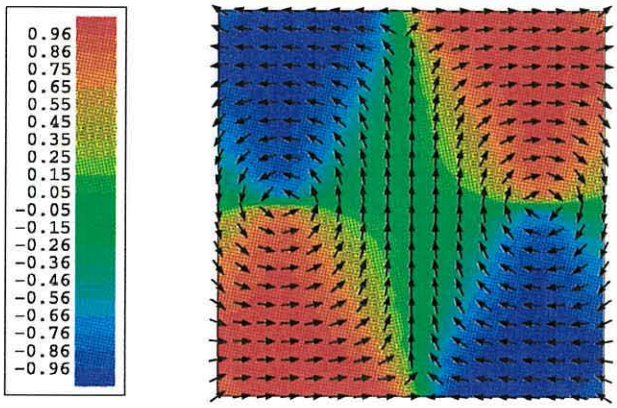

Figure 5.14: 1.0μm $\times$ 1.0μm

as shown by Figure 5.15. Here the particle size is not capable of supporting any increase in energy from domain wall formation and so it remains in a single domain configuration. By carrying out simulations on smaller particle sizes, the size at below which only a single domain state is supported was found to be about 0.1μm.

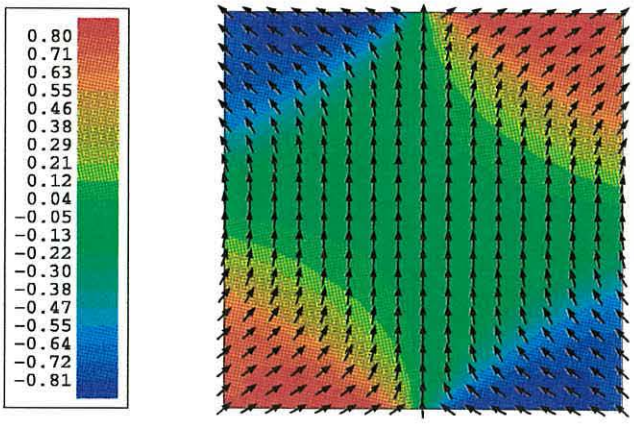

Figure 5.15: 0.068μm $\times$ 0.068μm

Now that we have looked at decreasing particle sizes for a single aspect ratio, we shall proceed to look at the effects of an increase in the elongation by considering a 2:1 aspect ratio nanoelement. This is necessary as any transitions will be dependent upon the magnetostatic energy which in turn is directly determined by the elongation of the particle.

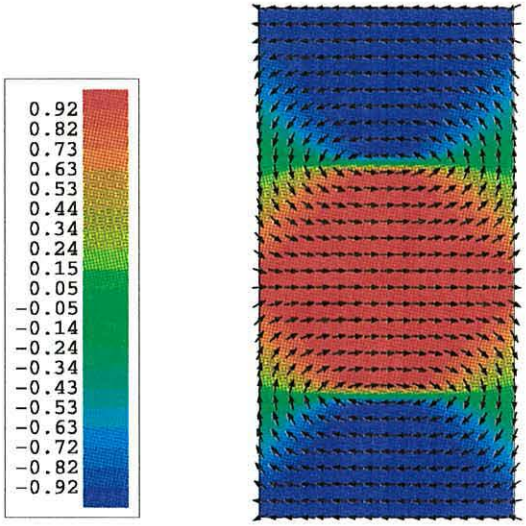

Figure 5.16: 1.4μm $\times$ 2.8μm

For this series of simulations we found that particle sizes above 0.15μm $\times$ 0.3μm were all capable of supporting multi domain states. At these sizes the domain wall energy is supported by the reduction in total energy due to the domains. However as we decrease the particle size we observe the transition from pseudo single domain to single domain at about 0.09μm $\times$ 0.18μm at the point where the reduction in the total energy is insufficient enough to support the domain wall energy. In Figure 5.16 we observe a classic 7 domain configuration for a particle of size 1.4μm $\times$ 2.8μm with the two vortices occurring to accommodate the domain walls. We also see a similar configuration in 5.17 which shows a particle of size 1.2μm $\times$ 2.4μm, here the reduction in particle size causes the domain wall energy to have slightly more overall effect by beginning to separate the vortices, this in turn will increase the total system energy and thus force the particle into a pseudo single domain state as shown by Figure 5.18 and then ultimately a single domain state.

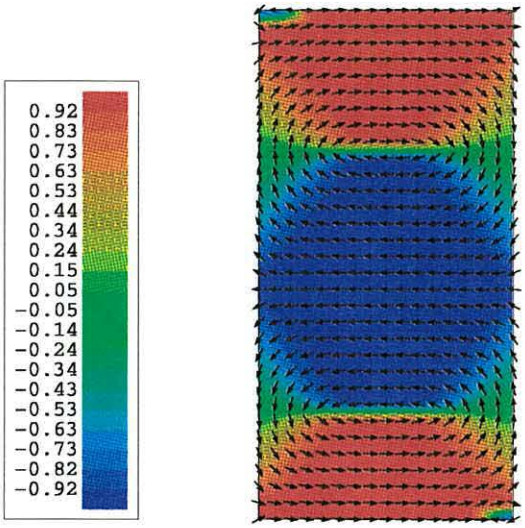

Figure 5.17: 1.2μm $\times$ 2.4μm

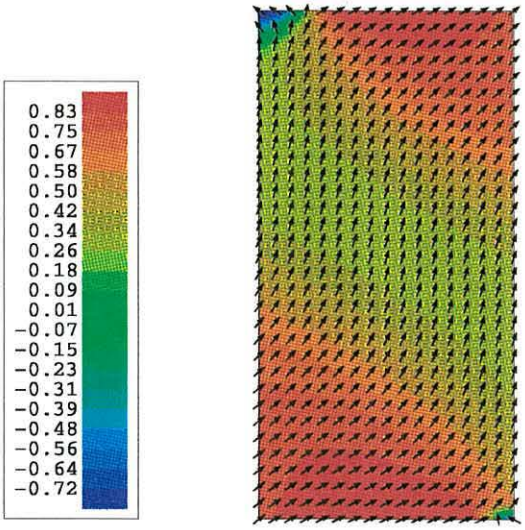

Figure 5.18: 0.1μm $\times$ 0.2μm

Turning our attention to nanoelements with a 3:1 aspect ratio we expect the elongation to have an effect on the transitions due to it being a major factor in determining the overall magnetostatic energy. If we firstly look at a particle of size 0.2μm $\times$ 0.6μm we see a 13 domain configuration as shown in Figure 5.19 with the nucleation of two inner and outer vortices. By a slight reduction in particle size to 0.17μm $\times$ 0.51μm as shown by Figure 5.20 we see the an increase in the overall magnetostatic energy as the two inner vortices grow to join the others at the top and bottom of the nanoelement.

The size at which the formation of several domains is no longer possible was found to be about 0.1μm $\times$ 0.3μm at which point the configuration becomes single domain as shown in Figure 5.21. It is interesting to note that the $3:1$ aspect ratio case supports single domain configurations to greater particle sizes than the $1:1$ and $2:1$ aspect ratio cases. In the case of nanoelements with a 4:1 aspect ratio we observe similar effects as in the previous case with the particle being able to support single domain states to larger particle dimensions.

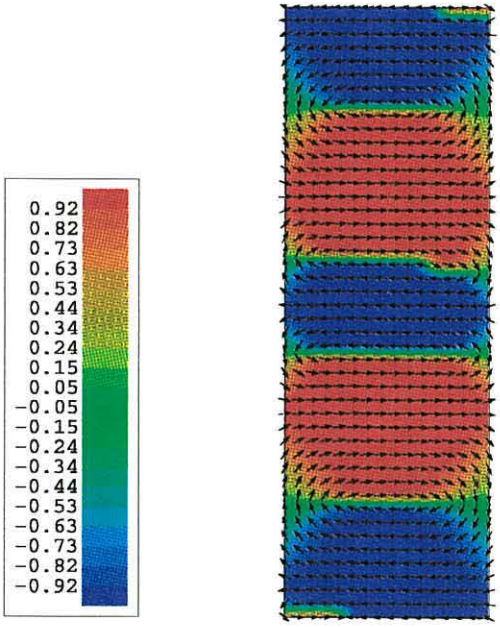

Figure 5.19: 0.2μm $\times$ 0.6μm

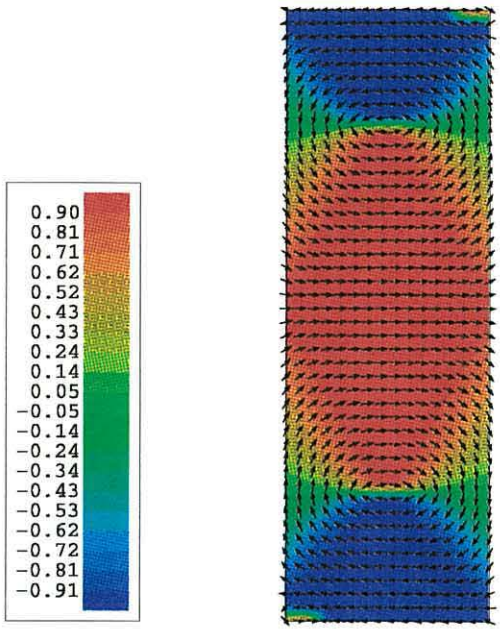

Figure 5.20: $0.17\mu m \times 0.51\mu m$

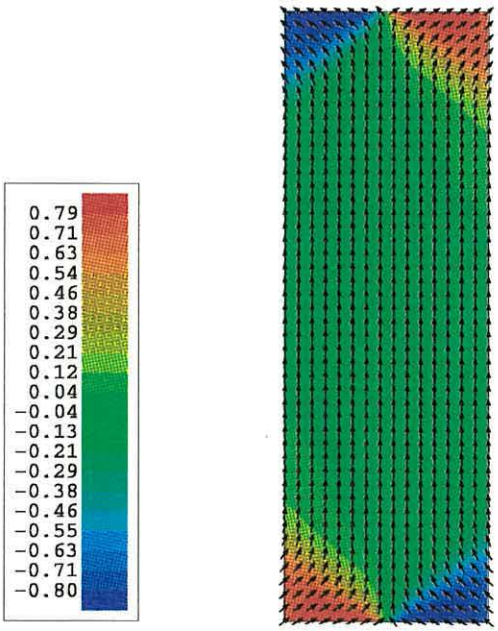

Figure 5.21: $0.1\mu m \times 0.3\mu m$

The lower magnetostatic energy due to the aspect ratio ensures that a nanoelement of size $0.2\mu m \times 0.8\mu m$ is capable of supporting the extra energy from the domain walls and thus leads to a multi domain configuration as shown in Figure 5.22. However on reduction of the particle size to $0.12\mu m \times 0.48\mu m$ the decrease in the total magnetostatic energy does not make the formation of domain walls energetically feasible and we observe a pseudo single domain state with the appearance of only small vortex nucleation near the two opposite ends of the particle as shown in Figure 5.23. The transition to single domain behaviour with this aspect ratio occurs at a particle size of about $0.11\mu m \times 0.44\mu m$. At particle sizes below this the overall magnetostatic energy is too large to allow anything but single domain behaviour as shown in Figure 5.24.

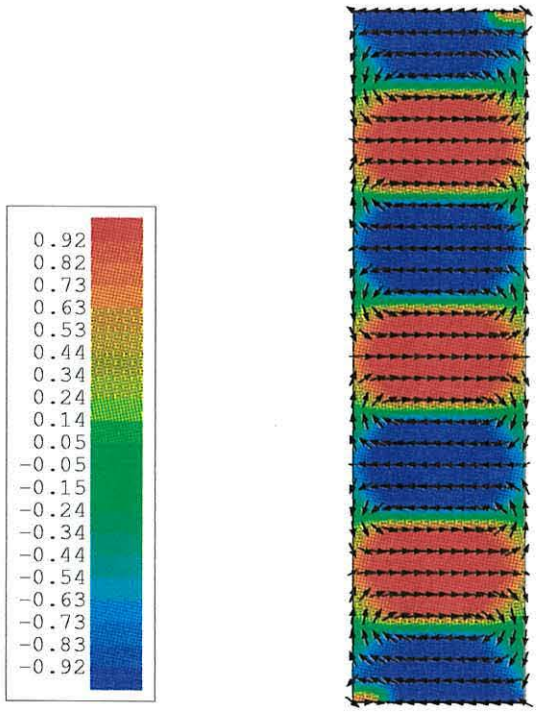

Figure 5.22: $0.2\mu m \times 0.8\mu m$

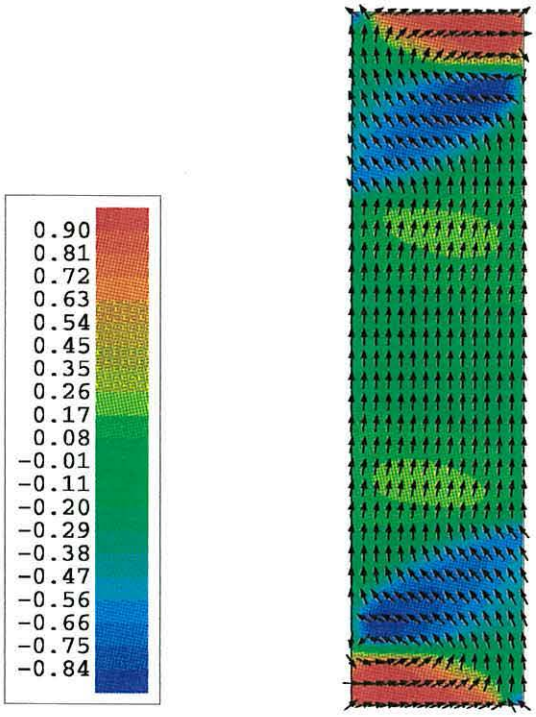

Figure 5.23: 0.12μm $\times$ 0.48μm

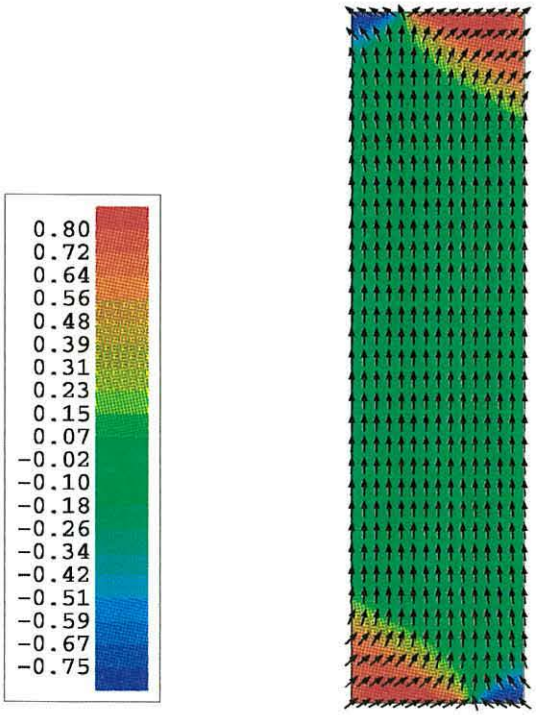

Figure 5.24: 0.05μm $\times$ 0.2μm

The simulations we have carried out so far indicate that the transition to the single domain state is determined by the particle size and elongation. We shall extend the results by recording the size of particle for each transition with each aspect ratio in turn. This data is given by Figure 5.25 in the form of a phase transition diagram for each aspect ratio as a function of elongation of the length of the nanoelement. We can see from the graph that if we take any specific particle of fixed length and then decrease its width this will eventually become single domain.

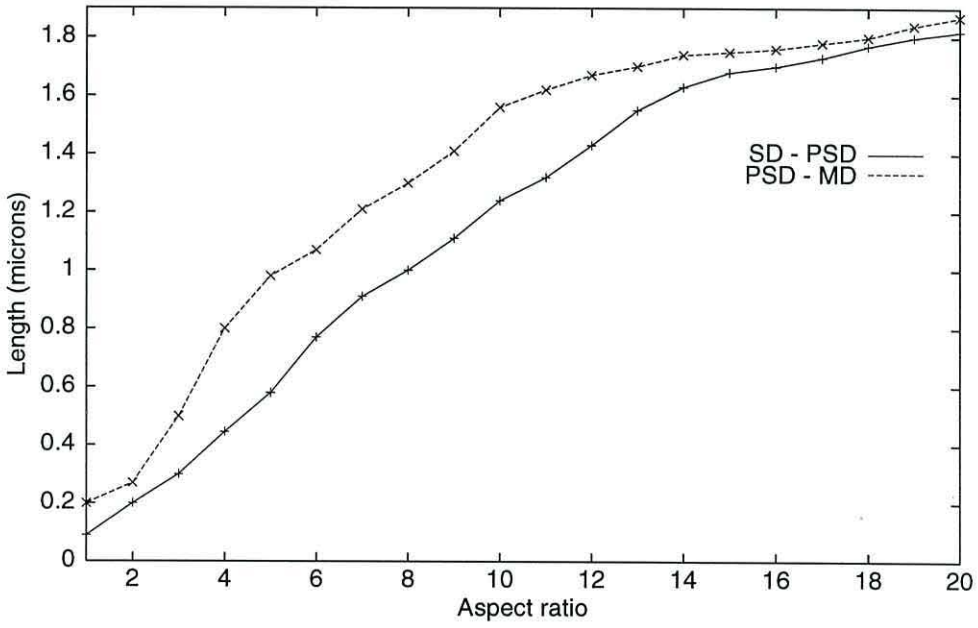

Figure 5.25: Transition for single / pseudo single / multi domain states

The noticeable feature of the graph is that for very high aspect ratios the transition from multi domain to single domain occurs more directly since the PSD states are less stable due to the presence of the transverse anisotropy. Also the nanoelements with higher aspect ratios maintained the single domain state to larger particle sizes. For further investigation we shall consider extreme cases of both SD and MD behaviour in the next two subsections. Because of the single domain feature of the higher aspect ratios we have chosen to investigate their hysteresis properties for possible magnetic recording applications. In order to investigate the behaviour

we chose a single nanoelement of size 0.1μm $\times$ 1.6μm as this has already been considered in [21].

5.4.1 Single domain behaviour of a high aspect ratio particle

As mentioned at the end of the last section we found that nanoelements with high aspect ratios exhibited single domain behaviour to larger particle dimensions than those with smaller aspect ratios. We saw that the magnetization state remained stable in the nanoelement without any applied field so the next stage is to look at the hysteresis experiment.

When we obtain the hysteresis curve of a 0.1μm $\times$ 1.6μm nanoelement as shown in Figure 5.26 it is obvious that the particle exhibits single domain behaviour from the high remanence value of $M_r = 0.98$ and coercivity. Again the magnetization reversal proceeds via vortex nucleation of domain structures from opposite ends of the nanoelement which is evident in the remanence state in Figure 5.27. This is featured on the curve as the initial small decrease in magnetization. The reversal after this then proceeds via further nucleation of domains which propagate towards the centre of the nanoelement as shown by Figure 5.28. This hysteresis behaviour exhibited by this particle is that which is required by a good recording medium as described in Chapter 1, i.e. high coercivity and remanence.

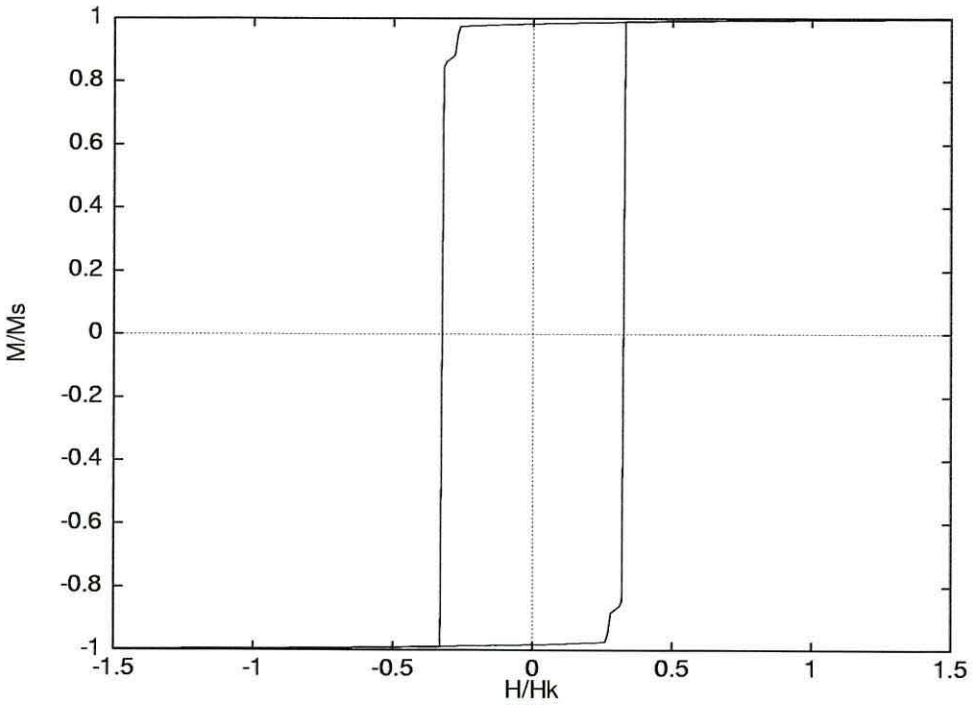

Figure 5.26: Hysteresis loop for a 0.1μm $\times$ 1.6μm nanoelement

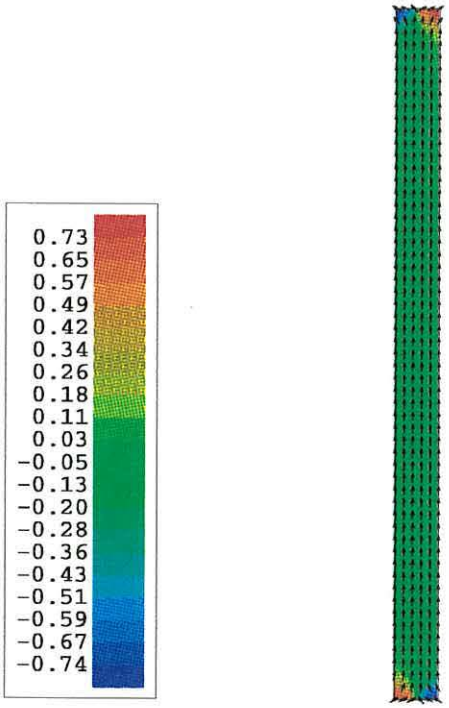

Figure 5.27: Remanence state of a 0.1μm $\times$ 1.6μm nanoelement

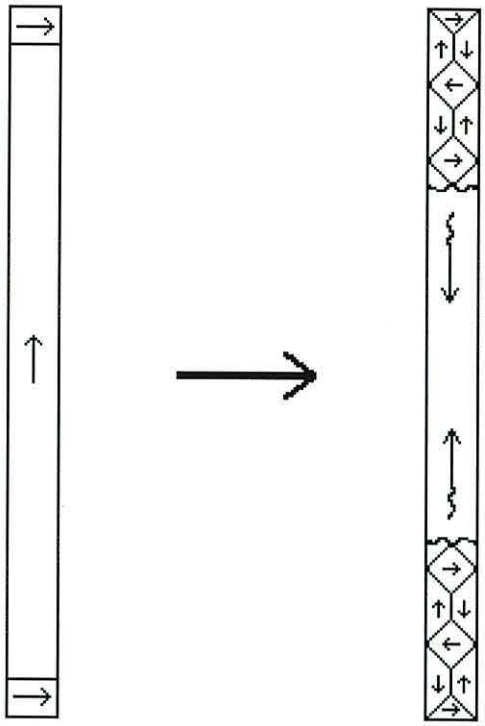

Figure 5.28: Reversal process via vortex nucleation and propagation

So far we have performed a systematic investigation on the transition behaviour from single domain to multi domain states in nanoelement. We mentioned at the beginning of this section that the formation of domains is dependent upon the total system energy being lowered by a reduction in magnetization and hence the magnetostatic energy such that the energy produced from the domain wall motion may be compensated. During the course of our investigation we have seen that since the magnetostatic energy is determined by the aspect ratio of the nanoelement this also has a strong influence on the transition states. All the simulations have been performed under the assumption of an infinitely fast removal of a saturating field, we shall now discuss the effect of introducing a slow field variation and the consequence this has on transitions.

5.4.2 Effect of magnetization dynamics

We now look at the difference between performing a particular simulation at different rates of reduction of the saturating field. As an example we choose to look at a single 0.2μm $\times$ 1.2μm nanoelement. The remanent magnetization configurations are shown in Figure 5.29 for (a) instantaneous removal and (b) gradual reduction of an applied field by steps of $0.1H_k$. Here we see that the configurations depend on the dynamics of the magnetization process. Specifically, a gradual reduction of the magnetic field produces slightly different domain structures compared with those produced without the presence of an applied field.

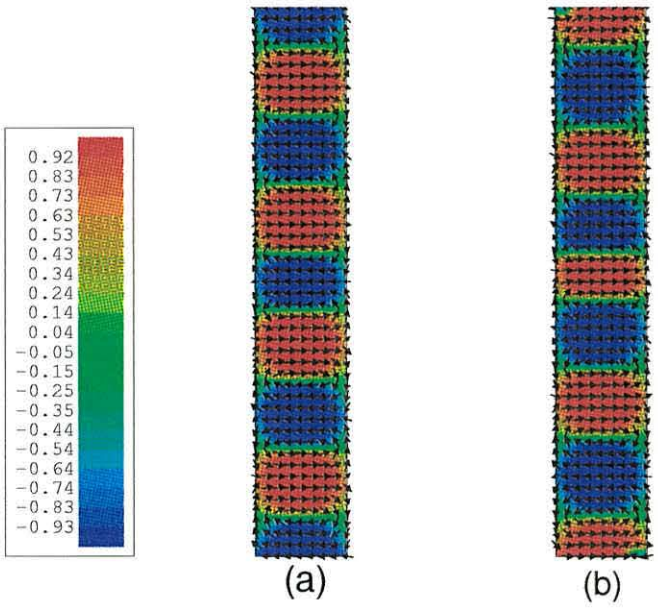

Figure 5.29: Remanent state with (a) instantaneous and (b) gradual relaxation of an applied field

On further investigation we also found that the configuration in Figure 5.29(b) exhibits an 8% lower energy than that in Figure 5.29(a). We see that a multi domain state is observed in both cases which is consistent with the results in Figure 5.25, however since there is less energy from the nanoelement after the gradual reduction of an applied field, we would expect the transition size to single domain to be marginally lower.

The slightly larger domains in Figure 5.29(b) are driven by the demagnetizing effects at the ends of the nanoelement and the lower magnetostatic energy. They are stabilized by the transverse anisotropy. The hysteresis curve for this particular simulation is shown in Figure 5.30.

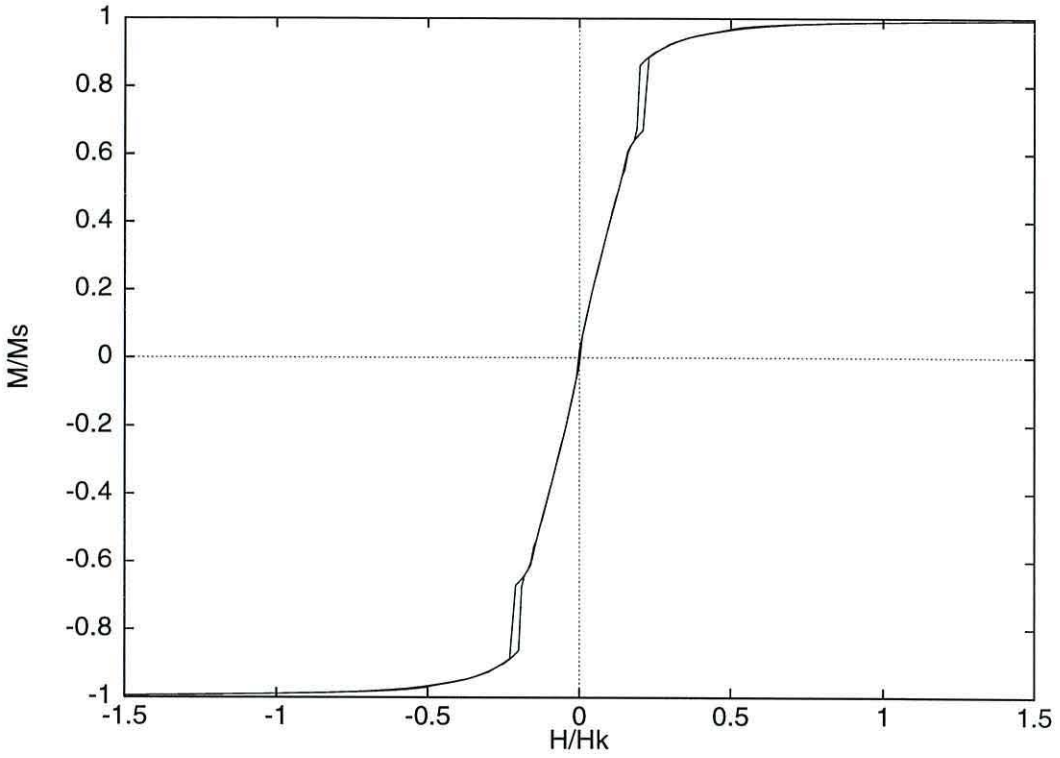

Figure 5.30: Hysteresis loop for 6:1 aspect ratio nanoelement

The reversal process proceeds via vortex nucleation of end domains giving rise to an initially large change in the magnetization as shown by point (a) in Figure 5.31 and Figure 5.32(a). At this point an irreversible magnetization change occurs. The domain structure then propagates reversibly along the entire element as shown by point (b) and Figure 5.32(b). Again, the reversal mechanism is by domain propagation from the two ends of the nanoelement towards the centre. As we continue along the curve to point (c) we see that the magnetization is beginning to align itself with the applied field as shown in Figure 5.32(c). Finally at point (d) we see that the domains begin to disappear from the centre of the nanoelement as it comes close to saturation in the opposite direction as shown by Figure 5.32(d).

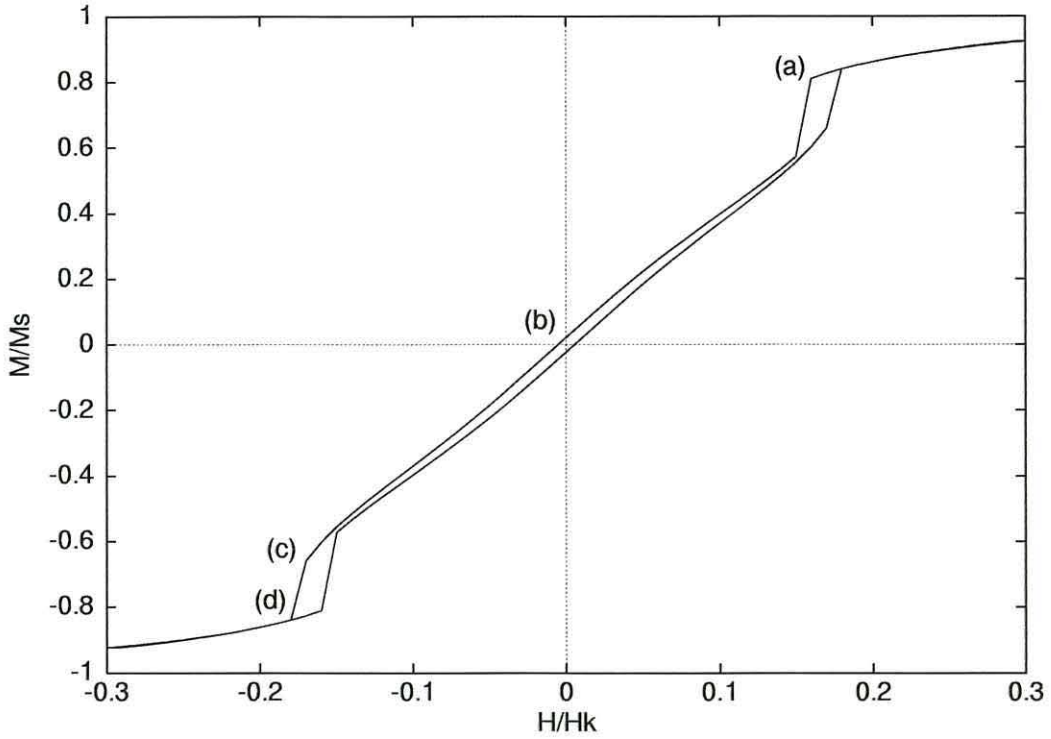

Figure 5.31: The reversal process

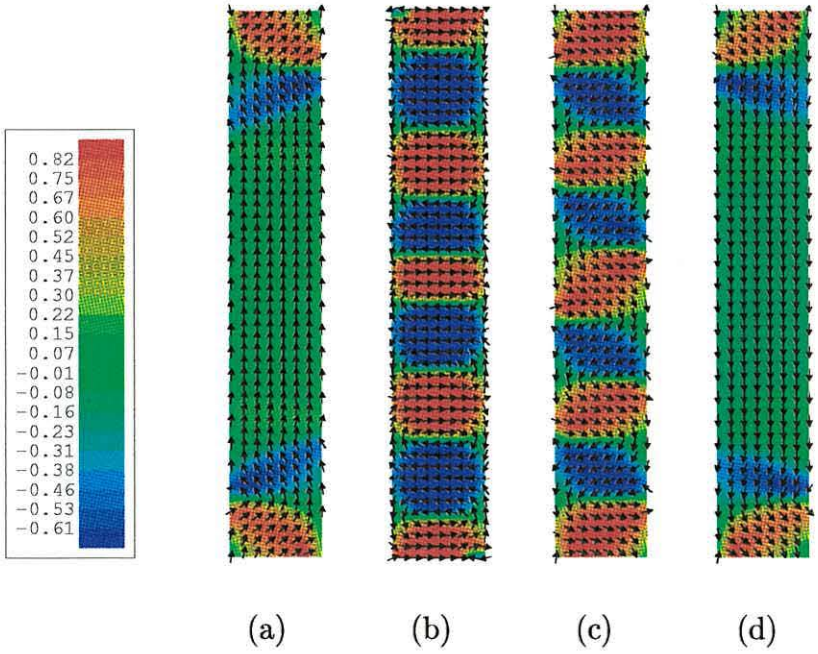

Figure 5.32: Magnetization states along the hysteresis curve

Experimental investigation of this type of nanoelement has been performed by Hefferman *et al* [20]. The loop from our simulation is qualitative in agreement with these experimental results and may be classified under the type 'C' observation.

From our observations we can conclude that in rectangular nanoelements, the transition from single domain to multi domain behaviour is not simply straightforward, instead as the dimensions increase there is a slow transition through pseudo single domain states which are characterized by the highly non uniform magnetization structures.

The occurrence of single domain formation happens when the particle in question cannot support the additional energy from domain walls. We have shown this to be dependent upon both the size and aspect ratio of the nanoelement. We have also looked briefly at the effects of the dynamics of the magnetization process. The next stage in our investigations will be to look at the effects on transitions determined by the geometry of the nanoelement.

5.5 More complex geometries

More investigation into the properties of nanoelements will be required over the next few years, especially those with irregular geometries. This is partially due to their application in the development of magnetic random access memories (MRAM) and magnetic sensors [63]. Research into non-volatile, high density, fast access solid-state storage of information is one of the major concerns of today's information society. New approaches for high density, fast read/write, low power MRAMs using magnetic nanoelements are currently in development [64].

Previous investigation has included looking at the switching field of nanoelements with pointed ends [21]. We shall begin with these more complicated geometries by looking at the domain structure of nanoelements with a single pointed end. For this geometry we define the pitch of the nanoelement to be as shown in Figure 5.33. In terms of the finite element method we are able to deal with such complicated geometries with ease. As an example we show the evolution of the domain structure of a nanoelement with dimensions of the rectangular part being 0.2μm $\times$ 1.2μm and the pitch is 0.4μm. Since the ends of the nanoelement have previously played such an important role in the magnetization reversal process, we expect the addition of a pointed end to a nanoelement to have an effect on this mechanism.

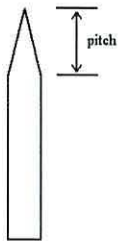

Figure 5.33: The pitch of the nanoelement

The results for this particle size are shown in Figure 5.34. Here we see from left to right the reversal of magnetization predominantly beginning from the flat end and a stabilization effect at the pointed end. This in turn causes the domains to propagate from the flat end and then occupy the entire nanoelement. This reversal process may be explained by the following. The nucleation of reversed domains begins near the corners of the nanoelements where there is a strong transverse demagnetizing field. Close to the apex of the pointed end, the demagnetizing field eminating from the two opposite inclined faces due to the magnetic surface charges cancel out which results in a zero net field component in the transverse direction. This is not the case in the region joining the rectangular and triangular regions. Here, a transverse component of the demagnetizing field occurs and initiates magnetization reversal in addition to the reversal from the flat end.

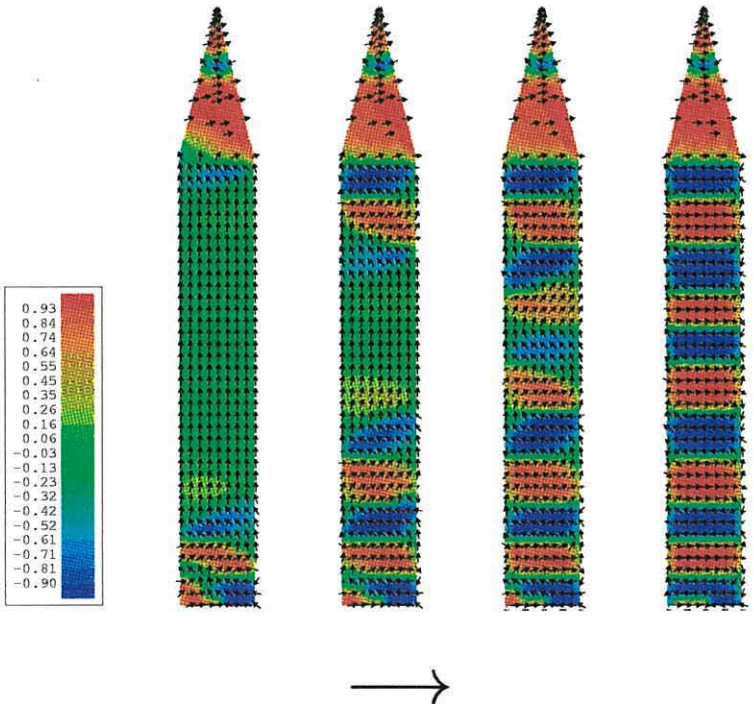

Figure 5.34: Transition into zero field equilibrium for a 0.2μm $\times$ 1.6μm nanoelement

Since the likelihood of the reversal of the nanoelement is reduced by the addition of a pointed end we observe an increase in coercivity when compared to a rectangular nanoelement of comparable size. This implies that the single point type of geometry would also maintain single domain behaviour to larger particle dimensions.

When we add two pointed ends to a nanoelement we require a much larger field for reversal than for a comparatively sized rectangular particle and a coercive force of more than double the rectangular nanoelement case. This has also been reported in [21]. If, for example we look at the magnetization behaviour of a 0.2μm $\times$ 1.2μm nanoelement then we observe the remanent configurations shown in Figure 5.35. Here we observe a pseudo single domain state. The effect of altering the pitch from (a) 0.2μm to (b) 0.3μm increases the demagnetizing field with micromagnetic detail appearing in the regions joining the rectangular and triangular regions where the reversal process is being initiated by the transverse component of the demagnetizing field. Referring back to the phase transition graph in Figure 5.25 we see that a rectangular nanoelement of this size indicated by the cross in Figure 5.36 would exhibit multi domain behaviour.

The stabilization of the pseudo single domain state to larger particle dimensions occurs in nanoelements with two pointed ends, this is not surprising since the chance of domain formation and propagation is half as likely as in the case of one pointed end as discussed earlier.

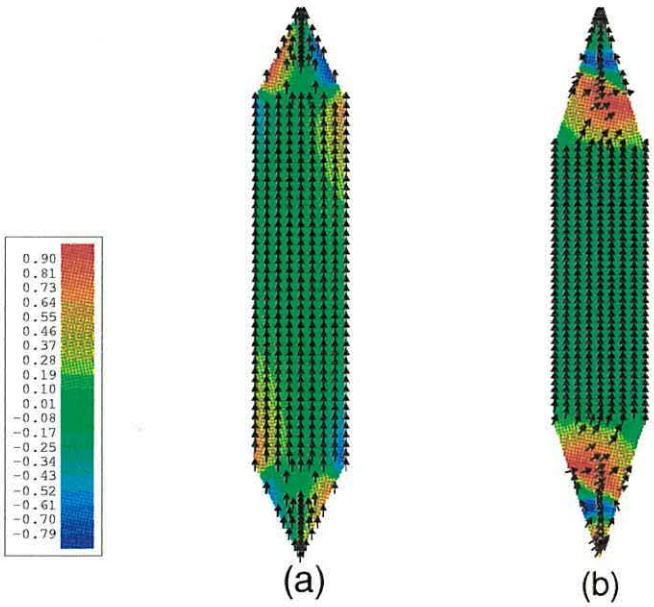

Figure 5.35: Remanent states for a 0.2μm $\times$ 1.2μm nanoelement with two pointed ends, varying pitch

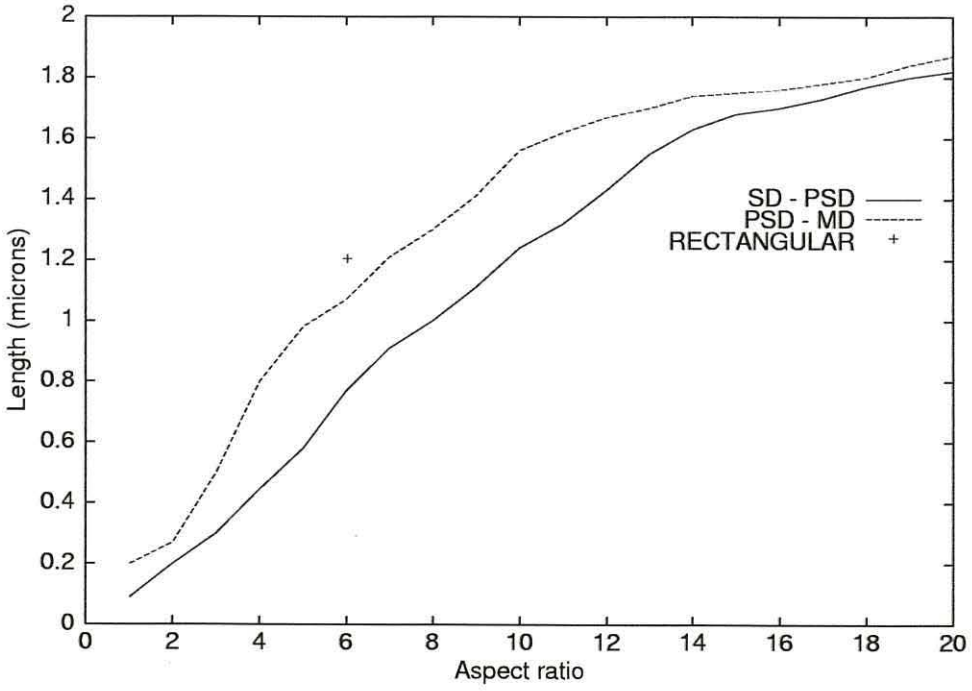

Figure 5.36: Transition for single / pseudo single / multi domain states

5.6 Summary

We started this chapter off by a series of tests of our finite element solution to the calculation of the demagnetizing field via a scalar potential method. The tests were carried out by comparing our explicit and implicit methods using quadratic finite elements with a refinment indicator and analytical solutions. We also gave an indication of the computational requirements of the calculation.

After a full testing of this calculation, we were ready to implement this into our complete micromagnetic model which was described in Chapter 3. However, before using this to produce any new results, another test had to be carried out. This was performed by generating results for comparison with existing scientific work on rectangular permalloy nanoelements. Our results were similar, therefore we were able to proceed with our investigations and look at the transition states of nanoelements from multi to single domain behaviour for decreasing particle size.

Since the formation of domains in a particle is linked to the magnetostatic energy which itself is determined to some extent by the elongation of the particle we also had to look at the effect of altering the aspect ratios. We carried out the study by looking at each aspect ratio in turn. The particle size at which we started was governed by previous experimental observations of multi domain behaviour. We predicted multi domain behaviour at this stage consistent with the experimental data. The particle size was then reduced until the total energy reduction from any domain formation was not enough to compensate for the increase in domain wall energy and a single domain state was observed.

We recorded our theoretical observations on transition states in the form of a phase diagram. As expected the nanoelements with greater elongation remained single domain to larger particle dimensions. Up to this point, our simulations on transition states had been performed under the assumption of instantaneous reduction of the applied field, to observe the hysteresis effects with a view on magnetic

recording applications, we chose a high aspect ratio case to investigate this further.

It was suspected at the beginning of these simulations that the rate of reduction of the applied field would have some bearing on the magnetization dynamics and thus the transition size. Indeed this is the case as we demonstrated with a 6 : 1 aspect ratio nanoelement which exhibited a small reduction in energy after the gradual reduction of an applied field as when compared with the saturating field being removed instantaneously. The reversal mechanism observed was one of domain propagation via vortex nucleation from the two ends of the nanoelement. Again qualitative agreement with experimental work was observed with the corresponding hysteresis experiment.

Bearing in mind the full capabilities of the finite element method in dealing with arbitrary shaped regions we have also looked at the effect of altering the nanoelement geometry by the addition of one or two pointed ends. This more complicated geometry is of particular importance in MRAM and magnetic sensor applications.

In the case of a nanoelement with a single pointed end we observed a reversal mechanism in which the formation of domains started from the flat end of the particle with some interaction around the region where the rectangular and triangular region joined one another. This was due to the magnetostatic interactions at the pointed end compensating each other and giving rise to reduced local fields. This causes the nanoelement to have a higher coercivity than in the rectangular case and to exhibit single domain behaviour to larger particle dimensions. As expected the addition of two pointed ends to a nanoelement caused an even greater increase in the coercivity and thus further increase in the particle size to which single domain behaviour is supported.

In this chapter we have made a systematic study on single nanoelements only. The next step is to look at the behaviour of arrays of interacting nanoelements which we shall discuss in the next chapter in relation to experimental observations.

Chapter 6

Investigation of arrays of interacting nanoelements

6.1 Introduction

Investigation into the behaviour of arrays of nanoelements is of particular importance to determine their suitability for future high density data storage [65]. Current research in this area is being carried out experimentally by Kirk *et al* [66] to investigate magnetostatic interaction effects due to spacing between the nanoelements. The main advantage behind the use of nanoelements as patterned media for writing is that their coercivity can be less than that for continuous media, this means less demand on the miniaturised write heads. Also noise is not a problem since the aim is to write 1 bit per nanoelement.

The simulations we have considered so far have all been carried out on single nanoelements. These results are an initial study on the domain behaviour and hysteresis properties of the particles. However to apply the nanoelements to magnetic recording, we must extend our model to be able to look at arrays of particles.

For this chapter we use our model to look at the magnetization behaviour of arrays of interacting rectangular nanoelements. The experiments are carried out with varying space between the nanoelements and both longitudinal and trans-

verse material anisotropy. We consider both single arrays and several of them in placed in row and column formations. Following the same procedure as for single nanoelements, we must firstly do a simple test of the model by comparing initial results involving an array of nanoelements with existing scientific work.

The obvious consequence in terms of our model is that of an increase in terms of computational requirements needed for such a simulation. So far we have only looked at a single particle with a discretization of one or two thousand quadratic finite elements. In this situation we are going to have to deal with at least three times the computational requirements, however this is within the capabilities of our finite element solver due to the sparse matrix solver routine as described in Chapter 4.

We may now proceed with the testing process. The experimental results of Rührig and coworkers [19] were concerned with 'large' scale domain structures in nanoelements with longitudinal anisotropy as shown by Figure 6.1. These 'large' scale domain structures were caused by the magnetostatic interactions around the ends of the nanoelements. It is a good test for our model to simulate these results since they involve 'large' domains which do not require a high level of discretization to model correctly and hence are less computationally intensive.

To simulate this magnetization behaviour we introduced longitudinal material anistotropy to our model and created a finite element mesh for three interacting nanoelements each of size 0.2μm $\times$ 1.6μm with inter nanoelement spacing of 0.1μm. To be able to compare with the experimental observations we saturated the nanoelements parallel to the anisotropy direction and then removed the saturating field instantly at the beginning of the simulation.

Our results are shown in Figure 6.2 in the form of greyscale images with black and white representing $+1$ and -1 respectively for the longitudinal component of magnetization m_y. We observe a similar 'large scale' domain structure to the ex-

perimental results. We notice that the two outer nanoelements have the same kind of domain structure with a single 180^o domain wall whereas the central nanoelement has two 180^o domain walls. In all 3 nanoelements we also see the formation of end structures. These configurations may be explained by the magnetization in the central nanoelement being forced parallel to the anisotropy axis due to the strong demagnetizing effect between nanoelements. On further comparison with the experimental results we notice that our predicted domain structures in the outer nanoelements show the domain walls shifted outwards more than in the experimental case. This is caused by weaker interactions and is due to the different rates of reduction of the applied field between the experimental case and our theoretical predictions.

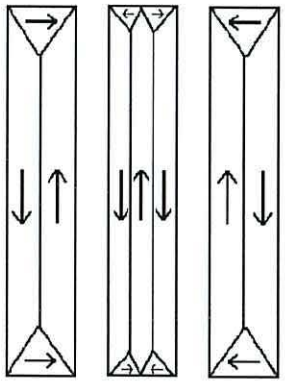

Figure 6.1: 'Large' scale domain structure observed experimentally in 3 interacting nanoelements

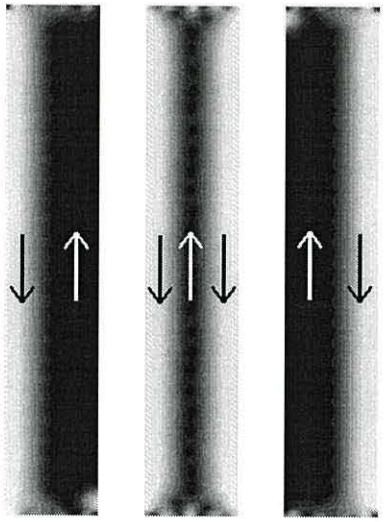

Figure 6.2: Equilibrium state for an array of three 0.2μm $\times$ 1.6μm nanoelements with longitudinal anisotropy and spacing 0.1μm

Now that we are satisfied that the model is correctly simulating the interaction effects between nanoelements, we may proceed with some new results on the slightly more complicated case of nanoelements with transverse material anisotropy.

6.2 Three interacting nanoelements

To begin our investigation into the magnetization behaviour in arrays of nanoelements we shall continue at the simplest level, i.e. three rectangular nanoelements placed side by side in a row formation.

In terms of mesh considerations, we expect there to be significant interaction effects between nanoelements so in order to observe this in our simulations we enforce a high degree of mesh refinement along the inter-nanoelement edges and the space between the nanoelements. As a result of this we obtain a type of mesh as shown in Figure 6.3 which contains 6460 finite elements and 12937 quadratic nodes. The refinement between the nanoelements is shown in greater detail in Figure 6.4.

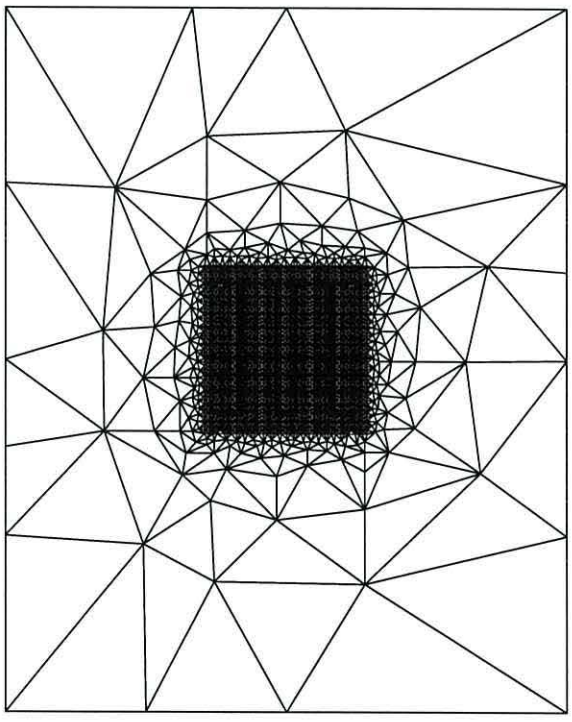

Figure 6.3: Mesh discretization for three interacting nanoelements

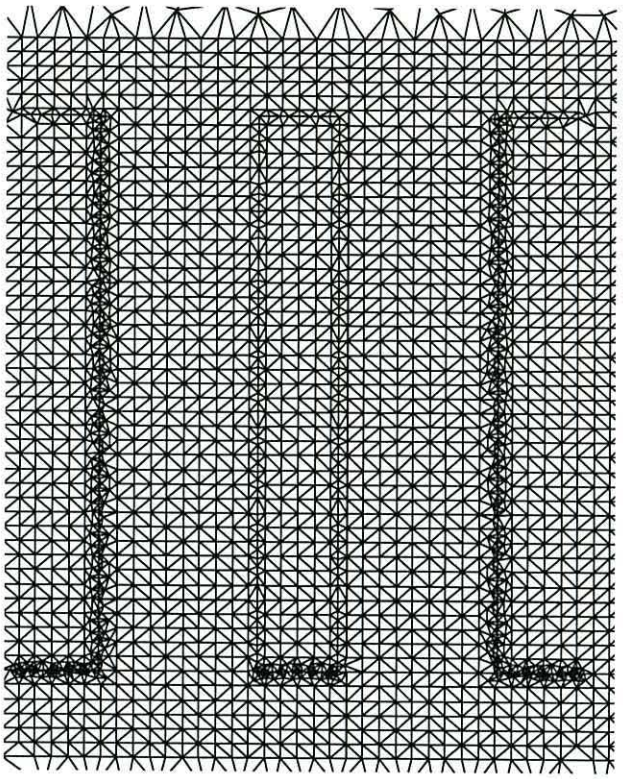

Figure 6.4: Extra mesh refinement between the interacting nanoelements

For our first series of simulations we are going to use the same material parameters as mentioned in 5.4 and we shall consider nanoelements of a size which previously exhibited multi domain behaviour with transverse anisotropy. This will enable us to observe any interaction effects due to the element spacing.

As an example we perform our first simulation on three interacting 0.2μm $\times$ 1.6μm nanoelements with thickness 20nm. Here, the nanoelements are initially saturated with a uniform magnetization distribution in a direction going from the bottom to the top of the particle. As in the case of the single nanoelement simulation which was performed at the beginning of the previous chapter we simulate the evolution of the magnetization of the particle without any externally applied field.

We start off with an inter-element spacing of 0.05μm as shown by the results given in Figure 6.5. The 8 : 1 aspect ratio of these individual nanoelements make the elongation large enough to have significant effect on the magnetostatic energy

of the particle. The implication of this is that there will be a very strong stray interaction field around the ends of the nanoelements.

The reversal mechanism for this particular array is one where the reversal begins by the vortex nucleation of reversed domains from the two opposite ends of the two outer nanoelements. The domain structure then expands throughout the whole of the outer nanoelements while the central particle remains almost saturated.

In Figures 6.5 - 6.7 we show zero field domain structures for separations of 0.05μm, 0.4μm and 0.8μm respectively. In Figure 6.5 we observe the stabilization of a single domain state in the central nanoelement but not in the two outer ones although the domain structures in the outer elements are considerably different from that of the isolated element. Here we see the stabilization of a transient state as in Figure 5.32(c). If we were to consider the array of nanoelements to be one large particle roughly of size 0.7μm $\times$ 1.6μm ignoring the non magnetic spacing, then referring back to the transition diagram in Figure 5.25 a nanoelement of this size and aspect ratio would certainly exhibit multi domain behaviour. However from the single domain state in the central nanoelement, our results for the interacting case display clear evidence of interaction effects.

The effects of interactions between nanoelements can be explained by the existence of the large magnetostatic interactions. We mentioned earlier that there will be a strong stray field around the ends of the nanoelements from the large magnetostatic energy present there.

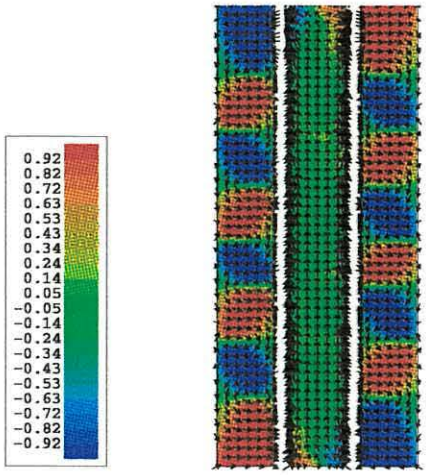

Figure 6.5: Equilibrium state for a 0.2μm$\times 1.6\mu$m array of nanoelements, spacing 0.05μm

The two outer nanoelements break up into multi domain states and thus lower their individual magnetization and therefore magnetostatic energies. The strong magnetostatic field at the ends of the nanoelements then forces the magnetization of the central nanoelement to be perpendicular to the anisotropy axis in order to minimize the total exchange energy of the system. We again observe the stabilization of transient states in the two outer nanoelements in comparison with the non interacting case as shown in the last chapter by Figure 5.8. The central nanoelement is not capable of supporting a multi domain structure with this spacing since the reduction in energy needed by any further domain wall formation would not be sufficient to compensate for the increase in energy associated with any extra domain walls.

When we increase the separation between the nanoelements to 0.4μm, as shown in Figure 6.6, we observe that the central element is still being prevented from forming a multi domain structure due the large stray fields originating from the ends of the nanoelements as a consequence of the magnetostatic interactions. However in

this case we notice that there is slightly more end structure occurring in the central nanoelement due to the large increase in space between the particles. Recent experimental observations [68] have suggested that for nanoelements of comparable size to our example with a 4 : 1 aspect ratio, magnetostatic interactions are only strong enough to have any significant effect on the domain behaviour at spacings less than the width of the nanoelement. Our results are showing evidence of interaction effects at spacings of twice the nanoelement widths and may be justified by the 8 : 1 aspect ratio of our particles since this will cause the nanoelements to have magnetostatic interactions far greater than those exhibited by the 4 : 1 aspect ratio cases.

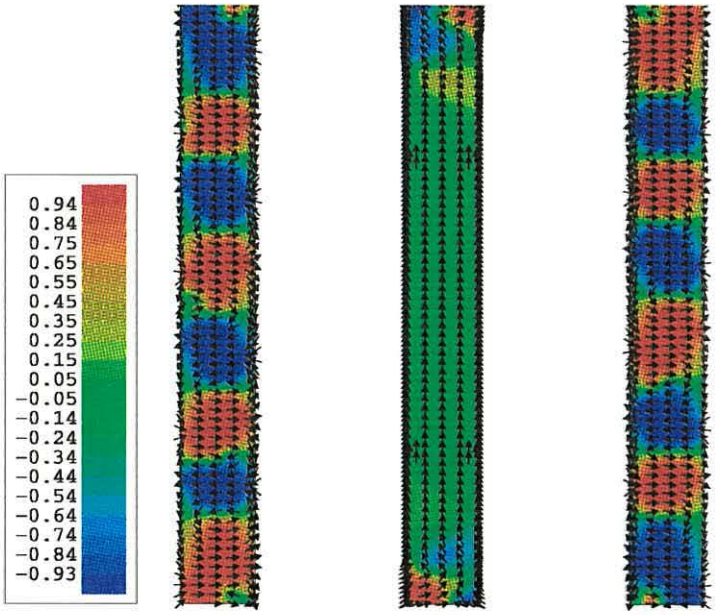

Figure 6.6: Equilibrium for 0.2μm×1.6μm array of nanoelements, spacing 0.4μm

When we increase the separation to 0.8μm, shown by Figure 6.7, the central element does form a multi domain structure much like the two outer ones and the domain structures in all elements reverts to that obtained earlier in Figure 5.8. At this level of inter nanoelement spacing the magnetostatic interactions originating from the ends of the particles are clearly not significant enough to have stabilized

a single domain state in the central nanoelement. However we do see slightly different domain structures to that observed in the non interacting case as shown in Figure 5.8 suggesting that magnetostatic interactions effect the evolution of the local field.

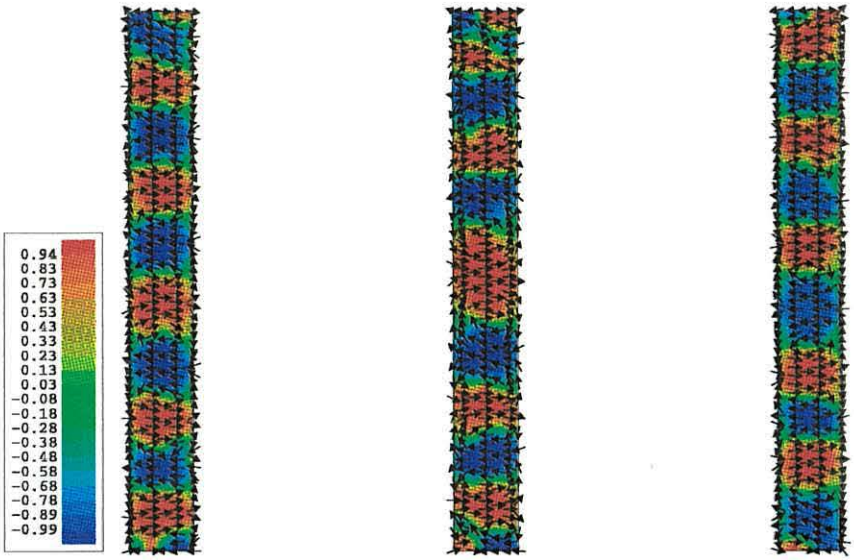

Figure 6.7: Equilibrium for 0.2μm$\times 1.6\mu$m array of nanoelements, spacing 0.8μm

Again this may be explained by the very large demagnetizing effects from the $8:1$ aspect ratios. If we investigate this behaviour further by comparing the total energy of the individual nanoelements in this example with the non interacting case given in the previous chapter, then the two outer nanoelements exhibit 18% lower energy than the non interacting case whereas the central nanoelement exhibits a reduction of 11%. This is evidence that the magnetostatic interactions are still present.

We can estimate the importance of interactions as follows. The distance of separation at which the magnetization energy is equal to the anisotropy energy is given

by the formula

$$R^3 = \frac{M_s^2 w^2 t}{K} \tag{6.1}$$

where R is the separation distance, $M_s = 800\text{emu/cm}^3$ is the saturation magnetization, the uniaxial anisotropy constant, $K = 5 \times 10^3\text{erg/cm}^3$, and the width and thickness of each nanoelement is given by $w = 2 \times 10^{-5}\text{cm}$ and $t = 2 \times 10^{-6}\text{cm}$ respectively. Using these parameters, we obtain a value of $R = 0.47\mu\text{m}$. This is in agreement with our observations since we expect the nanoelements to become non interacting at a separation of well above this value for R.

We may illustrate the interaction effects further by comparing graphs which give the total magnetization of the system over time for the non interacting and interacting cases. In Figure 6.8 we have the relaxation of the magnetization for a single non interacting case, here we observe a small initial variation in magnetization at the beginning of the reversal process, when the domain structure begins to form from the two outer ends of the nanoelement. The rate of change of magnetization

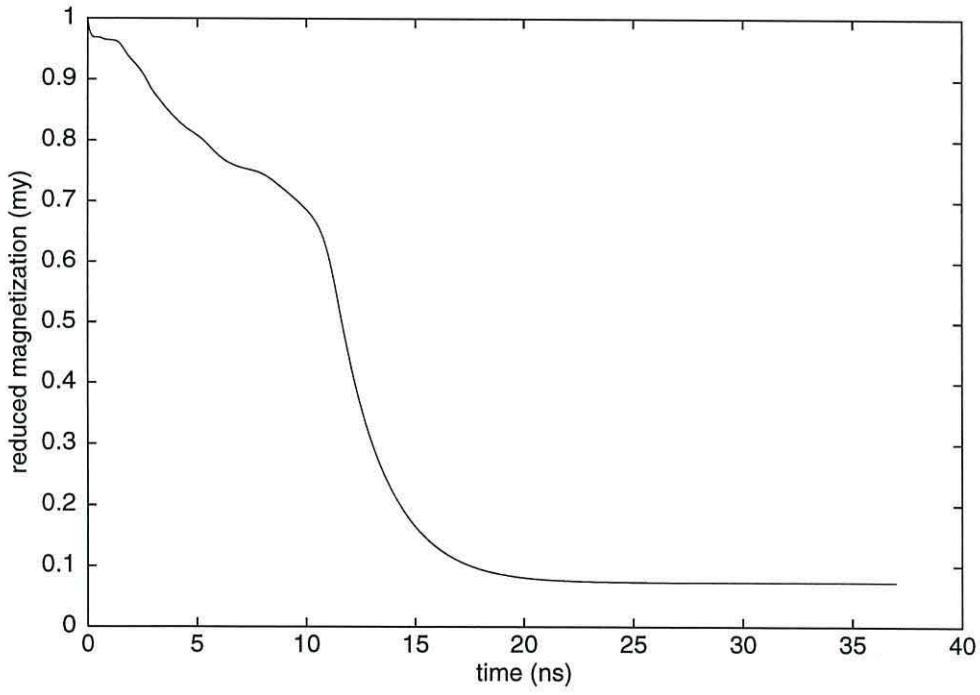

Figure 6.8: Relaxation of the non interacting nanoelement

then rapidly increases as the domains propagate throughout the entire nanoelement

towards the centre and stabilize as we reach the equilibrium state at remanence.

When we look at the interacting case with a spacing of 0.4μm as shown by the graph in Figure 6.9 a similar effect is observed only over a longer period of time. Here we have measured the total magnetization by combining the three individual values of the nanoelements. However when we give the relaxation of each

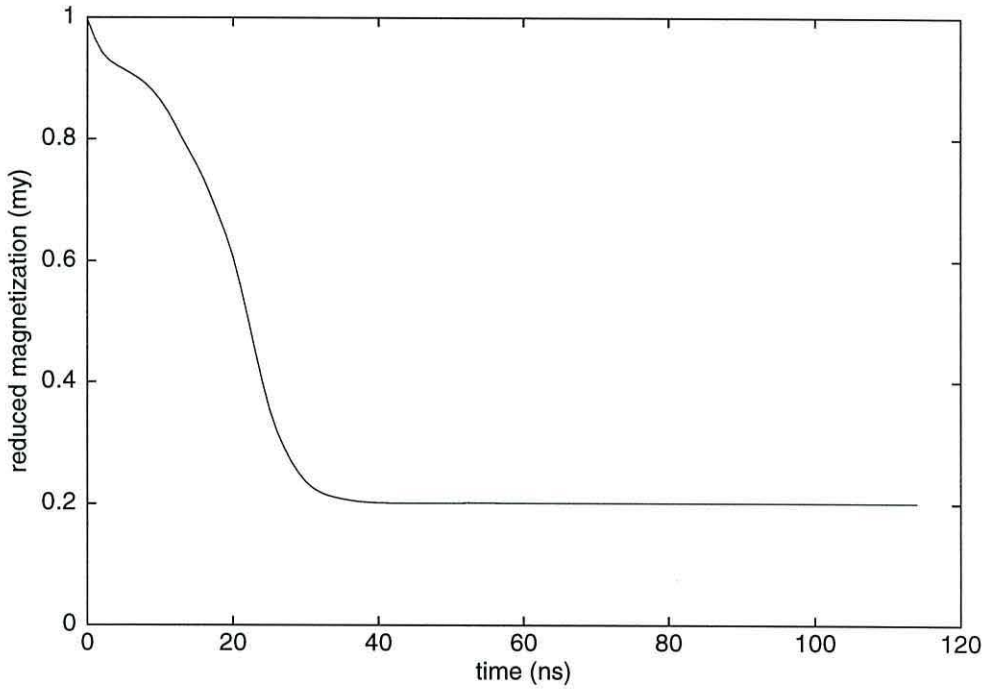

Figure 6.9: Total relaxation of the whole system

individual nanoelement as a function of time as shown in Figure 6.10, we observe a different effect. For reference we have labeled the nanoelements by N1,N2 and N3 from left to right. For the outer nanoelement there is initially a relatively slow variation of the magnetization associated with the nucleation of a reversed area of magnetization followed by a more rapid propagation. The magnetization structure of the central nanoelement changes early in the process, but stabilizes rapidly.

So far in this chapter we have discussed the magnetization behaviour of arrays of three nanoelements with varying separation. We have given an idea on the increase in computational requirement needed by our model to perform such simulations. The results have concentrated on the effect of the stabilization of the

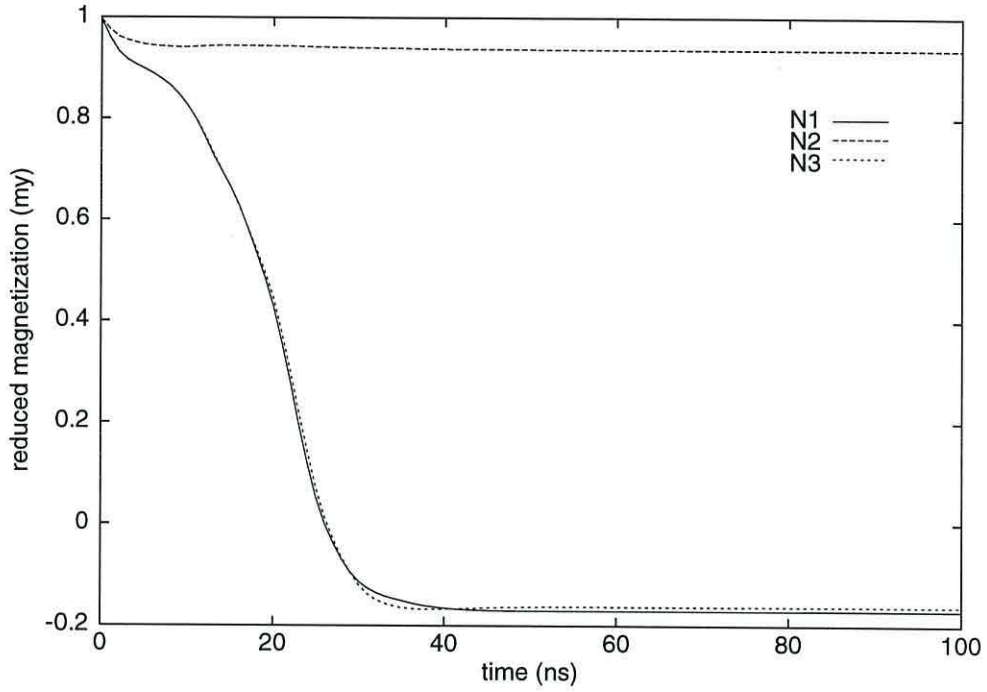

Figure 6.10: Relaxation of each individual nanoelement in the system

single domain state in the central nanoelement due to magnetostatic interactions. Current experimental work is being carried out on larger rows and arrays of nanoelements to determine their use in future recording applications hence the next stage for our model is to look at larger numbers of nanoelements in both row and array formations and then make theoretical and experimental comparisons.

6.3 Interacting nanoelements in a two dimensional array

At the beginning of this chapter we mentioned the reason for the investigation into the behaviour of arrays of nanoelements. This is of course due to their possible future application in high density data storage. For use as patterned magnetic media each individual nanoelement would store 1 bit. Thin films with exchange coupled grains such as Permalloy or Cobalt would be used to fabricate the nanoelements. Previous experiments on these films have shown that each nanoelement behaves in an almost single domain manner and therefore has two stable magnetic states which is ideal for data storage.

Recent experimental work in this area has been carried out by Kirk *et al* [66]. In the experiments arrays of permalloy nanoelements are created by electron beam lithography and lift off patterning. The nanoelements are fabricated in short rows or in arrays which are made up from 3 rows close together. The magnetic imaging is carried out in a modified Philips CM20 transmission electron microscope (TEM) in which samples may be viewed in field free conditions or in variable applied fields. To create the hysteresis experiments a global field is applied using the objective lens of the microscope which is de-activated for field free experiments. The array was magnetized by tilting it in the vertical field from the objective lens in the TEM, thus giving a field component in the plane of the sample. The field was aligned along the long axis of the nanoelements.

To perform the hysteresis experiment, the sample was first tilted to a high angle to produce a large in plane field component to saturate the elements in one direction. The sample was then returned to 0^o tilt and then gradually tilted in the other direction to obtain an increasing reverse field until all the nanoelements have reversed. The same procedure is then performed to return the nanoelements back to their initial configuration. Throughout the magnetization cycle images are recorded on a CCD camera. Configurations are displayed by either Fresnel or

Differential Phase Contrast (DPC) mode imaging. The former method involves de-focusing the microscope until the deflection beam by the magnetic induction of the sample causes visible regions of varying electron density to appear in the image whereas in the DPC mode the nanoelements appear either dark or light depending upon their direction of magnetization. A more detailed explanation of TEM studies of these experiments can be found in [67].

Since these small arrays are amenable to computational studies, we are now going to perform simulations on similar arrays of nanoelements and then make comparisons with the experimental observations. The geometries considered will be either arrays or rows of rectangular nanoelements as shown in Figure 6.11(a) and (b) respectively.

For the arrays we denote the intra row spacing by x and the inter row spacing by y. The simulations which we shall consider will be on arrangements of 6 nanoelements in a single row and 6×3 nanoelements in an array. The obvious concern with the simulation of these setups is of computational requirement, for the two dimensional arrays we have to deal with 18 nanoelements. Indeed to create a finite element mesh with the correct level of refinement we need approximately 8000 quadratic finite elements. This leads to the formation of a very large stiffness matrix which requires the sparse matrix solver to be used to full potential.

For these particular array simulations we use a typical mesh as given in Figure 6.12. The extra refinement needed to successfully be able to simulate the magnetostatic interactions between nanoelements is shown in Figure 6.13, a mesh with refinement in similar areas is also used for the single row simulation. For these simulations we initially saturate each individual nanoelement with a magnetization distribution parallel to a direction going from the bottom to the top of the nanoelement. The standard material parameters for permalloy are again used which are the exchange constant, $A = 1.3 \times 10^{-6}$erg/cm, the uniaxial anisotropy, $K = 5 \times 10^{3}$erg/cm^3 and the saturation magnetization, $M_s = 800$emu/cm^3. We also fix the thickness of each

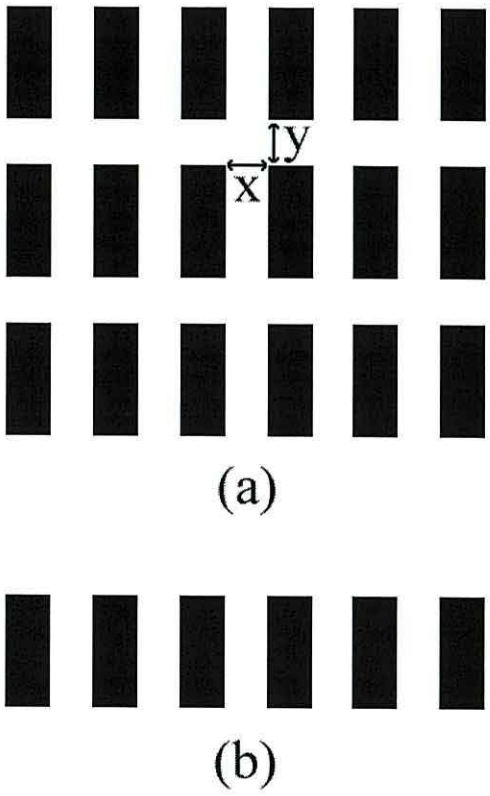

Figure 6.11: One and two dimensional arrays of nanoelements

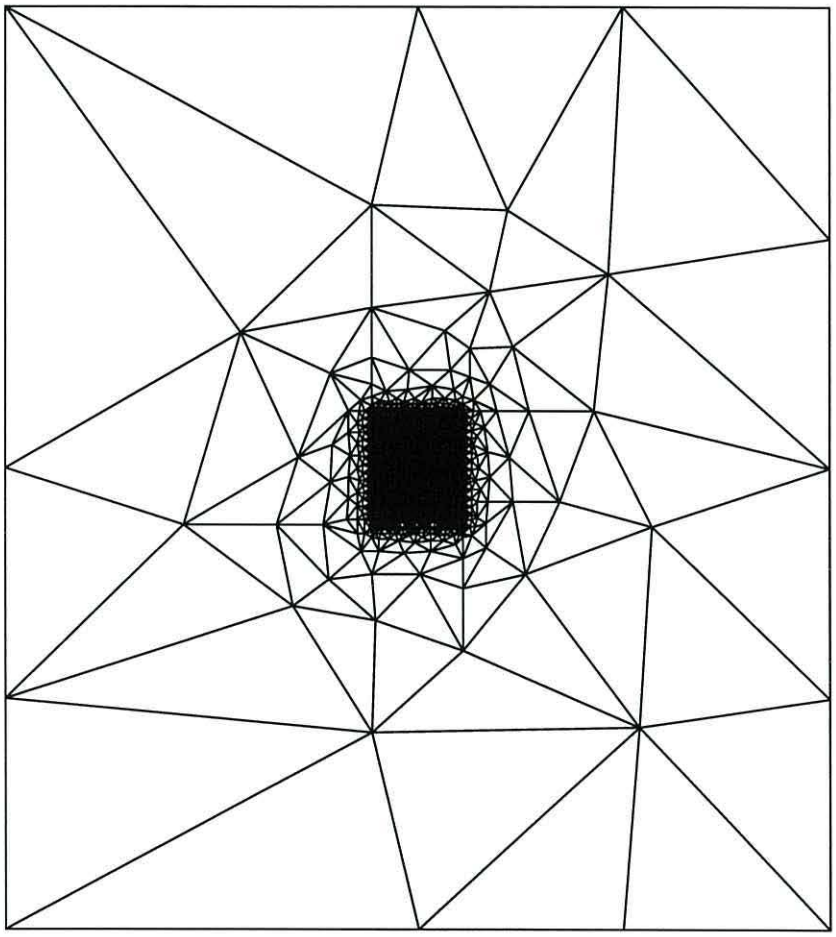

Figure 6.12: Mesh for the array of eighteen nanoelements

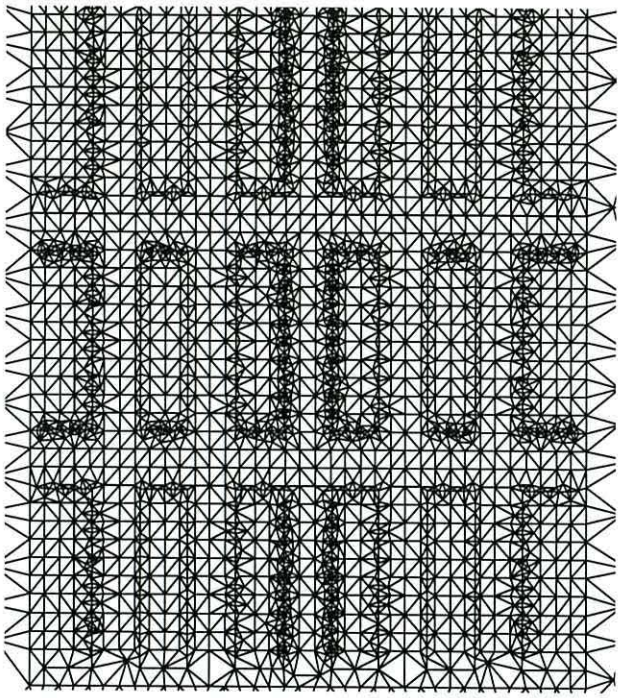

Figure 6.13: Refinement of mesh

individual nanoelement to be 20nm. To emulate the dispersion of the anisotropy distribution throughout the individual nanoelements in the array we use a planar random anisotropy distribution.

In our first simulations we shall consider a row and array of nanoelements of size 300nm $\times$ 80nm with an intra row spacing of 80nm and for the array an inter row spacing of 100nm. Previous experimental investigations of similar arrangements have already been performed by Kirk *et al* [68], the hysteresis curves are given in Figure 6.14. The reversal occurs sooner in the rows than in the arrays, which is due to the inter row magnetostatic interactions.

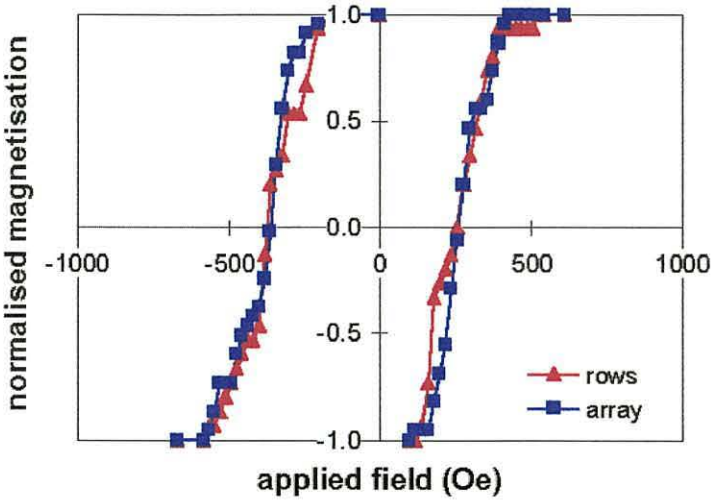

Figure 6.14: Experimental hysteresis curves for rows and arrays of 300nm×80nm interacting nanoelements after Kirk *et al*

To obtain our theoretical results for comparison, we apply a strong saturating field and then reduce it by field steps of 6.25Oe, $(0.5H_k)$ until all the nanoelements have reversed. We also record some interesting magnetization plots which indicate the strength of the net magnetization of each individual nanoelement, this is represented by the standard colour map for magnetization with red, green and blue representing $M = 1$, $M = 0$ and $M = -1$ respectively. For this particular simulation in order to simulate the hysteresis curve we needed approximately 34hrs of C.P.U. time on a single EV6 processor.

Our results are shown in Figure 6.15. Here we observe good agreement between the experimentally observed value and our predicted value of the coercivity. Also our estimation of the average switching field distribution (SFD) is 117Oe which is significantly smaller than the experimental observation of 330Oe which was re-

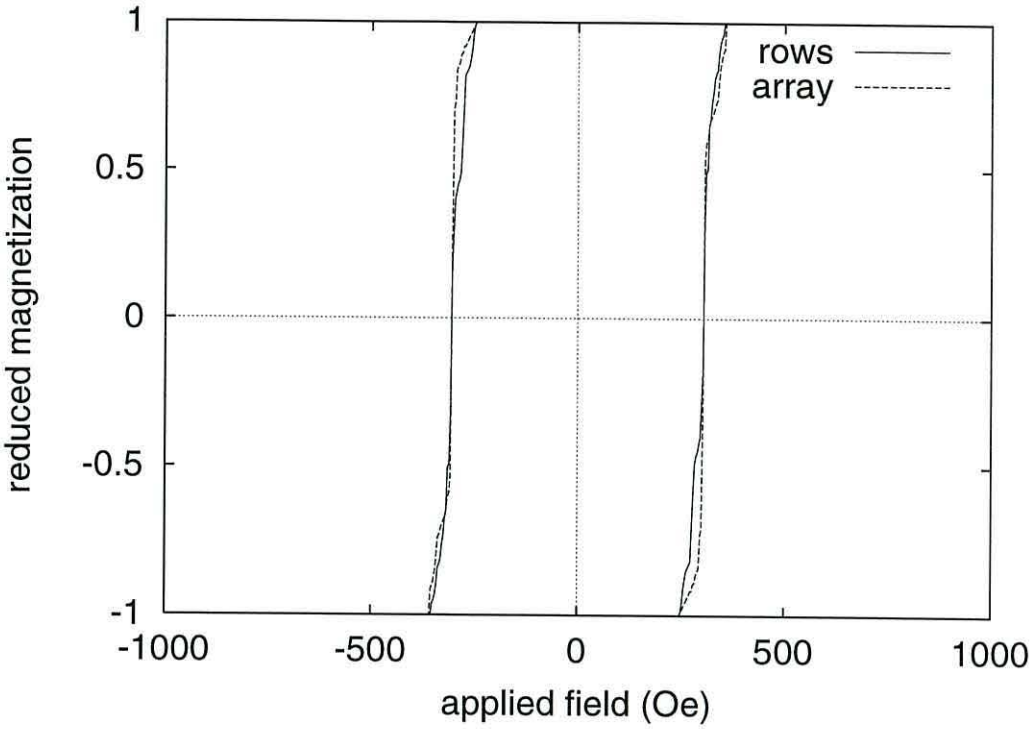

Figure 6.15: Theoretical hysteresis curves for rows and arrays of 300nm×80nm interacting nanoelements

ported in [69]. The higher value for the experimental case may be ascribed to a dispersion of the intrinsic properties of the individual nanoelements in the experimental samples.

The reversal process in the experiments is via a mechanism of random columns of nanoelements switching together and is described in [68]. This unordered mechanism is also observed in our results and again occurs by entire columns of nanoelements reversing at random. To illustrate this effect we shall consider the following magnetization plots as shown in Figures 6.16 - 6.19. In Figure 6.16 we see that the far right and second from far left column have almost reversed together. In Figure 6.17 we see additional columns reversing due to the magnetostatic interactions.

To justify the random behaviour of this reversal mechanism we have also performed simulations whereby a single column is forced to reverse at the beginning of the simulation. In reality this type of reversal event could be due to thermal

activation. In the case illustrated in Figure 6.18 the column one right from the centre of the array was forced to reverse by applying a large negative field to the column and then instantly removing it once the entire column had become saturated in the opposite direction. The random switching behaviour is also observed in this case as shown in Figure 6.19 with no apparent order of the switching of the individual columns.

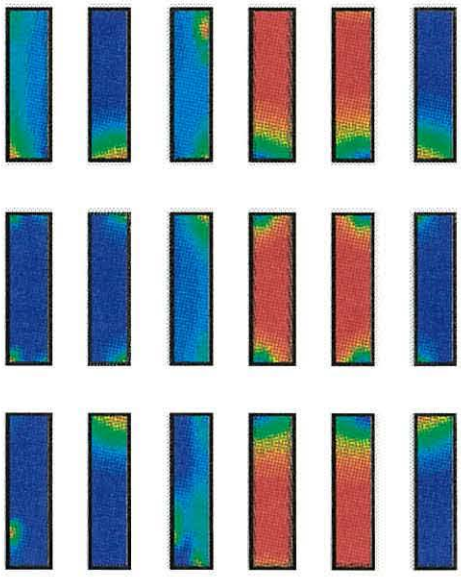

Figure 6.16: Magnetization plot for array at −290Oe

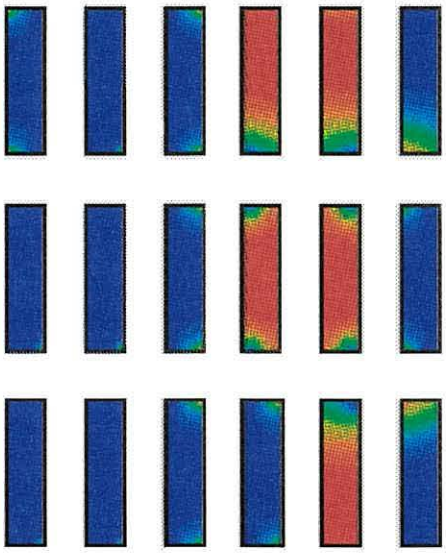

Figure 6.17: Magnetization plot for array at −305Oe

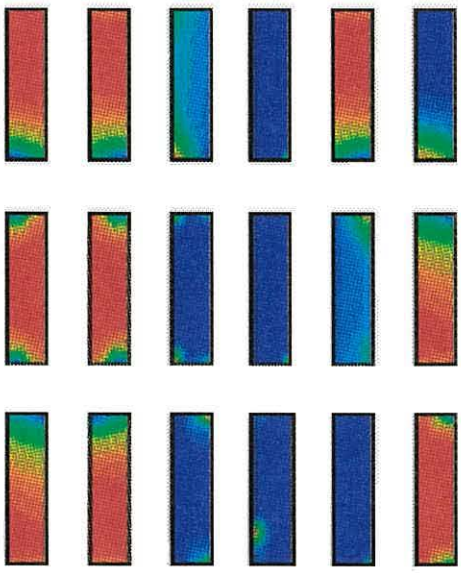

Figure 6.18: Magnetization plot for array at −290Oe with forced reversal

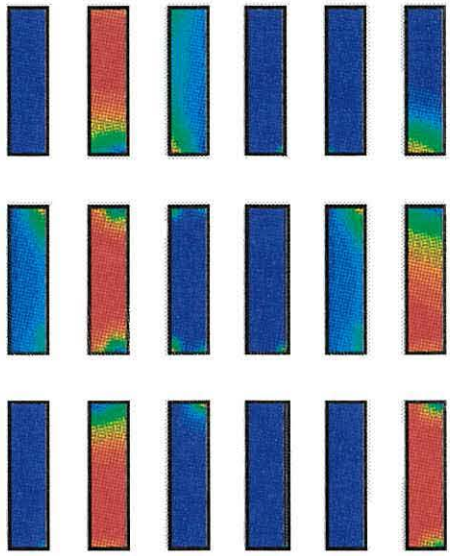

Figure 6.19: Magnetization plot for array at −305Oe with forced reversal

It was observed in [66] that magnetostatic interactions are dependent on the size and spacing of the nanoelements. So to investigate this observation we shall now consider rows and arrays of 300nm × 50nm nanoelements with an intra row spacing of 50nm and an inter row spacing of 100nm. The experimental results of Kirk *et al* [68] are shown in Figure 6.20. Here we observe a similar hysteresis curve to Figure 6.14. However, we notice a much higher coercivity which may be ascribed to the increase in elongation of the nanoelements and larger magnetostatic interaction effects within the rows as well as between the individual rows.

Our results are shown in Figure 6.21, here we also observe an increase in the system coercivity in agreement with the experimental results. Also our predicted switching field distribution was 335Oe this again is much lower than the experimental observation of 670Oe which was recorded in [69] and can be interpreted as implying that the experimental samples have a significant dispersion of intrinsic properties. Again the reversal mechanism is via a randomly ordered entire column process as is the case of the 300nm × 80nm nanoelements.

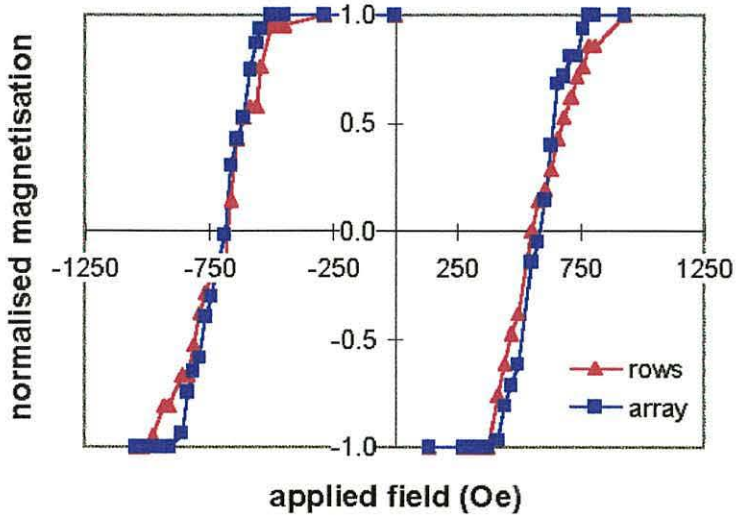

Figure 6.20: Experimental hysteresis curves for rows and arrays of 300nm × 50nm interacting nanoelements after Kirk *et al*

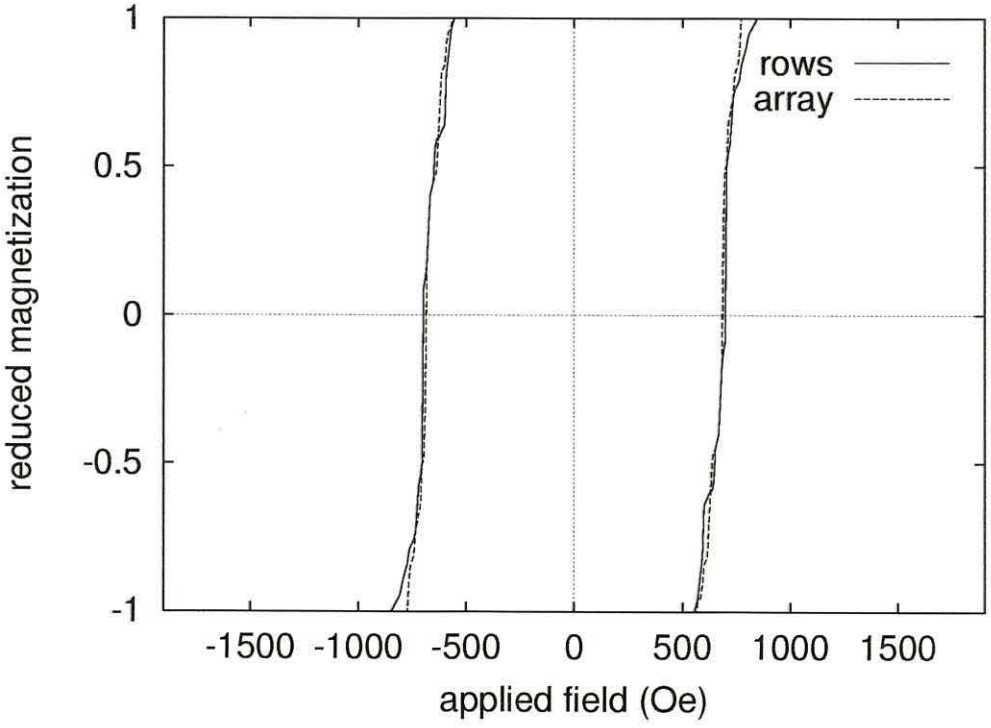

Figure 6.21: Theoretical hysteresis curves for rows and arrays of 300nm × 50nm interacting nanoelements

So far in this section we have investigated the behaviour of arrays of interacting nanoelements with a planar random anisotropy distribution to simulate to some extent the dispersion of the properties in the experimental samples. We have obtained good agreement between the experimental results and our predicted behaviour, however we shall now extend this investigation by considering new results on these array setups with the introduction of ordered anisotropy distributions. This is expected to influence the hysteresis behaviour and the reversal mechanism.

For the next simulations we shall use an ordered anisotropy distribution throughout the nanoelements, i.e. a transverse component of $K = 5 \times 10^3 \text{erg/cm}^3$ with the easy axis parallel to a direction going from the left to the right of the individual nanoelements.

We shall firstly consider the case of the 300nm $\times$ 80nm array and row setup. The results are shown in Figure 6.22 and were obtained under the same external field conditions as the previous hysteresis simulations. Here we see very large collective reversal events just before the system coercivity for both the rows and array. Although the coercivity still agrees with previous calculations. The reversal mechanism we have seen so far was via random columns of nanoelements switching. Here columns of reversed nanoelements are also observed, however in the individual rows of the array, alternately switched nanoelements are seen. The reason for whole columns of nanoelements switching in both cases of ordered and unordered anisotropy distributions may be explained by the strong magnetostatic interactions in the long axis direction forcing the nanoelements to switch together whereas the interactions in the short axis direction tend to stabilize neighboring nanoelements that have not switched.

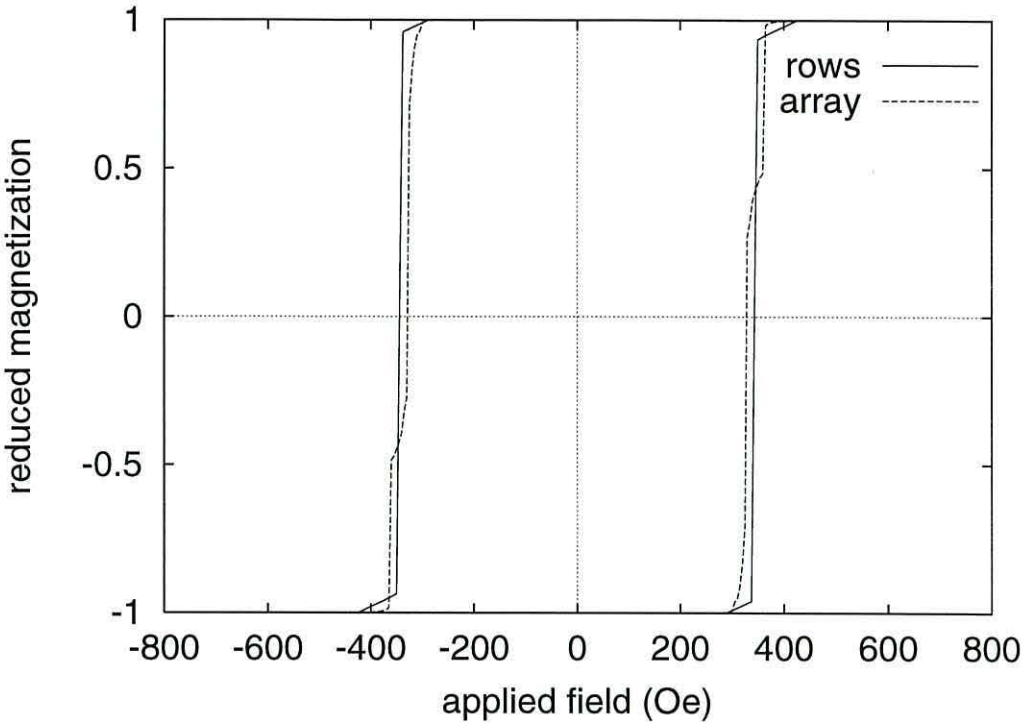

Figure 6.22: Theoretical hysteresis curves for rows and arrays of 300nm × 80nm interacting nanoelements

If we turn our attention to the magnetization plots in Figures 6.23 - 6.26 we can look at the reversal process in detail. In Figure 6.23 which was recorded at the beginning of the reversal we see very small interaction effects around the ends of the outer nanoelements. The reversal then starts by the two outer columns of nanoelements switching together as shown in Figure 6.24. The columns of reversed nanoelements then evolve towards the centre of the array as shown in Figure 6.25. The reversal here takes place via a collective motion which involves a high degree of symmetry. This mechanism was not present in the earlier results with the planar random anisotropy distribution. A similar collective reversal process is also observed in our single row simulations as shown in Figure 6.26.

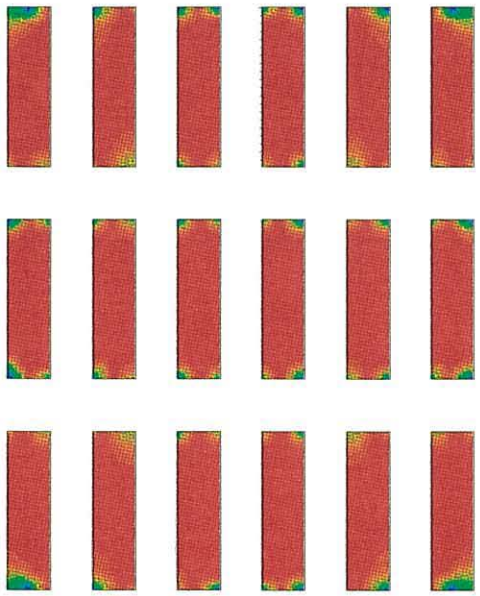

Figure 6.23: Magnetization plot for array at −295Oe

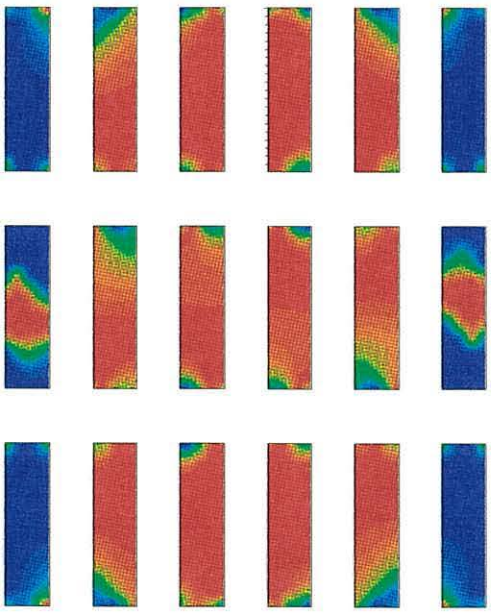

Figure 6.24: Magnetization plot for array at −305Oe

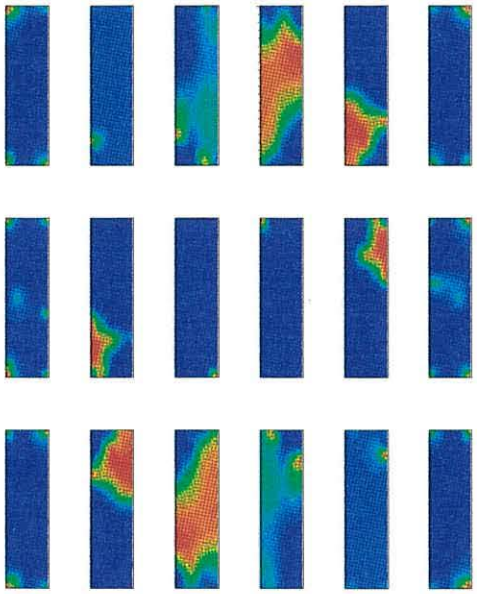

Figure 6.25: Magnetization plot for array at −325Oe

Figure 6.26: Magnetization plot for row at −347Oe

The next stage is to investigate the interaction effects by considering the case of 300nm × 50nm setups. Our results are shown in Figure 6.27. An interesting situation arises here as we observe that the reversal of the row is via a completely collective mechanism whereas the reversal in the array is by 3 large collective reversal events where batches of columns of nanoelements have switched. Our sim-

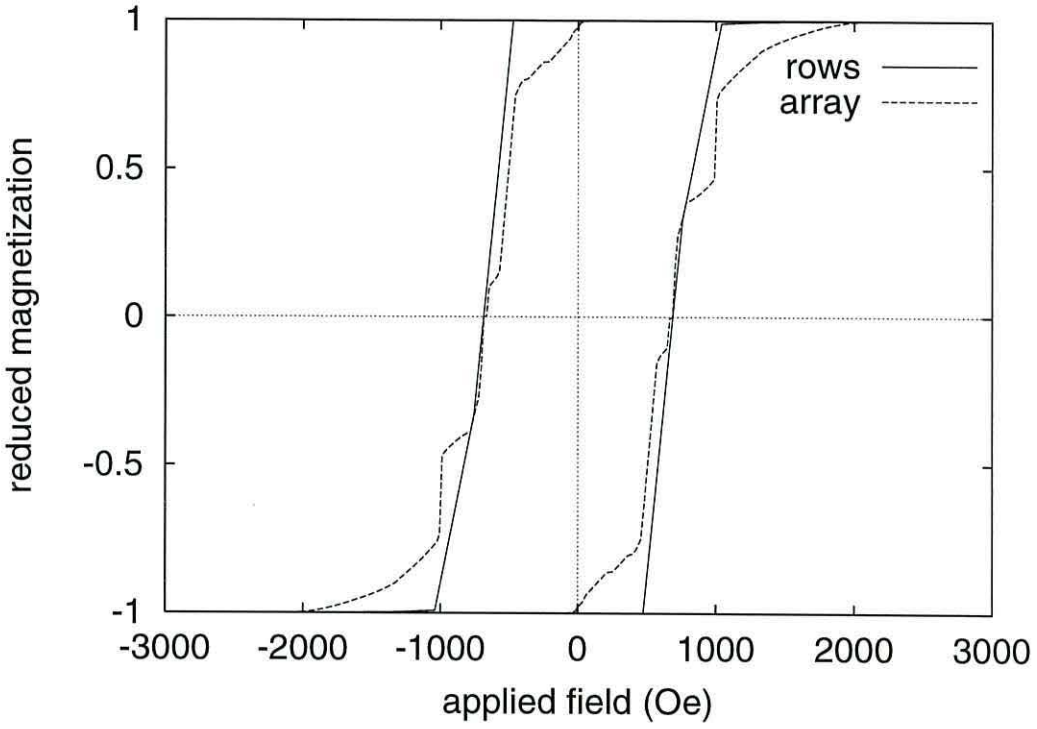

Figure 6.27: Theoretical hysteresis curves for rows and arrays of 300nm × 50nm interacting nanoelements

ulation again predicts an increase in system coercivity. This is due to an increase in demagnetizing effects due to the spacing which confirms the experimental observations in [68]. This process again occurs by entire columns of nanoelements reversing in a symmetrically collective manner. However, the reversal in this case is initiated from one column in from the ends of the array as shown in Figure 6.28. This effect is also observed in the single row case as shown in Figure 6.29.

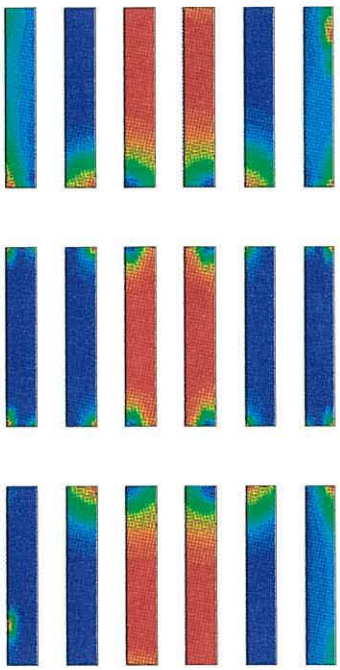

Figure 6.28: Magnetization plot for array at −800Oe

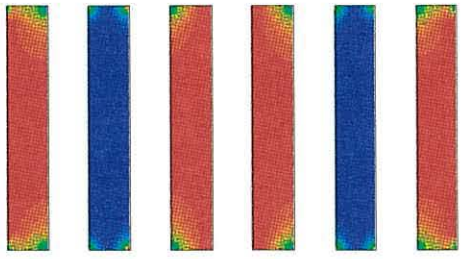

Figure 6.29: Magnetization plot for row at −600Oe

We can investigate the interactions in between rows of nanoelements in the array formations by decreasing the spacing in the longitudinal axis direction, the results are shown in Figure 6.30 for the 300nm × 80nm array and Figure 6.31 for the 300nm × 50nm array. In both cases we observe an increase in system coercivity when the inter row spacing is reduced from 100nm to 50nm. This is due to the interactions at the elements ends suppressing any stable intermediate magnetic states.

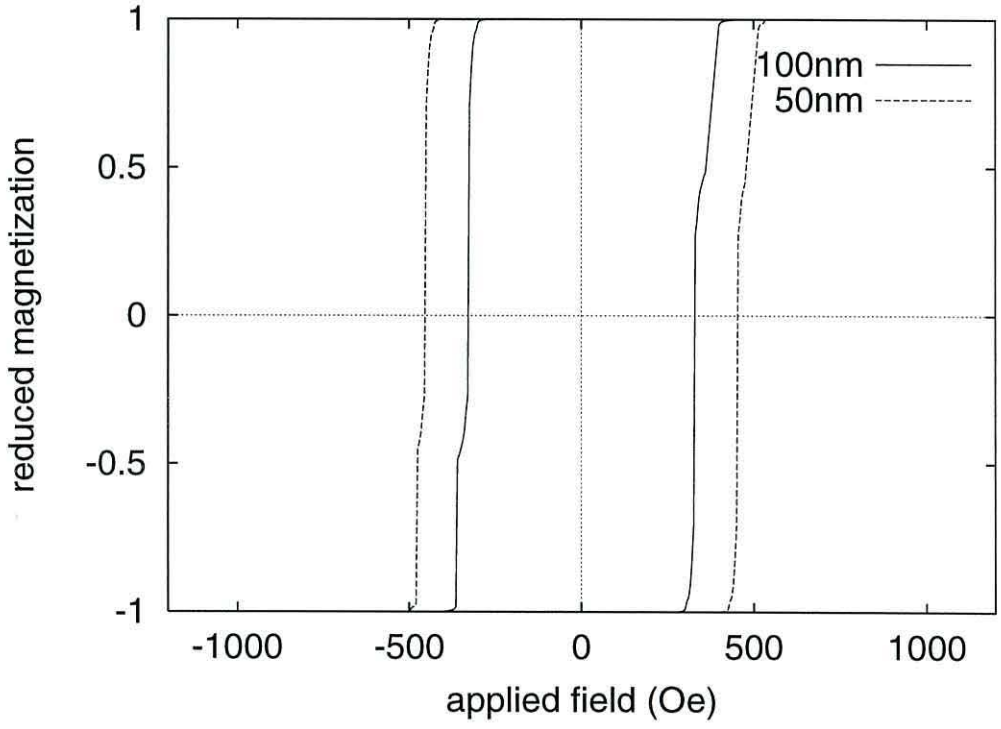

Figure 6.30: Comparison of inter row spacing for the 300nm × 80nm array

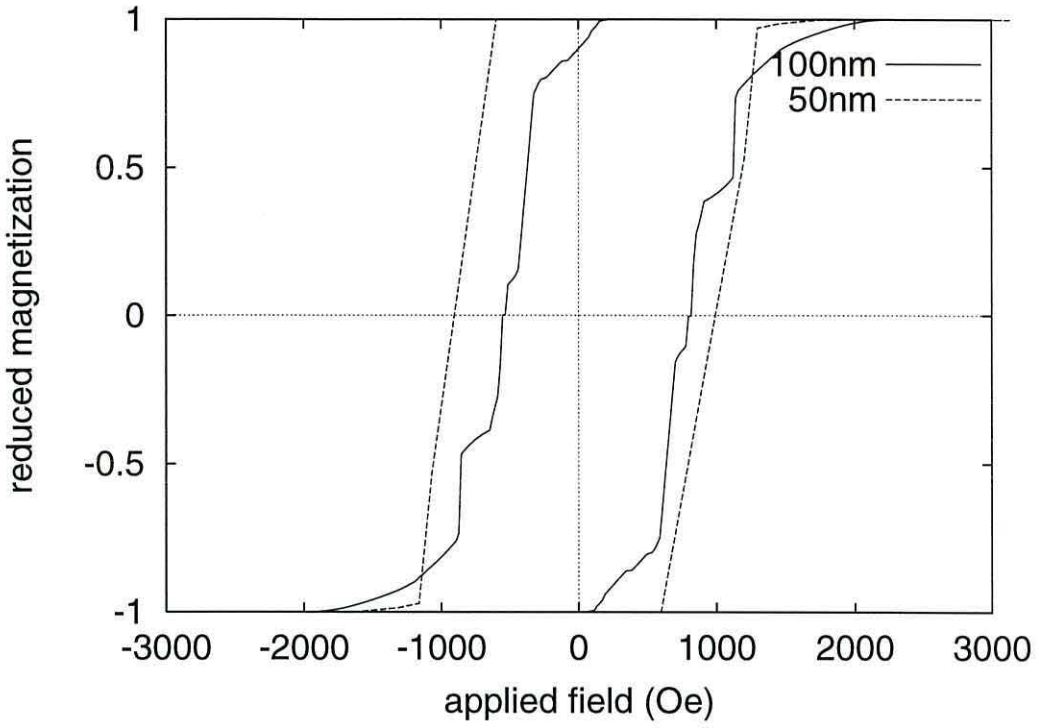

Figure 6.31: Comparison of inter row spacing for the 300nm × 50nm array

Now that we have looked at the effect of introducing an ordered anisotropy we shall now look at increasing the interaction effects along the longitudinal direction by changing the anisotropy direction to be longitudinal to the nanoelements with the easy axis parallel to a direction going from the botton to the top of each individual nanoelement. For the 300nm × 80nm array and rows our results are shown in Figure 6.32.

Again the reversal is by a symmetrically collective mechanism. However we notice that the introduction of the longitudinal anisotropy has initiated small jumps in the curves where intermediate magnetic states are stabilized. In the case of the 300nm × 50nm array and rows as shown in Figure 6.33 we see an increase in the system coercivity which was observed in our previous simulations and experimentally in [68]. However the stable intermediate magnetization states are not observed which is probably due to the increase in magnetostatic interactions and the elongation of the nanoelements.

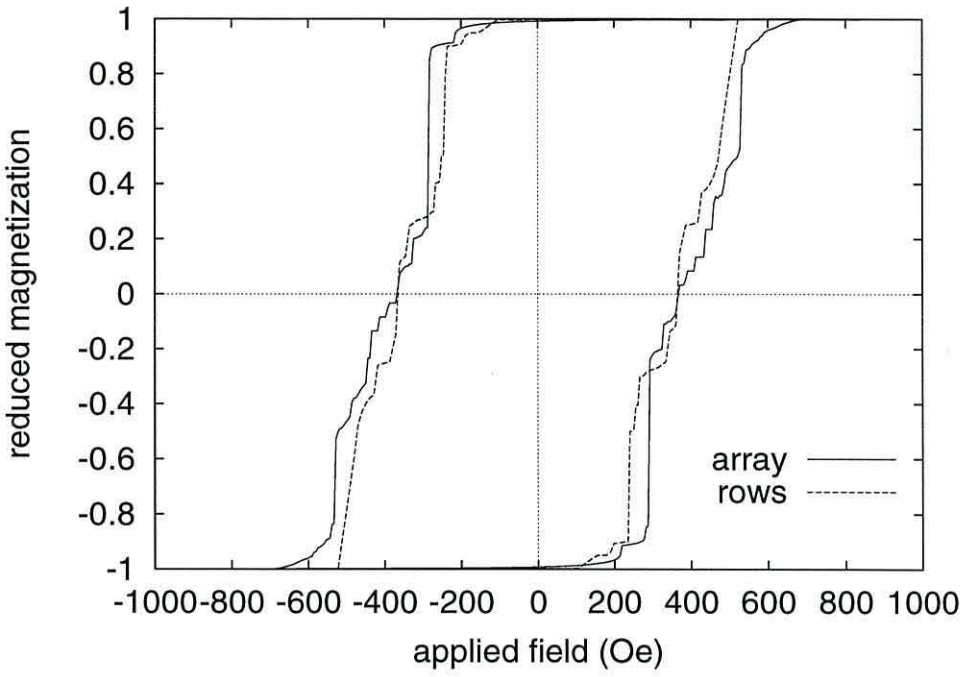

Figure 6.32: Theoretical hysteresis curves for rows and arrays of 300nm × 80nm interacting nanoelements

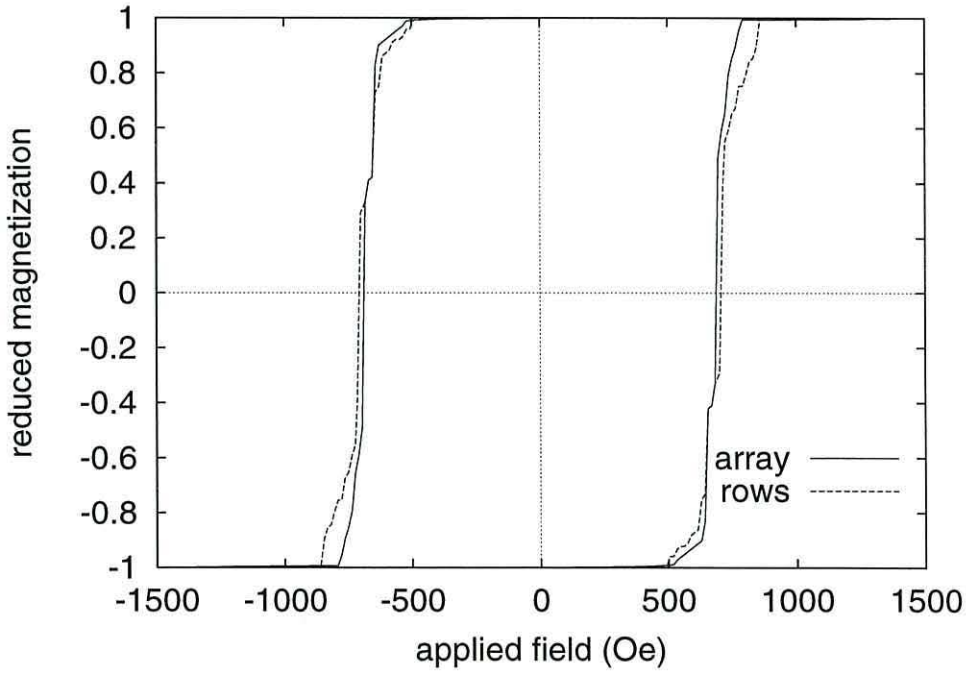

Figure 6.33: Theoretical hysteresis curves for rows and arrays of 300nm × 50nm interacting nanoelements

We shall now look at increasing the anisotropy contribution to the interaction effects. For this we shall introduce a longitudinal component of uniaxial anisotropy, $K = 5 \times 10^4 \text{erg/cm}^3$ with the easy axis parallel to a direction going from the botton to the top of the individual nanoelements. The results in Figure 6.34 show 3 large collective reversal events occurring due to batches of switching nanoelements. This process is driven by the magnetostatic interactions. Also the higher anisotropy is strong enough to stabilize the intermediate state - the combination of the alignment and strength of the anisotropy gives rise to the collective reversal and the stable intermediate magnetic states.

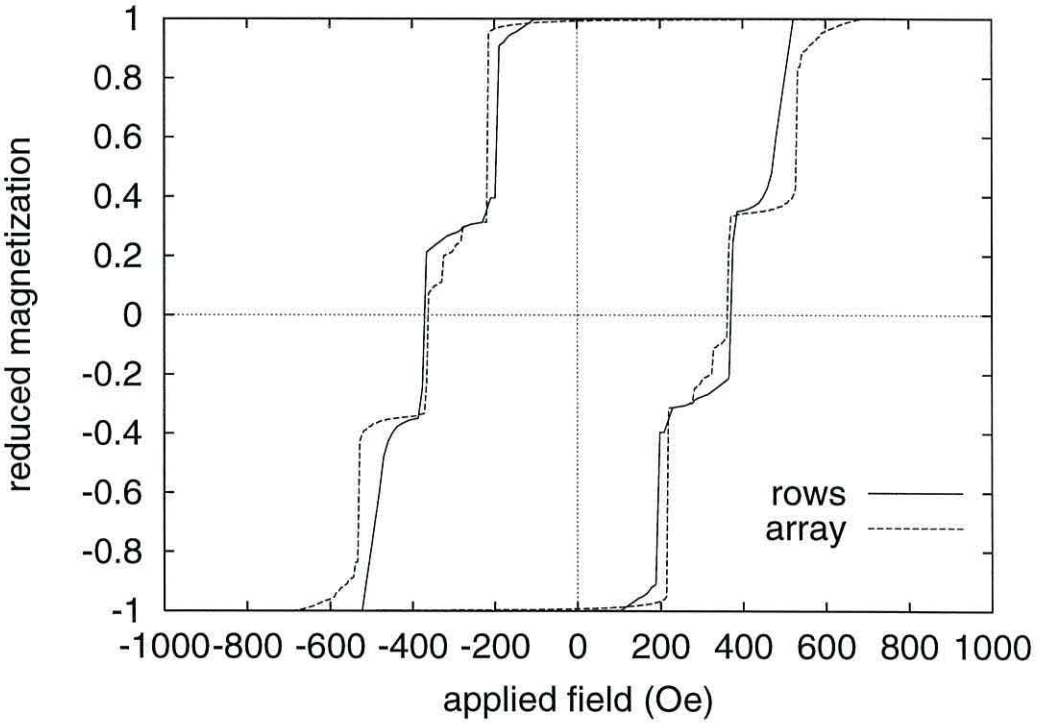

Figure 6.34: Theoretical hysteresis curves for rows and arrays of 300nm × 80nm interacting nanoelements

The next stage is to consider the case of 300nm × 50nm setups. Our results are shown in Figure 6.35. The neighbouring columns of nanoelements which switch

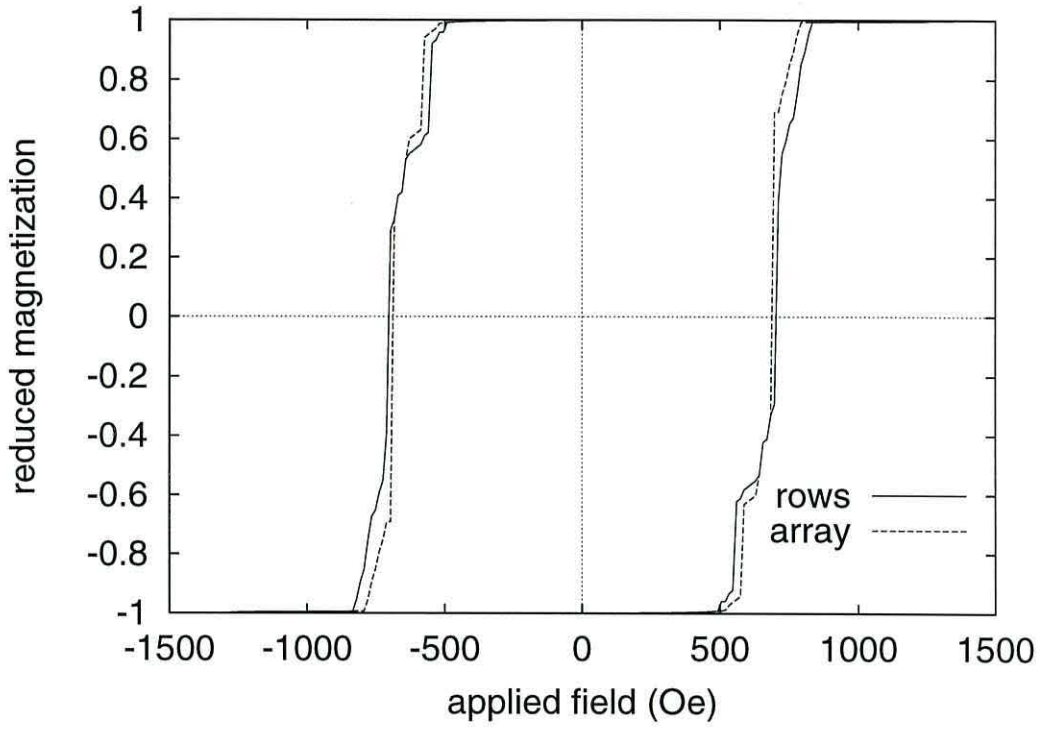

Figure 6.35: Theoretical hysteresis curves for rows and arrays of 300nm × 50nm interacting nanoelements

in our simulations may be explained by the longitudinal anisotropy which was not present in the experimental samples or in our earlier simulations. The anisotropy tends to keep the reversal symmetric about the centre of the array.

In both cases of size and spacing the magnetization reversal is initiated faster for rows than for the array, in agreement with previous findings. The computational results predict large collective reversal events during the decrease from the saturated state.

The theoretical predictions give good qualitative agreement with experiment and suggest that both interactions and variations in intrinsic properties contribute significantly to the system coercivity.

6.4 Summary

This chapter began with a brief introduction to the study of arrays of nanoelements and their possible application in future high density data storage. We introduced the idea of varying the space between individual nanoelements in order to look at their interaction effects.

The results we presented in Chapter 5 were all concerning non interacting nanoelements. These findings gave us a useful indication on the domain behaviour and hysteresis properties of the particles but we now needed to extend the capabilities of our model to be able to look at more than one nanoelement. We discussed the implications of this at the beginning of this chapter in terms of the increased demand on computational resources due to the extra number of finite elements needed. This is not however a major problem since we have already implemented sparse matrix storage and solver routines, however simulations will now require far more C.P.U. time.

Before producing any new results it was necessary to carry out a testing of the model for comparison with existing scientific work. This was performed by simulating existing results on 3 interacting nanoelements with longitudinal anisotropy. From the presence of this anisotropy we expected a 'large' scale domain structure to form as was observed in the experiments. Indeed our model produced similar results with a domain configuration that was symmetrical about the central nanoelement.

We then proceeded with further results on nanoelements with transverse material anisotropy. The reason for this was to be able to make comparison between the stabilization of the single domain state in single nanoelements as discussed in Chapter 5 against new results on arrays of three particles. Before discussing any results we gave a brief indication on the areas of the finite element mesh which required a high level of refinement, namely around the area between the nanoele-

ments.

We could then proceed in a discussion on the effects of the stabilization of the single domain state in the central nanoelement. We began this series of experiments by considering a nanoelement which we knew from our previous observations would fall into a multi domain configuration at remanence. As expected from experimental findings at small inter nanoelement spacing we observed a single domain configuration in the central nanoelement due to the very large magnetostatic interaction effects between particles. When we increased this spacing however, interactions became less prominent but nevertheless were still present.

So far we had not looked at the reversal mechanism of the arrays. Further investigation into this was carried out by looking at the time evolution of the reversal process and comparing with the non interacting case. In the case of the arrays we noticed that the domains formed in the outer nanoelements propagating from the two opposite ends to the particle centre. In the case of arrays where the nanoelements were spaced at intervals large enough to exhibit multi domain behaviour it was the central nanoelement which was the last to become multi domain.

To conclude the results on arrays of nanoelements we continued our studies by looking at the larger systems as already investigated in current experimental research. These systems consisted of single arrays of 6 interacting nanoelements and 18 nanoelements arranged in 6×3 arrays.

The reason for studying such systems is to investigate the effect of the nanoelement spacing between rows and columns on the system coercivity and magnetostatic interactions. We performed simulations on nanoelements of two different sizes and spacing for a direct comparison with the experimental results. From our simulations we saw an increase in the magnetostatic interaction effects when the spacing was decreased as predicted by the experiments.

The results also indicated that in both sizes of nanoelement the reversal was initiated faster in the rows than in the arrays. The reversal mechanism of the array as a whole is very sensitive to the degree of disorder. In the case of an aligned uniaxial anisotropy a highly symmetric cooperative switching mechanism is observed to take place. A large anisotropy has the effect of stablizing states during the reversal process leading to the distinctive switching. A random anisotropy breaks this high symmetry sufficiently to reduce the cooperative switching. This leads to a relatively random reversal of individual elements. Our theoretical observations gave good agreement with the experimental findings. However, the predicted Switching field distributions were narrow in comparison with experiment. In the case of the simulations the SFD essentially arises because of interaction effects and our predicted values indicate that interaction effects are small but significant, since they account for half of the width of the SFD. The discrepancy between the experimental and calculated SFD's probably suggests that there is a dispersion of the intrinsic element properties, which is not considered in the current model.

Throughout the last two chapters we have discussed the magnetization behaviour of both interacting and non interacting nanoelements. In the case of the single rectangular nanoelements we have studied their transition effects from multi domain to single domain behaviour. We have also looked at altering the geometry of the nanoelement and the effect this has on the stabilization of the single domain state in relation to particle dimensions. In the case of arrays of nanoelements we have investigated their domain behaviour in relation to their separation. At this point we may now conclude this work with a discussion on the context of this thesis in relation to magnetic recording in general and of course an overview of the limitations of our model and how these may be overcome by further work and development.

Chapter 7

Concluding remarks

It is quite noticeable that magnetic recording technology is a very dynamic area of scientific research. The heavy demands of the modern consumer audio and video market and the information storage requirements of both domestic and industrial computer users is the main driving force behind most of the current research in magnetism and magnetic materials. The aim is then to develop a recording process which gives the user the fastest access time coupled with the ability to store vast amounts of data on the smallest area of physical material.

To achieve an improved method of magnetic recording we must investigate the method of reading and writing data to the medium from the recording head and the magnetic properties of the recording media. The recording heads used in modern digital recording applications are predominantly the magnetic sensor and magneto optic type. For the head applications it is necessary to understand the properties of the material at the sub micron level, hence looking at the behaviour of nanoelements may be useful, especially in the development of the giant magnetoresistive type applications. Whatever recording medium we choose from the vast number of materials available we look for a high remanent magnetization to retain information after writing, high saturation magnetization to give a large signal during recording and a high coercivity to prevent unwanted loss of data.

The continuous media which is in production today is of a granular structure.

With each bit being represented by many individual grains. To keep the signal to noise ratio constant as the density increases the number of grains must remain approximately constant. Thus as we increase the storage density the grain size must become smaller. However, at some grain size the particles will become unstable to thermal fluctuations which will cause the particles to spontaneously reverse and thus make the medium unsuitable for information storage. One possible solution to this problem would be to use the nanoelement array type structures introduced in Chapter 6, with each nanoelement storing one bit of information.

During the past few years the everyday reliance on computers has continued to grow exponentially. As long as this continues, there will be work for the magnetic recording scientist as the need for efficient storage methods will remain.

This thesis is the result of a study into a specific type of recording media, namely that of the thin film permalloy nanostructured type. This has been carried out by developing a numerical model based on a theoretical micromagnetic approach. Indeed the functioning of this model itself depends upon the use of powerful modern computer resources. The interesting point here is that we need to utilize the facilities made possible by previous research into magnetic recording in order to improve the situation for the future. Also during the production of the scientific data presented in this work, the practical recording speeds and capacities have increased by at least 6 times.

For a realistic understanding of the behaviour of the magnetization process within a modern recording material, we must look at the sample at least at the microstructural level. This may be done experimentally by using methods such as electron beam lithography and other imaging techniques. The fact that some experimentally observed microstructures possess irregularity may cause problems with their theoretical study. We have overcome such difficulties in our work by implementing the finite element method within the micromagnetic model.

The practical implementation of such a method is not by any means a trivial matter as we discussed in Chapter 4. The high discretisation needed to mimic experimental results requires high capacity storage and processing facilities, this in itself led us to look at ways of reducing such costs within the solver, namely via the use of a sparse matrix solver routine. Also, since the magnetic material in question is of the thin film type, we have a physical and therefore mathematical justification for modelling the finite element field calculation in two dimensions since the variation in the out of plane component is minimal, this reduces computation even further.

To model the dynamics of the magnetization process we chose the Landau-Lifshitz equation of motion with an effective field having individual magnetostatic, exchange, anisotropic and external contributing components. Again we were faced with another numerical problem, solving a large number of coupled ordinary differential equations arising from the Landau-Lifshitz equation. To tackle this problem we looked at the use of suitable numerical time integration routines such as the Euler and predictor-corrector methods. We concluded that the use of the predictor-corrector scheme dealt with larger systems involving several nanoparticles more efficiently due to the ability to use larger time steps.

The micromagnetic simulations performed by our model are intended to give insight into the magnetization behaviour of very small magnetic particles at the sub micron level which are termed nanoelements. We have looked at different geometries and both single and interacting arrangements of particle system with varying size. The observed domain structures were found to be dependent upon these factors and on the dynamics of the magnetization process specifically. By this we mean that the final equilibrium configuration is also dependent upon the initial magnetization distribution and whether or not equilibrium was obtained with gradual or instantaneous removal of an applied external field.

Further work which would be interesting would be to investigate the dynamics

and rate of convergence of the magnetization process as a result of varying the value of the damping constant before the dissipative term in the Landau-Lifshitz equation. Also we could compare results with the use of the Gilbert form of the equation of motion.

The results presented in Chapters 5 and 6 illustrate the non uniform magnetization structures obtained from simulations on thin film permalloy. For this particular type of recording media we can justify the efficiency of our model in terms of mathematical accuracy and computational requirements. Our finite element calculation is an efficient approach to the problem since the magnetization dynamics is modelled in three dimensions by the Landau-Lifshitz equation of motion. However for a material with a large enough third dimension to require the modelling of domain structures in this dimension we recognize the limitation of our model in terms of the two dimensional demagnetizing field calculation.

For a complete generalization of the model to a true three dimensional simulation would not be a trivial task by any means and would be the subject of future work. We could implement this by using tetrahedral finite elements which would then enable us to make a more direct comparison of our results against the methods used in [70] and [22] or more recently the general dynamical approach (GDM) by Yang and Fredkin [71].

Another possible improvement to the model would be to adopt a strategy of adaptive mesh refinement. This approach could use the refinement indicators for the exchange and magnetostatic forces as used by Tako *et al* [18] to locate areas within the mesh where rapid changes in the magnetization are occurring. A suitable refinement algorithm would then be used to increase the number of elements around these areas. The subject of adaptive finite element mesh strategies on soft magnetic platelet calculations is described in depth in [72] by a comparison of two different methods to adaptively refine tetrahedral finite element meshes.

To complete the refinement strategy we would certainly also need de-refinement of the mesh to decrease computational needs when the magnetization is quite uniform such as when the nanoelement is under the influence of a high external field. However the process of refinement and de-refinement of the mesh would itself put great strains on the computational resources in terms of memory and processing time. This was approached by Tako *et al* by only using the refinement procedure on remanent magnetization states. More recently, an advanced method of mesh refinement has been successfully implemented by Schrefl *et al* [73] to model domain wall motion in Co thin films. The refinement indicator in this method is based on the local variation of the magnetization which causes refinement in areas of high variation and de-refinement where the magnetization is uniform. This gives a moving mesh algorithm which enables the mesh to move with the domain wall. The implementation of this algorithm in our model would definitely be useful in decreasing computation and increasing accuracy.

On the numerical side of the field calculation further investigation into the accuracy of the solution would be another improvement to the model. We discussed at the beginning of Chapter 5 that as we refine the mesh finite element nodes become located closer to the interface and are therefore a possible source of error. To overcome this problem we would need to look at alternative numerical methods for calculating field values at these points. One such strategy would be to implement a method of self-adaptive wavelets for the calculation of this field. This would certainly provide grounding for interesting further research work.

Another important area for future work within the finite element formalism is that concerned with the calculation of the exchange field. In Chapter 3 we gave our formalism in terms of a discrete approximation to the exchange energy integral, this however could be improved by the use of an implicit finite element approach. Whereby the standard energy integral expression is bought into the minimization routine via the use of the interpolation functions. This variational approach has already been implemented in [71]. However, this model requires a larger amount

of computational resources in terms of processor time and storage in memory than our existing model.

The way forward for this model would be motivated by the constant need for future high density magnetic storage media. The scope for numerical improvement and the development of our own finite element GDM in micromagnetics would also be the subject of future developments. A theoretical study of periodic magnetic nanostructures such as those studied by electron beam lithography methods [74] would then be an interesting challenge for the model.

Other consideration for further development to our model would be the inclusion of thermal activation. This could be implemented in a similar way to that described in [41], the only complication arising from this would be that we could no longer use our existing predictor-corrector method however this could easily be overcome by the use of a similar method.

Recent calculations on the effect of surface anisotropy [75] in calculations of nucleation fields in small ferromagnetic particles suggest that this term should not be neglected in theoretical simulations. However further investigation in determining the values of the surface anisotropy constant K_s still needs to be carried out.

Further studies of the magnetostatic interaction effects should also be performed on the larger arrays of nanoelement it is possible that the theory may shed further light on the behaviour of such systems and therefore offer enormous practical advantages to the study of future high density storage. With our current model we have given some initial predictions on this work, however to simulate certain experimental findings we would need to consider the intrinsic properties of each individual nanoelement separately.

In Chapter 6 the predicted Switching field distributions were narrow in comparison with experiment. In our simulations the SFD essentially arises because of inter-

action effects and our predicted values indicated that interaction effects are small but significant. The discrepancy between the experimental and calculated SFD's probably suggests that there was a dispersion of the intrinsic element properties. Our current model could be adapted to take account of this by introducing some random variation in the properties of each individual nanoelement in the array.

To summarize, the starting point for the improvement of our model would be to make the demagnetizing field calculation three dimensional. We could then minimize the computation by implementing a mesh refinement algorithm. To increase the numerical accuracy of the exchange field calculation we could implement a variational approach to the entire problem. Finally to model the experimental observations more realistically we could bring thermal effects, surface anisotropy and varying intrinsic material properties into our model.

Appendix A

Integrating products of area coordinates over an element

We wish to find an expression for

$$I = \int_A L_1^m L_2^n L_3^p dxdy \tag{A.1}$$

Since $L_1 + L_2 + L_3 = 1$ we may rewrite I as

$$I = \int_A L_1^m L_2^n (1 - L_1 - L_2)^p dxdy \tag{A.2}$$

Referring to equations (2.28) - (2.29) we may say that

$$\begin{aligned} dxdy &= \begin{vmatrix} x_1 - x_3 & x_2 - x_3 \\ y_1 - y_3 & y_2 - y_3 \end{vmatrix} dL_1 dL_2 \\ &= 2A dL_1 dL_2 \end{aligned} \tag{A.3}$$

Hence

$$I = 2A \int_0^1 L_1^m dL_1 \int_0^{1-L_1} L_2^n (1 - L_1 - L_2)^p dL_2 \tag{A.4}$$

If we consider

$$\begin{aligned} I(a,b) &= \int_0^\alpha t^a (\alpha - t)^b dt \\ &= \left[\frac{t^{a+1}}{a+1} (\alpha - t)^b \right]_{t=0}^{t=\alpha} + \frac{b}{a+1} \int_0^\alpha t^{a+1} (\alpha - t)^{b-1} dt \\ &= \frac{b}{a+1} I(a+1, b-1) \end{aligned} \tag{A.5}$$

Hence

$$\begin{aligned} I(a,b) &= \frac{b(b-1)(b-2)...(2)(1)}{(a+1)(a+2)(a+3)...(a+b)} I(a+b,0) \\ &= \frac{a!b!}{(a+b)!} I(a+b,0) \end{aligned} \tag{A.6}$$

Now

$$\begin{aligned} I(a+b,0) &= \int_0^\alpha t^{a+b} dt \\ &= \frac{\alpha^{a+b+1}}{a+b+1} \end{aligned} \tag{A.7}$$

so that

$$I(a,b) = \frac{a!b!}{(a+b+1)!} \alpha^{a+b+1} \tag{A.8}$$

Therefore

$$\begin{aligned} I &= \frac{2An!p!}{(n+p+1)!} \int_0^1 L_1^m (1-L_1)^{n+p+1} dL_1 \\ &= \frac{2An!p!}{(n+p+1)!} \frac{m!(n+p+1)!}{(m+(n+p+1)+1)!} \\ &= \frac{2Am!n!p!}{(m+n+p+2)!} \end{aligned} \tag{A.9}$$

Appendix B

Use of the mesh generation software "Triangle"

B.1 Introduction

The finite element meshes used in this work were all created with the use of the two-dimensional quality mesh generator and Delaunay triangulator, "Triangle". We will now give a brief mention on its practical usage and implementation within our work.

Before deciding to use "Triangle", we tested other mesh generators which were both freely and commercially available but chose to use "Triangle" because of its ease of use in creating meshes involving two regions where one is inside the other.

To create a finite element mesh we must first present "Triangle" with an input file containing details in the form of a Planar Straight Line Graph (PSLG). This is simply a data file containing a collection of points, line segments and their connectivity. Segments are simply edges, whose endpoints are points in the PSLG. The conventional file format for PSLGs is .poly files. For our application .poly files will define the location of the nanoelements and the extent of initial discretisation, this will consist of an outline of the nanoelement geometries and the artificial boundary which surrounds them.

Typically a .poly file will be

- First line : number of points, dimension (must be 2), number of attributes, number of boundary markers (0 or 1)
- Following lines : node number, x, y, attributes, boundary marker
- One line : number of segments, number of boundary markers (0 or 1)
- Following lines : segment, endpoint, endpoint, boundary marker

The first line is used to define the number of nodes, boundary markers and their attributes, after this the following lines will define the location of a particular node, whether it is on a boundary or not and its attributes which may be the initial value of the magnetisation at that point. After this we need to define the geometry of the nanoelements which is done in the remaining lines where we say how certain nodes are connected in terms of boundaries (nanoelements).

Let us denote the PSLG file as fname.poly, then to create a desired mesh we may now call "Triangle" by

triangle -pq fname.poly

Where the p switch prompts "Triangle" to read a .poly file and the q switch generates a constrained conforming Delaunay triangulation from the given data. This ensures that there are no small angles, and is thus suitable for finite element analysis. A wide variety of command line switches are catered for by "Triangle" enabling such features as mesh refinement, boundary marking, area tolerances and angle tolerances.

At this stage "Triangle" will have generated .node and .ele files containing details of the mesh topology with respect to nodal coordinates and finite elements respectively.

The .node file will consist of

- First line : number of points, dimension (must be 2), number of attributes, number of boundary markers (0 or 1)
- Remaining lines : node number, x, y, attributes, boundary marker

This file will define the nodal coordinates of the output mesh. The other file needed to completely define the mesh consists of

- First line : number of elements, number of points per element, number of attributes
- Remaining lines : element number, point 1, point 2, point 3 ..., attributes

Points are indices into the corresponding .node file. The first three points are the corners, and are listed in counterclockwise order around each triangular element. (The remaining points, if any, depend on the type of finite element used.) The attributes are just like those of .node files. If however when we wish to proceed to higher order finite elements i.e. quadratic, we must issue the command

triangle -pqo2 fname.poly

which tells "Triangle" to generate the mesh topology for a quadratic finite element mesh. In this case the .ele file, all elements have six points each with the fourth, fifth, and sixth points being on the midpoints of the edges opposite the first, second, and third corners. Both the .node and .ele files together define a finite element mesh which is now ready for use in our code.

"Triangle" is distributed freely at [37] and comes with an additional program "Show Me". The main purpose of "Show Me" is to display meshes on the screen or in PostScript format. It also serves as a checking routine for the input files such as fname.poly.

Appendix C

Publications

Most of the work presented in this thesis has been published as papers in several scientific journals. The papers have been presented at conferences on magnetism either as talks or poster presentations. At the time of writing this thesis not all have been published, however the following lists them in chronological order.

- **Finite element modelling of nanoelements**
  P. H. W. Ridley, G. W. Roberts, M. A. Wongsam, R. W. Chantrell
  J. Magn. Magn. Mater., vol. 193, 1999, 423-426

- **Modelling the evolution of domains in nanoelements using finite elements**
  P. H. W. Ridley, G. W. Roberts, M. A. Wongsam, R. W. Chantrell, J. Gore and M. Maylin
  IEEE Trans. Magn., vol. 35(5), 1999, 3874-3876

- **Investigation of magnetisation behaviour in nanoelements using the finite element method**
  P. H. W. Ridley, G. W. Roberts and R. W. Chantrell
  J. Appl. Phys., vol. 87(9), 2000, 5523-5525

- **Computational and experimental micromagnetics of arrays of 2-d platelets**
  P. H. W. Ridley, K. J. Kirk, G. W. Roberts, R. W. Chantrell and J. N. Chapman
  IEEE Trans. Magn., to be published

ELSEVIER

Journal of Magnetism and Magnetic Materials 193 (1999) 423–426

Journal of magnetism and magnetic materials

Finite element modelling of nanoelements

P.H.W. Ridley[a,*], G.W. Roberts[b], M.A. Wongsam[a], R.W. Chantrell[a]

[a]*SEECS, University of Wales Bangor, Dean Street, Bangor Gwynedd LL57 1UT, UK*
[b]*School of Mathematics, University of Wales Bangor, Dean Street, Bangor, Gwynedd LL57 1UT, UK*

Abstract

The numerical simulation of the magnetisation structure of two-dimensional permalloy nanoelements is described. The nanoelements have a uniform magnetisation structure and consist of bars with flat and/or pointed ends. The Landau–Lifschitz–Gilbert equation of motion is used to described the time evolution of the system and the numerical simulation consists of a finite element spatial discretisation coupled with a time-stepping scheme. The Poisson equation for the demagnetising field scalar potential ϕ is solved by a standard finite element variational or stationary functional formulation. The jump condition in $\nabla\phi$ at a nanoelement boundary is integrated into the finite element formulation so that ϕ is obtained globally, both inside and outside the nanoelement, thus allowing interactions between two or more nanoelements to be modelled easily. The work will be compared to previously published experimental and numerical results for single nanoelements.

Keywords: Micromagnetics; Field calculations; Finite element method; Permalloy

1. Introduction

The interest in the magnetic behaviour of permalloy material has increased recently due to advances in numerical micromagnetic methods on the theoretical side and high accuracy electron-beam lithography methods experimentally. The great practical uses of such materials include magnetic sensors. When the material is discretised into a nano-element structure of small enough dimensions, micromagnetic calculations may be carried out in order to investigate the material behaviour.

Previous work has been done experimentally by M. Rührig and coworkers [1], who investigated the magnetic microstructure and switching behaviour of high-resolution electron beam fabricated thin film tips using transmission electron microscope techniques. Smyth and coworkers [2] investigated the effect of particle size and aspect ratio on hysteresis behaviour in arrays of particles by using experimental and numerical techniques to carry out their work and make comparisons between methods where applicable. More recently, Schrefl and coworkers [3] investigated the influence of the width and shape of the ends of nano-elements on the formation and structure of domains in NiFe bars, also involving two alternative numerical techniques in magnetostatics, namely the use of spatial transformations and a hybrid finite element/boundary element technique.

2. Micromagnetic model description

The total effective field in any realistic theory of magnetisation dynamics is made up of the three energy terms exchange, anisotropy and magnetostatic. In our simulations we denote the total effective field by $\boldsymbol{H}_t$, working in reduced units, the total reduced effective field, $\boldsymbol{h}_t = \boldsymbol{H}_t/H_k$ is given by $\boldsymbol{h}_t = \boldsymbol{h}_d + \boldsymbol{h}_{ex} + \boldsymbol{h}_a$, where $\boldsymbol{h}_d$, $\boldsymbol{h}_{ex}$ and $\boldsymbol{h}_a$ represent the reduced demagnetising, exchange and anisotropy field terms, respectively. $\boldsymbol{H}_k = 2K/M_s$ is the magnetocrystalline anisotropy field, M_s is the saturation magnetisation and K is the uniaxial anisotropy

* Corresponding author. Tel.: + 44-1248-382739; fax: + 44-1248-361429; e-mail: phil@sees.bangor.ac.uk.

0304-8853/99/$ – see front matter
PII: S0304-8853(98)00467-3

constant. The governing equation for the magnetisation dynamics may be chosen from either the Landau–Lifschitz equation of motion or the alternative Gilbert form [4] depending upon the system damping. We chose the Landau–Lifschitz form given by

$$\frac{d\boldsymbol{m}}{d\tau} = -\boldsymbol{m}\times\boldsymbol{h}_t - \alpha(\boldsymbol{m}\times(\boldsymbol{m}\times\boldsymbol{h}_t)), \tag{1}$$

where $\boldsymbol{m} = \boldsymbol{M}/M_s$ is the reduced magnetisation, $\alpha = \lambda/\gamma$ is the reduced damping constant and $\tau = t\gamma H_k$ is the reduced time. λ is the damping constant and γ the gyromagnetic ratio. The system equations which are coupled through the components of $\boldsymbol{m}$, arising from (1) are solved by an explicit Euler method, using a suitably small time step, with a convergence criterion for steady state stability of $|d\boldsymbol{m}/d\tau| < 10^{-6}$.

2.1. Field formulation

The demagnetising field is calculated via a magnetic scalar potential [4], such that $\boldsymbol{H}_d = -\nabla\phi$ where ϕ is the solution to Poisson's equation within the magnetic region Ω_{int} and Laplace's equation everywhere outside Ω_{ext}; so we have

$$\nabla^2\phi_{int} = 4\pi\nabla\cdot\boldsymbol{M} \quad \forall\boldsymbol{x}\in\Omega_{int} \tag{2}$$

$$\nabla^2\phi_{ext} = 0 \quad \forall\boldsymbol{x}\in\Omega_{ext} \tag{3}$$

where $\Omega_{int}\cup\Omega_{ext} = \varepsilon^2$, Ω_{int} is the magnetic region, Ω_{ext} is the external region, $\partial\Omega$ is the boundary between Ω_{int} and Ω_{ext}.

Because of the abrupt change in material properties across $\partial\Omega$ we have the interface condition

$$\frac{\partial\phi_{int}}{\partial n} - \frac{\partial\phi_{ext}}{\partial n} = 4\pi\boldsymbol{M}\cdot\hat{n} \quad \forall\boldsymbol{x}\in\partial\Omega \tag{4}$$

and continuity condition

$$\phi_{int} = \phi_{ext} \quad \forall\boldsymbol{x}\in\partial\Omega, \tag{5}$$

where $\hat{n}$ is the unit normal to the surface in question. Eqs. (3)–(5) define an open boundary problem, and have been solved by several authors in different ways. Since it was first applied to a micromagnetics problem in 1987 [5], the finite element method (FEM) and boundary element method (BEM) has been used.

Alternative methods include integro differential equations [6], and spatial transformations [7]. These methods formulate the problem for the magnetic material only and so avoid the need to introduce any artificial boundary conditions. Fredkin and Koehler [8] formulated the potential as $\phi = \phi_1 + \phi_2$, where ϕ_1 is the solution to Poisson's equation within the magnetic region subject to a natural boundary condition, which may be solved by the FEM, ϕ_2 is solved by a boundary integral along the magnetic material boundary. We present a new method for finding ϕ by the use of the FEM. The essence of the method is to replace the open boundary by a suitably large closed boundary $\partial\Re$ which is far enough away from the magnetic region Ω_{int} and enclosing Ω_{ext}. As with any FEM solution, a suitable transformation method is used to map each element to a simple parent element in order to simplify the integration over the whole region. We then apply a standard Rayleigh–Ritz stationary functional method which leads up to the formation of a system of n linear equations, where n is the number of nodes in the spatial discretisation scheme. Interface condition (4) is integrated into the linear equations by replacing any row number which corresponds to a node on $\partial\Omega$ by formulating explicitly the jump condition in terms of the transformations. Then by performing an LU decomposition on the stiffness matrix, ϕ may be obtained by matrix multiplication (this is to reduce the computation at each time step, provided no re-meshing is involved). Thus $\boldsymbol{h}_d$ may be obtained globally, a significant advantage over previous methods since we now have the capability of considering interactions between nano-elements.

3. Results and discussion

It is well known that a high proportion of the computational requirement of any simulation in micromagnetics is taken up by the demagnetising field calculation, so our initial studies used linear finite elements because of potential CPU limitations. However, linear elements were found unsuitable for our method, even after intensive mesh refinement in areas of great spatial variation.

Table 1
Relative error in $\boldsymbol{h}_d$ compared with the analytical solution

Nodes (Ω_{int} + Ω_{ext})	Elements (Ω_{int} + Ω_{ext})	Point 1	Point 2	Point 3
839 + 416	342 + 278	3.9×10^{-2}	4.5×10^{-2}	1.8×10^{-1}
1287 + 864	790 + 278	3.4×10^{-2}	4.2×10^{-2}	1.0×10^{-1}
2217 + 1472	1326 + 512	3.3×10^{-2}	2.4×10^{-2}	5.5×10^{-2}
3033 + 2288	2142 + 512	3.2×10^{-2}	1.9×10^{-2}	3.6×10^{-2}

This was found to be due to the enforcing of continuity in ϕ and the interface condition (4) along $\partial\Omega$. This problem was resolved by the use of quadratic finite elements. Table 1 gives results for the relative error in the demagnetising field for a single rectangular nano-element of dimensions 0.2 μm × 1.6 μm with a uniform magnetisation distribution parallel to the length of the nano-element. These calculations give the error relative to the analytical solution for a rectangular magnetic region given by Aharoni [8], with point 1 close to corner, point 2 further in from corner, point 3 edge of centre of nano-element. The solution was also used to evaluate a refinement indicator for $\boldsymbol{h}_d$ [9]

$$\eta_i^d = \frac{[(\nabla \times \boldsymbol{h}_d)^2 + (\nabla \cdot \boldsymbol{h}_d)^2]A_i}{\sum_{j=1}^{N} \|\boldsymbol{h}_s\|^2}, \tag{6}$$

where A_i denotes the area of element i and $\|\boldsymbol{h}_s\|$ is the value of $\|\boldsymbol{h}_d\|$ computed at the element centre. Previously (6) has been used to define areas of the simulations where refinement of the mesh was required. However, the refinement indicator does not represent a direct calculation of the error in the field calculation. Fig. 1 shows the calculated error relative to the analytical solution. It seems reasonable the errors are largest at the end of the element, where the field is most non-uniform. This situation is reflected in the refinement indicator, shown in Fig. 2, which essentially defines the area of largest error for mesh refinement.

Once the stiffness matrix has been inverted the calculation of the field at each time step is computationally fast. We have tested our method by calculating the time evolution of the magnetisation of a saturated element in zero field, for comparison with the work of Schrefl et al. [3]. The images in Fig. 3 show the time evolution of the magnetisation of a 0.2 μm × 1.6 μm infinitely thin permalloy platelet with a transverse anisotropy of 5×10^5 erg/cm^3. The evolution of the domain structure into zero field equilibrium state is consistent with that of Schrefl et al.

Acknowledgements

The author wishes to acknowledge Jonathan Richard Shewchuk of School of Computer Science/Carnegie Mellon University, 5000 Forbes Avenue/Pittsburgh, Pennsylvania 15213-3891 for the use of the Two-Dimensional Quality Mesh Generator and Delaunay Triangulator (Version 1.3) in these simulations. The financial support of EPSRC is gratefully acknowledged.

Fig. 1. Plot of relative error in $\boldsymbol{h}_d$ compared with the analytical solution for a 0.2 μm × 1.6 μm nano-element.

Fig. 2. Plot of relative error in $\boldsymbol{h}_d$ compared with the refinement indicator η_i^d for a 0.2 μm × 1.6 μm nano-element.

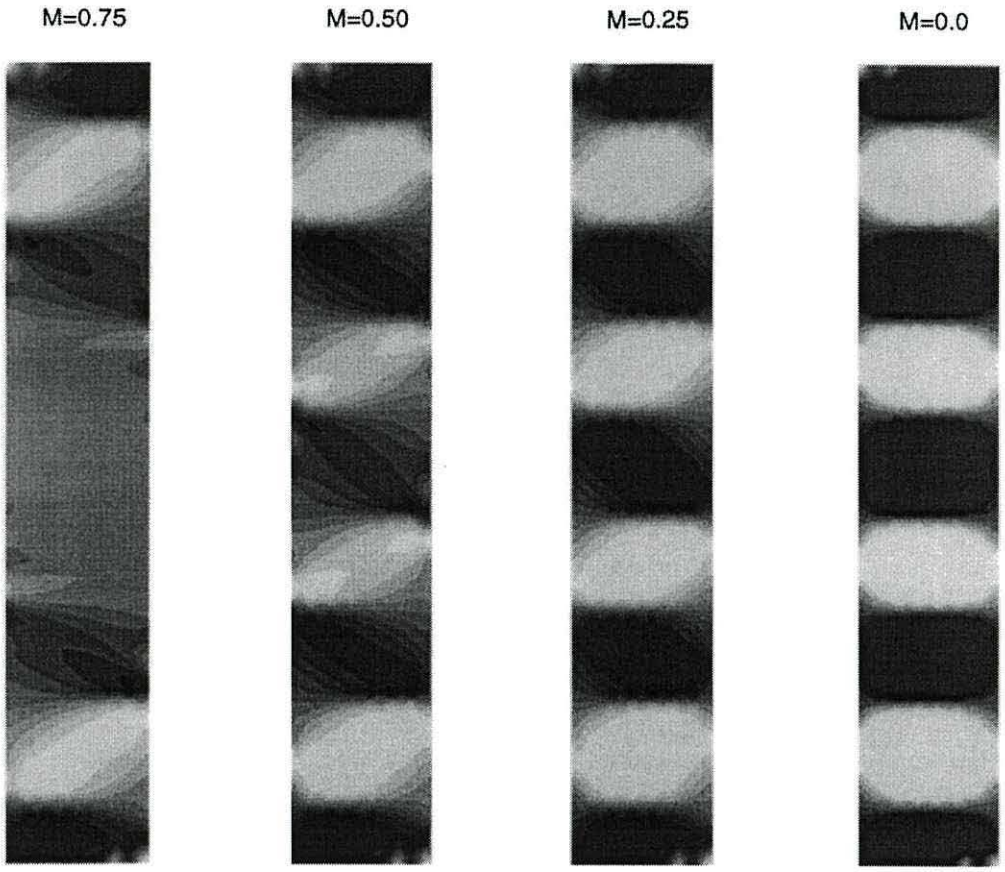

Fig. 3. Time series of magnetic domain patterns for a single 0.2 μm × 1.6 μm nano-element.

References

[1] M. Rührig, S. Porthun, J.C. Lodder, S. McVitie, L.J. Heyderman, A.B. Johnston, J.N. Chapman, J. Appl. Phys. 79 (1996) 2913.
[2] J.F. Smyth, S. Schulz, D.R. Fredkin, D.P. Kern, S.A. Rishton, H. Schmid, M. Cali, T.R. Koehler, J. Appl. Phys. 69 (1991) 5262.
[3] T. Schrefl, J. Fidler, K.J. Kirk, J.N. Chapman, IEEE Trans. Magn. 33 (1997) 4182.
[4] J.C. Mallinson, IEEE Trans. Magn. 23 (4) (1987) 2003.
[5] D.R. Fredkin, T.R. Koehler, IEEE Trans. Magn. 23 (5) (1987) 3385.
[6] A.G. Kalimov, M.L. Svedentsov, IEEE Trans. Magn. 32 (1996) 667.
[7] T. Schrefl, J. Fidler, H. Kronmüller, J. Magn. Magn. Mater. 138 (1994) 15.
[8] A. Aharoni, IEEE Trans. Magn. 27 (14) (1991) 3539.
[9] K.M. Tako, T. Schrefl, M.A. Wongsam, R.W. Chantrell, J. Appl. Phys. 81 (1997) 4082.

Modelling the Evolution of Domains in Nanoelements Using Finite Elements

P. H. W. Ridley[1], G. W. Roberts[2], M. A. Wongsam[1] and R. W. Chantrell[1]
SEECS[1], School of Mathematics[2], University of Wales Bangor, Gwynedd, LL57 1UT, U. K.

J. Gore and M. Maylin
Defence Evaluation Research Agency, Ively Road, Farnborough, GU14 0LX, U. K.

Abstract— Investigation into the theoretical magnetic behaviour of permalloy is described. The material is discretised into a structure of nanoelements, so that we may employ micromagnetic simulations in order to investigate the material behaviour. In this paper we describe the formation and structure of domains in an array of interacting nanoelements with varying space between them. The simulations begin at saturation and end when the nanoelements are in a zero field equilibrium state. The time evolution of the system is described by the Landau-Lifschitz equation of motion and the field calculations are carried out by the use of a finite element spatial discretisation scheme.

Index Terms—Domains, Field calculations, Finite element method, Nanoelements.

I. Introduction

THE investigation into the magnetic behaviour of permalloy has become more advanced due to improvements in numerical micromagnetic methods on the theoretical side and high accuracy electron-beam lithography methods experimentally. If the material is discretised into a nanoelement structure, micromagnetic calculations may be carried out in order to investigate the material behaviour. Recent work by T. Schrefl and coworkers [1] investigated the influence of the width and shape of the ends of nanoelements on the formation and structure of domains in single NiFe bars, also involving two alternative numerical techniques in magnetostatics, namely the use of spatial transformations and a hybrid finite element / boundary element technique. Here, we use a new finite element approach based on a minimisation scheme to calculate the demagnetising field via a magnetic scalar potential. The numerical simulation of the domain structure of an array of infinitely thin permalloy nanoelements is investigated. We investigate the zero field equilibrium state after the removal of a saturating field and look at the relaxation of each individual nanoelement as a function of time. The nanoelements initially have a uniform magnetization structure and consist of arrays of bars with varying spaces between them.

Manuscript received March 5, 1999; revised May 12, 1999.
P. H. W. Ridley, telephone : +44-1248-382739,
fax : +44-1248-361429, e-mail : phil@sees.bangor.ac.uk

II. Model description

The total effective field, $\mathbf{H}_t$ is given by the sum of the exchange, anisotropy and magnetostatic component fields. In our simulations working in reduced units, the total reduced effective field, $\mathbf{h}_t$ is given by $\mathbf{h}_t = \frac{\mathbf{H}_t}{H_k}$ where $\mathbf{h}_t = \mathbf{h}_d + \mathbf{h}_{ex} + \mathbf{h}_a$, with $\mathbf{h}_d$, $\mathbf{h}_{ex}$ and $\mathbf{h}_a$ representing the reduced demagnetising, exchange and anisotropy field terms respectively. $H_k = \frac{2K}{M_s}$ is the magnetocrystalline anisotropy, M_s is the saturation magnetization and K is the uniaxial anisotropy constant. The governing equation for the magnetization dynamics is the Landau-Lifshitz equation of motion.

$$\frac{d\mathbf{m}}{d\tau} = -\mathbf{m} \times \mathbf{h}_t - \alpha(\mathbf{m} \times (\mathbf{m} \times \mathbf{h}_t)) \qquad (1)$$

The reduced magnetization is given by $\mathbf{m} = \frac{\mathbf{M}}{M_s}$, the reduced damping constant $\alpha = \frac{\lambda}{\gamma}$ and $\tau = t\gamma H_k$ is the reduced time. λ is the damping constant and γ the gyromagnetic ratio. The system equations which are coupled through the components of $\mathbf{m}$ are solved by a 4th order Adams-Moulton predictor-corrector method described in [2] with a convergence criterion of $\left|\frac{d\mathbf{m}}{d\tau}\right| < 10^{-6}$.

III. Finite Element Field Calculation

The demagnetising field is calculated via a magnetic scalar potential, ϕ, such that $\mathbf{h}_d = -\nabla\phi$. Here ϕ is the solution to Poisson's equation within the magnetic region, Ω_{int} and Laplace's equation everywhere outside, Ω_{ext}; so we have

$$\begin{aligned} \nabla^2\phi_{int} &= 4\pi\nabla\cdot\mathbf{m} \quad \forall \mathbf{x} \in \Omega_{int} \\ \nabla^2\phi_{ext} &= 0 \quad \forall \mathbf{x} \in \Omega_{ext} \end{aligned} \qquad (2)$$

If we denote the boundary by $\partial\Omega$, then because of the abrupt change in material properties across $\partial\Omega$ we have the interface condition

$$\frac{\partial\phi_{int}}{\partial n} - \frac{\partial\phi_{ext}}{\partial n} = 4\pi\mathbf{m}\cdot\hat{\mathbf{n}} \quad \forall \mathbf{x} \in \partial\Omega \qquad (3)$$

and continuity condition

$$\phi_{int} = \phi_{ext} \quad \forall \mathbf{x} \in \partial\Omega \qquad (4)$$

where $\hat{\mathbf{n}}$ is the unit normal to the nanoelement boundary. We calculate ϕ globally by the use of a variational finite element formulation, thus allowing the modelling of

interactions between nanoelements. The equations (2)-(4) define a problem which needs to be solved over entire space. Several authors have formulated finite element solutions to this problem. A widely used method is that by D. R. Fredkin and T. R. Koehler [3] who formulate the solution for the magnetic material only, here the potential is expressed as $\phi = \phi_1 + \phi_2$, where ϕ_1 is the solution to Poisson's equation within the magnetic region subject to a natural boundary condition, which may be solved by the FEM, ϕ_2 is solved by a boundary integral along the magnetic material boundary. More recently the problem has been solved by enclosing the magnetic region within a finite part of external space [4]. The entire problem is then solved over a single mathematical domain consisting of a magnetic and non-magnetic region, with an artificial boundary condition imposed on the outer region's boundary and condition (3) being imposed along the interface between the two materials. We calculate ϕ by the use of the FEM using the same concept of modelling (2)-(4) as a single problem. The method we have developed replaces the infinite boundary by a suitably large closed boundary $\partial\Re$ which is a distance away from the magnetic region Ω_{int} and enclosing Ω_{ext}. This distance is determined by comparing our solution with the analytical result for a rectangular magnetic region with a uniform magnetization structure parallel to the positive direction of the longitudinal axis given by A. Aharoni [8]. On $\partial\Re$ we impose the artificial boundary condition $\phi = 0$. As with any FEM solution, a suitable transformation method is used to map each element to a simple parent element in order to simplify the integration over the whole region. We have used two different numerical methods of imposing the interface condition (3) within the finite element solution of (2)-(4). In the first method we apply a standard Rayleigh-Ritz stationary functional method which leads up to the formation of a system of n linear equations, where n is the number of nodes in the spatial discretisation scheme. Condition (3) is integrated into the linear equations by replacing any row number which corresponds to a node on $\partial\Omega$ by formulating explicitly the jump condition in terms of the transformations. The alternative approach that we have formulated uses an implicit formulation of imposing (3) using a Galerkin technique described in [5]. Both ways have worked adequately in our simulations but for the high degree of accuracy required for our simulations it is necessary to use quadratic finite elements. The stiffness matrices produced in our finite element formulations are very sparse, so in order to reduce the need for large storage requirements, we store only the non-zero entries with their corresponding row and column numbers. We then apply a sparse matrix solver routine from the netlib library [6] which keeps CPU requirements to a minimum to obtain ϕ globally. Thus allowing us to model interactions between nanoelements. The following calculations were performed on a 500MHz single processor with 1 GB of RAM. The simulations take an average CPU time of 412.8 minutes.

IV. Results

In this section we describe the results produced from applying our numerical model in simulating the formation of domain structures in an array of 3 infinitely thin permalloy nanoelements. We investigate the zero field equilibrium state of the nanoelements after the removal of a saturating field. These experiments are carried out with varying space between the nanoelements and longitudinal and transverse material anisotropy. We also describe the relaxation of each individual nanoelement as a function of time. Initially the nanoelements have a uniform magnetization structure parallel to the positive direction of the longitudinal axis, they each have dimensions of 0.2μm $\times$ 1.6μm and consist of rectangular bars. The material parameters used are typical for those of permalloy.

The following figures represent the in plane components of reduced magnetization, $\mathbf{m}$ in the form of greyscale images with black and white representing $+1$ and -1 respectively. The left image shows the x component of magnetization, m_x and the right image shows the y component of magnetization, m_y. The nanoelements have a transverse anisotropy of 5×10^3 erg/cm^3.

The images in Fig. 1 show the magnetization configuration for the zero field equilibrium state for 3 nanoelements with a spacing of 0.05μm. The outer nanoelements relax into configurations of several domains whereas the central element remains almost saturated except at the ends where magnetostatic interactions have initiated a small scale domain structure to form.

Fig. 1. magnetization configuration, spacing 0.05μm

When we increase the separation between the nanoelements to 0.4μm, Fig. 2, we observe that the central element is still being prevented from forming a multi-domain structure due to interactions. However when we increase

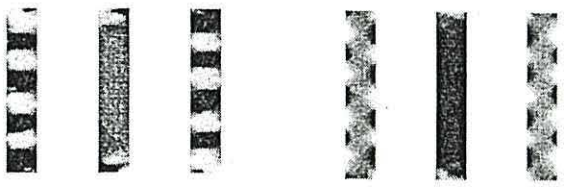

Fig. 2. magnetization configuration, spacing 0.4μm

the separation to 0.8μm, see Fig. 3 and Fig. 4, the central element forms a multi-domain structure much like the two outer ones. Here we see an increase in the number

of domains due to less magnetostatic interaction. In all cases the nucleation occurs simultaneously at one end of the outer nanoelements and propagates along the length.

Fig. 3. x component of magnetization, spacing 0.8μm

Fig. 4. y component of magnetization, spacing 0.8μm

We illustrate this effect by the graph in Fig. 5 which shows the relaxation of each individual nanoelement as a function of time for the case when the nanoelement spacing is 0.4μm. The nanoelements are denoted by N1,N2 and N3 from left to right. For the outer nanoelement there is initially a relatively slow variation of the magnetisation associated with the nucleation of a reversed area of magnetisation followed by a more rapid propagation. The magnetisation structure of the central nanoelement changes early in the process, but stabilises rapidly. We have performed the same sequence of simulations on

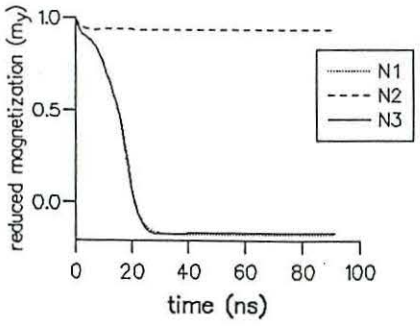

Fig. 5. relaxation of each individual nanoelement

nanoelements with longitudinal anisotropy and have o served a similar effect, however the elements now ha a large scale domain structure Fig. 6 which compar well with experimental data [7]. It was found that tl magnetization configurations depended on the dynami of the magnetization process specifically, a gradual redu tion of the magnetic field produced slightly different d main structures and will be described in a separate pul lication.

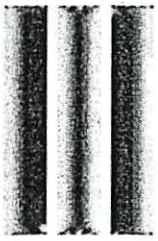

Fig. 6. y component of magnetization for nanoelements with longitudinal anisotropy and spacing 0.05μm

Acknowledgments

The authors would like to acknowledge J. R. Shewchul of The School of Computer Science / Carnegie Mellor University, 5000 Forbes Avenue / Pittsburgh, Pennsylvania 15213-3891 for the use of the Two-Dimensional Quality Mesh Generator and Delaunay Triangulator (Version 1.3) in these simulations. The financial support of EPSRC and the Defence Evaluation Research Agency is gratefully acknowledged.

References

[1] T. Schrefl, J. Fidler, K. J. Kirk and J. N. Chapman, "A higher order FEM-BEM method for the calculation of domain processes in magnetic nanoelements," *IEEE Trans. Magn.*, vol. 33 pp. 4182-4184, 1997

[2] E. W. Cheney and D. R. Kincaid, *Numerical Mathematics and Computing*, 2nd ed., Brooks/Cole Publishing Company, Monterey, California, 1985, pp.397–409.

[3] D. R. Fredkin and T. R. Koehler, "Hybrid method for computing demagnetizing fields," *IEEE Trans. Magn.*, vol. 26 pp. 415-417, 1990

[4] B. Yang and D. R. Fredkin, "Dynamical finite element method in micromagnetics," *IEEE Trans. Magn.*, vol. 35 pp. 740-741, 1998

[5] J. Simkin and C. W. Trowbridge, "On the use of the total scalar potential in the numerical solution of field problems in electromagnetics," *International J. For Numerical Methods In Engineering*, vol. 14 pp. 423-440, 1979

[6] Z. Zlatev, J. Wasniewski, K. Schaumburg,"Comparison of 2 algorithms for solving large linear-systems," *SIAM J. On Scientific and Statistical Computing*, vol. 3 pp. 119-135, 1982

[7] S. J. Hefferman, J.N. Chapman and S. McVitie, "In-situ magnetising experiments on small regularly shaped permalloy particles," *J. Magnetism Magn. Mater.*, vol. 95 pp. 76-84, 1991

[8] A. Aharoni, "Magnetostatic energy calculations," *IEEE Trans. Magn.*, vol. 27 pp. 3539-3547, 1991

Investigation of magnetization behavior in nanoelements using the finite element method

P. H. W. Ridley,[a] G. W. Roberts, and R. W. Chantrell
SEECS, University of Wales Bangor, Gwynedd, LL57 1UT, United Kingdom

A model of thin film permalloy using an efficient finite element variational approach to the magnetostatic field calculation is described. The material is discretized into a nanoelement structure at the micron level which enables us to investigate material properties due to patterning. Predicted domain structures agree well with experimental data. Interactions between elements are significant and it will be shown that the domain structure in the central element differs from that of its neighbors. As expected, the addition of pointed ends stabilizes the single-domain state. Elements with two pointed ends exhibit pseudo-single-domain behavior. We have studied the single-domain/pseudo-single-domain transition for permalloy platelets, results for noninteracting platelets are given as a function of the elongation. Interactions are shown to increase or decrease the critical size depending on the geometry. © *2000 American Institute of Physics.* [S0021-8979(00)78608-7]

I. INTRODUCTION

Much interest has developed recently in the study of the behavior of thin film magnetic materials patterned at the submicron level.[1] The motivation behind gaining further insight into the material behavior at this level is mainly due to its technological application in magnetic recording and magnetic sensors.[2] In order to investigate material behavior, experimental techniques such as transmission electron microscopy and electron beam lithography are currently being used.[3] In order to maintain theoretical results which are comparable to the high resolution capabilities of the experimental techniques, one must use a numerical approach enabling a very high discretization of the material. With this in mind, our model for investigating the domain structures in thin film magnetic material uses a finite element variational approach. This enables us to reproduce results comparable to experimental observations.

In this work, we carry out a numerical simulation of the domain structure and hysteresis effects of single nanoelements with respect to their shape and size. We also observe the interaction effects of an array of nanoelements in relation to their separation. The shape of the nanoelements considered will be restricted to rectangular bars with one, two, or no pointed ends with their lengths being in the region of 0.1–2.0 μm.

II. MODEL DESCRIPTION

We represent the magnetization distribution within a nanoelement by the pointwise vector $\mathbf{M}$ with each point corresponding to a node within the finite element spatial discretization scheme.

The total effective field $\mathbf{H}_t$ is given by the sum of the component field terms exchange, anisotropy, magnetostatic and applied. For convenience, we work in reduced units by scaling the individual field terms with respect to the anisotropy field strength H_k, so that the reduced total effective field is given by $\mathbf{h}_t=\mathbf{H}_t/H_k$ where $\mathbf{h}_t=\mathbf{h}_d+\mathbf{h}_{ex}+\mathbf{h}_a+\mathbf{h}_z$ with $\mathbf{h}_d$, $\mathbf{h}_{ex}$, $\mathbf{h}_a$, and $\mathbf{h}_z$ representing the reduced demagnetizing, exchange, anisotropy, and applied field terms, respectively. $H_k=2K/M_s$ is the magnetocrystalline anisotropy, M_s is the saturation magnetization, and K is the uniaxial anisotropy constant. We also represent the reduced magnetization by $\mathbf{m}$ where $\mathbf{m}=\mathbf{M}/M_s$. The governing equation for the magnetization dynamics is the Landau–Lifshitz equation of motion given by

$$\frac{d\mathbf{m}}{d\tau}=-\mathbf{m}\times\mathbf{h}_t-\alpha(\mathbf{m}\times(\mathbf{m}\times\mathbf{h}_t)), \tag{1}$$

where the reduced damping constant $\alpha=\lambda/\gamma$, $\tau=t\gamma H_k$ is the reduced time, λ the damping constant, and γ the gyromagnetic ratio. The system equations which are coupled through the components of $\mathbf{m}$ are solved by a fourth-order Adams–Moulton predictor–corrector method.

III. FIELD CALCULATIONS

The exchange field $\mathbf{h}_{ex}$ is calculated from the discrete expression used in Ref. 4 which is very suited to the finite element method. We calculate the magnetostatic field by expressing the demagnetizing field, $\mathbf{h}_d$, in terms of a magnetic scalar potential ϕ, such that $\mathbf{h}_d=-\nabla\phi$ as described in Ref. 5. We can then obtain values for ϕ both inside and outside the nanoelements by the use of a variational finite element approach which allows us to look at interaction effects between particles. The finite element formulation uses a Galerkin weighted residual approach coupled with the use of quadratic finite elements in order to maintain the high degree of accuracy required to realistically model domain processes. To keep computational requirements to a minimum we use a sparse matrix routine from the netlib library[6] and only store the nonzero entries in our stiffness matrix. The efficiency of this calculation enables us to perform an average simulation with a CPU time of 7 h on a 500 MHz single processor with 1 Gbyte of random access memory.

[a]Electronic mail: phil@sees.bangor.ac.uk

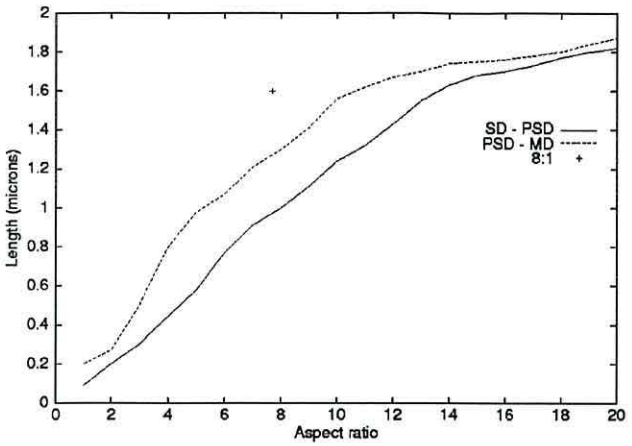

FIG. 1. Transition for single-domain / pseudo-single-domain states.

IV. RESULTS

In this section we describe the results produced from using our model in simulating the magnetization behavior of thin film permalloy. The material parameters used are $A = 1.3\times10^{-6}$ erg/cm, $K = 5\times10^{3}$ erg/cm^3, and $M_s = 800$ emu/cm^3 to emulate permalloy. We assume the nanoelements to be infinitely thin. Initially the nanoelements have a uniform magnetization distribution parallel to the positive direction of the longitudinal axis. We illustrate magnetization configurations of the nanoelements in the form of gray-scale images depicting the magnitude of the transverse component of the reduced magnetization **m** with black and white representing $+1$ and -1, respectively.

We begin by investigating the effect of elongation on the single-domain (SD)/pseudo-single-domain (PSD) transition and the PSD/multidomain (MD) transition for permalloy platelets with very small transverse anisotropy. Simulations to emulate the relaxation into the remanent states were carried out by removing the applied field with zero fall time. Figure 1 shows results for noninteracting single nanoelements, where transition states are given as a function of the elongation. Interactions are shown to increase or decrease the critical size depending on the geometry as will be demonstrated later.

It was found that the remanent magnetization configurations depended on the dynamics of the magnetization process. Specifically, a gradual reduction of the magnetic field

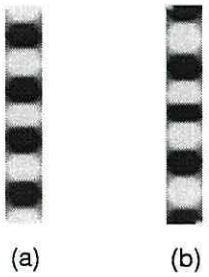

FIG. 2. Remanent state with (a) instantaneous and (b) gradual relaxation of the applied field.

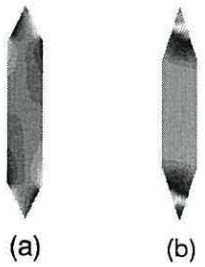

FIG. 3. Remanent state for two pointed ends with no applied field (a) pitch$=0.2\ \mu$m and (b) pitch$=0.3\ \mu$m.

produced slightly different domain structures compared with those produced without the presence of an applied field. These results are shown in Figs. 2(a) and 2(b), which show the remanent states of a single $0.2\ \mu\text{m}\times1.2\ \mu$m nanoelement obtained by instantaneous and gradual relaxation of the field, respectively. We noticed that the configuration in Fig. 2(b) exhibits an 8% lower energy than that in Fig. 2(a). The addition of a pointed end to a nanoelement causes the domains to propagate from the flat end. As seems reasonable, simulations for nanoelements with two pointed ends exhibit a pseudo-single-domain state to larger particle dimensions with micromagnetic detail appearing in the regions joining the rectangular and triangular regions. The remanent states for a $0.2\ \mu\text{m}\times1.2\ \mu$m nanoelement are shown in Fig. 3 showing the effect of altering the distance of the pointed end from the rectangular region (pitch) of the nanoelement.

Hysteresis loops for two particle sizes are shown in Fig. 4. The element of size $0.1\ \mu\text{m}\times1.6\ \mu$m shows a loop corresponding to SD behavior in Fig. 4(a). Reversal proceeds via nonuniform magnetization states at the element ends which lead to vortex nucleation and propagation of the reversed magnetization. Figure 4(b) shows the hysteresis behavior for an element of size $0.2\ \mu\text{m}\times1.6\ \mu$m which exhibits MD behavior. The field is applied along the long axis of the particle and in this case the anisotropy direction is taken as planar random. The magnetization proceeds by the nucleation of an end domain, giving rise to an initial steep change of magne-

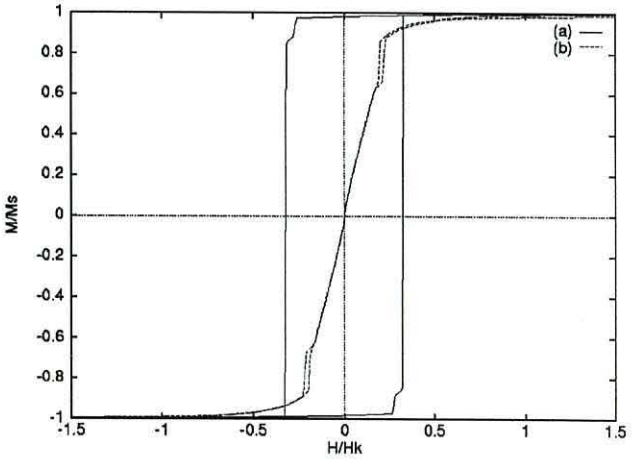

FIG. 4. Hysteresis loops for nanoelements of size (a) $0.1\ \mu\text{m}\times1.6\ \mu$m and (b) $0.2\ \mu\text{m}\times1.6$ m.

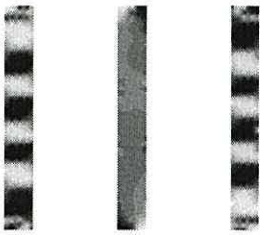

FIG. 5. Remanent state for an array of three interacting 0.2 μm$\times$1.6 μm nanoelements with spacing 0.6 μm and transverse anisotropy.

tization. The hysteresis at this point indicates that this magnetization change is irreversible. This domain structure gradually expands to fill the whole element.

In addition to investigating domain behavior in single nanoelements we have also looked at the interacting case. The formation of domain structures in arrays of three nanoelements was found to be dependent upon their separation, for example as shown in Fig. 5 the central element of three remains single domain at a size which allows domain structure to form in the outer elements. The elements do not become essentially noninteracting until a spacing of 0.8 μm. We have calculated the critical size for the central element at a spacing of 0.6 μm, which is represented as a single point in Fig. 1, demonstrating the increase resulting from interaction effects in this geometry.

V. CONCLUSIONS

We have given calculations of the magnetic properties of permalloy nanoelements. The shape of the elements and interactions between elements have a strong bearing on the transition to MD states. The effects of interactions are also dependent on the geometrical arrangement of the elements, as will be discussed elsewhere. Hysteresis loops for individual elements are qualitative in agreement with experiment. In particular the large platelet exhibits a loop similar to the type "C" loop observed experimentally by Hefferman *et al.*[7]

ACKNOWLEDGMENT

The financial support of the United Kingdom Engineering and Physical Sciences Research Council is gratefully acknowledged.

[1] T. Schrefl, J. Fidler, K. J. Kirk, and J. N. Chapman, J. Magn. Magn. Mater. **175**, 193 (1997).
[2] S. Y. Chou, M. Wei, P. R. Krauss, and P. B. Fishcher, J. Vac. Sci. Technol. B **12**, 3695 (1994).
[3] M. Rührig, B. Khameshpour, K. J. Kirk, J. N. Chapman, P. Aichison, S. McVitie, and C. D. Wilkinson, IEEE Trans. Magn. **32**, 4452 (1996).
[4] K. M. Tako, M. A. Wongsam, and R. W. Chantrell, J. Magn. Magn. Mater. **155**, 40 (1996).
[5] P. H. W. Ridley, G. W. Roberts, M. A. Wongsam, and R. W. Chantrell, J. Magn. Magn. Mater. **193**, 423 (1999).
[6] Z. Zlatev, J. Wasniewski, and K. Schaumburg, SIAM J. Sci. Comput. (USA) **3**, 119 (1982).
[7] S. J. Hefferman, J. N. Chapman, and S. McVitie, J. Magn. Magn. Mater. **95**, 76 (1991).

Computational and Experimental Micromagnetics of Arrays of 2-D Platelets

P. H. W. Ridley, G. W. Roberts, R. W. Chantrell, K. J. Kirk and J. N. Chapman.

Abstract— **2-D regular nanoelements are of interest as micromagnetic model systems and in a number of sensor applications. In this paper we concentrate on a recent development in the form of experimental structures of arrays of small nanoelements which are 300nm long and between 50 – 80nm wide in small arrays which are amenable to computational studies. A direct comparison of theoretical and experimental hysteresis loops gives good quantitative agreement and suggests that both interactions and variations in intrinsic properties contribute significantly to the width of the loops. The experimental samples were produced by electron beam lithography and consisted of either a 6×3 array or a 6 element row. The intra-row spacing was 50nm or 80nm and the inter-row spacing was 100nm. Magnetic images were obtained by Lorentz microscopy, from which the magnetization curves were determined. Computational studies were carried out using a finite element method with magnetostatic field calculations via the maximisation of the scalar potential. The technique is computationally efficient and allows the calculation of the properties of interacting elements.**

Index Terms— **Finite element method, Interactions, Nanoelements.**

I. Introduction

WHEN a magnetic material is patterned into structures at the sub micron level, the resulting shapes are termed nanoelements. At this level theoretical micromagnetic calculations and experimental imaging techniques may be performed in order to investigate the material behaviour.

Recent theoretical simulations have been concerned with the behaviour of single nanoelements [1] and more recently several of them placed in row formations [2]. On the experimental side, work has been carried out on larger rows and arrays of nanoelements to determine their use in future recording applications [3].

Manuscript received Feb 15, 2000, revised May 4, 2000.

P. H. W. Ridley is with the School of Informatics, University of Wales Bangor, Gwynedd, LL57 1UT, U. K., telephone : +44-1248-382739, fax : +44-1248-361429, e-mail : phil@sees.bangor.ac.uk

G. W. Roberts is with the School of Informatics, University of Wales Bangor, Gwynedd, LL57 1UT, U. K., telephone : +44-1248-382480, fax : +44-1248-361429, e-mail : g.w.roberts@bangor.ac.uk

R. W. Chantrell is with the Physics Department, University of Durham, Durham, DH1 3LE, U. K., telephone : +44-191-3743710, fax : +44-191-3743749, e-mail : r.w.chantrell@durham.ac.uk

K. J. Kirk is with the Department of Electronic Engineering and Physics, University of Paisley, Paisley, PA1 2BE , U. K.

J. N. Chapman is with the Department of Physics and Astronomy, University of Glasgow, Glasgow, G12 8QQ, U. K., telephone : +44-141-3304462, email : J.Chapman@physics.gla.ac.uk

The motivation behind the investigation into the behaviour of arrays of nanoelements is due to their possible future application in high density data storage. For use as patterned magnetic media each individual nanoelement would store 1 bit. Thin films with exchange coupled grains such as Permalloy or Cobalt would be used to fabricate the nanoelements. Previous experiments on these films have shown that each nanoelement behaves in an almost single domain manner and therefore has two stable magnetic states which is ideal for data storage.

In this work we shall use our theoretical micromagnetic model to simulate the magnetization behaviour in rows of 6 and arrays of 18 nanoelements. The size of the individual nanoelements will be 300nm × 80nm and 300nm × 50nm and spacing will be varied to match experimental results. We shall then make comparisons between our theoretical predictions and the recent experimental observations.

II. Model description

For the micromagnetic calculations we use the variational finite element minimization scheme as described earlier in [4] where the demagnetizing field is calculated via a magnetic scalar potential, ϕ to reduce computational requirements and to allow the convenient modelling of interactions between nanoelements. The dynamics of the magnetization process is governed by the Landau-Lifshitz equation of motion with effective field contributions arising from demagnetizing, exchange, anisotropy and external sources.

To simulate permalloy we use the standard material parameters which are the exchange constant, $A = 1.3 \times 10^{-6}$erg/cm, the uniaxial anisotropy, $K = 5 \times 10^{3}$erg/cm^3 and the saturation magnetization, $M_s = 800$emu/cm^3. For all of these simulations we initially saturate each individual nanoelement with a magnetization distribution parallel to a direction going from the bottom to the top of the nanoelement. The simulations are performed using quadratic finite elements with extra mesh refinement located around the nanoelement edges which is required to successfully be able to simulate the magnetostatic interactions between nanoelements. We also fix the thickness of each individual nanoelement to be 20nm.

In the experiments arrays of permalloy nanoelements are created by electron beam lithography and lift off patterning [5]. The magnetic imaging is carried out in a modified

Philips CM20 transmission electron microscope in which samples may be viewed in field free conditions or in variable applied fields. The arrays are magnetized by tilting the sample in the vertical field from the objective lens in the TEM, thus giving a field component of varying magnitude in the plane of the sample. The field is aligned along the long axis of the elements. For each magnetizing experiment, the sample is first tilted to a high angle to produce a large in plane field component to saturate the elements in one direction. The sample is returned to 0^o tilt and then gradually tilted in the other direction to obtain an increasing reverse field to return the nanoelements back to their initial configuration. Throughout the magnetization cycle configurations are recorded via Fresnel or Differential Phase Contrast (DPC) mode imaging. Further description is given in [6], [7].

III. Results

In this section we describe the results produced from applying our theoretical model in simulating the hysteresis curves for rows and arrays of interacting nanoelements.
The geometries considered will be either single rows of 6 rectangular nanoelements or arrays of 18 nanoelements made up from 3 rows placed close together. The actual sizes of the nanoelements will be either 300nm × 80nm or 300nm × 50nm.
For the rows we denote the distance between individual nanoelements as the intra row spacing and for the arrays we have additional inter row spacing between the individual rows. For our results the inter row spacing will be fixed at 100nm.
The obvious concern with the simulation of these setups is of computational requirement, for the two dimensional arrays we have to deal with 18 nanoelements. Indeed to create a finite element mesh with the correct level of refinement we need approximately 8000 quadratic finite elements. However requirements are kept to a minimum via our finite element solver and the total C.P.U. time needed for a typical simulation to calculate the hysteresis curve is approximately 34hrs on a single EV6 processor.
To obtain our theoretical predictions for comparison with the experimental observations, we apply a strong saturating field to the samples and then reduce it by field steps of 5.25Oe until all the nanoelements have reversed. These calculations were performed on a single EV6 processor.
For our first simulations we shall consider a row and array of nanoelements of size 300nm × 80nm with an intra row spacing of 80nm and for the array an inter row spacing of 100nm. Previous experimental investigations of similar arrangements have already been performed by Kirk et al, the hysteresis curves are given in Fig. 1. The reversal occurs sooner in the rows than in the arrays, which is due to the inter row magnetostatic interactions. Our theoretical predictions are shown in Fig. 2. The results in Fig. 2 were obtained for a uniaxial anisotropy distribution of $K = 5\times 10^3 \mathrm{erg/cm^3}$ with a planar random orientation throughout the nanoelements. Here we observe good agreement between the experimentally observed value and our predicted value of the coercivity. Also we obtain an average switching field distribution of 117Oe which is smaller than the experimental observation of 330Oe. This higher value for the experimental case may be ascribed to a dispersion of the intrinsic properties of the individual nanoelements in the experimental samples.

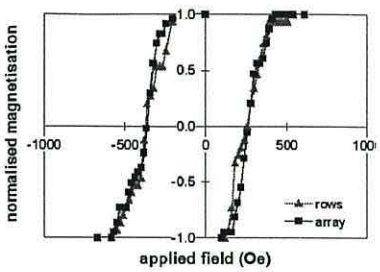

Fig. 1. Experimental hysteresis curves rows and arrays of 300nm×80nm interacting nanoelements

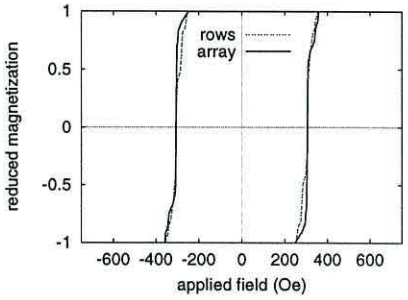

Fig. 2. Theoretical hysteresis curves rows and arrays of 300nm×80nm interacting nanoelements

We now consider the second experimental configurations, namely rows and arrays of 300nm × 50nm nanoelements with an intra row spacing of 50nm and an inter row spacing of 100nm. The experimental results of Kirk et al are shown in Fig. 3. Here we observe a similar hysteresis curve as in the previous experimental results. However, we notice a much higher coercivity which may be ascribed to the increase in the shape anisotropy arising from the increased aspect ratio of the elements. Our simulation also predicts an increase in system coercivity as shown in Fig. 4. Here we again observe good agreement between the experimental observations and our theoretical predic-

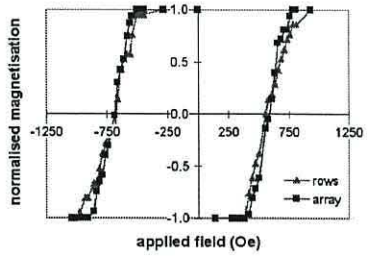

Fig. 3. Experimental hysteresis curves rows and arrays of 300nm×50nm interacting nanoelements

ions for the system coercivity. The difference in our

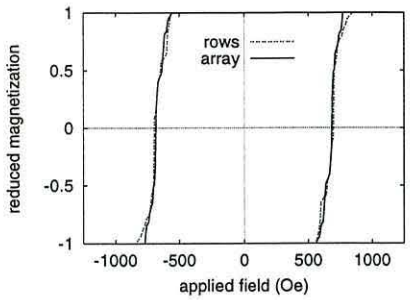

Fig. 4. Theoretical hysteresis curves rows and arrays of 300nm×50nm interacting nanoelements

predicted switching field distributions of 335Oe and the experimental observation of 670Oe is again caused by the intrinsic properties of the experimental samples.

We shall now investigate the effects of these properties further by performing simulations with ordered anisotropy. For these simulations we have introduced to each of the nanoelements a component of longitudinal anisotropy of $K = 5\times\ 10^4 \mathrm{erg/cm}^3$, i.e. a factor of 10 times larger than the previous calculations. For the 300nm×80nm case we see 3 large collective reversal events occurring due to patches of switching nanoelements as shown in Fig. 5.

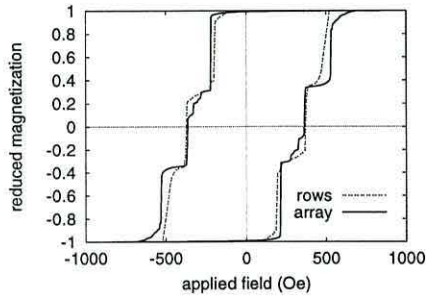

Fig. 5. Theoretical hysteresis curves rows and arrays of 300nm×80nm interacting nanoelements

In the case of 300nm×50nm we also see more prominent collective reversals in both the rows and arrays than in the results shown in Fig. 4. We also see an increase in the system coercivity as observed in the previous experimental and theoretical calculations. The results shown in Fig. 5 and Fig. 6 show the effect of the large anisotropy aligned with the long axis of the element - the combination of the alignment and strength of the anisotropy gives rise to the collective reversal and the stable intermediate magnetic states. The reversal process in the experiments is via a mechanism of random columns of nanoelements switching together, this is also observed in our results involving the random anisotropy distribution and again occurs by entire columns of nanoelements reversing at random. In both cases of size and spacing the magnetization reversal is initiated faster for rows than for the array, in agreement with experiment.

The reversal mechanism of the array as a whole is very sensitive to the degree of disorder. In the case of an aligned uniaxial anisotropy a highly symmetric cooperative switching mechanism is observed to take place. A large anisotropy has the effect of stablising states during the reversal process leading to the distinctive switching features of Fig 5. A random anisotropy breaks this high symmetry sufficiently to reduce the cooperative switching. This leads to a relatively random reversal of individual elements as will be discussed in more detail elsewhere. This reduction in collective reversal is consistent with experimental observations. The agreement between theory and experiment in terms of the coercivity is good. However, the predicted Switching field distribution is narrow in comparison with experiment. In the case of the simulations the SFD essentially arises because of interaction effects and our predicted values indicate that interaction effects are small but significant, since they account for half of the width of the SFD. The discrepancy between the experimental and calculated SFD's probably suggests that there is a dispersion of the intrinsic element properties, which is not considered in the current model.

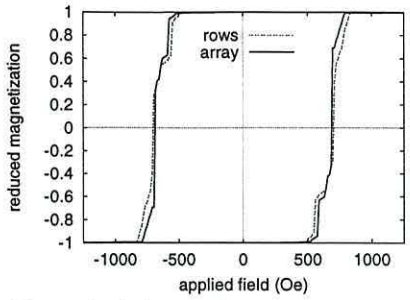

Fig. 6. Theoretical hysteresis curves rows and arrays of 300nm×50nm interacting nanoelements

Acknowledgments

The authors would like to acknowledge the financial support of the United Kingdom Engineering and Physical Sciences Research Council.

References

[1] T. Schrefl, J. Fidler, K. J. Kirk, and J. N. Chapman,"Simulation of magnetization reversal in polycrystalline patterned Co elements," *J. Appl. Phys.*, vol. 85, pp. 6169-6171, 1999

[2] B. Yang and D. R. Fredkin, "Dynamical micromagnetics by the finite element method," *IEEE Trans. Magn.*, vol. 34, pp. 3842-3852, 1998

[3] S. Y. Chou, P. R. Krauss and L. Kong, "Nanolithographically defined magnetic structures and quantum magnetic disk," *J. Appl. Phys.*, vol. 79, pp. 6101-6106, 1996

[4] P. H. W. Ridley, G. W. Roberts, M. A. Wongsam, R. W. Chantrell, J. Gore and M. Maylin, "Modelling the evolution of domains in nanoelements using finite elements," *IEEE Trans. Magn.*, vol. 35, pp. 3874-3876, 1999

[5] K. J. Kirk, J. N. Chapman and C. D. W. Wilkinson, "Lorentz microscopy of small magnetic structure," *J. Appl. Phys.*, vol. 85, pp. 5237-5242, 1999

[6] J. N. Chapman and M. R. Scheinfein, "Transmission electron microscopies of magnetic microstructures," *J. Magn. Magn. Mater.*, vol. 200, pp. 729-740, 1999

[7] K. J. Kirk, J. N. Chapman and C. D. W. Wilkinson, "Switching fields and magnetostatic interactions of thin film magnetic nanoelements," *Appl. Phys. Lett.*, vol. 71, pp. 539-541, 1997

References

[1] K. O' Grady, V. G. Lewis and D. P. E. Dickson, Alternating gradient force magnetometry : Applications and extension to low temperatures (invited), *J. Appl. Phys.*, vol. 73(10), 1993, 5608

[2] L. Landau and E. Lifshitz, *Physik. Z. Sowjetunion*, vol. 8, 1935, 153-169

[3] D. Jiles, *Introduction to magnetism and magnetic materials*, Chapman and Hall, UK, 1991

[4] R. G. Carter, *Electromagnetism for electronic engineers*, Chapman and Hall, 2nd Edition, 1992

[5] B. D. Cullity, *Introduction to Magnetic Materials*, Addison-Wesley, 1972

[6] E. C. Stoner and E. P. Wohlfarth, A mechanism of magnetic hysteresis in heterogeneous alloys, *IEEE Trans. Magn.*, vol. 27(4), 1991, 3475

[7] H. N. Bertram, *Theory of Magnetic Recording*, Cambridge University Press, UK, 1994

[8] J. C. Mallinson, A unified view of high density digital recording theory (invited), *IEEE Trans. Magn.*, vol. 11(5), 1975, 1166-1169

[9] W. F. Brown Jr., *Micromagnetics*, Wiley-Interscience, N. Y., 1963

[10] T. R. Koehler, Hybrid FEM-BEM method for fast micromagnetic calculations, *Physica B*, vol. 233, 1997, 302-307

[11] A. G. Kalimov and M. L. Svedentsov, Three dimensional magnetostatic field calculation using integro-differential equation for scalar potential, *IEEE Trans. Magn.*, vol. 32(3), 1996, 667-670

[12] H. F. Schmidts and H. Kronmüller,An algorithm for two-dimensional micromagnetic calculations for ferromagnetic materials, *J. Magn. Magn. Mater.*, vol. 130, 1994, 329-341

[13] S. W. Yuan and H. N. Bertram, Domain-wall dynamic transitions in thin-films, *Phys. Rev. B*, vol. 44(22), 1991, 12395

[14] D. R. Fredkin and T. R. Koehler, Numerical micromagnetics by the finite element method, *IEEE Trans. Magn.*, vol. 23(5), 1987, 3385-3387

[15] D. R. Fredkin and T. R. Koehler, Ab initio micromagnetic calculations for particles(invited), *J. Appl. Phys.*, vol. 67(9), 1990, 5544-5548

[16] T. Schrefl, J. Fidler and H. Kronmüller, Nucleation fields of hard magnetic particles in 2D and 3D micromagnetic calculations, *J. Magn. Magn. Mater.*, vol. 138, 1994, 15-30

[17] H. Kronmüller, R. Fischer, R. Hertel and T. Leineweber, Micromagnetism and the microstructure in nanocrystalline material, *J. Magn. Magn. Mater.*, vol. 175, 1997, 177-192

[18] K. M. Tako, T. Schrefl, M. A. Wongsam and R. W. Chantrell, Finite element micromagnetic simulations with adaptive mesh refinement, *J. Appl. Phys.*, vol. 81(8), 1997, 4082-4084

[19] M. Rührig, B. Khamsehpour, K. J. Kirk, J. N. Chapman, P. Aitchison, S. McVitie and C. D. W. Wilkinson, The fabrication and magnetic properties of acicular magnetic nano-elements, *IEEE Trans. Magn.*, vol. 32(5), 1996, 4452-4457

[20] S. J. Hefferman, J. N. Chapman and S. McVitie, In-situ magnetising experiments on small regularly shaped permalloy particles, *J. Magn. Magn. Mater.*, vol. 95, 1991, 76-84

[21] T. Schrefl, J. Fidler, K. J. Kirk and J. N. Chapman, Domain structures and switching mechanisms in patterned magnetic elements, *J. Magn. Magn. Mater.*, vol. 175, 1997, 193-204

[22] T. Schrefl, J. Fidler, K. J. Kirk and J. N. Chapman, A higher order FEM-BEM method for the calculation of domain processes in magnetic nano-elements, *IEEE Trans. Magn.*, vol. 33(5), 1997, 4182-4184

[23] A. Hrenikoff, Solution of problems in elasticity by the framework method, *J. Appl. Mech.*, vol. A8, 1941, 169-175

[24] D. McHenry, A lattice analogy for the solution of plane stress problems, *J. Inst. Civ. Eng.*, vol. 21, 1943, 59-82

[25] M. J. Turner, R. W. Clough, H. C. Martin and L. J. Topp, Stiffness and deflection analysis of complex structures, *J. Aero. Sci.*, vol. 23, 1956, 805-823

[26] R. W. Clough, The finite element method in plane stress analysis, *proc.* 2^{nd} *A.S.C.E. Conf. on Electronic Computation*, Pittsburgh, Pa., September 1960

[27] J. H. Argyris, Recent advances in matrix methods of structural analysis, *Progr. Aeron. Sci.*, vol. 4, 1964

[28] G. P. Bazeley, Y. K. Cheung, B. M. Irons and O. C. Zienkiewicz, Triangular elements in bending - conforming and non-conforming solutions, *Proc. Conf. Matrix Methods In Struct. Mech.*, Air Force Inst. Of Tech, Wright Patterson A.F. Base, Ohio, 1965, 547-576

[29] P. E. Grafton and D. R. Strome, Analysis of axi-symmetric shells by the direct stiffness method, *J. A. I. A. A.*, vol. 1, 1963, 2342-2347

[30] R. H. Gallagher, Analysis of plate and shell structures in applications of finite element in engineering, *A.S.C.E.*, 1969, 155-205

[31] O. C. Zienkiewicz and Y. K. Cheung, Finite elements in the solution of field problems, *The Engineer*, 1965, 507-510

[32] G. Birkhoff, M. H. Schultz and R. S. Varga, Piecewise hermite interpolation in one and two variables with applications to partial differential equations, *Numer. Math.* , vol. 116, 1968, 232-25

[33] O. C. Zienkiewicz, J. Lyness and D. R. J. Owen, Three-dimensional magnetic field determination using a scalar potential via a finite element solution, *I.E.E.E. Trans. Magnetics*, vol. 13, 1977, 1649-1656

[34] S. H. Crandall, *Engineering analysis*, McGraw-Hill, 1956

[35] C. S. Desai and J. F. Abel, *Introduction to the finite element method. A numerical method for engineering analysis*, Van Nostrand Rienhold, 1972

[36] R. W. Clough, Comparison of three-dimensional finite elements, *Proc. A.S.C.E. Symp. on application of finite element methods in civil engineering*, Vanderbilt University, Nashville, Tennessee, 1969, 1-26

[37] http://www.cs.cmu.edu/~quake/triangle.html

[38] A. Aharoni, Magnetostatic Energy Calculations, *IEEE Trans. Magn.*, vol. 27(4), 1991, 3539-3547

[39] K. M. Tako, M. A. Wongsam and R. W. Chantrell, Micromagnetics of polycrystalline two-dimensional platelets, *J. Appl. Phys.*, vol. 79(8), 1996, 5767-5769

[40] M. R. Gibbons, Micromagnetic simulation using the dynamic alternating direction implicit method, *J. Magn. Magn. Mater.*, vol. 186, 1998, 389-401

[41] J. D. Hannay, N. S. Walmsley and R. W. Chantrell, A computational model of thermally activated high speed magnetisation reversal in longitudinal thin film media, *J. Magn. Magn. Mater.*, vol. 193, 1999, 245-248

[42] J. C. Mallinson, On Damped Gyromagnetic Precession, *IEEE Trans. Magn.*, vol. 23(4), 1987, 2003-2004

[43] R. L. Burden, J. D. Faires and A. C. Reynolds, *Numerical Analysis,* 2^{nd} *edition*, Prundle, Weber and Schmidt, Boston, MA, 1981

[44] C. W. Gear, *Numerical initial value problems in ordinary differential equations*, Prentice-Hall, Inc., N.J., 1971

[45] W. Cheney and D. Kincaid, *Numerical Mathematics and computing,* 2^{nd} *edition*, Brooks Cole Publishing Company, Monterey California, 1986

[46] R. H. Victora, Micromagnetic predictions for barium ferrite particles, *J. Appl. Phys.*, vol. 63(8), 1988, 3423

[47] K. M. Tako, M. A. Wongsam and R. W. Chantrell, Numerical simulation of 2D thin films using the finite element method, *J. Magn. Magn. Mater.*, vol. 155, 1996, 40-42

[48] P. H. W. Ridley, G. W. Roberts, M. A. Wongsam and R. W. Chantrell, Finite element modelling of nanoelements, *J. Magn. Magn. Mater.*, vol. 193, 1999, 423-426

[49] N. S. Walmsley, *Theoretical studies of stray field images of magnetic systems*, PhD thesis, University of Central Lancashire, UK, June 1995

[50] D. V. Berkov, K. Ramstock and A. Hubert, Solving micromagnetic problems - towards an optimal numerical-method, *Physica Status Solidi (A) Applied Research*, vol. 137, 1993, 207

[51] A. J. Davies, *The Finite Element Method : A First Approach*, Oxford University Press, Walton Street, Oxford, OX2 6DP, 1980

[52] http://www.netlib.org

[53] B. Irons, A frontal solution program for finite element analysis, *International Journal for Numerical Methods in Engineering*, vol. 2, 1970, 5-32

[54] A. George, Nested dissection of regular finite element meshes, *SIAM Journal of Numerical Analysis*, vol. 11, 1973, 345-363

[55] R. Barrett, M. Berry, T. F. Chan, J. Demmel, J. Donato, J. Dongarra, V. Eijkhout, R. Pozo, C. Romine and H. Van der Vorst, Templates for the solution of linear systems: building blocks for iterative methods, *SIAM*, 1993

[56] Y. Saad and M. H. Schultz, GMRES: A generalized minimal residual algorithm for solving nonsymmetric linear systems, *SIAM Journal of Scientific and Statistical Computing*, vol. 7(3), 1986, 856-869

[57] I. Duff, R. Grimes and J. Lewis, Sparse matrix test problems, *ACM Transactions on Mathematical Software*, vol. 15, 1989, 1-14

[58] J. Simkin and C. W. Trowbridge, On the use of the total scalar potential in the numerical solution of field problems in electromagnetics, *International Journal for Numerical Methods in Engineering* , vol. 14, 1979, 423-440

[59] I. S. Gradshteyn and I. M. Ryzhik, *Tables of Integrals, Series and Products U. K. Edition*, Academic Press Inc. (London) Ltd., 28/28 Oval Road, London NW1 7DX, 1980.

[60] J. F. Smyth, S. Schulz, D. R. Fredkin, D. P. Kern, S. A. Rishton, H. Schmid, M. Cali and T. R. Koehler, Hysteresis in lithographic arrays of permalloy particles - experiment and theory, *J. Appl. Phys.*, vol. 69, 1991, 5262

[61] http://www.ctcms.nist.gov/~rdm/mumag.html

[62] http://www.ssp.gla.ac.uk/kirkka/magsh.htm

[63] M. Rührig, S. Porthun, J. C. Lodder, S. McVitie, L. J. Heyderman, A. B. Johnston and J. N. Chapman, Electron beam fabrication and characterization of high-resolution magnetic force microscopy tips, *J. Appl. Phys.*, vol. 79, 1996, 2913

[64] J. Zhu, Y. Zheng and G. Prinz, Ultra-high density vertical magnetoresistive random access memory (VMRAM), *J. Appl. Phys.*, vol. 87, 2000, 6668-6673

[65] S. Y. Chou, P. R. Krauss and L. Kong, Nanolithographically defined magnetic structures and quantum magnetic disk, *J. Appl. Phys.*, vol. 79, 1996, 6101-6106

[66] K. J. Kirk, J. N. Chapman and C. D. W. Wilkinson, Switching fields and magnetostatic interactions of thin film magnetic nanoelements, *Appl. Phys. Lett.*, vol. 71, 1997, 539-541

[67] J. N. Chapman and M. R. Scheinfein, Transmission electron microscopies of magnetic microstructures, *J. Magn. Magn. Mater.*, vol. 200, 1999, 729-740

[68] K. J. Kirk, J. N. Chapman and C. D. W. Wilkinson, Lorentz microscopy of small magnetic structure, *J. Appl. Phys.*, vol. 85, 1999, 5237-5242

[69] K. J. Kirk, J. N. Chapman, S. McVitie, P. R. Aitchison and C. D. W. Wilkinson, Interactions and switching field distributions of nanoscale magnetic elements, *J. Appl. Phys.*, vol. 87, 2000, 5105-5107

[70] D. R. Fredkin and T. R. Koehler, Finite element methods for micromagnetics, *IEEE Trans. Magn.*, vol. 28(2), 1992, 1239-1244

[71] B. Yang and D. R. Fredkin, Dynamical micromagnetics by the finite element method, *IEEE Trans. Magn.*, vol. 34(6), 1998, 3842-3852

[72] Riccardo Hertel and H. Kronmüller, Adaptive finite element mesh refinement techniques in three-dimensional micromagnetic modeling, *IEEE Trans. Magn.*, vol. 34(6), 1998, 3922-3930

[73] T. Schrefl, M. Zehetmayer, W. Scholz and J. Fidler, Micromagnetic simulation of 360 degree domain walls in thin Co films, *J. Appl. Phys.*, vol. 87, 2000, 5517-5519

[74] E. F. Wassermann, M. Thielen, S. Kirsch, A. Pollman, H. Weinforth and A. Carl, Fabrication of large scale periodic magnetic nanostructures, *J. Appl. Phys.*, vol. 83, 1998, 1753-1757

[75] A. Aharoni, Surface anisotropy in ferromagnetic prolate spheroids, *J. Appl. Phys.*, vol. 87, 2000, 5526-5528